Advanced Steam Measurement Techniques:

A study of how Electrical Capacitance Measurements are affected by the Spatial Positioning of Water within Wet Steam

David Walker B.Sc. (Hons), MIMA, AMIMECHE

Thesis submitted to the University of Nottingham for the degree of Engineering Doctorate in Carbon Capture and Storage and Cleaner Fossil Energy

August 2018

Supervisors: Dr D. Giddings; Dr G. Dimitrakis; Dr S. Barham

Produced in Partnership with the

University of Nottingham

General Electric

Abstract

This thesis gives an overview of the progress and difficulties in developing a better understanding of the effect of spatial positioning of the water phase on the Electrical Capacitance Tomography (ECT) measurement within a water steam mixture, and if this effect is different for an air water mixture.

A novel experiment was proposed and conducted to test the effect of spatial positioning on the ECT measurement, by using a specially designed test rig that allowed for single or multiple droplets to be injected into controlled regions of the diameter of the sensor filled with static dry steam.

In order to control the amount of water injected, an extensive study was conducted to predict and measure the size of droplets injected from different nozzles. The result of this gave rise to a novel way of modifying the Camsizer, to measure individual water droplets instead of dry particles, thus allowing for a droplet diameter measurement system that is able to photograph droplets. Further research was conducted with the measured droplets that theoretically predicted they would be able to survive being dropped through a dry steam environment.

The spatial positioning testing was initially conducted with seven droplets being injected together into air and steam. This gave evidence that the measurement behaviour of water air and water steam mixtures are different for adjacent electrode pairs, by the water steam mixture being more susceptible to spatial positioning of the water phase. The behaviour is similar for opposite electrode pairs, although they were shown to not be susceptible to spatial positioning.

To further improve the accuracy, the testing moved onto single droplet injections in steam. These results showed that opposite electrode pairs are not susceptible to spatial positioning. When the maximum recorded change in relative permittivity was compared to the parallel and droplet models of the permittivity of two phase flows, it was shown that the parallel

model better predicted the results. This effect has also been observed previously within the literature on the work on wet steam.

By modifying a flat plate capacitance model to measure the capacitance between curved electrodes in three dimensions, a novel 3D capacitance calculation program was developed for a four electrode electrical capacitance tomography system, in which to try to predict the measured results. The program was able to convert capacitances calculated to relative permittivity, and was shown to predict them with a difference of 0.18% to the parallel model. However when compared to the measured data for single droplets there was poor correlation.

A program was also built to generate low spatial resolution images of cross sections of the water steam mix within the sensor within the injection time. The results from these images showed that the reconstruction was able to locate the correct region of droplet injection.

Acknowledgements

It has taken me quite a long time to reach this point in my life. I never thought I would end up on this path when I first started years ago studying for my degree in Mathematics. I would like to thank the people that have helped on this journey and to its conclusion.

I would first like to thank my ever patient, soon to be wife Helena, who I owe a great deal to and has always been there for me whenever there is a problem. It has been hard at times throughout this, but the life we have and growing together is the most dearest and precious thing to me, and whatever the challenges in the future we will always face them together.

A big thankyou to my parents who have always been by my side in supporting me throughout this and making life easier for us both when things got difficult. You always believed in everything I did, and gave me the freedom to make the right choices.

It goes without saying that the huge support of the supervisory team have played a massive part in making this project a success. Dr Scott Barham, thank you giving me this chance and for always being able to help, you always knew when to give support and when to step back. Dr Donald Giddings and Dr George Dimitrakis, thank you for your encouragement and expertise over the last four years, especially with your support and time.

This project would not have got anywhere if not for the assistance of the laboratory staff. Thank you so much Mel for all your time with building and modifying the test rig, your work ensured that the rig was always working as it should. Thank you Mick Fletcher, for your constant advice and experience, I am sorry I borrowed Mel for so long, you run a really great team of engineers and are a credit to the university.

Finally thanks Alex Ottway for all of your help in rebuilding and rewiring the electrical capacitance tomography sensor. Whenever it malfunctioned you were always on hand to make it work again.

Contents

Chapter 1. Introduction 1

1.1 Project Aims 1

1.2 Overview 2

Chapter 2. Review of Wet Steam Measurement 4

2.1 Two phase Wet Steam Behaviour 5

2.1.1 Wet steam behaviour throughout the steam cycle 8

2.2 Measurement of Wet Steam within the Low Pressure Turbine 13

2.2.1 Photon Attenuation and Scattering Based Probes 14

2.2.2 Direct Optical Measurement Systems 16

2.2.3 Electrostatic Probes 17

2.2.4 Microwave Probes 18

2.3 Non Invasive Void Fraction Measurement of Wet Steam 20

2.3.1 Photon-Based Radiography and Tomography 21

2.3.2 Neutron-Based Imaging 28

2.3.3 Electrical Capacitance Tomography (ECT) 30

2.3.4 Ultrasonic tomography 33

2.4 Film Thickness and Velocity Measurement Techniques 35

2.4.1 Photons 36

2.4.2 Subatomic Particles 40

2.4.3 Conductance 42

2.4.4 Capacitance 44

2.4.5 Ultrasonic 47

2.5 Conclusions 48

Chapter 3. Recommissioning of the Electrical Capacitance Tomography Measurement System (ECT) 51

3.1 Fundamentals of Electrical Capacitance Tomography (ECT) 55

3.1.1 ECT Data Acquisition System 57

3.1.2 Effect of changing measurement frequency on the Permittivity of Pure Water 60

3.1.3 Generation of Relative Permittivity Measurement and Conversion to Volume Fraction 62

3.2 Electrical Capacitance Tomography Sensor for measuring Steam Wetness 65

3.2.1 TFL R5000 electronics system for the sensor 67

3.2.2 Design of the ECT sensor 70

3.3 Reconstruction and improvement of the Electrical Capacitance Tomography Sensor 71
3.3.1 State of the sensor after previous testing 72
3.3.2 Reassembly of the ECT sensor 74
3.4 Analysis of Changes in Capacitance Measurement within varying Environments 78
3.5 Capacitance measurement program in 3D 87
3.6 Principles of Linear Back Projection 90
3.7 Incorporation of the Tikhonov Regularization LBP method into the Capacitance measurement program 95
3.8 Conclusions 98
Chapter 4. Design, Construction and Analysis of the Droplet Injection System 99
4.1 Droplet Diameter and Formation Time Analysis 102
4.2 The effects of Superheated Steam on a Droplet falling through the Sensor. 109
4.2.1 Temperature rise in the droplets as they fall 113
4.2.2 Droplet Stability analysis 117
4.3 Initial Design of the Droplet Injector Manifold 120
4.3.1 Rejected Injector manifold design 126
4.4 Incorporation of Vacuum Brazing into the Design of the Droplet Injector Manifold 130
4.5 Final Design of the droplet Injector Manifold using the 1/16th inch Tubes 133
4.6 Design and Construction of the Full Droplet Injection System 138
4.7 Incorporation of the Injection Pattern into the 3D Model of the Sensor. 147
4.8 Conclusions 149
Chapter 5. Design and Construction of the Test Rig 150
5.1 Initial Test Rig Designs 152
5.2 Final Experimental Test Rig Design 155
5.2.1 Air Input system 157
5.2.2 Water removal section 158
5.2.3 3D layout of the Test Rig 159
5.3 Construction of the Test Rig 161
5.3.1 Construction of the steam and water removal lines 162
5.3.2 Final Assembly 167
5.4 Steam Control within the completed Test Rig 169

5.5 Conclusions 170

Chapter 6. Results, Analysis and Comparisons 171

6.1 The Testing Procedure 174

6.2 Calibration of the ECT sensor 176

6.3 Raw Capacitance Measurements 186

6.4 Fast Fourier Transform of the Data 189

6.5 Linear Drift Correction 195

6.6 Analysis of the linearly corrected relative permittivity results 198

6.6.1 Average relative permittivity change comparison 200

6.6.2 Change in relative permittivity for single droplets injected into the sensor regions in steam 206

6.7 Comparison of relative permittivity measurements of the opposite electrode pairs to the Parallel and droplet models 209

6.8 Comparison to the results from the 3D Capacitance Program 213

6.9 Spatial Position Imaging 216

Chapter 7. Conclusion 220

7.1 Future work 223

Chapter 8. References 225

Chapter 9. Appendix 242

Test 1 242

Test 2 244

Test 4 (back pressure regulator not used) 246

9.2 Appendix 2: 248

Results for the average change in relative permittivity Results for electrode pairs (1, 4) and (4, 1): 248

Results for electrode pairs (2, 3) and (3, 2): 249

Results for electrode pairs (3, 4) and (4, 3): 250

Results for electrode pairs (2, 4) and (4, 2): 251

9.3 Appendix 3 252

Maximum permittivity change for 1 droplet against the 3D capacitance program results 252

Figures

Chapter 2 Review of wet steam Measurement

Figure 2-1 Diagram of the five different types of flows with the gas content as blue and the liquid orange. (Hewitt 2018) 6
Figure 2-2 Flow regime of two phase flow in a vertical pipe, for liquid momentum flux x axis plotted against gaseous momentum flux y axis (Hewitt & Roberts, 1969) 7
Figure 2-3 Diagram of the different flow regimes for horizontal two phase flow (Hewitt 2018) 8
Figure 2-4 T and S diagram showing the typical steam cycle inside a nuclear power station, note the straight loss of temperature from point 3 to 4 due to no reheat. 9
Figure 2-5 Schematic of a turbine hall setup, note the moisture separator between the LP and HP turbine shown by the red circle (Turbines and Support Systems, 2011) 10
Figure 2-6 Diagram of where the different types of water droplets are formed inside the low pressure turbine (Martínez et al., 2011) 11
Figure 2-7 Structure of a water droplet as it hits a hard surface (K. K. Haller, 2002) 12
Figure 2-8 the portion of the FSSP-100 probe for droplet measurement on the left and the head of the probe for wetness pressure measurement on the right (Cai et al., 2009) 15
Figure 2-9 Structure of the probe portion of the sensor (Jean 2007) 20
Figure 2-10 Interior of the Compact detector arc (Bieberle et al., 2013) 21
Figure 2-11 Normalized experimental data and Monte Carlo simulation data used by Roshani, Nazemi, Feghhi, & Setayeshi for (a) transmission count, (b) total scattering count and (c) Compton edge count, the highest energy that can be deposited (Roshani et al., 2015). 23
Figure 2-12 an example of X-ray stereography showing how an object can be determined in the flow by two different X-ray sources (Theodore et al., 2005) 25
Figure 2-13 the generation 3 Trion detector developed at PTB (Zboray et al., 2014), further details can be found at (Mor et al., 2009) 29
Figure 2-14 Design of the ECT sensor electrode layout surrounding the pipe (Yang et al., 2004) 31
Figure 2-15 different types of electrode setup: diametric tomography and chordal tomography (Brook et al., 2014) 32
Figure 2-16 the arrangement of the electrodes for each meter (Brook et al., 2014) 33
Figure 2-17 Transmitter and receiver setup for the ultrasonic tomograph (Ruzairi et al., 2004) 34
Figure 2-18 two gas bubbles visualised using the linear back projection algorithm, showed by high concentration of gas by the red to green area (Mohd et al., 2012) 35
Figure 2-19 Setup of the laser extinction method for measuring liquid film thickness (Utaka et al., 2004) 39
Figure 2-20 Schematics of experimental setup (Daisuke et al., 2014) 44

Chapter 3 Recommissioning of the Electrical Capacitance Tomography measurement system

Figure 3-1 Layout of a 12 electrode ECT system fitted into a pipe (Wuqiang, 2010) 55
Figure 3-2 Measurement system for a typical ECT setup 56

Figure 3-3 Sensing electronics within an ECT measurement system (Cui et al., 2011). 58
Figure 3-4 Switch circuit in principle (Yang, 1999) 59
Figure 3-5 4 switch circuit demonstrating the solution to the switch coupling capacitance problem (Yang, 1999) 59
Figure 3-6 Relative permittivity change for water, from 330 MHz to 3 THz, from 0 C to 100 C (Water and Microwaves, 2017) data derived from (Franks, 1972) 61
Figure 3-7 Representations of water distribution described by the three models 63
Figure 3-8 The TFL R5000 electronics system (Barham, 2013) 68
Figure 3-9 Removal of the stray capacitance in the immune charge transfer circuit, (a) showing the full circuit, (b) demonstrating how the switches open and close and (c) / (d) illustrating how the stray capacitance is removed between two electrodes (Pląskowski et al., 1995). 69
Figure 3-10 3D model section of the ECT sensor 70
Figure 3-11 The two parts of the PTFE liner, showing where the electrodes are inserted. 71
Figure 3-12 Expansion of the PTFE causing the issues highlighted in the red circles. 72
Figure 3-13 Expansion of PTFE as temperature increases as well as increase in the coefficient of expansion as temperature increases (Kirby, 1956) 73
Figure 3-14 Tubular space assembly after previous testing on the left and how the tubular spacer fits within the electrode assembly on the right. 74
Figure 3-15 Previous electronics connection for the electrode connection rod shown in the bottom left, to the SMB type connector shown in the top right. 76
Figure 3-16 The reassembled ECT sensor, the end caps are what the cables are threaded into and held in place by the screw fitted into each end cap 77
Figure 3-17 Change in potential difference and electric field strength for the sensor with two excitation electrodes in red and two detection electrodes in black. 80
Figure 3-18 The layout of a 2 electrode capacitance sensor (2014) 82
Figure 3-19 The calculation of capacitance between electrodes A and B is split into five parts where the capacitance is calculated between A1 and B1 to A5 and B5, using the average permittivity of each space $\varepsilon 1$ to $\varepsilon 5$ 83
Figure 3-20 Calibration of the capacitance program using known relative permittivies, the blue line is for adjacent electrode pairs and the green line is for opposite electrode pairs. 84
Figure 3-21 Location of the four electrodes, where AB = pair 1, BC = pair 2, BD = pair 3, AD = pair 4, CD = pair 5, and AC = pair 6. 85
Figure 3-22 Comparison of the relative permittivity of different air and water mixtures calculated using the program against the relative permittivities predicted by the series, parallel and droplet model. 86
Figure 3-23 Comparison of the relative permittivity of increasing volume fractions of water within air calculated using the 3D program, against the relative permittivities predicted by the series, parallel and droplet model. 88
Figure 3-24 Plot of relative permittivity change over time for a volume fraction of $3.09 \times 10\text{-}5$ passing through the sensor four times, measured using electrode pair 1 89
Figure 3-25 Electrode sensitivity maps 92
Figure 3-26 Potential difference maps showing where the water is located within the sensor. The bar to the right of the image is the potential difference. 96

Figure 3-27 LBP using the Tikhonov Regularization for the two respective droplet locations 97

Chapter 4 Design, Construction and Analysis of the Droplet Injection System

Figure 4-1 Demonstration of the angle from the inner wall of the needle. 102
Figure 4-2 The eight needles used for testing, the G refers to the scale which is in the Birmingham gauge. 103
Figure 4-3 Predicted droplet radii, calculated from the nozzle radii (internal radius) for each needle 105
Figure 2-4 Droplet diameter measurement setup; 1. Is the Gilson pump, 2 is the needle holder, 3 is the pure water and 4 is the Camsizer. 106
Figure 4-5 Predicted droplet radii plotted against measured droplet radii produced from the eight needles. 107
Figure 4-6 Still images captured using the Camsizer, showing a droplet produced from a 27g nozzle and a droplet produced from a 16g nozzle 108
Figure 4-7 the velocity of the droplets as they fell through the three different steam conditions of 10 Bara 181°C, 11 Bara at 184°C and 12 Bara at 190°C 111
Figure 4-8 Reynolds number plotted over the time the droplet fell through the three different steam conditions of 10 Bara 181°C, 11 Bara at 185°C and 12 Bara at 190°C 112
Figure 4-9 Amount of energy required to heat the droplet at each time step of length 0.001 seconds 114
Figure 4-10 Temperature increases of the different size droplets over 0.205 S 115
Figure 4-11 Temperature change as droplets are injected into steam at 160°C 116
Figure 4-12 Weber number for droplets produced by the 16G and 27G nozzle traveling through steam at 10, 11 and 12 Bara 118
Figure 4-13 Biot number plotted for every time step of 0.001 seconds for a droplet within 10, 11 and 12 Bara of superheated steam 119
Figure 4-14 The 2D velocity profile within the nozzle 121
Figure 4-15 Velocity change as the nozzle size and the amount of injectors increases. 122
Figure 4-16 Droplet formation times for the measured droplet diameters using 5, 10, 20, 40 and 80 injectors. 123
Figure 4-17 Dryness fractions produced by 5, 10, 20, 40 and 80 droplets of different radii injected into steam with a pressure of 12 Bara 126
Figure 4-18 The first design for the droplet injection manifold 128
Figure 4-19 How the droplet injection manifold connected to the sensor 129
Figure 4-20 How the tensile strength of a joint changes with thickness (Handy and Hardman 2001) 130
Figure 4-21 Design of a custom 34 gauge tube injector that could be made using vacuum brazing 131
Figure 4-22 Layout of the holes for the blind flange utilising vacuum brazing 132
Figure 4-23 Measured droplet radius produced from the 1/16th inch tube shown in red against the predicted radius shown in yellow 133
Figure 4-24 Dryness fraction for a plane of droplets produced by 1, 7, 14, 21 and 28 injectors using 1/16th inch tubes 135

Figure 4-25 View looking directly down upon the sensor, quadrant A is red, quadrant B is blue, quadrant C is brown and quadrant D is yellow. The steam bleed line and air line are shown in black. 136
Figure 4-26 Sideways view of the final design of the droplet injection manifold 137
Figure 4-27 Layout of the seven and five way ball valves (Swagelok) 138
Figure 4-28 Line layout showing feeder system for quadrant D and location of the 2 way ball valves 139
Figure 4-29 CAD drawing of the initial quadrant flow splitter with the added needle valves. 140
Figure 4-30 Full design of the droplet injection system 141
Figure 4-31 Constructed initial flow rate splitter, where 4 controls quadrant D, 3 controls quadrant C, 2 controls quadrant B and 1 controls quadrant A. 142
Figure 4-32 Measured mass flow rate over 1 minute for the quadrants and the central injector with the needle valves ¾ tightened 143
Figure 4-33 Tube length measurements for the water injection system 144
Figure 4-34 Calculated mass flow rates ml/min for each injector assuming equal flow rate split. 145
Figure 4-35 Formation times for each injector assuming equal division of the volumetric flow rate 146
Figure 4-36 Droplet injection pattern into the model for a maximum of six droplets being injected into each quadrant 147
Figure 4-37 Six droplets injected in steam into each of quadrants A, B, C and D as well as the central injector 148

Chapter 5 Design and Construction of the Test Rig

Figure 5-1 Designs of the gasket failure test rig using an oven or heating tape by Veiga et al., (2009) 153
Figure 5-2 Initial design using electric heating tape and blankets 154
Figure 5-3 Final schematic for the droplet injection test rig 156
Figure 5-4 Cross section of the water removal section 158
Figure 5-5 3D layout of the relief valve, pressure transducer and needle valve two 159
Figure 5-6 3D CAD model of the test rig, laid out in the ideal way 160
Figure 5-7 Outline of the selected Nabertherm oven with the selectable hole positions for each side (Nabertherm 2018) 161
Figure 5-8 Water removal section constructed 162
Figure 5-9 A non-insulated pipe where r1 is the radius from the centre of the pipe to the inner wall, r2 is the radius of the centre of the pipe to the outer wall, T1 is the temperature inside the pipe and T2 is the temperature on the outside of the pipe (Engineers Edge 2018). 163
Figure 5-10 Insulated pipe where T3 is the temperature on the outside of the pipe and r3 is the radius of the pipe through all the insulating material. (Engineers Edge 2018). 164
Figure 5-11 Heat transfer rate as the insulation thickness increases 165
Figure 5-12 Zoomed in change in insulation against heat transfer rate starting with an insulation thickness of 0.004 m. 165
Figure 5-13 Left side of the oven with the steam removal and the injection sections shown 166

Figure 5-14 Fully assembled rig inside the oven with the ECT system, droplet injection system, air injection system and the water/steam removal section fitted together. 167
Figure 5-15 Test rig workbench setup showing each of the components 168

Chapter 6 Results, Analysis and Comparisons

Figure 6-1 The 11 different injection patterns, red denotes region A, blue denotes region B, brown denotes region C and yellow denotes region D. 175
Figure 6-2 Relative permittivity change with temperature at constant pressures 178
Figure 6-3 Relative permittivity change with pressure at constant temperature 178
Figure 6-4 Pressure change during testing, where test 1 and 2 are the ones where the back pressure regulator was used and 3 and 4 are where the steam was left to condense 179
Figure 6-5 Capacitance recording for the four tests using electrode pair (1, 3), where the first number denotes the circuit used in the recording system 180
Figure 6-6 Capacitance recording for the four tests using electrode pair (2, 3) 181
Figure 6-7 Capacitance plotted against calculated relative permittivity for non-reversed opposite and adjacent electrode pairs using IAPWS -97 182
Figure 6-8 Capacitance plotted against calculated relative permittivity for reversed opposite and adjacent electrode pairs using IAPWS -97 183
Figure 6-9 Capacitance measurement trace for electrode pair (2, 3) and (3, 2), for droplets injected in section A into superheated steam under 10 Bara, detailing the three parts of the tests. 186
Figure 6-10 Corrupted capacitance measurement example using the result from electrode pair (1, 4) and (4, 1) for droplets being injected into section A in 10 Bara 187
Figure 6-11 Variance for electrode pairs (1, 4) and (4, 1) baseline 188
Figure 6-12 baseline for steam under 10 Bara for pair (2, 3) for 2 seconds 191
Figure 6-13 Example signal containing a 50 Hz sinusoid of amplitude 0.7 and a 120 Hz sinusoid of amplitude 1 with random noise added 191
Figure 6-14 FFT of the signal in figure 2, showing the two waves at frequency of 50 Hz and 120 Hz 192
Figure 6-15 FFT of the modified signal with the additional sinusoidal waves at 340 and 450 Hz. 192
Figure 6-16 FFT of the signal with an increased number of sampling points caused by increasing N to 100000 193
Figure 6-17 FFT result from the raw capacitance data of 7 droplets injected into section A under 10 Bara 194
Figure 6-18 FFT of the raw data with an added sinusoidal wave of 400 Hz, to see if it is detected on the FFT 194
Figure 6-19 Relative permittivity measurement against time for electrode pair (2, 3) and (3, 2), not linearly corrected 195
Figure 6-20 The procedure for linearly correcting each of the test results using the known relative permittivity of superheated steam from the baseline. 196
Figure 6-21 The measurement drift of the electronics over 6 hours for electrode pairs (2, 3) and (3, 2) 197
Figure 6-22 Extra two injection patterns to test the effect of the high flowrate injector 198

Figure 6-23 Results of the comparative tests to determine the effect of the higher flow rate injector 199
Figure 6-24 comparison of the average change in relative permittivity for electrode pairs (1, 2) and (2, 1) for droplets injected in steam at 10, 11 and 12 Bara and air at 4.27, 4.68 and 5.08 Bara. 201
Figure 6-25 Comparison of the average change in relative permittivity for electrode pairs (1, 3) and (3, 1) for droplets injected in steam at 10, 11 and 12 Bara and air at 4.27, 4.68 and 5.08 Bara 202
Figure 6-26 Significant differences 10 Bara steam vs 4.27 Bara air 204
Figure 6-27 Significant differences 11 Bara steam vs 4.68 Bara air 204
Figure 6-28 Significant differences 12 Bara steam vs 5.08 Bara air 205
Figure 6-29 Maximum relative permittivity change for 1 droplet injected in section A, B, C, D, and central at 10, 11 and 12 Bara. 207
Figure 6-30 Difference between the maximum change within the injection time for the centre, A, B, C, and D against predicted by the droplet and parallel models for 10 Bara. 210
Figure 6-31 Difference between the maximum change within the injection time for the centre, A, B, C, and D against predicted by the droplet and parallel models for 11 Bara. 210
Figure 6-32 Difference between the maximum change within the injection time for the centre, A, B, C, and D against predicted by the droplet and parallel models for 11 Bara 211
Figure 6-33 Change in relative permittivity for a single droplet injected in each region at 10 Bara compared to the results calculated by the program 214
Figure 6-34 Change in relative permittivity for a single droplet injected in each region at 11 Bara compared to the results calculated by the program 214
Figure 6-35 Change in relative permittivity for a single droplet injected in each region at 10 Bara compared to the results calculated by the program 215
Figure 6-36 7 droplets injected into section C at 10, 11 and 12 Bara 217
Figure 6-37 LBP of each of the 11 injection patterns into steam at 12 Bara 218

Tables

Chapter 3 Recommissioning of the Electrical Capacitance Tomography measurement system

Table 3-1 Comparative table showing relative permittivity resolution from the droplet and parallel models and wetness resolution at different pressures. (Barham, 2013) 55

Chapter 4 Design, Construction and Analysis of the Droplet Injection System

Table 4-1 Dimensions of the eight needles that will be used for testing 104
Table 4-2 Mass flow rate per injector for 5, 10, 20, 40 and 80 injectors 110
Table 4-3 Mass flow rate per injector for 5, 10, 20, 40 and 80 injectors 121
Table 4-4 Dryness fraction after one second of water injection 125
Table 4-5 Formation times for 1, 7, 14, 21 and 28 droplets from 1/16th inch tubes 134

Chapter 5 Design and Construction of the Test Rig

Table 5-1 Different initial masses of water to achieve 10, 11 and 12 Bara of steam pressure 169

Chapter 6 Results, Analysis and Comparisons

Table 6-1 Gradients for each regression model for each electrode pair 184
Table 6-2 Y intercepts for each regression model for each electrode pair 184
Table 6-3 Regression model equation for each electrode pair 185

Chapter 1. Introduction

This thesis details a project that builds upon the previous work of steam wetness measurement by Scott Barham (Barham, 2013), by using his developed prototype sensor to determine the effect on the electrical capacitance measurement by the spatial positioning of the water present within wet steam, and how the magnitude of the effect changes when an air and water mixture is used.

This chapter initially gives an overview of the project aims and specification, after which giving an introduction to why the project is required and the effect on the underlying problem of wet steam measurement.

1.1 Project Aims

This piece of work was completed in partnership with General Electric and the University of Nottingham, and was focused on improving the accuracy of wet steam measurement using an electrical capacitance tomography sensor (ECT), developing an understanding of how the spatial positioning of water within wet steam affects the electrical capacitance measurement.

Project Summary:

This research is on the effect of the electrical capacitance measurement between electrode pairs within a four electrode ECT sensor, when the spatial positioning of a set volume of water is altered within a set volume of dry steam and within an identical volume of dry air.

The overall goal of the project is to develop an understanding of the effect of spatial positioning and thus show that it does not impede the accuracy of wet steam measurement using an ECT sensor, such as the one previously developed.

The secondary longer term aim is to produce a program that can accurately predict the effect of spatial positioning for wet steam under varying pressures and temperatures, for ECT sensors with different numbers of electrodes

1.2 Overview

The current method of measuring wetness in high pressure steam flows is by using radioactive tracer technology; this is a mature technology that is currently used by the industrial sponsor and is internationally recognised as the best current technology for determining steam wetness in nuclear power stations.

The method measures the moisture content of the wet steam also known as steam wetness, by measuring the liquid mass flow rate within the wet steam between two points. The total wet steam flow rate and the steam wetness are then calculated using heat and mass balances over power station equipment. A key overview of how this technique is applied to measure steam quality in a boiling water reactor was given by Hary (1959), who showed that the steam quality can be calculated by 1 minus the activity ratio, this is defined as the radioactivity in the steam and water mixture divided by the radioactivity in an equal volume of reactor feed water.

It has been shown that it is possible to measure the mass flow of the liquid phase in wet steam with an accuracy of +/- 0.5% (Yamada & Lindberg, 2008). The technique was first developed for wet steam flows with the work by Herzog *et al.*, (1972). Since the work of Herzog *et al.,* the technique is used by a number of companies to accurately determine the efficiency of their system. The major drawback is that it cannot be used as feedback system, as the technique is only suitable for short measurement times with the standard length of a measurement being <1 hour.

Therefore, a new method of measuring steam wetness was required, which could measure the system in time to create a feedback loop, thereby increasing the efficiency of the steam cycle within a nuclear power station. Thus, greater plant overview and a better understanding of wet steam through the cycle would mean that a nuclear power station could run smoother, more efficient and would require less down time. As an example, the effect of a small percentage increase in power output on a current nuclear plant such as

the soon to be built Hinkley Point C, a 0.1% increase in output would equate to an additional 3.2MW of extra power. Over a year this would produce up to 24GW hours of extra energy (Barham, 2013), (assuming 44 weeks of running a year, with 8 weeks maintenance shutdown).

A new technique was proposed developed by Scott Barham, who proposed using an electrical capacitance tomography system (ECT) to detect changes in the relative permittivity of the wet steam as the volume of the water phase of the steam was increased or decreased in wetness. This system was built and tested at a prototype level, and showed that it was possible to measure steam wetness with an accuracy of ± 0.5%.

During testing, it became apparent that the behaviour of the steam water mixture gave a much higher change in relative permittivity than measuring an air water mixture. The steam water mixture showed little susceptibility to spatial positioning of the water phase. This is of great importance, because if the change in relative permittivity for a steam water mixture is easier to detect, then at the operating pressure of 70 Bar inside a nuclear power station, it would make the sensor more sensitive to changes in water volume contained within the steam.

Because of this need to understand the behaviour change, this study was proposed to tackle the problem of how the spatial positioning of water affects the measurement of the relative permittivity change using the previously discussed ECT system, and to see if the behaviour of the measurement of a steam water mixture is indeed different from an air water mixture.

The first step in this project is to identify the key ideas behind wet steam measurement, such as: what is wet steam; how it behaves as a two phase flow, and how the wetness can be calculated. Secondly, a review is required to show the other methods of steam wetness measurement that are also available, and how they could be applied to wet steam measurement, these concepts will be discussed in the next chapter.

Chapter 2. Review of Wet Steam Measurement

Nomenclature

A Absorbance of the material

E Error

F Neutron radiant fluence

G Grey scale

G_0 Offset term of the grey scale

h Heat transfer coefficient

h_f Heat of vaporisation

$C\phi_{th}$ Incident neutron flux

g Gravitational acceleration $[m^2/s]$

k Thermal conductivity $\left[\frac{W}{mK}\right]$

D Diameter [m]

j Velocity $[s^2m]$

L Length of the flow [m]

N Number of frames

Nu Nusselt's number

I Transmitted intensity

T Temperature

ρ Density $[kg/m^3]$

μ Linear absorption coefficient

x Thickness

δ Film thickness of liquid [mm]

Σ_l Total microscopic cross section of the liquid phase

η Viscosity [kg/ms]

Subscripts

1 Reference phase 1

2 Reference Phase 2

l Liquid

c Condenser

w Wall

v Vapour

It was shown in the literature that it would be an annular mist flow, with water droplets entrained within the centre of the flow and a liquid film travelling along the inside wall of the pipe, due to the steam being below boiling point of water under the respective pressure. The literature showed that the flow structure could change depending upon the steam wetness. Therefore the change in the wet steam behaviour throughout the steam cycle of a nuclear power station was accessed. This highlighted areas where wet steam measurement had been thoroughly researched, such as within the low pressure turbine. The review also demonstrated that monitoring the steam in real time at key points, such as before, during and after the turbines, could provide data that could be used to control a feedback loop improving the efficiency of the steam cycle.

As the current technique using radioactive tracer technology could not be used, a new system was required. The research pointed towards using a combination of void fraction, film thickness and film velocity measurement to accurately determine the mass flow of the liquid phase within the wet steam, measuring the steam wetness.

This chapter is split up into five sections, where section 1 details what the behaviour of wet steam is within a nuclear power station throughout the steam cycle. Section 2 discusses how wet steam is measured within the low pressure turbine. Section 3 explains the techniques that can be used to measure the void fraction of a two phase flow. Section 4 details how the liquid film velocity and thickness can be measured.

2.1 Two phase Wet Steam Behaviour

A fine balance between the pressure and temperature of the steam is required to maintain the desired steam wetness and steam quality. These two measures of the wet steam depend upon the mass flow of the liquid phase, the mass flow of the gaseous steam phase and the total mass flow of the wet steam. Equations 2.1 and 2.2 define these two concepts:

$$Steam\ quality = \frac{mass\ flow\ steam\ vapour}{total\ mass\ flow\ of\ wet\ steam} \tag{2.1}$$

$$Steam\ Wetness = \frac{mass\ flow\ liquid\ phase}{total\ mass\ flow\ of\ wet\ steam} \tag{2.2}$$

From these principles the two phase flow can be further divided into two main groups, flow pattern regimes for vertical flows and flow pattern regimes for horizontal flows. For vertical flows there are five main types, these are illustrated below:

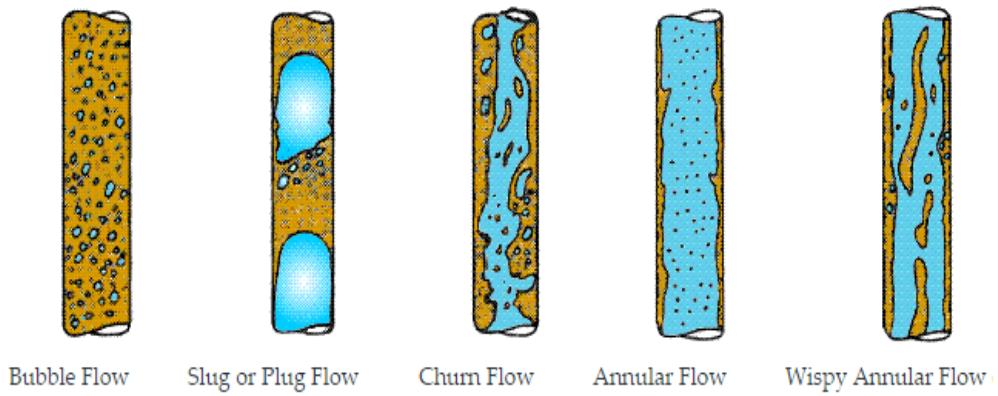


Figure 2-1 Diagram of the five different types of flows with the gas content as blue and the liquid orange. (Hewitt 2018)

Water that is at the point of boiling inside a vertical tube starts as bubbly flow, where there is a large liquid content at a high flow rate and a small gaseous content at a medium flow rate. From here as the water is heated further, the size of the gaseous phase increases until there are singular large slugs that span the diameter of the pipe, at this point the flow regime is known as slug flow. As the void fraction of the flow begins to increase and the speed of the gaseous phase rises, the slugs form together creating a turbulent gaseous central column that drags the remaining liquid along inside the flow, this is known as churn flow. When the gaseous phase's velocity rises beyond a certain point which is dependent on the overall flow rate, the remaining liquid is dragged along as entrained droplets, in the centre of the flow and as a thin

wavy film along the edges of the pipe, this flow regime is known as annular flow. If the liquid phase is at a high enough speed, then the droplets entrained in the flow can form together into wisps of liquid that are carried along, this final regime is known as wispy annular flow.

These regions are shown in figure 2.1, where the momentum flux of the liquid phase is plotted against the momentum flux of the gaseous phase. This work was first completed in 1969 by Hewitt and Roberts, whereby using x-rays and photography were able to identify the different flow regimes of a two phase flow inside a vertical pipe (Hewitt & Roberts, 1969).

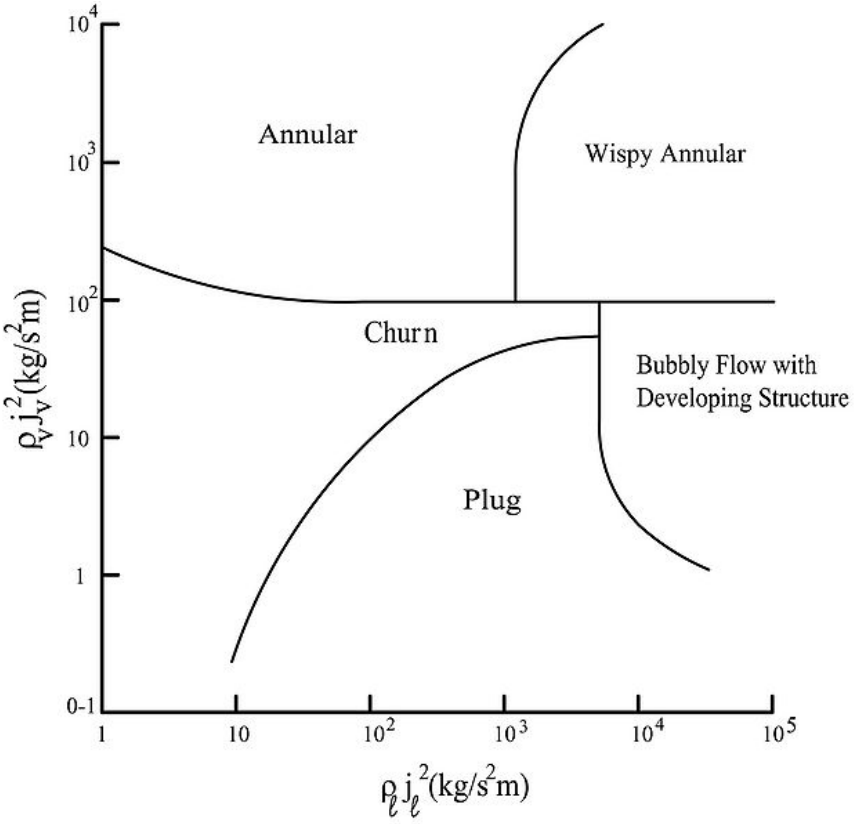


Figure 2-2 Flow regime of two phase flow in a vertical pipe, for liquid momentum flux x axis plotted against gaseous momentum flux y axis (Hewitt & Roberts, 1969)

For horizontal pipes there are similar flow regimes, the only differences being that there is one extra flow regime known as stratified flow, where at low liquid speeds gravity separates the two phases, in which with a low

gaseous speed the liquid has no waves and is smooth while at high gaseous speeds wavy stratified flow develops. The second difference is that plug flow is separate to slug and describes smaller bubbles that are carried along in the liquid phase, but do not cross all of the pipe's diameter. Figure 2.3 demonstrates the different horizontal flow regimes.

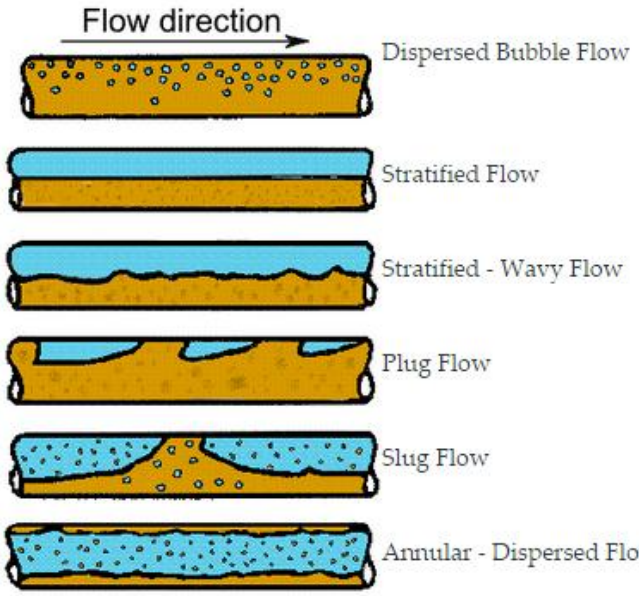


Figure 2-3 Diagram of the different flow regimes for horizontal two phase flow (Hewitt 2018)

There are differences from horizontal to vertical two phase flow, this is due to the influence of gravity upon the liquid phase, which is clearly evident when the film of liquid is considered inside the pipe when there is annular flow, and the liquid film is thicker at the bottom of the pipe and thinnest at the top. The next stage is to see how the steam develops as it passes through the cycle inside a power station, and what flow regime it will have when it enters the low pressure turbine.

2.1.1 Wet steam behaviour throughout the steam cycle

In the case of nuclear power stations the heat used to drive the steam cycle is produced by an overlap with the cooling system of the nuclear reactor, different types of reactors have ether a single heat transfer system that directly becomes part of the steam cycle, called a boiling water reactor (BWR),

or the more efficient and common type which is to have two cycles, pressurised water reactor (PWR), one which takes heat away from the reactor and transfers it via tubes to the integrated steam cycle.

Once one of the cycles has transferred heat energy to the water, the less than 1% wet steam flows through the high pressure turbine, as it is not super-heated it has a wispy annular flow regime, this means that it will lose energy causing the formation of larger droplets. This process is further exaggerated because in a nuclear power station there is no reheat, so the steam straight away passes into the low pressure turbine stages. This process is shown below in figure 2.4:

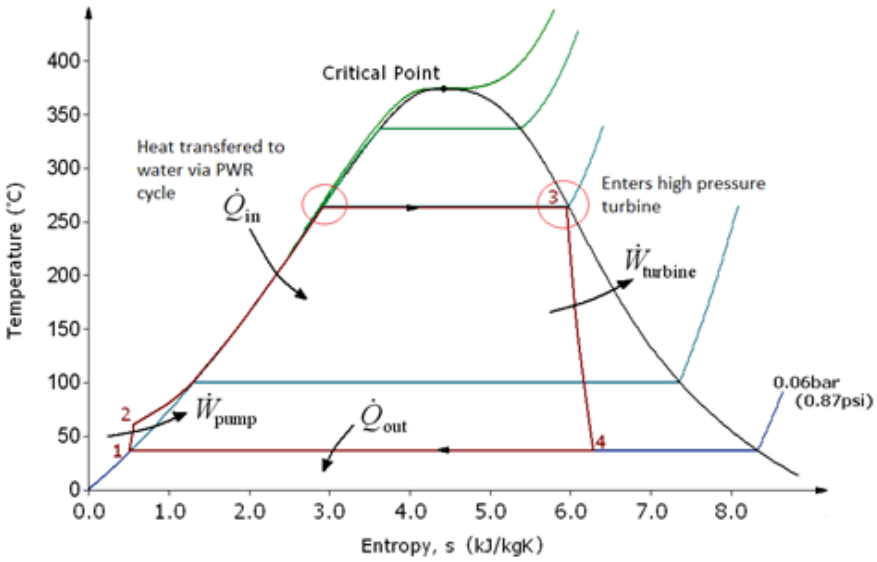


Figure 2-4 T and S diagram showing the typical steam cycle inside a nuclear power station, note the straight loss of temperature from point 3 to 4 due to no reheat.

There is a real danger of blade erosion and pitting happening due to the presence of water as an annular flow in the last stage of the low pressure turbines; this danger is present for both nuclear and conventional power stations.

To extract as much energy as possible from the steam, a standard plant uses three stages of low pressure turbines, the first stage is not directly connected to the high pressure turbine, instead steam flows into a moisture separator with a temperature of 170 degrees at 900KPa containing 10% moisture, the separator removes the moisture meaning steam enters the low pressure turbine at 170 degrees with a pressure of 900Kpa, at the back end of the third stage exhaust steam exits to a condenser at a temperature of 35 degrees at 5Kpa with 10% moisture content (Bereznai 2005), the schematic below gives details on a turbine set-up.

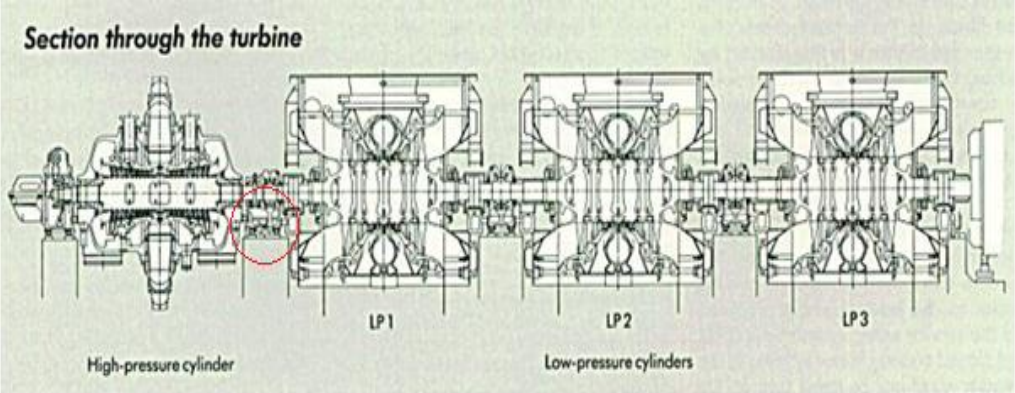


Figure 2-5 Schematic of a turbine hall setup, note the moisture separator between the LP and HP turbine shown by the red circle (Turbines and Support Systems, 2011)

Steam becomes less dry as it loses thermal energy and pressure, this process will occur inside a low pressure turbine as the steam passes through each stage of blades. At each stage the steam will lose energy due to work being performed on the turbine blades, this energy loss causes water droplets to form and a film of liquid to flow across blade surfaces. Martínez et al., (2011) looked into this process and tried to find out where nucleation of water droplets occurs inside a low pressure turbine, from a intial review they found that there are specific regions in the low pressure turbine where different types of water droplets are formed, which are either homogenous or non-homegenous droplets, the diagram 2-6 on the next page shows these regions.

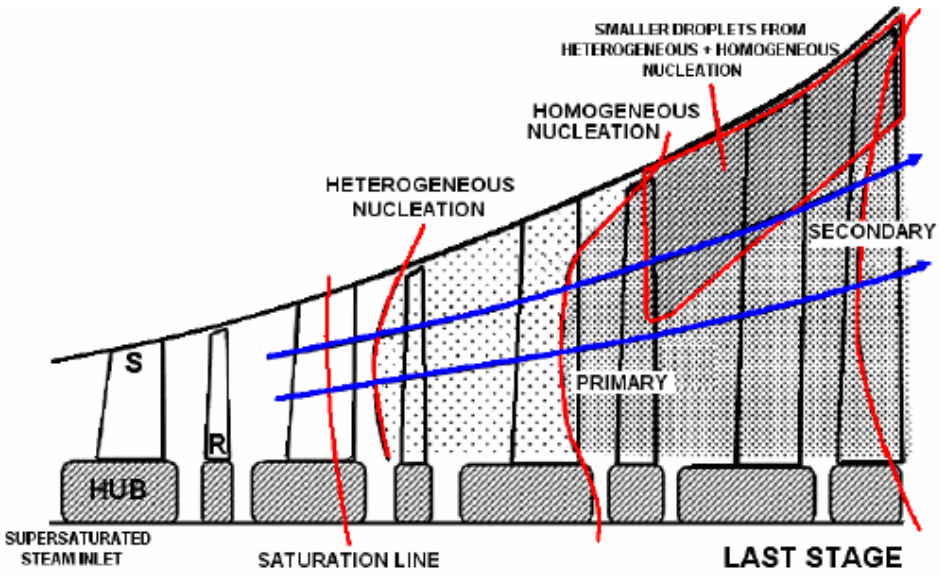


Figure 2-6 Diagram of where the different types of water droplets are formed inside the low pressure turbine (Martínez et al., 2011)

As the diagram shows, there are two different types of droplets formed inside the low pressure turbine; the first type produced are from heterogeneous nucleation which is where droplets are produced as steam below the saturation point comes into contact with the surface of the rotors and stators, homogeneous nucleation is where the steam has lost enough energy to allow water molecules to stay close enough together for surface tension to take effect causing the formation of microscopic droplet, finally as the steam enters the last stage the two effects combine together to form smaller droplets as well as the larger ones from below. These droplets are responsible for the erosion rate of a turbine blade. A PhD investigation was performed by Haller on the effects of droplets hitting a rigid surface, his work showed that droplets will cause damage due to a shock front and pressure difference (Haller, 2002).

The structure of a droplet impact with a hard surface is explained with the following diagram.

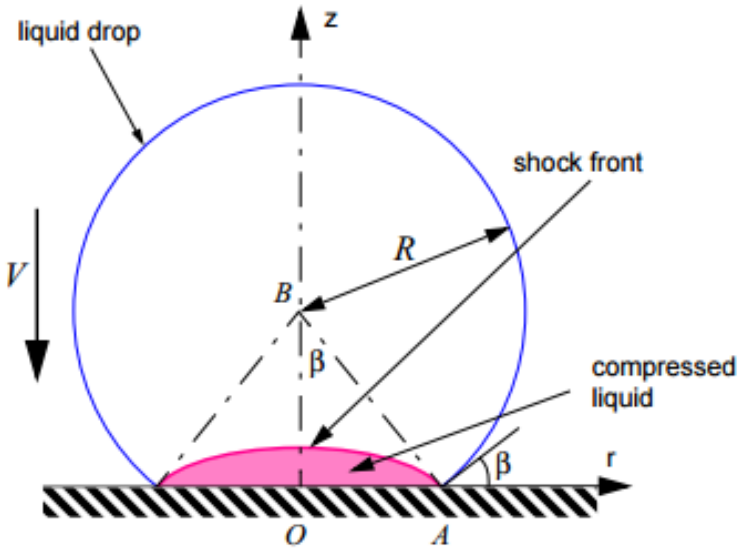


Figure 2-7 Structure of a water droplet as it hits a hard surface (K. K. Haller, 2002)

These problems were looked into by Ryzhenkov, Lebedeva, and Mednikov in 2011, where they observed erosion rates on last stage blades made by most of the leading turbine blade manufactures including Alstom, they found that the erosion rate was linked to the amount and size of droplets present in the flow.

This behaviour of the wet steam produces moisture damage that becomes the main reason why a low pressure turbine blade would fail. To counter this, techniques have been developed that measure the steam quality and steam wetness within the low pressure turbines. The next section will discuss the array of methods that have been utilised.

2.2 Measurement of Wet Steam within the Low Pressure Turbine

Once the steam is inside the turbine, it is imperative that continuous monitoring of quality is maintained. By the beginning of the 1960's, the process of water vapour condensation was quite well understood; an analysis conducted in 1954 highlighted the progress of research into water vapour condensation in high speed flows. The research by Wegener (1954) allowed for the prediction of the nucleation rate of droplets within the condensing flow. This also gave rise to a method of calculating thermodynamic properties using only the static pressure and the channel geometry. When water droplet formation was applied to steam turbines it indicated methods by which the erosion of the turbine blades can occur. This process was further explored by Gardner (1963) whereby the history of the research was reviewed and possible explanations for erosion patterns were given. Some of the most important findings were the calculations and experiments that indicated that large droplets are mainly produced by the stators; the effect of this means that due to their size, they do not flow within the steam flow over the rotor blades, and instead impact the blades, becoming the main cause of droplet erosion.

Therefore, measurement of this droplet phase is extremely important to be able to better understand the causes of heterogeneous and homogeneous nucleation, as well being able to better predict the effects upon the low pressure turbine over time, and to be able to calculate the liquid fraction of the steam. The current knowledge of droplet phase measurement within a confined and complex moving geometry, as distinct from void fraction measurement in a pipe, is compiled into the following sections: photon attenuation and scattering; direct optical measurement; Electrostatic and microwave.

2.2.1 Photon Attenuation and Scattering Based Probes

Photon based probes can use a number of techniques such as forward scattering spectrometry, X-ray and visible photography, attenuation methods or techniques using holographic and microvideographic probes. These methods can then be split into two groups: those that look at the flow locally, droplet by droplet, and those that look at the difference in the scattering of light caused by different sizes of droplets. Focusing on light scattering based probes, the technique is best suited for fine droplet sizes.

Early investigations focused on calibrating the equipment using metal and metal oxide clusters to represent different droplet sizes. Moses and Stein (1977) used laser light scattering to measure droplet growth at the phase of homogeneous nucleation. They found excellent agreement throughout the measurements with nucleation rate expression and the droplet growth model by Gyarmathy (1963) and (Gyarmathy and Meyer 1965). This was expanded further by using Forward Scattering Spectrometer Probes (FSSP) developed by Knollenberg in 1981. They published a series of papers whereby the use of the probes on droplets of different sizes and speeds was analysed (Dye and Baumgardner 1984). Using a 632.8 nm laser beam for each probe, they demonstrated measurement differences between various probe applications, including scattering angles over which light is collected and the focal length of the collecting lens. This process highlighted uncertainties with calibration and showed that limitations of the probes are down to electronic response, optical resolution and calibration uncertainties. The last paper in the series concentrated on time response and the laser inhomogeneity (Baumgardner and Spowart 1990). The findings demonstrated that as airspeeds exceeded 50 ms^{-1} the size of the droplets were underestimated and the size distributions became broader due to the non-uniformity of the laser beam. To counter these uncertainties an improved version was developed, the fast Forward Scattering Spectrometer Probe (FSSP). Brenguier *et al.*, (1998) tested the fast-FSSP on droplet size distribution to see how the accuracy was improved. Each of the previous uncertainties were analysed, showing improvements upon the

standard FSSP. Additional variables such as pulse duration and interarrival times between measurements were shown to be useful for further improvement of the sizing of the particles. Finally, there was a clear distinction between the standard FSSP and the improved FSSP, whereby the improved could show higher concentrations of droplets within a smaller range.

In 2005 the Forward Scattering Spectrometer Probe – 100 (FSSP -100) was tested to produce procedures that could correct instrumental artefacts in droplet measurement (Coelho *et al.,* 2005). The correction procedures were tested with a model that reproduced some of the key features. An improved system was developed that was based upon measuring the attenuation rate of light, and had a pressure measurement tip; this probe was used to measure local wetness, total wetness of exhaust steam and the size distribution of fine droplets (Cai *et al.,* 2009). The measurement head has four holes and is wedge-shaped. Figure 2.8 shows the probe can be rotated within the flow at 0.5 degrees and inserted by steps of 0.5 mm.

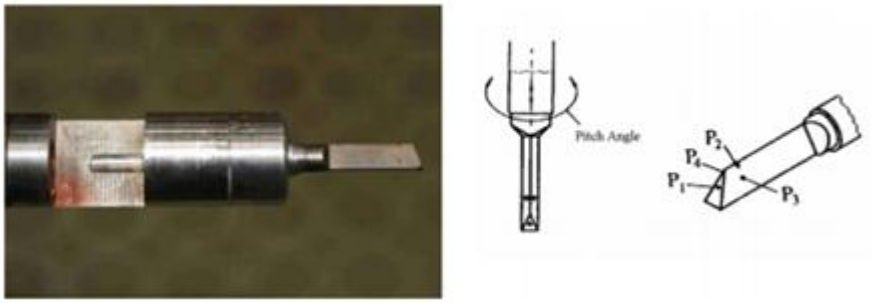


Figure 2-8 the portion of the FSSP-100 probe for droplet measurement on the left and the head of the probe for wetness pressure measurement on the right (Cai et al., 2009)

The combined probe was able to show that the local wetness in the middle region of the blade is twice that of the hub and tip regions. The probe gave the mean diameter of fine droplets to be 0.8 μm. Another novel method for measuring light scattering caused by droplets was developed, called an Optical Backscatter Probe. The probe has the ability to measure droplets from

40 to 100 μm at speeds of up to 200 ms^{-1} (Bosdas *et al.,* 2016). A droplet generator was used to calibrate the probe, the error with size was ±4.7 μm with a speed error of 2.3 ms^{-1}. The probe was used in an axel turbine test facility (LISA), where it showed that as airflow increased, the droplet diameter decreased. Finally if the turbine has a part load condition then droplet velocity increases by 40% and erosion can increase by as much as 32 times. Therefore the advantages with this type of probe is that it is possible to measure single droplets and steam wetness together. Coupled with being able to rotate and alter the position of the probe, using a suitable computer system it would be possible for real time measurements.

2.2.2 Direct Optical Measurement Systems

Another way of optically viewing the flow patterns and droplets, can be by individually viewing them using photography; an early investigation into two phase flow pattern photography was conducted by Hewitt and Roberts who looked at X-ray radiography and flash photography (Hewitt and Roberts 1969). They were able to identify the flow regimes plug, churn, annular and wispy annular flow. An advancement of the process is holography, where a particle is illuminated by a laser and a sensitive film records the light scattered by the object of a reference beam. The process was investigated in depth on a wide variety of experiments. Belz and Menzel (1977) analysed particles and liquid droplets using holography. In particular they compared the quality of the reconstructed data with the effect on image quality. Their results showed that turbulence was an issue which caused a mottling effect on the background and caused difficulty recognising objects. This highlighted the problem in a low pressure turbine of taking images of a foggy, high density, very turbulent flow. To overcome this Kleitz and Courant (1989) used a more advanced holographic probe that analysed the images of coal particles using a video circuit which displayed the results in a histogram. The team also used a "Microvideographic" probe, which they developed to be used in higher droplet densities and could be made much simpler, due to working with white light and not having to use a ruby or YAG (Yttrium Aluminium Garnet) laser.

Due to the discussed limitations of holographic probes, a better method was required to measure high density droplet flows with high turbulence. Photographic methods were shown to be useful in validating condensing flow theory (White *et al.,* 1996). A previous review of wet steam measurement techniques (Kleitz and Dorey 2004) highlighted the use of shadowgraphy and the working principles of the Microvideo probe.

Shadowgraphy works due to droplets appearing as dark spots on a clear background; the blurriness of each droplet depends on how out of focus the droplet is and its size. A CCD camera records the images for real time analysis. The results are given by a histogram with a range of measurement between 5 and 500 μm. The video images are analysed between 10 and 25 Hz. An extensive study into using a photographic probe that used shadowgraphy was carried out on wet steam by Vernon (2014). The work detailed the first time that LED illumination was used inside a probe, this had the advantage of removing motion blur of the droplets.

To conclude, photographic methods of measuring droplet size of wet steam, give useful insights into the effects of condensation inside a low pressure turbine. They allow for visualisation of droplets produced through heterogeneous and homogenous nucleation, giving a clear view of the different condensation regions. However, direct optical measurement has the drawback of not being able to calculate the total or local steam wetness. Other techniques such as electrical or microwave based would be more suited.

2.2.3 Electrostatic Probes

Early tests of droplet size measurement in water sprays were conducted in the 1960s, based upon work by Gardiner (1964); Thorpe and Wood (1967) analysed the best way to measure droplets in the low pressure stage of a 350 MW steam turbine. They decided upon using an invasive electrostatic probe, which protruded into the flow so that half an inch of wire was exposed as the detection area. Their results showed that droplets from 50-200 μm could be detected. However, there were problems and limitations

with the probe, this was because a defect of the design caused a film of liquid to alter the signal, and accuracy of large droplet sizing to become an issue. An accurate method was developed that was used to measure bubble sizes inside a bubble column (Yamashita *et al.,* 1979). The probe worked by having two electrodes; one, a barbed tip of wire and the other, a platinum wire used as the insulated conductor. They were able to determine the shape of the bubbles and sizes ranging from 2 to 12 mm. These results were tested against a photographic method and showed strong correlation.

From this point the majority of electric probe testing goes onto liquid film measurement. However, electrical probes started to be used to analyse the volume charge density of droplets and the effects on the low pressure turbine. This property with links to steam condensation and corrosion damage was studied in depth (Kachuriner and Orlik 2007). Further study with experimental validation using an electrical probe showed the droplet charges and how the charge can change across the rotors and stators (Tarelin 2014), in which there is extensive review on the current knowledge of charge polarity of droplets and the effects on erosion. The probe is then used to measure the ionisation of the steam flow; this highlighted identification and validated the major factors that cause electrochemical corrosion of turbine blades.

2.2.4 Microwave Probes

Since the 1970s, microwave techniques such as microwave spectroscopy have been studied in depth to measure mixtures of gases. It was not until the 1980s and 1990s that microwave methods were truly used on wet steam or water vapour. An early study looked into using a microwave sensor to measure permittivity changes in methane caused by water vapour (Amaud *et al.,* 1992). This work was expanded upon by measuring water vapour and ethylene oxide using a microwave spectrometer in different gas mixtures (Zhu *et al.,* 1996). A problem was identified with microwave spectroscopy; absorption line broadening. This was solved by dilation with nitrogen.

These solutions were then utilised in an experiment where a microwave sensor was designed and built to detect water vapour within sulphur hexafluoride at as little as 3 ppm (Rouleau *et al.,* 2000). The system worked by measuring the voltage difference using a measuring cavity resonator and a reference resonator with sulphur hexafluoride; the difference is the amount of water vapour contained. The system continued to be improved; by the early 2000's microwave cavity resonator based systems were starting to be used for measuring wet steam in turbines. An example of this work (Yongqian *et al.,* 2006), used a frequency tracking unit inserted into the system. This allowed for the voltage controlled oscillator to follow the resonant frequency of the resonator, filled with wet steam. Comparing the experimental permittivity results from the sensor to theoretical results showed a strong agreement between them, demonstrating the feasibility of the system. Error analysis was then performed on the system in 2010, with more improvements allowing for higher quality measurements (Zhang and Liu 2010). The team went on to analyse uncertainty in the formula for measuring the humidity of wet steam. Finally, from their results, they concluded that energy storage of an electric field equals the energy storage of a magnetic field when resonance occurs, using a formula they deduced from the theory. This formula improved the measurement accuracy more than three times.

Another method of microwave sensing is using an interferometer; this particular technique was used to measure the quality of steam at a generator plant (Jean 2007). The interferometer, shown in Figure 2.9 works by measuring the differential path length between two transmission lines, this determines the change in permittivity as the quality of steam changes. The device was able to measure a frequency shift from 10.346 GHz for 100% dry steam to 10.275 GHz for a steam quality of 50%.

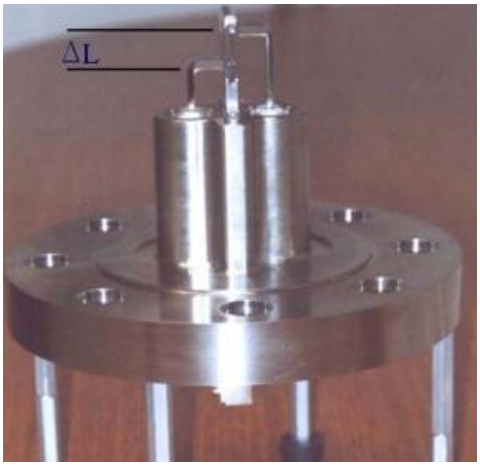


Figure 2-9 Structure of the probe portion of the sensor (Jean 2007)

When microwave probes are used to measure a droplet laden flow at the final stages of a low pressure turbine the results show good correlation to the theoretical predictions. The technique is straightforward to implement, notably if the interferometer is used, the device becomes much more simple to attach to the system in-line.

This concludes the review on steam wetness techniques within the low pressure turbine, the next section will review how the void fraction can be measured within the pipes.

2.3 Non Invasive Void Fraction Measurement of Wet Steam

The main way that images are obtained of the structure of the multiphase flow inside a pipe is by using different tomography methods; this is where sensors placed around the pipe detect changes to an emitted physical signal as it passes through the different phases inside the flow. An algorithm such as the linear back projection method, takes this data and converts it into a set of images showing a 2D cross section of the phase density across the flow. Reviews of the different tomography techniques have been conducted before (Mohd *et al.,* 2012) and where they could be implemented (Jamaludin *et al.,* 2013).

2.3.1 Photon-Based Radiography and Tomography

Two different types of energised photons are used for tomography: gamma rays and X rays; these techniques are an advancement of film measurements where the detectors measure the attenuation rate of the transmitted signal to build up a cross-section of the flow. Looking into gamma ray tomography, a comprehensive background and layout of how a system works was written in 2007 called Industrial Process Gamma Tomography (2008). This report details the progress of gamma tomography around the world from 2003 to 2007.

Andre Bieberle and his team designed a sensor that could detect gamma rays with high resolution (Bieberle *et al.,* 2013) as shown in Figure 2.10

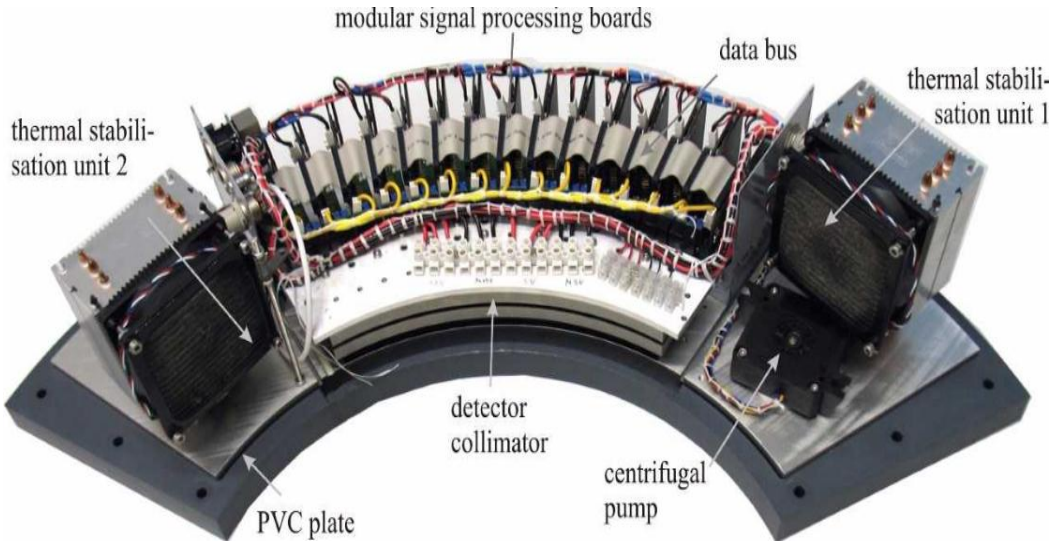


Figure 2-10 Interior of the Compact detector arc (Bieberle et al., 2013)

They first tested its resolution capabilities by seeing how the gamma source was detected through a slit between two lead bricks; they also tested it by seeing how it could reproduce an image of an aluminium block. Once it was found that the scan could accuracy reproduce images of objects with a maximum diameter of 130mm, the detector was used to create an image of a cross-section of a suspension of beads in water by having the detector fixed to

a rotating plate surrounding the pipe containing the flow; the plate could rotate at a speed of 0.025 rpm up to 10 rpm delivering a signal every 0.9 angular minutes (Bieberle *et al.,* 2013). The results showed that the detector could reproduce images of any sort of flow of beads in water from stratified to annular.

Following this they looked into using gamma-ray tomography to measure bubbly flow inside a pipe as well as for inclined rotating fixed bed reactors. For the first experiment they used three different designs of gas into liquid sparger to give different bubbly flow distributions, then placed the sensor at different distances along the flow and recorded the images (Bieberle *et al.,* 2013a).

The latest advancement of this technique was performed by Roshani *et al.,* (2015) who used a gamma densitometer. They used a Monte Carlo simulation of the densitometry measurement characteristics (i.e. photon scattering within the sample) to predict results from known void fractions and flow regimes such as annular, stratified and homogeneous. Although the liquid used for the tests was neither wet steam nor a water and air mixture, but for gasoil and air, the results can still give insight into how well the system works. Firstly, the team found that they were able to accurately predict the void fraction of annular, stratified and homogeneous regimes, to within an error of less than 1%. Figure 2.11 illustrates the comparison of experimental and simulation data obtained. The RD means the percentage difference between experimental and simulation data. Graph a in figure 2.11 describes the transmission count, graph b describes the total scattering count and graph c describes the Compton edge count.

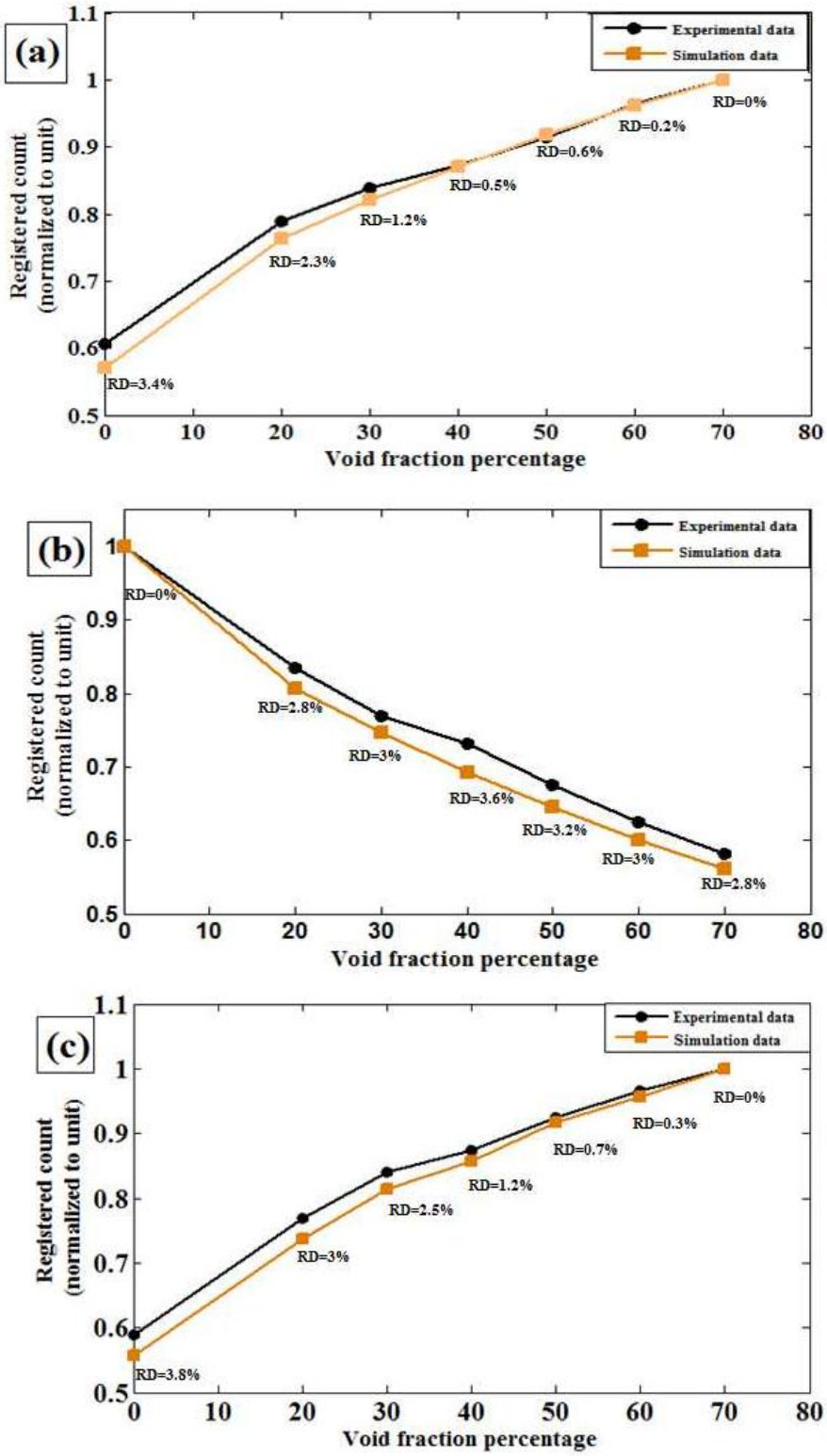


Figure 2-11 Normalized experimental data and Monte Carlo simulation data used by Roshani, Nazemi, Feghhi, & Setayeshi for (a) transmission count, (b) total scattering count and (c) Compton edge count, the highest energy that can be deposited (Roshani et al., 2015).

X-ray methods work around the same process, the only difference being the higher attenuation rate due to the lower energy photons being absorbed more easily. Axel Seeger and his team (Seeger *et al.,* 2002) looked into using two different methods to visualise a multiphase flow; the first method being measurement of the three dimensional velocity field by X-ray based particle tracking velocimetry (PTV) where a single image was taken every 20 ms resulting in 25 image pairs per second, this could give up 1000 images made from 500 image pairs. The second method being liquid flow visualisation in a bubble column by injecting an X-ray absorbing liquid. The results from these experiments were promising: they were able to show how the velocity field changed.

X-ray radiography, tomography and stereography were explored by Theodore *et al.,* (2005); X ray radiography is where a 2D image is taken of a 3D object by recording the X-ray attenuation through the object; the team were looking into visualising a rubber ball falling through a water-filled column, then analysed how a bubble of gas rises through a column of water 32cm long, as well as taking velocity measurements (Theodore *et al.,* 2005). They then moved onto X-ray tomography in which images were produced of an air and water bubbly column by rotating an X-ray source and detector around the target; the results of this experiment also gave velocity readings of 3, 10 and 18 cm/s (Theodore *et al.,* 2005). Finally, X ray stereography was explored (Figure 2.12), highlighting how the three-dimensional position of a bubble can be determined in a column of water, amongst other characteristics such as object movement and changes in time.

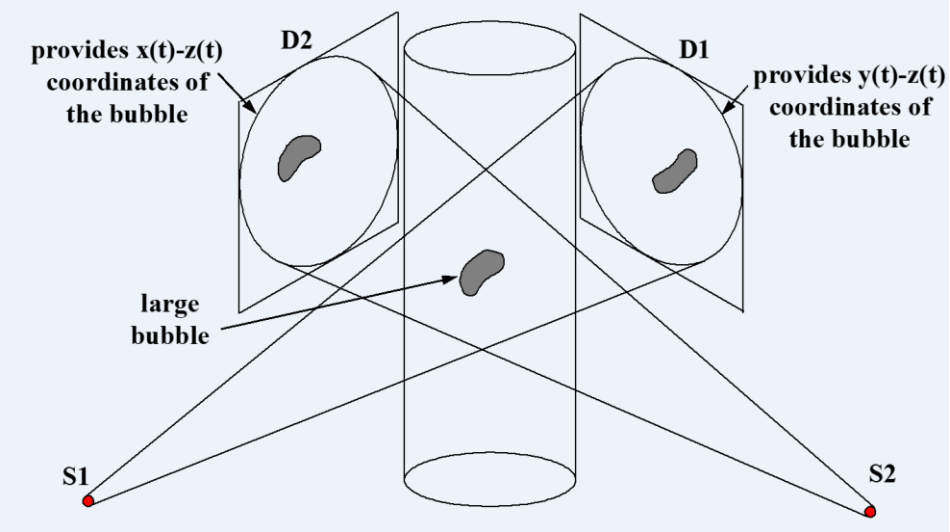


Figure 2-12 an example of X-ray stereography showing how an object can be determined in the flow by two different X-ray sources (Theodore et al., 2005)

X-ray Radiography and Tomography were further analysed by Theodore, Terrence and Joseph, who took images of bubbly multiphase flow using X-ray radiography. For the experiment, they injected a mixture of 10% polyethylene glycol into a water flow where the viscosity was slowly increased; using radiography they were able to see individual bubbles when the flow was sufficiently slow (Theodore *et al.,* 2007). X-ray tomography was explored by taking images of a water system flowing at 2cm/s, and the resolution provided reasonably accurate results showing bubble positions and the void fraction in the flow.

Bin Hu *et al.,* (2011) used an X-ray tomography system to measure a multiphase flow for an air and water system; they set up the system with two emitters and detectors, where one was positioned above the flow and one to the side, producing a top down and a cross sectional view. The system was tested for stratified and slug flow with a sampling rate of 300 Hz, clearly showing how the liquid moved slower than the gas by 2 to 5 m/s; other results included different projection views which could show wave propagation and phase distribution. Following on from this they used an improved

reconstruction algorithm to show cross-sectional slices of the flow as well as building them up into a 3D image.

Another form of X-ray tomography is known as electron beam X-ray tomography; one of the earliest examples of research in this area was carried out by Hampel *et al.,* (2005), who used an electron source to hit a tungsten target which emitted X-rays across an area. The changes in these waves were then picked up by a semicircle detector.

An evaluation of the technique was conducted by Bieberle and Hampel (2006) in which different algorithms and noise levels were tested using the data. They found that noise levels could be decreased to less than 2% for bubbly flow, where the bubbles were less than 5mm and had a good lateral resolution measuring down to 1mm. This research idea was further tested by Fischer and his team, who were able to make the beam move around the target, then take images from different angles (Fischer *et al.,* 2008), (Fischer and Hampel 2010). They achieved a maximum frame rate of 7 kHz and accurately showed a picture of a flow, provided that it was moving less than $5ms^{-1}$. The images were reconstructed using the standard linear back projection technique referred to in Tomographic Image Reconstruction (2015).

Bieberle *et al.,* (2010) investigated the possibilities of dual plane tomography to measure the velocity of the flow. They also compared electron beam tomography to a wire mesh sensor to see the differences in resolution and reconstruction of the flow image. What is immediately noticeable is the difference in resolution of the images: the non-invasive technique gives much clearer images, meaning that much smaller bubbles are visible. Stürzel *et al.,* (2011) furthered this idea by expanding to 3D electron beam tomography (i.e. a scanning X-ray beam which is stimulated by an electron beam), which meant objects could be scanned above 1KHz, but slower than using 2D electron beam tomography (Stürzel *et al.,*); however it was not tested on a multiphase flow, and instead, circular phantom models were used for the tests; due to increasing the time frames the spatial resolution was reduced to 1.2 mm. Following on from this the technique was reviewed by Bieberle, Stürzel and

Hampel where it was compared to 2D tomography and duel plane tomography (Bieberle *et al.,* 2012); it was highlighted that the problem with 3D is that it can only be used on static volumes. The benefits of 2D dual plane is that it can be used on multiphase flows giving a resolution of less than 1 mm and can be used for accurate velocity calculations.

From that point on, specific parts of electron beam tomography were analysed to see how they could be improved upon. Halls evaluated the X-ray source used for 2D and 3D electron beam tomography, comparing Advanced Photon Source (APS) synchrotron - a narrowband X-ray source, to a broadband X-ray source (Halls *et al.,* 2014). The results showed that APS was able to overcome several limitations of the broadband source, such as having sufficient attenuation, and was able to resolve special features down to 10 – 12 µm. Bieberle *et al.,* (2015) looked into the most time consuming part of the tomography process: the data processing of the CT images. They adapted the data processing and reconstruction algorithms to allow for use in parallel processing CPUs with six cores. This allowed an improvement where up to 137 slice images can be reconstructed per second. The most recent review of the area was produced by Barthel *et al.,* (2015), who looked into analysing the velocity measurement of the flow. They looked at all different techniques that can measure velocity from electron beam tomography. They looked at how velocity information can be extracted from the CT images, how a single bubble can have its velocity measured, this was expanded to measuring the velocity of particulates within a gas/liquid two phase flow. Finally the team looked into velocity measurement of a single phase flow using a contrast agent.

To conclude, from the available photon methods, APS would be very useful for wet steam measurement as droplets produced can have diameters as small as 10 µm from heterogeneous and homogeneous nucleation, so the technique would have the resolution to pick up presence of the liquid phase. Velocity measurement would be helpful as well because it would give an accurate assessment of the mass flow rate.

2.3.2 Neutron-Based Imaging

Mishima *et al.,* (1997) designed and built a sensor based upon previous work that used neutron radiography to produce images that were sufficiently clear to accurately measure the droplet flow regime. They firstly used the microscopic neutron cross-section scaling method which is a quantification method, a technique they developed in 1996; secondly, they recorded images over a long period of time up to 20 minutes using 250, 500 or 1000 frames per second. Finally as before with using gamma ray, the strength of the beam has to be assessed so that there is the maximum difference in the attenuation rate between the gas and liquid phases. In the case of this experiment, Mishima, Hibiki, & Nishihara used thermal neutrons in the region of 2 eV with a neutron flux of $1.5 \times 10^{8} cm^{-2} s^{-1}$ (Mishima *et al.,* 1997). This technique produced images of slug flow, bubbly flow, churn flow and annular flow; the team were able to calculate the void fraction for each of these flow regimes, with an error of as little as 5%. What is interesting from this paper is that the technique can be used to show the change in the flow regime in real time as well as in slow motion, and can calculate the void fraction in each time frame.

The following year they published more work further exploring neutron radiography with high frame rates. Using a similar setup as before they looked into how the effect of neutron scattering affects the accuracy of the images of the void fraction (Mishima and Hibiki 1998); the following equation denotes how the error is related to the neutron radiant fluence, which is the radiant energy received by a surface per unit area as in equation 2.3.

$$E = \frac{1}{\sqrt{F}} = \frac{\sqrt{F}}{F} \tag{2.3}$$

By integrating N consecutive frames the error can be decreased by E' shown in equation 2.4 (Mishima and Hibiki 1998).

$$E' = \frac{\sqrt{F/N}}{F} \tag{2.4}$$

Many of the experiments past this point for neutron image methods focus on examining flows through a fuel bundle in a nuclear power plant (Takenaka and Asano 2005); (Mor *et al.,* 2009) differed from this approach and looked into the same area as Mishima, Hibiki, & Nishihara (Mishima *et al.,* 1997); they used a machine called Trion generation 1, made by Mor *et al.,* (Mor *et al.,* 2009). The machine used high frame rate neutron radiography combined with the option of adding gamma-ray radiography to further inspect an object (Mor *et al.,* 2009); Zboray *et al.,* (2014) used the third generation of the Trion (Figure 2.13) without the gamma radiography to measure a bubbly flow system using polychromatic fast neutron beam line, which produces neutrons from the d + Be reaction, this gives neutrons with a fluence averaged neutron beam energy of near 5.5 MeV.

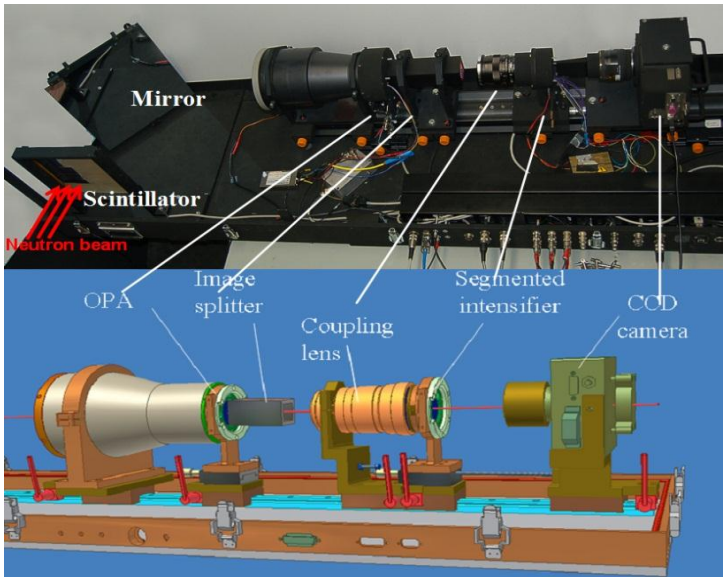


Figure 2-13 the generation 3 Trion detector developed at PTB (Zboray et al., 2014), further details can be found at (Mor et al., 2009)

Slug and bubbly flows were recorded by the computerised fluid dynamics device showing the instantaneous gas volume fraction for every 30 ms; the following year, the same experiment was improved upon (Zboray *et al.,* 2015), whereby the exposure time was reduced to 0.33 ms, which was combined with looking at different post processing techniques to further show abilities of the high speed method.

2.3.3 Electrical Capacitance Tomography (ECT)

The next type of measurement technique Electrical Capacitance Tomography was explored before in Barham (2013.) The following review is an outline of the current knowledge on electrical capacitance tomography. A more in depth discussion and analysis of the technique will be covered in chapter 3.

Electrical capacitance tomography gives a low resolution complete cross-section of what the flow regime is. It works upon the theory that in the case of an air and water mixture or wet steam, as pressure is increased, there is a greater difference between the permittivity of the two phases and thus a greater change between the capacitance of the phases present in the mixture; it is by measuring these changes that an image is reproduced of the flow regime.

An example of how the system works was published by Yang *et al.,* (2004), the sensor they used was set with four pairs of opposite electrodes, connected to an image reconstruction circuit. The design of the sensor is shown in Figure 2.14.

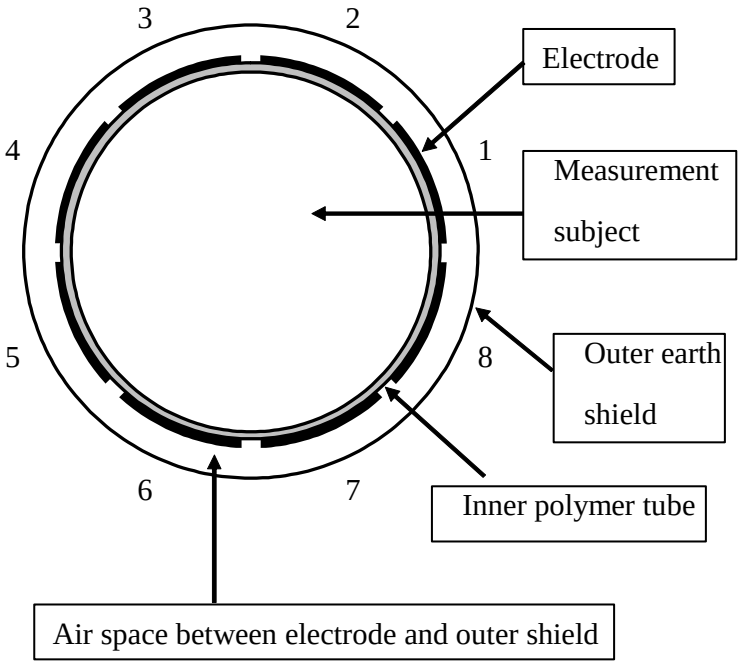


Figure 2-14 Design of the ECT sensor electrode layout surrounding the pipe (Yang et al., 2004)

The sensor was calibrated by inserting solid foam with a known permittivity into the testing area, then 5 mm holes were cut into the foam and filled with a higher permittivity material with a relative permittivity of 7; the reconstructed image on the screen then showed the approximate area where there was a permittivity change. At the end of this testing, the sensor was in an actual test rig called Twister, which was designed to simulate wet gas flowing through the sensor. It was found that the sensor could measure tiny changes in relative permittivity of between 1 and 1.06 and was ideally suited to measuring wet gas flows from 0.95 to 0.05 dryness fraction.

Shafquet *et al.,* (2010) looked into an ECT system which is calibrated correctly to measure the void fraction in different types of bubbly flow; nine different cases of bubbly flow regimes with different gas and liquid speeds were tested. The team modelled the void fraction distribution using the same three different models: parallel, series and Maxwell. They found that superficial gas velocity is a critical component that can affect void fraction significantly, as they showed that as the gas velocity increases the void fraction increased to a maximum value of 31% (Shafquet, Ismail and Karsiti 2010).

Following on from this calibration work the team used an ECT sensor with 12 electrodes to estimate the size of a void fraction inside a bubbly flow of air and deionized water. The same setup as before was used with different speeds of gas and liquid passing between the sensors. The results from the experiment backed up their earlier work that the superficial gas velocity is directly linked to the void fraction; they moved on to trying to optimise methods for calculating the void fraction from the ECT image, looking into using three different techniques: estimation of void fraction using ECT, estimation of void fraction from differential pressure (delta p) method arrangement and estimation using photographs and calculation using normalised pixels. It was found that delta p and the calculation using normalised pixels were in good agreement; further calibration work with the sensor using deionized water and air showed the predicted differences for measurement of the void fraction between the three different models (Shafquet and Ismail 2012).

The work from Yang *et al.,* (2004), Shafquet *et al.,* (2010) and Ismail *et al.,* (2011) showed that results could be changed or made inaccurate based upon how the sensor was built, as well as how the electrodes were arranged. Brook *et al.,* (2014) analysed the effect of placement of electrodes using two different types of electrode setup, diametric tomography and chordal tomography shown in figure 2.15, would have on the measurement of the flow

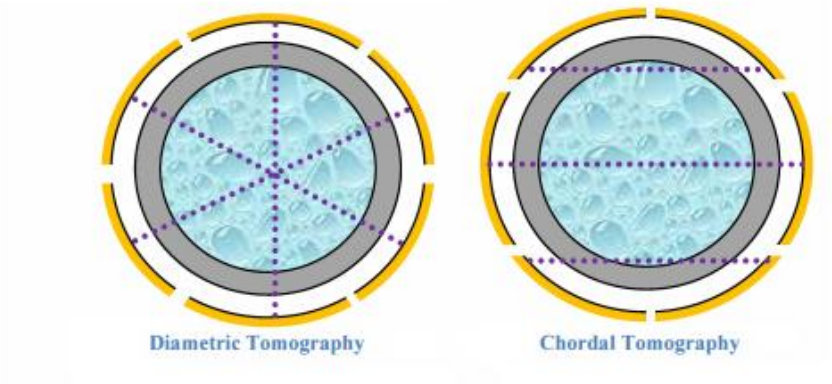


Figure 2-15 different types of electrode setup: diametric tomography and chordal tomography (Brook et al., 2014)

To analyse this they built a sensor that combined these two properties and allowed the use of adaptive electrode measurement. This sensor is composed of three meters that contains two electrodes in meter 1 four in meter two and six in meter three figure 2.16.

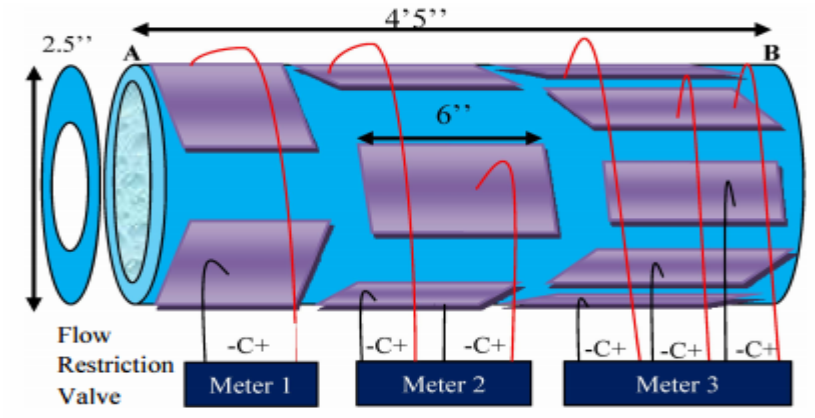


Figure 2-16 the arrangement of the electrodes for each meter (Brook et al., 2014)

The different electrode configurations allowed for a comparison between the sensitivity of different amounts of electrodes; the team found that as the number of electrodes increases from 2 to 6, the range of measurable capacitance values decreases from 67-69 pF for two electrodes to 50.8–60.5 pF for six electrodes; but that details can be visualised with a greater number of electrodes; they concluded that, for small bubbles of 1mm, a four electrode system is optimal.

For wet steam measurement, there would not be a difference between using Chordal or Diametric tomography for opposite electrode pairs due to the small sensitivity; the main difference would come from the resolution generated from the amount of electrodes used and what droplet size could be measured.

2.3.4 Ultrasonic tomography

Using ultrasonic emitters in an array around the tube, is a technique called ultrasonic tomography. Some of the earliest investigations into the technique were conducted by Asher (1983) and by Hoyle (1996). Building upon

this Ruzairi *et al.,* (2004), studied how to implement an ultrasonic tomography device for the measurment of a multiphase flow; the team used 16 pairs of transmitters and recievers shown in figure 2.17 to build up a cross-section of the flow in real time using the technique by Li and Hoyle for spectral analysis strategy, which examined the phase information of reflected ultrasonic signal detected by a transducer (Li and Hoyle 1997).

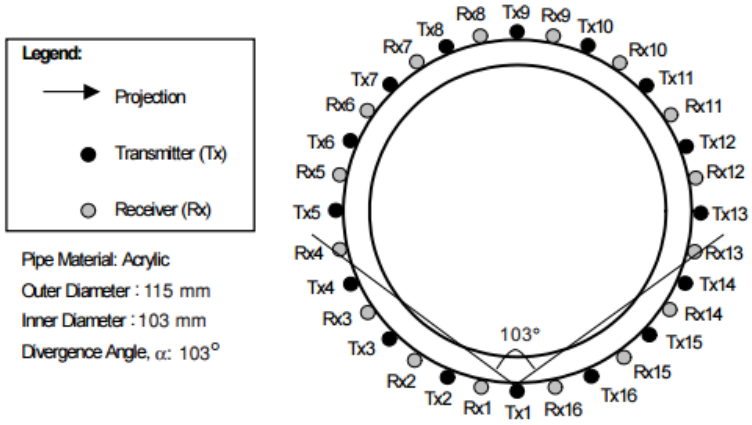


Figure 2-17 Transmitter and receiver setup for the ultrasonic tomograph (Ruzairi et al., 2004)

The paper (Ruzairi *et al.,* 2004) highlighted the problems with the technique, such as the total reflection by liquids inside the flow which give errors, as well as the technique being suited to flows with a high void fraction due to the large difference in density.

A practical application of the technology was explored by Abdul *et al.,* (2011), where they used a different algorithm to visualise multiphase flows as well as mixtures with solids, liquids and gases. This was achieved by combining all the reflections together, which were received at each transducer. An initial test was carried out with a fixed length of pipe filled with liquid. When this process was applied, it converted the signals into a concentration matrix, which was then converted to pixels using linear back projection to produce a tomogram of the cross section of the pipe. Their results showed that it was an accurate method to measure different flow regimes, but they did not measure annular flow (Abdul *et al.,* 2011).

Taking the method further, the team looked into the linear back projection algorithm to build up actual real time images of gas bubbles inside the flow (Mohd *et al.,* 2012); their results showed where any errors would arise from with the technique, and they were able to map images of multiple gas bubbles of different sizes; the image in Figure 10 shows how two gas bubbles have been mapped using the LBP algorithm.

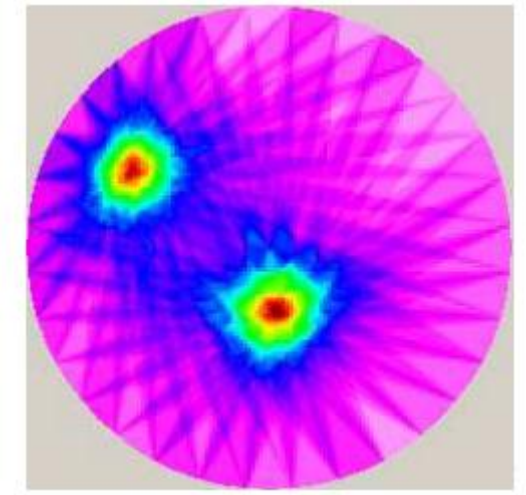


Figure 2-18 two gas bubbles visualised using the linear back projection algorithm, showed by high concentration of gas by the red to green area (Mohd et al., 2012)

Liu *et al.,* (2013) detailed how this technology works and the algorithm they used to process all the reflections from each of the waves produced by the multiple transducers. The algorithm they use is based upon eclipses, and how the reflections from the waves from each set of transducers within an eclipse are picked up by another set of transducers within another eclipse (Liu *et al.,* 2013). The paper states that, by increasing the number of transducers used, the resolution of the image can be improved. With 80 transducers details in the images can be seen at less than 500 µm.

2.4 Film Thickness and Velocity Measurement Techniques

One of the key parts in being able to measure the overall mass flow of steam is being able to measure the liquid content, since wet steam can have annular flow structure, therefore there will be droplets present in the core of

the flow and a liquid film of varying thickness flowing along the inner wall of the pipe; both of these amounts of liquid require measurement in order to calculate the mass flow of steam. From a review by Cristiano *et al.,* (2010), whereby different film measurement techniques were classified based upon their core technology, the following classes arose: optical, acoustic, electrical and nuclear. This paper uses these classifications as a basis to find the relevant literature, then critically analyses techniques that are non-intrusive so as not to disturb the flow and are able to measure films of less than 100 μm thick.

2.4.1 Photons

One of the more straightforward ways of measuring a film of liquid is by measuring changes in photons' attenuation rate as they pass through a material; the amount of energy the photons have will determine what photon behaviour will be tested in order to gain results. In the case of measuring high energy photons such as gamma rays, the measurement works around the principle of the difference in the attenuation coefficient between solids, liquids and gases, meaning that radiation in the form of gamma rays and X-rays moves through solids and liquids slower than they would pass through a gas. Therefore when beams of radiation are aimed at a two phase flow, the difference in the attenuation coefficient will highlight the size of the void fractions, and be able to pick out areas of high liquid content such as a film.

Abouelwafa and Kendall first summarised advancements in alpha particle tomography in 1980 (Abouelwafa and Kendall 1980). The first and most important point they realised was that there has to be a significant difference between the attenuation coefficients of the different materials involved. They used this information to work out how to calculate the thickness of different phases inside a multiphase flow, such as a two phase annular flow; equations 2.5 and 2.6 details what they calculated for measuring the thickness of two different phases inside such a flow.

$$x_1 = \frac{\ln\left(\frac{I}{I_1}\right)}{\mu_2 - \mu_1}$$

(2.4)

$$x_2 = \frac{\ln\left(\frac{I}{I_1}\right)}{\mu_1 - \mu_2}$$

(2.5)

Jiang and Rezkallah used these advances, along with work completed previously, to build their own gamma ray densitometer which could accurately measure void fractions inside a small diameter pipe; they used an air and water mixture and tested the device on slug flow and annular flow (Jiang and Rezkallah 1993). The densitometer works by firing a beam of γ rays produced by caesium 134 at a target section of pipe, a detector at the other side of the pipe measures the transmitted intensity of the beam.

No measurements were taken of the thickness of the film, but the technique was used to measure the overall void fraction of the flow for slug and annular flow patterns using the densitometer. What was also found to be of interest was that the strength of the gamma stream in the test section affected the accuracy of the measurements, thus they chose to use a clear plastic pipe as the test section, as it allowed the use of a less powerful gamma source which gave a greater difference in the attenuation coefficient. Later, Zhao *et al.,* (2013) performed the same experiment using a very similar setup, testing on a variety of different flow regimes, ranging from bubbly flow to annular flow; they were also able to record that there was liquid film present and calculate the speed of the film being close to the results presented before (Zhao *et al.,* 2013).

Stepping down in energy from gamma, techniques that utilise the properties of X-rays have also been shown to be effective in measuring the thickness of thin films; a review by Chason and Mayor (1997) critically analysed

the use of specular X-ray reflectivity (XRR) which can measure film thicknesses of different materials from 0.1 to 100 nm (Chason and Mayor 1997); they also explored the best way to measure a liquid film using X-rays by use of a flow visualisation method.

In conclusion using techniques that can measure the thickness of a liquid film using gamma and X-rays are not largely explored. As demonstrated earlier in the review in section 2.1, they are much more suited to measuring the overall void fraction of the flow

Optical techniques that use photons in the visible spectrum have been shown to be more effective in measuring a film of liquid. Light attenuation is the same as using gamma rays to exploit the property that some photons will be absorbed as they pass through the flow. Because lower energy photons are used, there will be a greater difference in the attenuation; a laser is used for the photon source which will channel the photons across the flow coherently. Utaka *et al.,* (2004) used this technique to measure the liquid film thickness as a gas bubble passes between the detector and emitter. They passed a bubble with a diameter of 0.5 mm between the two at different velocities giving a slug flow (Utaka *et al.,* 2004), measuring the time it took the bubble to pass and the change in thickness; therefore, the film thickness was calculated using Lambert's law equation 2.7.

$$\delta = -\left({}^{1}/_{A}\right)\ln\left({}^{I}/_{I_1}\right) \tag{2.6}$$

Using this equation, the film thickness could be calculated from the setup illustrated in Figure 2.19.

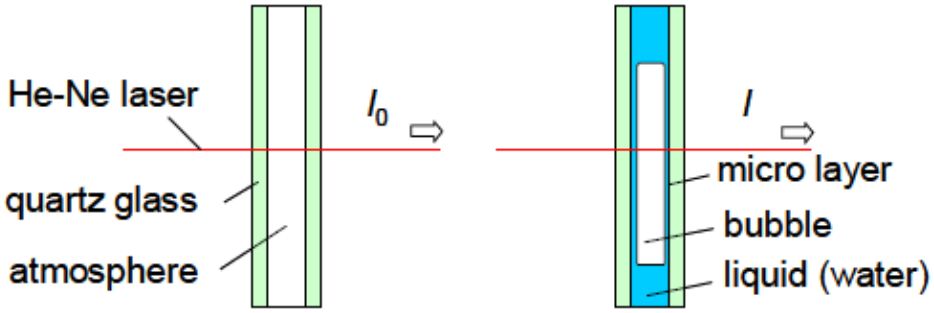


Figure 2-19 Setup of the laser extinction method for measuring liquid film thickness (Utaka et al., 2004)

The results of the experiment showed that a film thickness was measured for different bubble velocities and liquid temperatures; they showed that, for a bubble of 0.5 mm with a velocity of 0.38 m/s and a laser area concentration power of 2.5 kW/m^2, a film thickness of 5 µm was recorded. Increasing the power to 6.7 kW/m^2 with a velocity of 2.8 m/s gave a much larger film thickness of between 25 and 20 µm. These results showed that as the bubble takes longer to form the film thickness can be seen to decrease.

Other behaviours that can be observed are reflection and refraction caused by photons traveling through media with different densities. This is part of the general behaviour of photon scattering. By relying on this property, different phases of matter within the annular flow can be detected, by either seeing where the boundary is between the gas and liquid phase thus highlighting whether a film of liquid is present, or by detecting where there are high levels of photon scattering off the surface of the liquid in the flow again detecting the presence of a liquid by reflection. This principle was exploited by Yu *et al.,* (1996) who used a fibre optic sensor built into a trough to measure how light was reflected back from the liquid film phase boundary (Yu *et al.,* 1996). This setup was then used to calculate the variation of light intensities across the surface of the film. This technique was mainly used to determine

how to track the surface waviness of the film while the film thickness was predetermined: the reason for this was to see at what thickness the film had to be where the light receiving fibres could still obtain a signal of light intensity. They found that the level of light sensitivity was good from 0.5 mm to 1mm film thickness, but beyond 4mm the light intensity dropped off quickly.

In addition to this Oliveira *et al.,* (2006) used the technique with fibre-optic cables with receiving sensors set 3mm apart to measure the film of liquid in a trough. They first created a theoretical model of reflected light intensity predicting that films less than 500 µm thick could be measured; however they decided to run the experiment to measure films down to 1.5 mm which accurately matched the model, as well as concentrating on trying to measure thicker films up to 4mm; overall using photons with wavelengths in the visible spectrum as a film measurement technique can be very accurate and allow for measurement of films less than 100 nm (Oliveira *et al.,* 2006).

2.4.2 Subatomic Particles

Switching from photons to using neutrons, the advantages are a longer recording time, no trigger signal and a very high frame rate. The process works in the same way as photon techniques, by having a beam of neutrons pass through the test section. Sensors on the other side detect the amount of scattering and from this, build an image of the flow regime. Just like with gamma rays, it is very important that the correct source is chosen. Neutrons must have a sufficiently high neutron flux or concentration per unit time and volume. Secondly there are two types of neutrons that are used: cold neutrons with energies of up to 0.025 eV and thermal neutrons with energies above 0.025 eV (Arai and Crawford 2009). These two measures combine together to calculate the attenuation coefficient of the neutrons. In order to generate the correct amount of neutron flux, the correct neutron source must be used; these vary in size from small spontaneous fission materials to large high energy reactors. In most cases to gain results with a higher accuracy, the flux

should be as high as possible, therefore the source should be as large as practical for use with the experiment.

Research nuclear reactors rely upon the fission process equation (2.7) to produce a constant stream of neutrons.

$$U^{235} + n \rightarrow X + Y + 2.5n \tag{2.7}$$

Fission process for producing neutrons from uranium 235, where X and Y are fission products (Arai and Crawford 2009)

These sorts of reactors can produce up to $8 \times 10^{14}\ n/cm^2s$ of neutron flux for a 20MW reactor such as the FRM 2 (Forschungreaktor Munchen) and can be made quite compact. On the other side of the scale there are small spontaneous fission materials which have a low neutron flux, such as uranium-235 in which small isolated samples are used in the process above, or other heavy elements which have an unstable nucleus such as plutonium or californium.

Referring back to section 2.4.1 Mishima and Hibiki used neutron radiography to estimate the void fraction using the total microscopic cross-section scaling method (Mishima, Hibiki and Nishihara 1997), (Mishima and Hibiki 1998); a normalised grey scale was created from neutron scattering in which the void fraction was then calculated from, they obtained images for annular flow at different speeds where they were able to show different film thicknesses of at least 5mm, this film thickness was obtained by equation 2.8 (Mishima, Hibiki and Nishihara 1997).

$$G = C\phi_{th}e^{(-\Sigma L\delta_{ml})} + G_0 \tag{2.8}$$

The results gave calculated film thicknesses of between 0 and 7mm where they were compared against the film thickness derived from observing

the images produced from the microscopic cross-section scaling method giving an error of only 0.23% (Mishima and Hibiki 1998)

Zboray and Prasser (2013) used neutron radiography to measure film thickness in a two phase annular flow inside a fuel bundle; they setup a flow system whereby using water and air they were able to create a multiphase annular and slug flow.

The results from this experiment gave clear recordings of how the void fraction changed in accordance to the change in the velocity of the flow. What is shown is how the film thickness is calculated from the attenuation coefficient; this gives a minimum detectable film thickness for the technique of 25-30 µm. The maximum detectable film thickness was also calculated, which came out to be 5 mm. Finally the paper gives detailed graphs, showing the height of the film at various points along the channel and the film is between 0.05 mm and 1 mm thick.

To conclude, from the evidence using subatomic particles, they are ideally suited to detecting and measuring the thickness of a film that is present in an annular two phase flow of a water and air mixture, however from the literature there is very little work of actual film measurement of annular flow using neutron radiography, the downside to using neutrons is the neutron source, as it requires the use of a reactor to produce a constant stream at the required energy level (Mason *et al.,* 2000)

2.4.3 Conductance

Conductance techniques rely upon the simple principle of having a gap between two electrodes with an electric potential difference between them; as a flow passes through, the conductance will directly change due to the size of the liquid film entrained within the water and air flow. Coney developed a probe with two electrical strips mounted in the surface of the pipe separated by an insulating material (Coney 1973). A few interesting results were derived from his experiments, the main one being that he could measure films of water of less than 1mm and to a maximum of 2.5mm, resulting in the fact that

he found the accuracy of the measurements was directly related to the construction of the electrodes. This indicates that spacing the electrodes less than 1mm apart with adequate insulating material gave the degree of accuracy required.

Following on from these results, Thwaites, Kulov and Nedderman (1976) looked into measuring the wave velocity of films of liquid inside annular flow; they used an electrode probe design developed by Thwaites as part of his PhD thesis (Thwaites 1973). The probe section of the experiment consisted of two sets of probes set 1.685m apart. They measured different film thicknesses for different liquid velocities; they found that as the liquid velocity was increased, they recorded larger film thicknesses ranging from 0.1mm to more than 0.3mm. A possible explanation was given that as the liquid rate increased more mass of water was carried in the larger waves being produced.

The previous methods of conductance techniques all used an AC power source, however Tohru Fukano looked into new ways of measuring conductance using DC; he came up with different methods of using electrodes to either measure local film thickness in a particular area or for measuring the overall void fraction inside the test section (Fukano 1998). The first method used two electrodes which were brass rings connected to the test section, placed 30mm apart and flush with the pipe wall. These ring electrodes were used to deliver direct current to the test section, while two sensor electrodes situated at the base of each of the rings recorded the change in conductance.

This type of sensor gave excellent results when applied to measuring the average void fraction of the area such as with slug flow. The second method he developed was for measuring local film thickness; it worked upon the same principle as the earlier probe techniques. The design consisted of a central rod inside two rings, the central rod and the outer ring acted as power electrodes while the middle ring and the central rod were used to sense the change in conductance (Fukano 1998). This type of sensor gave good results when applied to local film thickness; it was able to measure peaks and troughs in the waves of the film down to a thickness of 0.12mm (Fukano 1998).

Ito *et al.,* (2014) used a hybrid method where they combined a liquid film conductance sensor with void fraction measurement using neutron radiography. The conductance sensor was used to measure the liquid film by Daisuke *et al.,* (2014), combining the film and void measurement techniques together in the following setup:

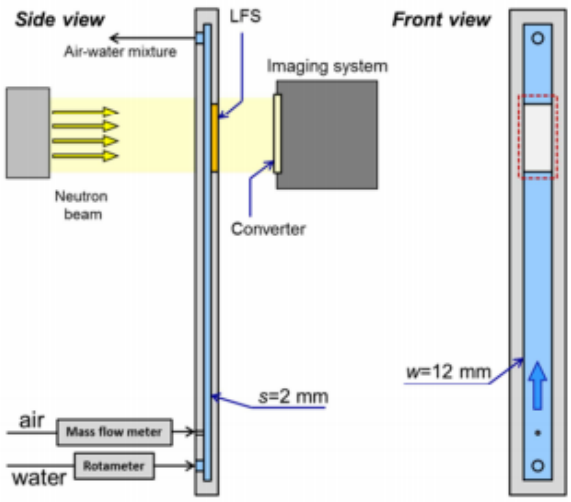


Figure 2-20 Schematics of experimental setup (Daisuke et al., 2014)

From this, they first took images of the multiphase flow and estimated the thickness of the film from these; they then measured the film using the conductance sensor and compared them to the estimated results from the images. They saw that the estimates were very close with a measured film of up to 100 µm.

2.4.4 Capacitance

Capacitance techniques work upon the principle of measuring the change in capacitance between different phases inside a mixture. This capacitance is a function of the geometry of the conducting material and its dielectric permittivity. At a basic level, a capacitance sensor directly measures the capacitance between plates that are a set distance apart.

A non-intrusive capacitance method was first proposed by Ozgut *et al.,* (1973), who designed a capacitance probe with two electrodes flush to the

edge of the pipe wall. This system worked on the simple principle that when a current was put across the two electrode plates a set capacitance is measured. When there is a liquid and gas mixture in the gap, the capacitance changes. Calibrating the film thickness to a set capacitance will mean local film thickness can be measured based upon the size of the capacitance between the plates.

The results from these tests showed the volume of liquid in the film for different lengths of bubbles passing through the pipe. It was found that as the bubble length increases, the length of the film increases and so there is a greater volume of liquid on the edge of the pipe. Although the paper mentions it is possible to measure local film thickness, no results were shown.

Further advancement of this technique was published by (Klausner *et al.,* 1992) where they used two sets of plates: one set at the top wall of the pipe and one set at the lower wall of the pipe. These sets can then independently measure the film thickness in their local regions by measuring the change in capacitance between each set of plates (Klausner *et al.,* 1992). This test was performed on a refrigerant R113 and different temperature ranges.

Due to the change in the mixture, the films that were measured were of an order larger than what would be recorded from annular flow with air and water. This meant that films were measured of between 1mm and 25mm. However, this still means that the sensor was accurate as it had an average error of as little as +-2%.

Damsohn and Prasser (2009) used a capacitance sensor which takes 1 dimensional measurements which is different from an electrical capacitance tomography as it does not calculate void fraction or show a full cross section of the flow. This sensor was made up of rows of small electrodes whereby the overall average potential field was measured for a film of water passing over each of them. The setup used a glass channel in which air from a fan was blown down while a module injected water on all four sides:

The technique was able to measure films from less than 100 microns all the way to 1mm before the potential field was saturated; what is interesting about the technique is that, if one line of electrode sensors are chosen over a set period of time, a profile of the wave structure of the film can be visualised, this technique shows a film structure with a core film of 700 µm.

Another capacitance method to measure film thickness of an annular flow was conducted by Li *et al.,* (2005), who measured the thickness of a film forming inside a thermosythen using evaporated water vapour. They used an ECT sensor 12 electrode setup giving 66 individual measurements, to give a cross-sectional view of the flow regime. Once they had the experimental data, it was compared to a model using the thermal conductivity of the fluid, this was derived from the equation for calculating Nusselt number:

$$Nu_l = \frac{hL}{k}$$

(2.9)

By performing a rearrangement of equation 2.9, the thermal conductivity of the fluid can be calculated. This dimensionless number forms the basis for Nusselt's equation for calculating a film of liquid on the inside of pipe, as Nusselt in 1916 modelled the flow of liquid on the pipe wall and made the simple assumption that there was no shear at the gas- liquid interface, thus he devised the following equation for film thickness:

$$\delta = \left[\frac{4\eta_l k_l L_c (T_v - T_w)}{g h_{fg} \rho_l (\rho_l - \rho_v)}\right]^{1/4}$$

(2.10)

Film thicknesses were recorded from 0.08 mm up to 0.27 mm, however the paper does not show what the uncertainties are with the measurements, so the accuracy of these results is unknown. These results of the film thickness of annular flow are also similar to tests completed by Cui *et al.,* (2014) on oil

film thickness in an annular flow, where they used eight electrodes of four pairs. Their results were also able to measure thicknesses of between 100 to 500 μm, with measured capacitances in the picofarad range.

2.4.5 Ultrasonic

This category of techniques relies upon the properties of ultrasonic waves that are above the audible range of human hearing; they are above 20000 hertz. The typical frequency used in materials testing is much higher beyond 20 MHz. This class of techniques first saw experimental use in 1955, in which they were mainly being tested by oil companies looking into finding a way to determine if there was a film of water in the oil flow (Lynnworth and Liu 2006). From that point on the technology has slowly been reduced in scale so that it can be attached to smaller and smaller pipes.

The basis of the technology is by using a transducer fixed to a length of pipe to generate ultrasonic waves, relying on the principle that the speed of the wave will change as it passes through one material to another. Because the speed of the wave changes as it goes through one material to another, the next property of waves comes into effect; this is refraction, where the frequency of the wave is constant. Then as the speed changes so must the wavelength thus refraction occurs, this is calculated using snell's law (Ultrasound 2006).

Sanehiro Wada, Hiroshige Kikura and Masanori Aritomi explored this effect as ultrasonic waves are passed through a plate submerged in water and measured what the best angle was to gain the maximum sound pressure using a longitudinal or a shear wave (Wada *et al.,* 2006).

Interestingly there are two peaks showing where the incident angle is optimal for a longitudinal wave at 0 degrees and for a shear wave at 45 degrees. They then needed to know which type of wave to use, since the transmission ratio for ultrasound depends on the difference between the different wave types, this showed that longitudinal waves were better for plexiglass, while shear waves were better for opaque media like carbon steel.

This was backed by earlier experiments by Morala *et al.,* (1983), who also found that shear waves were best for carbon steels. Wada *et al.,* (2006) tested their technique on annular flow running through a carbon steel pipe, they developed a method of testing the flow by measuring the spatio-temporal distribution of the ultrasound echoes.

The reviews all stated that the average film thickness found by the various experiments was between 50 and 500 µm; this technique allows the film thickness to be measured to the correct depth, but it does not give an overall view of the annular flow.

2.5 Conclusions

The literature review of the behaviour of a two phase wet steam and flow, and the techniques that have been developed, shows that it would be possible to develop a control and feedback loop to improve the efficiency of the steam cycle using one or a combination of the aforementioned methods.

For techniques that can be used in-line on the low or high pressure turbines, photon attenuation and scattering based probes are the most reliable choice; the size of the probe and the design allows insertion into multiple stages of the turbine, clearly defining how the steam is condensing and where problematic areas with erosion could occur. Electrostatic probes have been shown from research to be most useful at highlighting the property of the steam's electric charge, and the effect this has on blade erosion (Tarelin 2014). Using a mixture of electrostatic and photon probes would therefore allow for accurate measurement of the local/overall steam wetness and the charge of the wet steam at critical points. When used in conjunction with techniques that measure steam quality before the turbines, the efficiency of the steam cycle could be further improved.

For void fraction measurement, Photon based tomography systems such as gamma and X-ray have been shown to be highly accurate when there is a large difference in the attenuation rate between the different phases of the flow. Some systems such as the one by Nazemi *et al.,* (2015) included the

calculation of velocity, which would allow for a mass flow reading. Neutron tomography shares the same advantages, however, it would require a sufficiently large reactor to obtain the required neutron flux. Both techniques share the same disadvantage that, depending on the type of pipe used the source has to be more concentrated. Therefore for penetrating a metal pipe to see the flow, the difference in attenuation rates of the phases becomes smaller by comparison to the effect of the pipe wall, reducing the resolution.

Electrical capacitance tomography also works through a metal pipe by having electrodes fitted into the pipe wall. This allows for the permittivity to be measured for a cross section of the flow, highlighting phase changes. This system was shown to be highly versatile for all types of flow, giving accurate high resolution images depending upon the amount of electrodes used. It was shown that six to twelve electrodes is desirable for measuring bubbly flow, while four electrodes is better for annular droplet flow. Ultrasonic tomography can also work through any pipe material by having the transmitters and receivers fitted into the pipe wall; the technique was shown to work for simple flows due to liquid causing a near total reflection of the sound wave (Asher 1983) and (Hoyle 1996) that leads to large errors in the measurement. All tests carried out were on a flow with single gas bubbles.

Photon and nuclear based film measurement techniques rely upon measuring the difference in attenuation between a photon or neutron sent through air and air/water to a receiver; the accuracy is increased when plastic pipes are used instead of metal; optical methods work the same way using the additional process of measuring the reflection of the photon when it hits a phase boundary. The optical system based upon reflection could be used in a metal pipe as used by Yu *et al.*,, (1996); this is the same way that ultrasonic film measurement is conducted, which produces similar results. Electrical methods work by measuring the change in either capacitance or conductance, as the flow passes over the electrode. Using two or more electrodes in sets, it is possible to measure the velocity of the film.

From the information presented in this review a possible improvement would be to combine a cross sectional tomography measurement system with a film measurement device. Ito *et al.,* (2014), used a device that combined neutron radiography with a conductance sensor to image the two phase flow and provide a visualisation of the thickness of the wavy film. Such a system allows for a real-time mass flowing reading of the multiphase flow, giving clear indication of the void fraction and the liquid content.

Linking back to the original goal of steam wetness measurement, the main issues are the steam, phase difference between the steam and water, the size of the liquid phase and the pipe material. This limits the number of possible methods that can be applied in industry, to ones which are non-intrusive, for measuring steam before the turbine. This means that they can be integrated into the pipe wall or are able to pass through the wall and can show detectable difference in measurement between steam and water.

The remainder of this thesis focuses on ECT technology as it has been shown previously by Barham (2013) to be a viable candidate for future development. The following chapters will therefore go on to develop a better understanding of the effect of spatial positioning of the water phase, on the behaviour of wet steam within an ECT system

Chapter 3. Recommissioning of the Electrical Capacitance Tomography Measurement System (ECT)

Nomenclature

A Area

C Measured capacitance

$E(x, y, z)$ Electric Field

$D(x)$ Electric flux density in x dimension

G Gradient of the regression model

K Elliptic integral of the first kind

M Amount of measurements

N Number of samples

n Amount of electrodes

Q_c Charge

R_f Feedback resistance

V_0 Voltage at firing electrode

$V_0(t)$ Calculated output voltage

$V_i(t)$ Voltage the capacitor is charged to

$V(x, y, z)$ Potential difference in three dimensions

V Volume fraction

$\bar{x}$ Average signal length

x Signal value

ε' Real permittivity

ε'' Loss factor

ε Permittivity

ε_0 Vacuum permittivity

ω Angular frequency

φ Boundary condition for electric potential distribution

$\nabla\varphi$ Gradient of the electric potential distribution

ϕ_1 Position angle of electrode 1

ϕ_2 Position angle of electrode 2

$\varepsilon(x, y)$ Permittivity distribution in x and y dimensions

Subscripts

l Liquid

v Steam vapour

m Mixture

1 External material

2 Internal material

The previous chapter gave an overview of the types of multiphase flow that are encountered within the different regions of the steam cycle, when measuring wet steam. The literature highlighted, that it is well understood how the moisture content of wet steam within the low pressure turbine is measured, and that a technique is required to measure the steam wetness before the turbines. It has been shown that the percentage wetness can be calculated, with a combination of a measure of the void fraction and mass flow rate using techniques previously discussed. Furthermore, it has been highlighted that the behaviour of wet steam could affect measurement.

To address these issues, a previous project by Barham (2013), identified that an ECT system is the right method to use, which was predicted to be able to measure changes in steam wetness of 0.1% at 70 Bara, since it was able to measure a 0.5% change at 11 bar. This was then experimentally demonstrated. The outcomes of the research showed that the behaviour of the steam and water mixture could be different to an air and water mixture. Indicating that spatial positioning of the liquid water content within steam might affect the capacitance measurement, due to the water acting as a continuous path of high permittivity and least resistance.

Based upon the questions raised within the previous research, a novel method of testing the spatial positioning of the moisture content within a static volume of steam has been proposed. A review of Electrical Capacitance Tomography (ECT) systems was conducted, showing that the most cost efficient method, was to utilise the previous ECT system and to recondition the sensor to work within a high temperature environment, whereby it could continuously measure static volumes of mixtures.

Due to the complexity of the system required, the building of the equipment is split into three chapters: three, four and five. This chapter will detail how the ECT system functions, an overview of the previous ECT system,

and detail how the ECT was reconditioned. The chapter will also cover the building of a program that is able to run alongside the experiment to predict relative permittivity change measurement results, over a greater steam pressure range.

The chapter is split up into the following sections:

3.1 Fundamentals of Electrical Capacitance Tomography (ECT):

Discussion on how the principles of the technology work, the current state of the technology, and how steam wetness can be measured via relative permittivity.

3.2 Electrical Capacitance Tomography Sensor for Measuring Steam Wetness:

Details of how a sensor was designed to measure changes in steam wetness of as little as 1%, and how the capacitance measurement system functions.

3.3 Reconstruction and Improvement of the Electrical Capacitance Tomography Sensor:

Discussion on the condition of the ECT system after completion of previous work, how the system was reconstructed and what modifications were required to resume normal function.

3.4 Analysis of Changes in Capacitance Measurement within Varying Environments:

Development of a model of a sensor that can replicate capacitance measurement while it is partially, or fully-filled with different mediums with varying pressures and temperatures in 2 dimensions.

3.5 Capacitance Measurement Program in 3D:

Advancement of the model into three dimensions, discussing how the extra dimension was incorporated. An explanation of how a time varying 3D environment was also programmed to show changes in relative permittivity with time.

3.6 Principles of Linear Back Projection:

Discussion of how the Linear Back Projection (LBP) methods functions, detailing how the method is improved by using the Tikhonov Regularization.

3.7 Incorporation of the Tikhonov Regularization LBP Method into the Capacitance Measurement Program:

Explanation of how the Tikhonov Regularization LBP method is inserted into the program. Examples of the program producing reconstructed images for varying spatial positions of water is discussed.

3.8 Conclusion

3.1 Fundamentals of Electrical Capacitance Tomography (ECT)

The developments on how wet steam can be measured using capacitance measurement systems such as electrical capacitance tomography was demonstrated in chapter 2. This section will delve into the underlying principles of an ECT system and give an in depth explanation of how they work, and how they calculate the liquid volume fraction of wet steam flows.

A typical ECT sensor consists of an even number of electrodes arranged around or set into an insulating pipe, connected to a data acquisition system. Figure 3.1 shows the layout of a 12 electrode system fitted on a pipe:

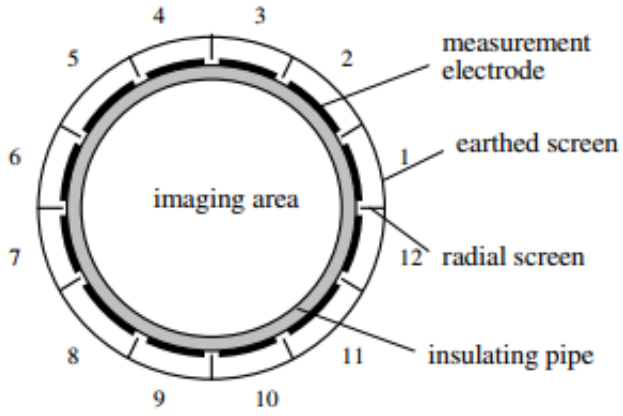


Figure 3-1 Layout of a 12 electrode ECT system fitted into a pipe (Wuqiang, 2010)

Each electrode is paired with every other electrode, measuring the capacitance between them; an even number of electrodes allows for measurement straight across the diameter of the pipe. The number of measurements that can be acquired per number of electrodes is set by equation 3.1:

$$M = \frac{n(n-1)}{2} \tag{3.1}$$

The size of each electrode and the resulting pipe diameter will govern the sensitivity of the system. In a basic flat plate capacitor increasing the area of the plates will increase the capacitance, whilst increasing the space between them will decrease the capacitance measured. In the same way increasing the electrode area will increase sensitivity and increasing pipe diameter will decrease sensitivity. The distance between electrodes can also be altered by how the electrodes are paired; Brook *et al.,* (2007) demonstrated this with the differences between chordal and diametric tomography, further information on their work can be found in chapter 2 page 45. These two types of electrode measurement can be combined together when each electrode is paired with every other electrode.

The capacitance measurement between a pair of electrodes is calculated by dividing the total charge by the potential difference between them. Figure 3.2 demonstrates the measurement system in place between a set of electrodes.

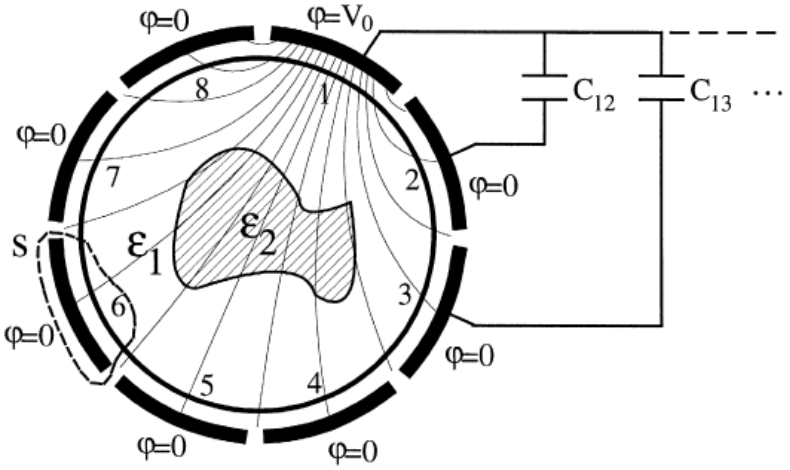


Figure 3-2 Measurement system for a typical ECT setup

ε_1 is the lower permittivity material, ε_2 is the higher permittivity material and φ represents the boundary conditions for electric potential distribution which are set between $\varphi = V_0$ for the fired electrode and $\varphi = 0$ for every other electrode (Dyakowski *et al.,*, 2000).

The equation for capacitance between a set of electrodes is found by finding a solution for the total charge, which can be derived from a rearrangement of Gauss' law. Owing to the total electric flux over all the electrodes being equal to 0, this equates the volume charge density equal to 0. Thus the electric flux density is defined in the following way (Dyakowski *et al.,* 2000).

$$D(r) = -\varepsilon(r)\nabla\varphi(r) \tag{3.2}$$

Integrating 3.2 over a defined area will give the total charge, substituting this into the equation to find the capacitance between two plates gives the following definition, for the calculation of capacitance within a closed ECT system (Dyakowski *et al.,* 2000).

$$C = \frac{Q}{V_0} = -\frac{\oint_S \varepsilon(\mathrm{x},\mathrm{y})\nabla\varphi(x,y)ds}{V_0} \tag{3.3}$$

The calculation of capacitance from 3.3 means that if the capacitance is known first then it is possible to reconstruct the permittivity distribution within the sensor between each electrode pair, the more electrode pairs give a clearer picture how the permittivity is distributed. Thus the goal of the ECT system is to clearly define the permittivity distribution, which will in turn define areas of high liquid or gas content giving a measure for volume fraction. The next section will discuss how the data acquisition system functions, how a capacitance measurement reading is acquired, and how data acquisition problems are mitigated.

3.1.1 ECT Data Acquisition System

ECT measurement systems work using ether a digital or analogue signal, with analogue devices being the less accurate of the two, and requiring a demodulation module, whereby conventional methods of demodulation take 120 µs for the signal to fall within 0.1% of the final value (Gonzalez-

Nakazawa, Gamio *et al.,* 2005). Focusing on analogue measurement, the layout of a typical system is demonstrated in figure 3.3:

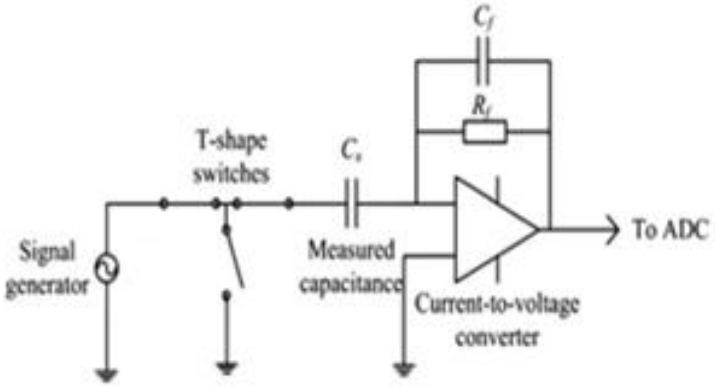


Figure 3-3 Sensing electronics within an ECT measurement system (Cui et al., 2011).

An analogue signal operated using a firing voltage with a frequency in the MHz range is used to charge an unknown capacitance C_x the capacitance between the electrodes is charged and discharged by a speed set by the frequency of the signal. Stray capacitance is removed by the sequencing of the T shape switches. The sequencing of the switches only allows through the discharge current of the unknown capacitance; this discharge current enters the current to voltage converter circuit labelled in the centre of figure 3.3, which gives an output ac voltage. This voltage can be calculated in the following way in equation 3.4, by highlighting the relationship between the measured capacitance and the current to voltage converter.

$$V_0(t) = -\frac{j\omega C_x R_f}{1 + j\omega C_f R_f} V_i(t) \tag{3.4}$$

After the current to voltage converter the output voltage can then be amplified and processed by the Programmable Gain Amplifier (PGA), or processed through a low/high pass filter. The signal is then sent to the analogue digital converter, where afterwards capacitance measurements for the electrode pair can be viewed via a computer.

The circuit allows for each electrode to be used both for excitation and detection, the frequency of switching between the modes is given by the frequency of the signal. The t shape switches control whether an electrode is in excitation mode or detection mode. In theory, only two switches are required as shown in figure 3.4:

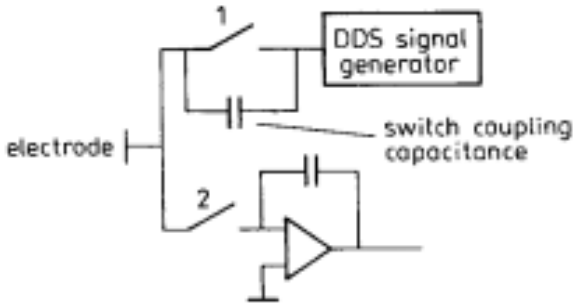


Figure 3-4 Switch circuit in principle (Yang, 1999)

However the two switch circuit is problematic, in that where switch 2 is closed in detection mode, it would mean the capacitance from the electrode pair and the switch 1 coupling capacitance would be in parallel; this will cause unsatisfactory levels of noise reducing accuracy. To fix this problem, four switches are used as shown in figure 3.5.

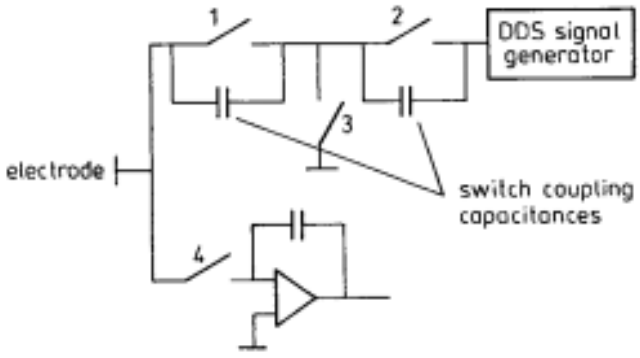


Figure 3-5 4 switch circuit demonstrating the solution to the switch coupling capacitance problem (Yang, 1999)

The four switch circuit has the electrode in excitation when switches 1 and 2 are closed, and in detection mode when 3 and 4 closed. This solves the

problem by having the coupling capacitance of switch 1 connected to earth in detection mode when switch 3 is closed.

It can be seen that the measurement frequency affects the measurement of the system, however permittivity can also be affected by frequency, the next section will explain and analyse this effect on water.

3.1.2 Effect of changing measurement frequency on the Permittivity of Pure Water

When an electric field is applied to the space between two plates from plate a to plate b, the polarized dipolar water molecules will be aligned within the field. When the direction of the electric field switches, there will be a momentarily lag before the polarization of the water molecules within the field switch.

This lag is a loss factor, and so must be taken into account as frequency increases, as this can cause a loss in permittivity. To express this, the permittivity is described as being complex and is made of a real component and an imaginary component, the loss factor $i\varepsilon''$:

$$\varepsilon = \varepsilon'(\omega) - i\varepsilon''(\omega) \tag{3.5}$$

Thus it can be seen that as the angular frequency increases, the loss factor in equation 3.5 will increase. However, this trend does not continue linearly. Instead it reaches a maximum point for a defined angular frequency. This is given by 1 over the relaxation time for water. Beyond this point as the frequency further increases, the permittivity continues to drop as does the loss factor. Figure 3.6 on the next page demonstrates this for how the relative permittivity of water changes with temperature and frequency:

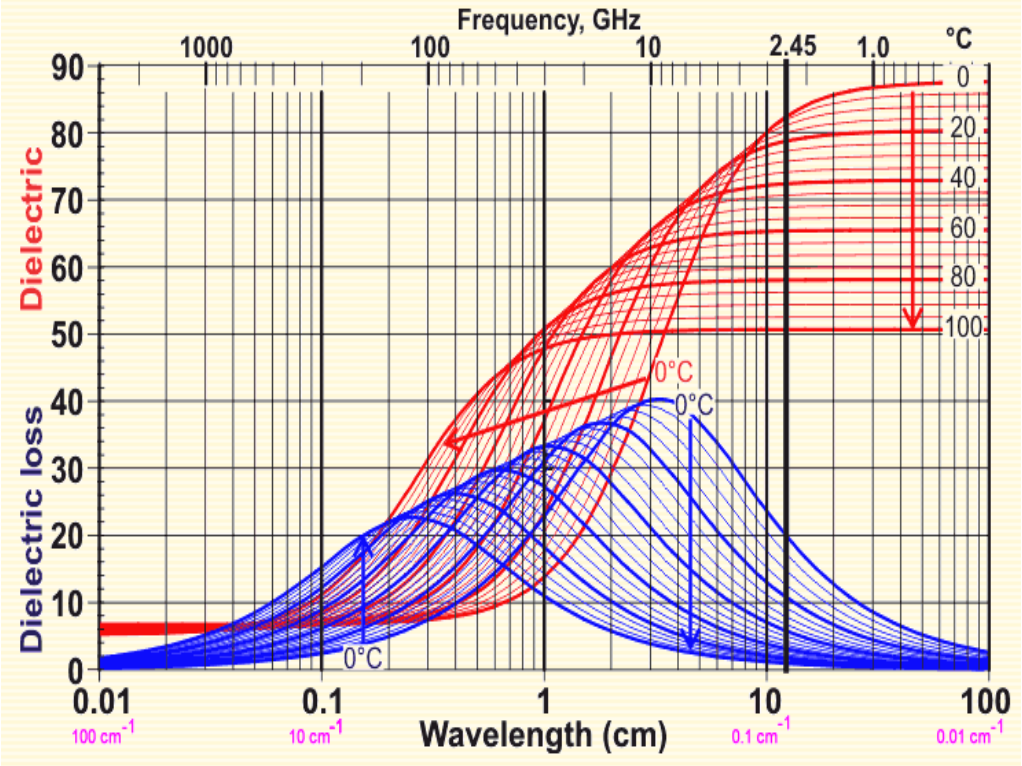


Figure 3-6 Relative permittivity change for water, from 330 MHz to 3 THz, from 0 C to 100 C (Water and Microwaves, 2017) data derived from (Franks, 1972)

Figure 3.6 demonstrates that the relative permittivity of water only changes with frequency above 1 GHz. Below this point, the relative permittivity only changes with temperature and pressure, therefore with ECT the frequency is 2.4 MHz. The measurement does not affect the permittivity of the phases.

Since the permittivity of the steam vapor and liquid water within the sensor will only change due to pressure and temperature, the next step is to look at how the relative permittivity across each electrode pair is generated and how those relative permittivities can be converted into a measure of the volume fraction of liquid.

3.1.3 Generation of Relative Permittivity Measurement and Conversion to Volume Fraction

As the permittivity within the sensor changes, the capacitance of each electrode pair will change in step. This however is not a 1:1 ratio: as mentioned earlier, the electrode spacing and the electrode shape will govern the rate of capacitance change for a defined change in relative permittivity, this is the sensitivity of the electrodes and must be calibrated for each electrode pair within the sensor. Commonly for two phase flows this process is completed by measuring the capacitance at multiple known points of relative permittivity and fitting a linear regression model to them, giving a rate of change for capacitance to relative permittivity, this can be defined as:

$$C = G\varepsilon_r + constant \tag{3.6}$$

The G value is the gradient of the regression model for each electrode pair. The gradient of the regression models defined for the calibration curves for adjacent electrode pairs will be larger than the gradient for opposite electrode pairs, as the adjacent electrodes are more sensitive to spatial permittivity change.

The relative permittivity within the sensing area between the measuring electrode pairs can also be calculated from the predicted mixture permittivity ε_m. The mixture permittivity of wet steam is affected by the volume of liquid water present, and by the pressure the water and steam are under. This is because as pressure is increased the volume fraction of liquid increases within a total volume of steam. This has the effect of raising the permittivity. The other effect on mixture permittivity is the path the electric charge can take across the measuring section from the excitation electrode to the detection electrode. The change in path can be attributed to where the volume of water is present within the sensing area.

Thus, the relationship between permittivity and liquid volume depends upon the amount, the pressure and spatial positioning of the liquid.

This relationship for the volume fraction of liquid was derived by Hunt *et al.,* (2010), based upon the work of Wagner (1914), and combined with work on spheres homogeneously distributed in a fluid by Sillars (1937). This gives the following equation 3.7, which describes the relationship between mixture permittivity and volume fraction.

$$V_l = (\varepsilon_m - \varepsilon_v)\left(\frac{\varepsilon_l + \varepsilon_v(n-1)}{\varepsilon_v n(\varepsilon_l - \varepsilon_v) + (\varepsilon_m - \varepsilon_v)(\varepsilon_l - \varepsilon_v)}\right) \quad (3.7)$$

The adjustment factor n describes the spatial position of the droplets in relation to the detection and excitation electrodes. The factor can have a value from 1 to 1000, where n = 1 is the water as a film on one electrode, called the series model and n = 1000 is the water forming a continuous path between both electrodes, called the parallel model. Between these two extremes, an n value of 3 will describe droplets thinly distributed between the electrodes, called the droplet model. Figure 3.7 demonstrates the water positioning between the electrodes:

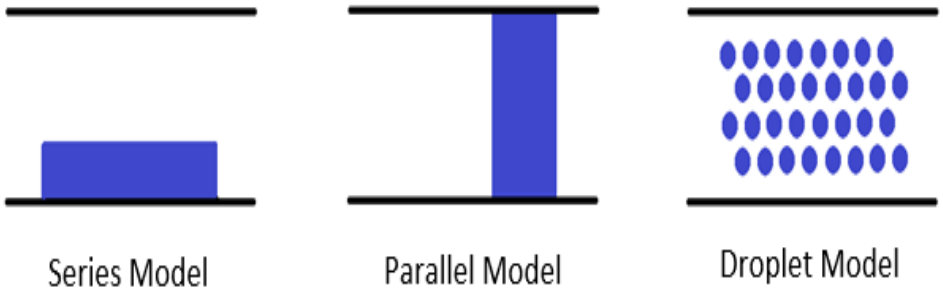


Figure 3-7 Representations of water distribution described by the three models

When the volume fraction is known and the mixture permittivity is required, an equation can be derived for the series, droplet and parallel model by setting the n value in equation 3.7 to 1, 3 or 1000 respectively. The formulas for each of the three models which describe the relationship

between water distribution and mixture permittivity are shown below in equations 3.8, 3.9 and 3.10:

Series Model

$$\varepsilon_m = \frac{\varepsilon_v \varepsilon_l}{\varepsilon_l + V_l(\varepsilon_v - \varepsilon_l)} \tag{3.8}$$

Parallel Model

$$\varepsilon_m = V_l \varepsilon_l + (1 - V_l)\varepsilon_v \tag{3.9}$$

Droplet Model

$$\varepsilon_m = \frac{\varepsilon_v(-2\varepsilon_v V_l + 2\varepsilon_v + 2\varepsilon_l V_l + \varepsilon_l)}{\varepsilon_v \varepsilon_l + 2\varepsilon_v - \varepsilon_l V_l + \varepsilon_l} \tag{3.10}$$

It is not known how the water droplet positioning within the steam affects the permittivity measurement. Previous work by Scott Barham (2013) indicated that for a wet steam flow, the relative permittivity measured was in close agreement with the parallel model, implying that the droplets form a path of high permittivity across the electrodes which has the effect of raising the relative permittivity.

The other interesting indication from the work was that for air and water mixtures, the relative permittivity was in close agreement with the droplet model; this implies that steam and water mixtures do not behave in the same way. Similar results were found by Cimorelli & Evangelisti (1967); Jaworek *et al.,* (2004) and Zunft & Bissinger (1999), although no further investigations were performed.

Hence, in order to be able to measure the liquid volume fraction of wet steam accurately using an ECT system, the effect of spatial position of

droplets on the relative permittivity measurement must be known. Secondly it must be determined if water and air mixtures do behave differently from water steam mixtures, as relative permittivity measurement of water and air mixtures are heavily dependent on the spatial position of the droplets.

3.2 Electrical Capacitance Tomography Sensor for measuring Steam Wetness

The previous section showed that sensitivity is due to the size of the electrodes and the radius of the ECT sensor, for these reasons, a standard commercial ECT sensor would not have been sufficient for the investigation. However the previous project conducted by Scott Barham, showed that an ECT sensor can be made that would accurately measure the relative permittivity of wet steam. Thus, it was decided to progress forward using Barham's sensor

Detailed below is an overview of the sensor designed and constructed by Scott Barham with Alstom and Atout from 2009 to 2013. A more detailed breakdown of the technologies and principles that went into building the sensor can be found in the following work: Scott Barham, 2013, chapters 4 and 5.

The previous project was to design and build a sensor that could detect changes in steam wetness of 0.1 % at 70 bar. Due to the cost and difficulty of testing a sensor at this pressure, it was proposed that intermediate pressure testing was completed at 11 bar due to the available equipment. In order for an ECT system to have the correct resolution in wetness, it must be able to detect changes in capacitance or relative permittivity. Since the relationship between wetness and permittivity changes with pressure, if the system can measure a fixed permittivity resolution, then the system will measure different wetness resolutions with changes in pressure. Table 3.1 shown below details the difference in wetness resolution from 1 bar to 70 bar, it also shows the constant corresponding relative

permittivity resolution which is the smallest relative permittivity change that can be detected as predicted by the parallel and droplet model.

Table 3-1 Comparative table showing relative permittivity resolution from the droplet and parallel models and wetness resolution at different pressures. (Barham, 2013)

	Relative Permittivity resolution			Wetness resolution		
	1 bar	11 bar	70bar	1 bar	11 bar	70bar
Droplet Model	1.610×10^{-4}	1.610×10^{-4}	1.610×10^{-4}	8.40%	0.95%	0.10%
Parallel Model	1.015×10^{-3}	1.015×10^{-3}	1.015×10^{-3}	3.20%	0.54%	0.10%

The table above highlights the difficulty in the size of the relative permittivity change that is required to be detected. The drop in wetness resolution between the droplet and parallel model at 1 and 11 bar is caused by the smaller change in relative permittivity for the droplet model for same percentage wetness.

The sensor used was an Atout Flow-S 120 mm sensor, normally used to test dry gas solid flows. The system was tested by dropping ping pong balls filled with a set volume of flour mixed with varying quantities of deionised water from 0-10 g, further details of the testing procedure can found in (Barham, 2013), page 130.

The results from these tests were analysed to determine the minimum resolution. This value is determined by the level of RMS (root mean square) noise. This value is calculated over 1 second due the system having a constant drift in the baseline capacitance measured with time. Equation 3.11 details the procedure to calculate the RMS from the measured values.

$$RMS = \sqrt{\frac{1}{N}\sum_{i=1}^{N}(x_i - \bar{x})^2} \tag{3.11}$$

The calculated RMS noise from the sensor was found to be 5×10^{-4} relative permittivity units using a TFL R5000 electronics system. This was larger than the resolution required by the droplet model, and so a new sensor had to be designed that had an improved resolution. The following two sections detail first the electronics of the TFL R5000, and secondly the design of the new sensor to lower the RMS noise to the required level.

3.2.1 TFL R5000 electronics system for the sensor

The standard electronics system used; was designed by Atout Process and Process Tomography, at the University of Nottingham, this is the main system that is popular for ECT research. The system can support from a 2 to a 16 electrode ECT system. The electronics also have the capability to support two planes of ECT measurement, with having up to 8 electrodes on each plane. The advantages of the system is that it is a stand-alone unit and can be used with any ECT sensor, allowing for a multiple of different sensor designs to be used, or even different electrode shapes. Figure 3.8 shows the TFL



R5000 model:

Figure 3-8 The TFL R5000 electronics system (Barham, 2013)

The ECT electronics system works in the same way as a typical system described in section 3.1.1, and has the same components. The electronics design was developed at the University of Manchester Institute of Science and Technology (UMIST), a detailed description can be found in Pląskowski *et al.,* (1995).

The accuracy of the capacitance measurement comes from the way the stray capacitances are removed before the current to voltage converter. As shown in section 3.1.1 four switches are required to remove the stray capacitance. This is no different in the TFL R5000, Figure 3.9 (a) shows the layout of the four switches next to the charge measuring circuit, where A and B are the electrodes, C_x is the unknown capacitance and C_{P1}, C_{P2}, C_{S1}, C_{S2}, C'_{p1} and C'_{p2} are stray capacitances that must be eliminated. The same principle is applied in controlling the switches, where switch 1 and 2 are closed as the capacitance between A and B is charged, then 3 and 4 are opened when the capacitance is discharged, this is demonstrated in figure 3.9 (b). Figure 3.9 (c) explains this method further showing the direction of current in the circuit diagram.

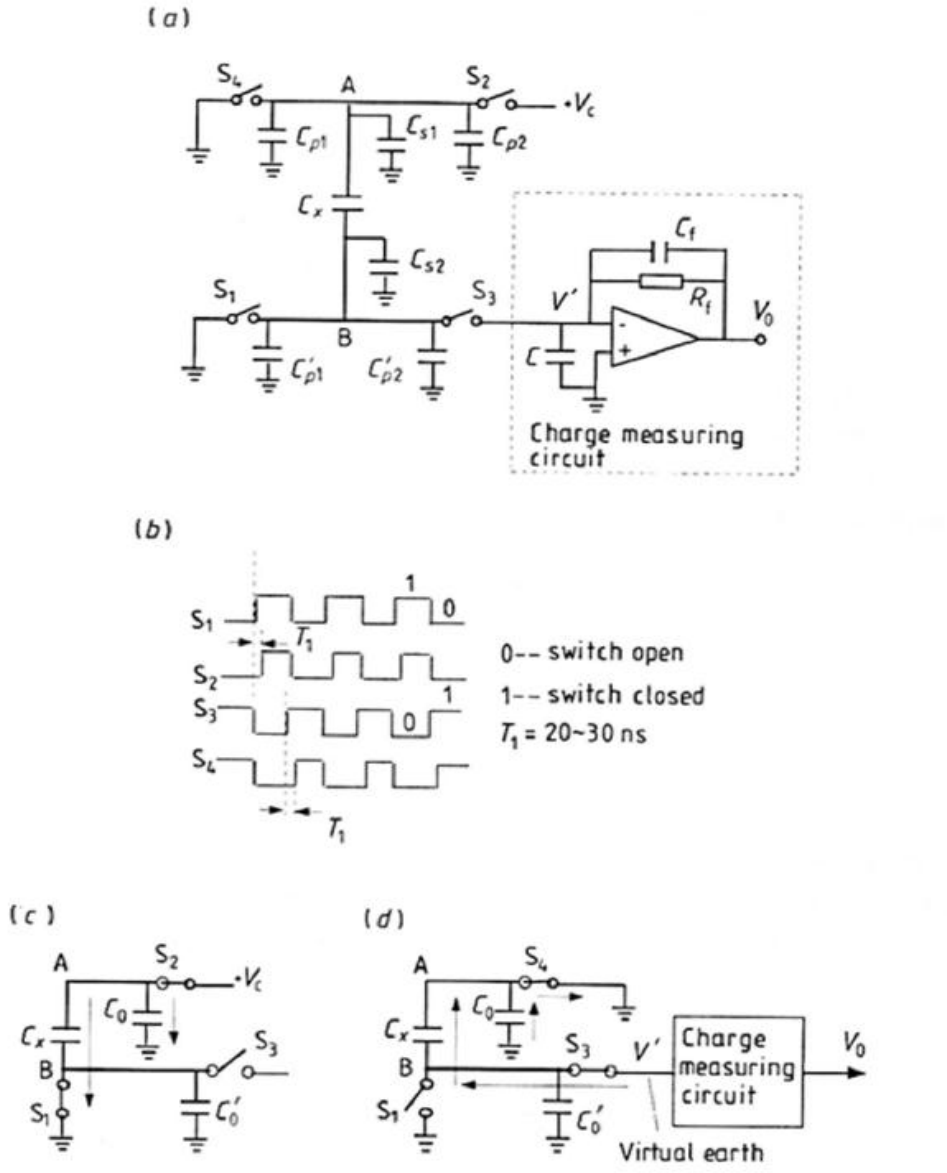


Figure 3-9 Removal of the stray capacitance in the immune charge transfer circuit, (a) showing the full circuit, (b) demonstrating how the switches open and close and (c) / (d) illustrating how the stray capacitance is removed between two electrodes (Pląskowski et al., 1995).

The voltage output V_0 has a range between 0 and 1.8V for the entire capacitance range of the TFL R5000. This voltage output is then combined with an offset voltage of 0.6V and sent to the 3V 16-bit analogue to digital convertor. This increases the output voltage sent to the converter to a range of 0.6V – 2.4V, this allows for a 33% margin above and below the capacitance

range, before the ADC is out of range (Barham, 2013). Further details can be found in Byars, (2009). The following section will describe the design of the new sensor that could lower the RMS noise further.

3.2.2 Design of the ECT sensor

This system removes the stray capacitances and allows for a RMS of 5×10^{-4} relative permittivity units, however to lower the noise further an increase in sensitivity between the electrodes was required. The original system that the design was based upon had eight electrodes, each being 30 mm long. To increase the signal to noise ratio, the new sensor would have to be designed to increase the capacitance change measured by a factor of 10 (Barham, 2013). This was done by dropping the number of electrodes from 8 to 4, doubling the electrode width, and making each electrode five times longer.

The sensor had an outer case of stainless steel grade 1.4404 (316L). Inside was a PTFE liner with space for four electrodes each 150mm long, with a 75 mm PTFE spacer on each end of them, holding the electrodes in the middle of the casing. The sensor was designed to be suitable for temperatures of up to 200°C, and was pressure tested using nitrogen up to 25 bar (Hunt, 2013) and (Barham, 2013). Figure 3.10 demonstrates a section of a 3D model of the sensor:

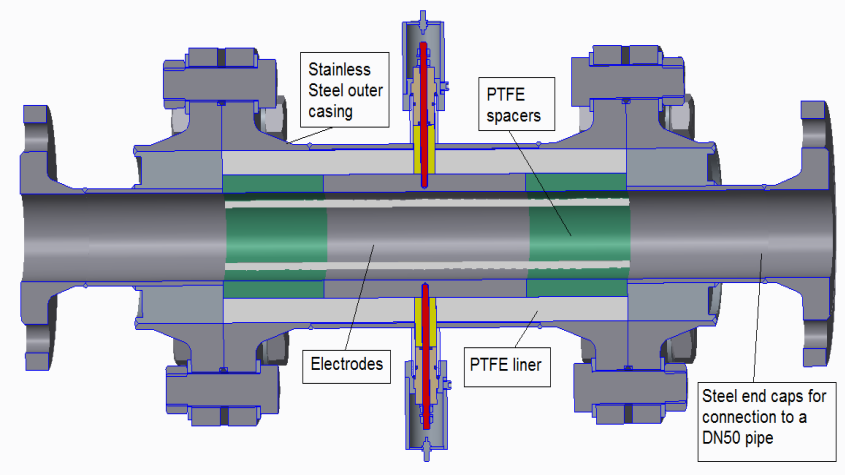
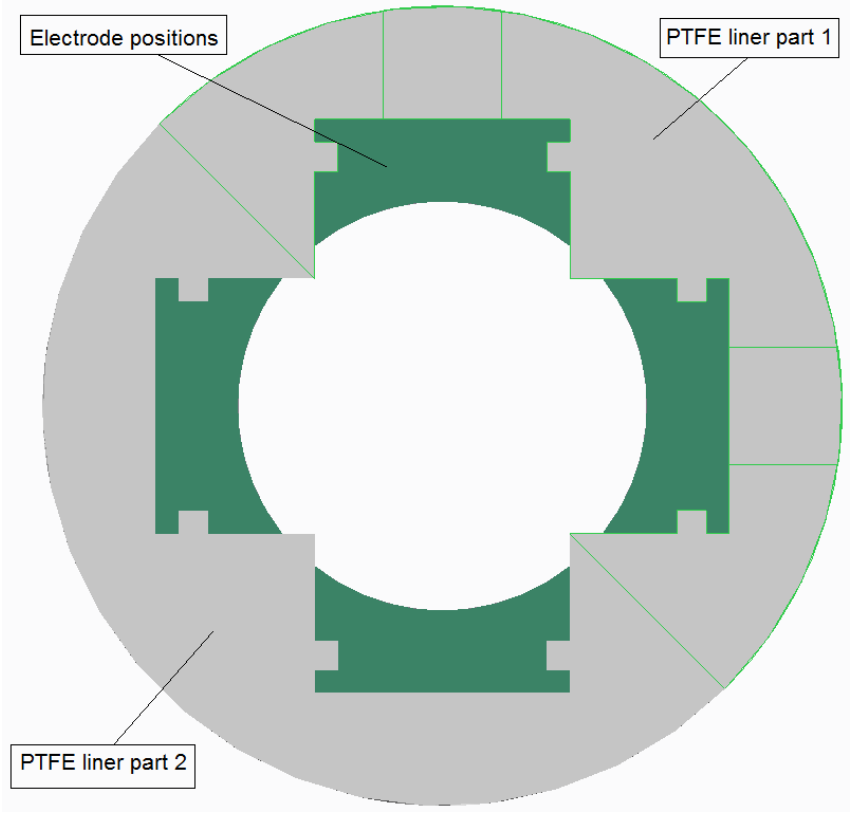


Figure 3-10 3D model section of the ECT sensor

Figure 3.11 explains the positon of the electrodes within the PTFE lining, the figure also demonstrates the correct shape of the PTFE liner within the



outer casing

Figure 3-11 The two parts of the PTFE liner, showing where the electrodes are inserted.

The modifications to the sensor electrode area allowed for a reduction in the RMS noise by a factor of 10 to 5×10^{-5}. Due to this the sensor was a success and it was shown it was possible to measure steam wetness at 11 bar with an accuracy of ± 0.5 % (Barham, 2013). The next section details the state of sensor after testing and how it was reconditioned for future use.

3.3 Reconstruction and improvement of the Electrical Capacitance Tomography Sensor

After testing, the sensor shown in the previous section was disassembled before being sent back to Atout. The testing process and the

disassembly damaged the sensor to the point where remanufacture of some of the sensors components was required before the rebuild could commence.

The sensor was to be reconstructed to match the original design, with exception that the external components would have to be able to withstand temperatures up to 220°C. This was because the sensor would be containing a static volume of superheated steam, therefore all the sensor would need to be kept above the saturation temperature of steam for a given pressure.

3.3.1 State of the sensor after previous testing

When the sensor was returned, the PTFE lining did not fit back into the casing and the electrodes as well as the PTFE spacers did not fit properly into the PTFE lining. Figure 3.12 demonstrates these initial issues with the condition of the PTFE liner.

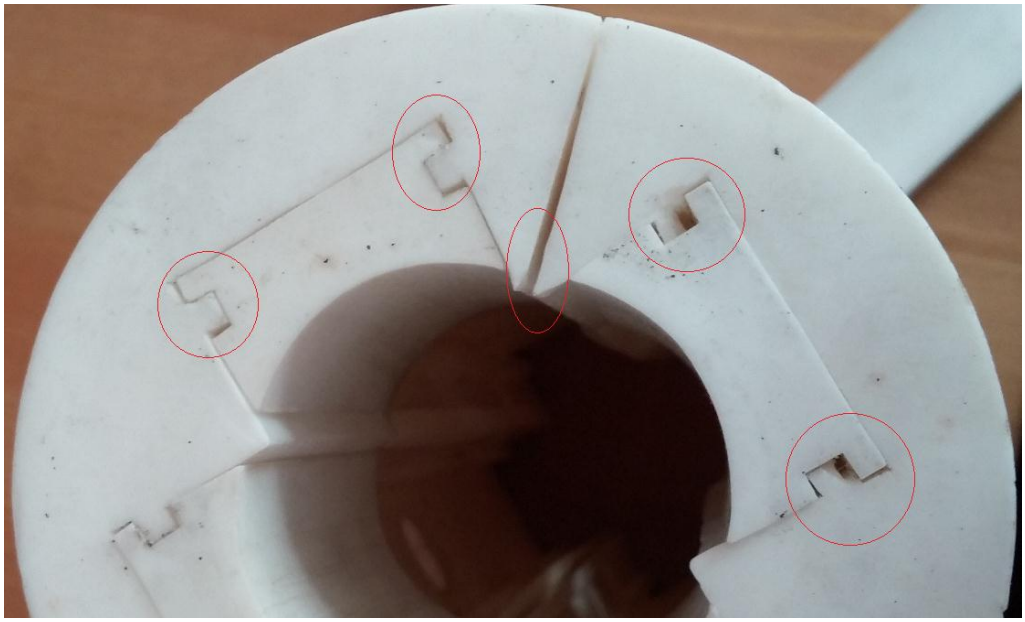


Figure 3-12 Expansion of the PTFE causing the issues highlighted in the red circles.

The issues with the PTFE deformation were caused because the PTFE had been heated above its glass transition temperature of 114.5°C, and as such had become rubbery and pliable. Furthermore the coefficient of expansion increases as the PTFE is further heated leading to greater expansion. Figure 3.13 demonstrates this principle causing the problems.

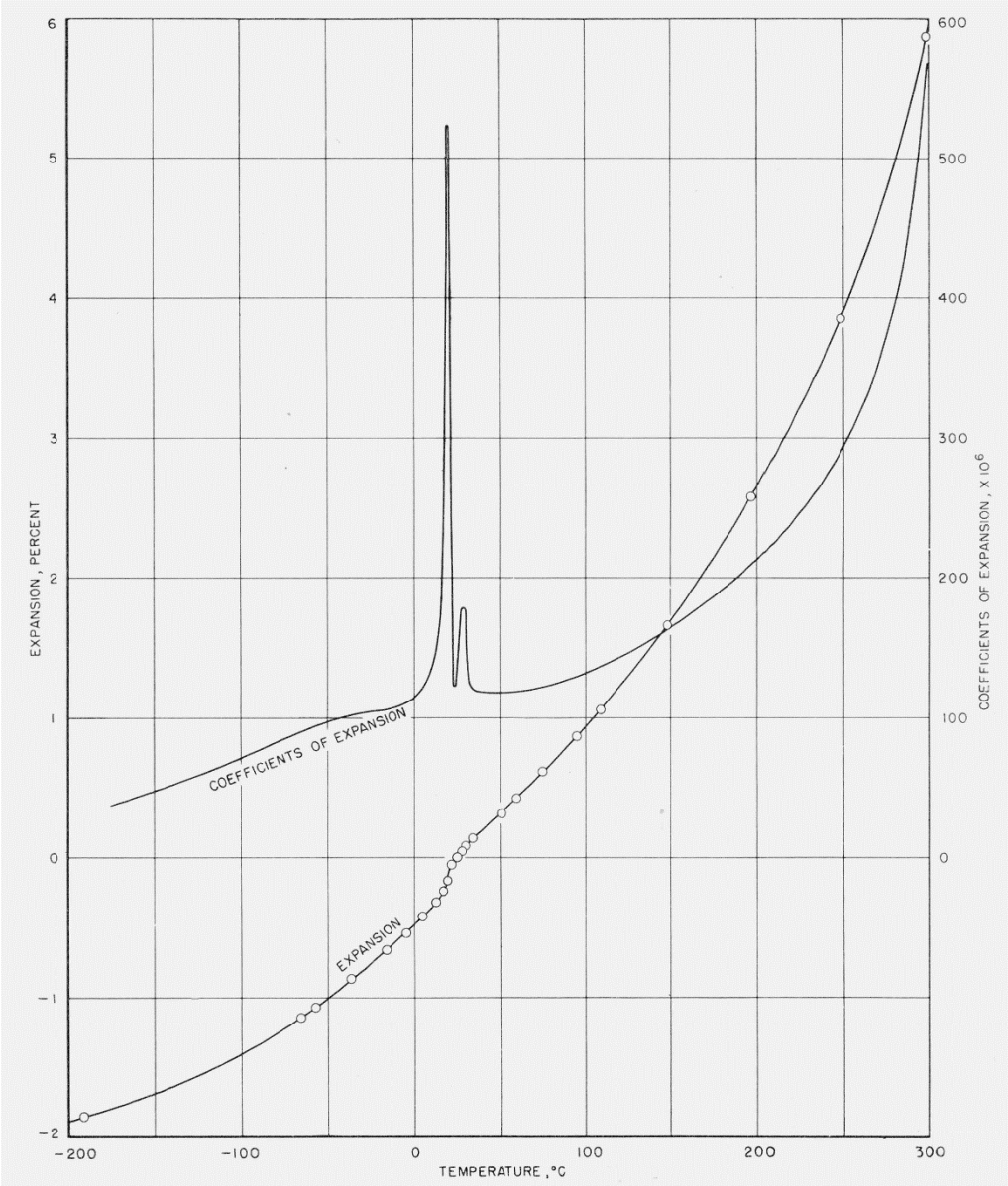


Figure 3-13 Expansion of PTFE as temperature increases as well as increase in the coefficient of expansion as temperature increases (Kirby, 1956)

PTFE expansion problems also caused the tubular spacers shown in figure 3.14, to not fit back into their designed slots. Meaning these would need to be replaced.

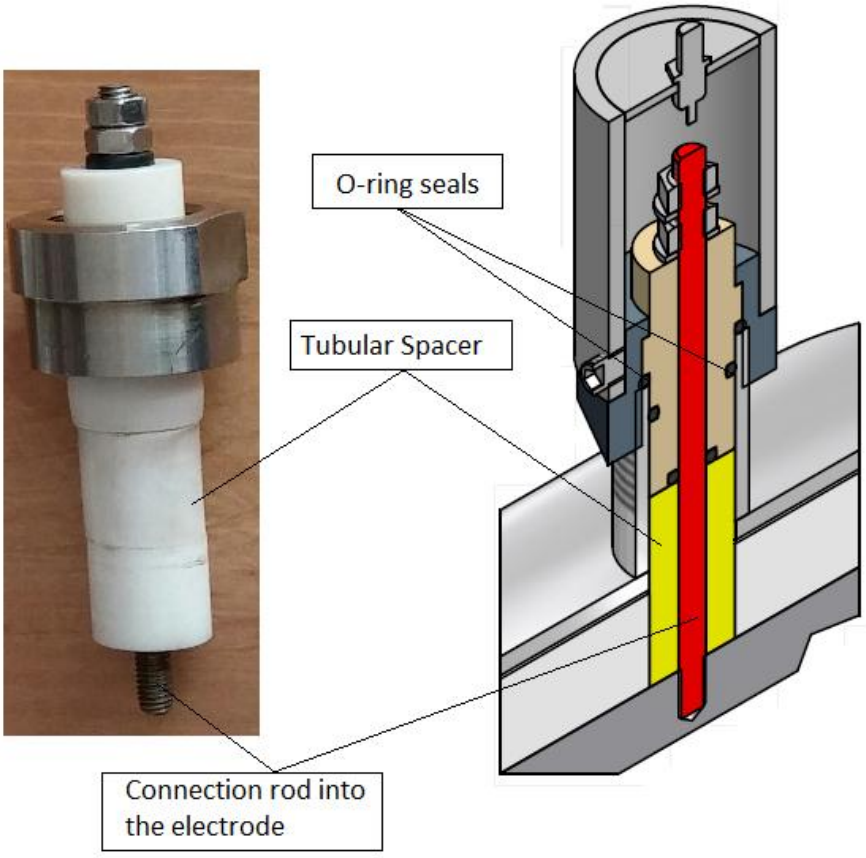


Figure 3-14 Tubular space assembly after previous testing on the left and how the tubular spacer fits within the electrode assembly on the right.

The final problem was the electronics, the wires that connect each connection rod to their corresponding plug had been broken or were badly frayed, and these required replacing with more durable wires that could take temperatures up to 220°C. The following section describes how each of the components were reassembled.

3.3.2 Reassembly of the ECT sensor

After identifying the issues discussed previously, solutions were sought to either replace the damaged components with ones made from more durable materials, or to identify which parts could be reused on the rebuilt ECT sensor. The PTFE components were thought to be a weak point on the old sensor and so an analysis was conducted to determine if the PTFE could be replaced with PEEK (PolyEtherEtherKetone). The analysis compared

the cost of PTFE to the cost of PEEK, the glass transition temperatures and the materials respective stable running conditions.

PEEK was found to have a higher glass transition temperature of 143°C and a higher melting point of 343°C. VICTREX® also had tested PEEK 450G to exposure to steam at 200°C for 2000 hours, concluding that the material was stable enough to be used in a steam environment. The water absorption of PEEK was found to be as low as that of PTFE. This information gave a clear picture that PEEK could be used to replace the PTFE within the sensor. However a cost estimate of remaking one PTFE lining out of PEEK, gave an estimate of over £3000. This was unfortunately too expensive to make with our limited budget, and so we had to go with the second option of either remaking the parts from PTFE or reassembling them if they were not damaged.

The PTFE liners shown in figure 3.12 were found to be able to go back into the sensor outer casing by firstly sliding one liner all the way in while partially having the second liner inserted, this was to align the outer casing rod holes with the PTFE liner holes. Once this had been completed, the second PTFE liner was gently tapped into position. The PTFE spacers that hold the electrodes in place, were found to get stuck due to the problems highlighted in figure 3.12.This led to the insertion grooves shown by the four outer red circles, to be filed down to the point where the spacers and electrodes could be smoothly tapped into position. After this, the connection rods shown in figure 3.14 were screwed into their respective electrodes. Using the rods as a guide, the tubular spacers were then pushed into position. The expansion of the tubular spacers due to earlier testing had caused them not to fit back into the outer casing holes or the PTFE liner holes: these were replaced with new components. Finally the end caps containing the O-ring seals and the tightening nuts, were fastened into place.

The assembly concludes with the attachment of the electronics to each electrode. Originally, the sensor had each electrode connected to a SMB

type connector mounted on the outer casing, this meant that wires from the TFL R5000 could be easily plugged into the sensor. For this testing the sensor had to take up to 220°C, since no SMB type connector would take those temperatures, a coaxial cable would have to be directly connected to each electrode, whereby they would be long enough to allow for the electronics system and computer to be connected from a safe distance. Figure 3.15 demonstrates the electronics setup for each electrode, before the replacement of the components due to temperature.

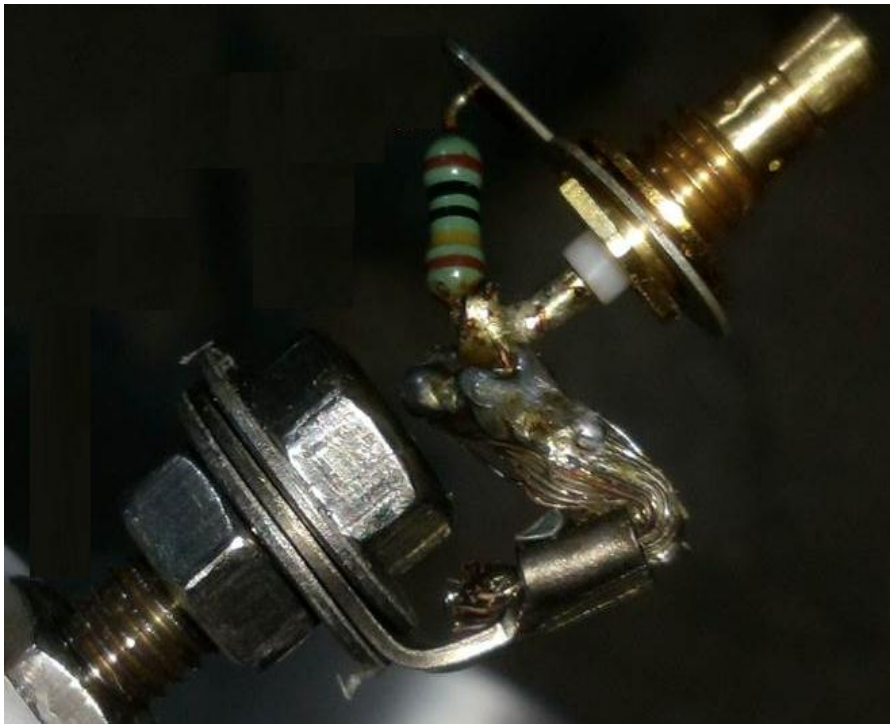


Figure 3-15 Previous electronics connection for the electrode connection rod shown in the bottom left, to the SMB type connector shown in the top right.

The purpose of the resistor is so that the current is converted into a voltage. It was important that the sensor had only one earth connection as two would cause a faulty signal, giving errors for the capacitance readings.

Once each cable had been wired to each electrode rod and a SMB type connector had been attached, the sensor was checked for shorts. It was found that the end caps shown in figure 3.16 would cause the system to short if they

were attached too tight, this problem was averted by using a screw thread to hold the cap on the end of the fitting. The finished sensor electronics is shown in figure 3.16.



Figure 3-16 The reassembled ECT sensor, the end caps are what the cables are threaded into and held in place by the screw fitted into each end cap

The reconstructed sensor was pressure tested up to 20 Bara using water. After which the electronics were tested again for shorts; none were found indicating that the pressure had not pushed any of the connections closer together, which meant that the sensor was ready for normal operation.

This concludes the reassembly of the sensor, the next section details the theoretical modelling of the capacitance measurement between the

electrodes and the set-up of a program that can predict the capacitance measurement, as well as the relative permittivity of mixtures.

3.4 Analysis of Changes in Capacitance Measurement within varying Environments

A program is required, that can theoretically predict the capacitance between pairs of electrodes, with varying mixtures of water air or steam between them, thus allowing for measurement of the mixture permittivity. The advantage of the program, is that it will be able to test on mixtures under pressures far in excess of what the test can produce, and so would be able to test on steam used in a nuclear power station under 70 bar.

A code for calculating electrical properties across a set spatial area was created by Ian Cooper, 2016. The first part detailed how to create a mesh, whereby N amount of charges can be placed. This is to model how the charges affect the potential difference within a set space. The potential difference at every point $V(x,y,z)$ within the mesh can be defined by equation 3.12.

$$V(x,y,z) = \sum_{c=1}^{N} \frac{Q_c}{4\pi\varepsilon_0 \left|\overrightarrow{R(x,y,z)} - \overrightarrow{R(x,y,z)_c}\right|} \tag{3.12}$$

$R(x,y,z)$ is the position vector and $R(x,y,z)_c$ is the position vector of charge Q_1 to Q_N (Cooper 2016).

Likewise using Coulomb's law where the force between two charges can be calculated from their respective charges, the distance between them and Coulomb's constant. The electric field in each of the three spatial planes can be derived from equations 3.13 to 3.15.

$$E_x(x,y,z) = \sum_{c=1}^{N} \frac{Q_c}{4\pi\varepsilon_0} \frac{(x - x_c)}{\left|\overrightarrow{R(x,y,z)} - \overrightarrow{R(x,y,z)_c}\right|^3}$$

(3.13)

$$E_y(x,y,z) = \sum_{c=1}^{N} \frac{Q_c}{4\pi\varepsilon_0} \frac{(y - y_c)}{\left|\overrightarrow{R(x,y,z)} - \overrightarrow{R(x,y,z)_c}\right|^3}$$

(3.14)

$$E_z(x,y,z) = \sum_{c=1}^{N} \frac{Q_c}{4\pi\varepsilon_0} \frac{(z - z_c)}{\left|\overrightarrow{R(x,y,z)} - \overrightarrow{R(x,y,z)_c}\right|^3}$$

(3.15)

There are limitations for the above equations, like when the denominator of each equation goes to 0 or if the nominator tends to 0. To fix these, limits were set to each variable so the program has a maximum electric field strength and maximum potential difference assigned, as well as a minimum distance for each point to a charge in each plane.

Using the equations 3.12 to 3.15 and the limiting constants allows for a code to be made that can plot electric field strength and potential difference change across two flat electrodes. The rebuilt ECT sensor had four electrodes of known curvature, therefore the code was modified by the author to be able to model the electric field strength and potential difference for the sensor layout. On top of this, to map the strength of the electric field, electric field lines were plotted that were perpendicular to the equipotential surfaces at every point due to $\overrightarrow{E} = -\nabla V$. This allowed for a 2D representation of the sensor to be created in figure 3.17, showing how the potential difference changes, and where the electric field strength is strongest from the excitation electrode to the detection electrode.

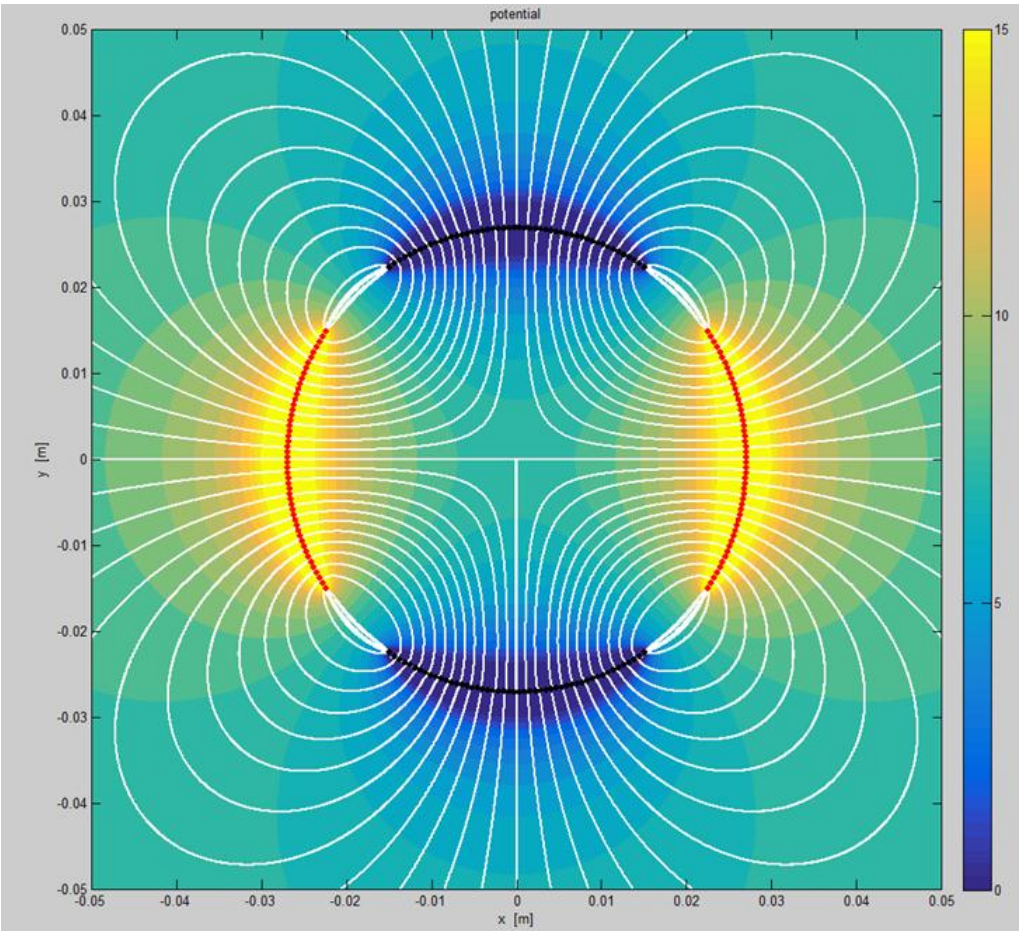


Figure 3-17 Change in potential difference and electric field strength for the sensor with two excitation electrodes in red and two detection electrodes in black.

The map of the sensor shown in figure 3.17 is an ideal scenario; however in reality each electrode in turn acts as the excitation electrode, while every other electrode in turn acts as the detection electrode. As this process is repeated for every electrode, the other two electrodes will still have an equal effect as the detection electrode, so the direction of the electric field goes from the excitation electrode to n-1 detection electrodes.

It can be seen from figure 3.17 that for adjacent electrodes, the area with the strongest electric field is the closest point between a red and black electrode, which is the corners of the sensor. This is where a local permittivity

change within the whole permittivity mixture will have the greatest effect on the capacitance being measured.

To show this is correct, the program must have the ability to measure capacitance between each electrode pair and to be able to insert areas of high sensitivity into the sensor represented by areas of high relative permittivity, that can cause a change in the measurement. The measurement was completed using a formula for measuring the capacitance between two curved plates by Chen *et al.,* (2014). The formula was derived from calculating the capacitance between two curved patch electrodes situated around a dielectric rod. The equation below defines the capacitance per metre length of electrode.

$$C = \frac{(\varepsilon_1 + \varepsilon_2)K(t)}{K(\sqrt{1 - t^2}}$$

(3.16)

Where t is defined as:

$$t = \sin\frac{\phi_1 - \phi_0}{2} \Big/ \sin\frac{\phi_1 + \phi_0}{2}$$

(3.17)

figure 3.18 below demonstrates this and what ϕ_1 and ϕ_0 are.

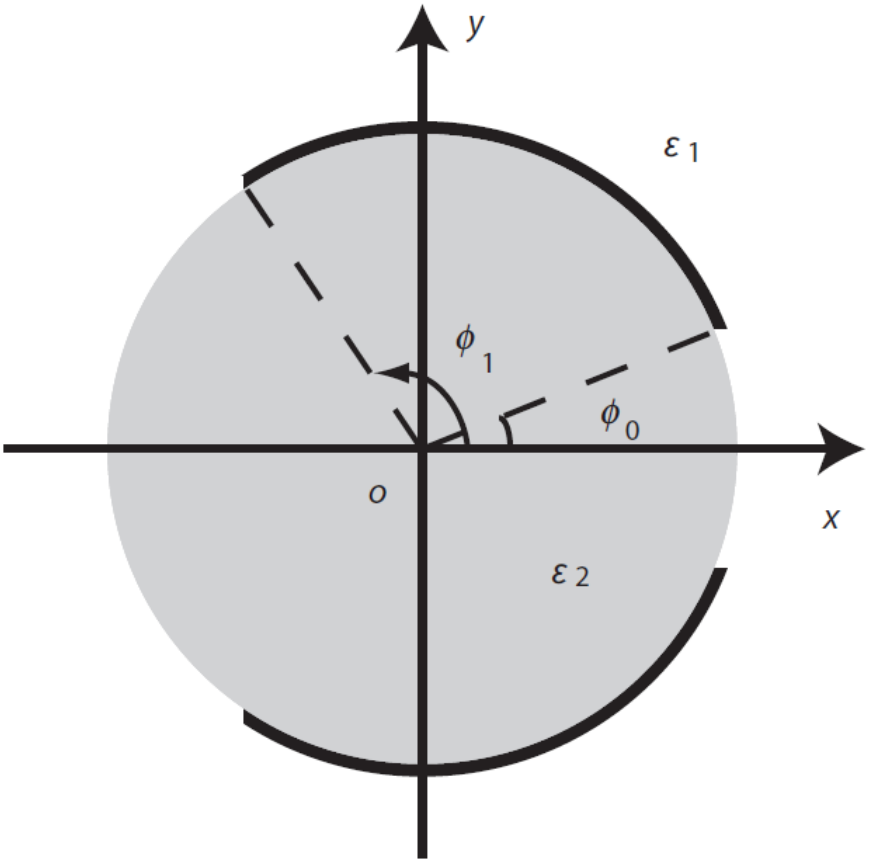


Figure 3-18 The layout of a 2 electrode capacitance sensor (2014)

Using ϕ_1 *and* ϕ_0 the positioning of the electrodes can be changed from adjacent electrodes to opposite electrodes. The equation 3.16 only uses the permittivity of the whole space ε_2, therefore the mixture permittivity would have to be known, and this could be calculated using the parallel, droplet or series model. To give a more accurate result, the capacitance should be calculated in sections, whereby each electrode is split into n parts, figure 3.19 illustrates this:

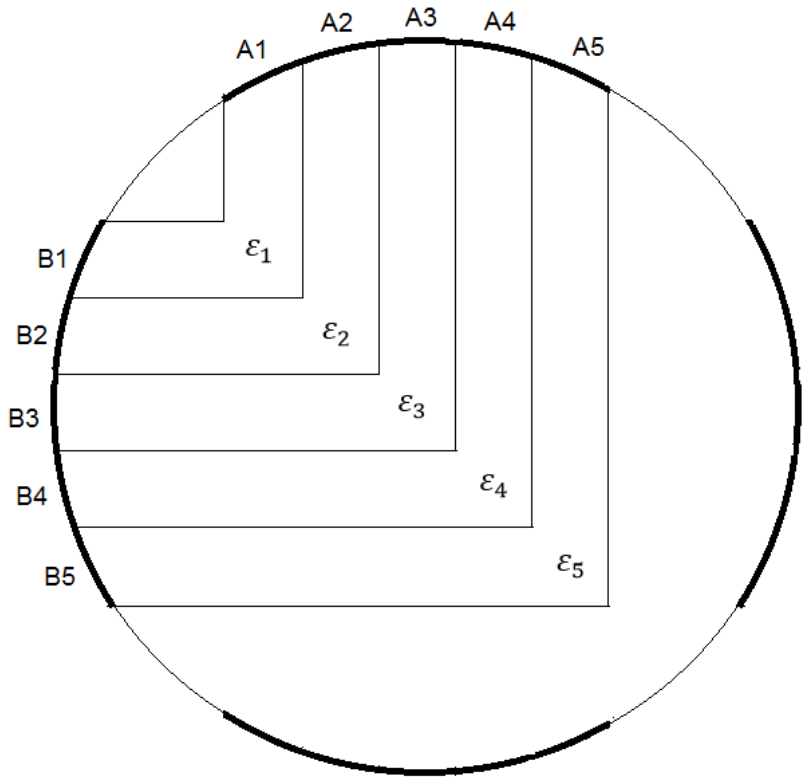


Figure 3-19 The calculation of capacitance between electrodes A and B is split into five parts where the capacitance is calculated between A1 and B1 to A5 and B5, using the average permittivity of each space ε_1 to ε_5

The overall capacitance is calculated by summing all the split capacitances, because they are all in parallel. This means that the more slices each electrode is sliced into the more accurate the effect of local high permittivity concentration will be on the measurement. For the model, each electrode is split into 50 slices to allow for reasonable calculation time by the computer.

To simulate a local high permittivity concentration, a map of permittivities across the sensor using a 1000 x 1000 matrix was constructed. The map has a real world size of 0.1 x 0.1 m, whereby the sensor with four electrodes was positioned in the centre with a diameter of 0.054 m. This allowed for the permittivity outside and inside the sensor to be fixed at every point, this meant that water concentrations of different sizes and shapes could be inserted wherever needed.

The calculation of capacitance could not be made truly 2D due to equation 3.16 calculating the capacitance per metre length of electrode. To proceed; firstly the capacitance was multiplied by 0.15, meaning the capacitance is calculated for the same length electrodes as the rebuilt sensor. This effectively modelled a column of high permittivity material inserted into the sensor.

The capacitance measurement is half of the picture, as with a real sensor, once the capacitances have been measured for a range of known permittivities, using the method in section 3.1.3, the sensor can be calibrated to measure unknown permittivities. This same process was completed on the capacitance program, by having the entire permittivity map fixed at range of relative permittivies from 1 to 2. The area outside the sensor was always fixed at a relative permittivity of 1 to simulate an air environment. Figure 3.20 shows the calibration of the sensor with the fitted regression model.

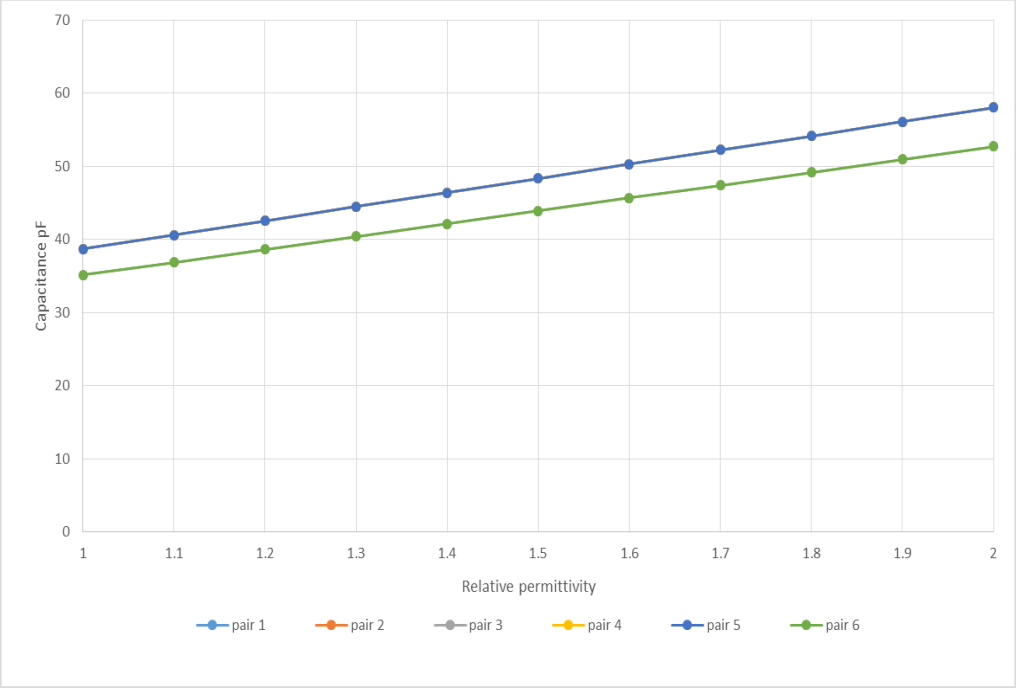


Figure 3-20 Calibration of the capacitance program using known relative permittivies, the blue line is for adjacent electrode pairs and the green line is for opposite electrode pairs. Pairs 2, 4 and 5 are under pair 1 and pair 3 is under pair 6.

A useful benchmark for the program was to see how well it could predict mixture permittivity inside the sensor area against the mixture permittivity calculated by the parallel, droplet and series model. For this test, five different sized columns of water were used, ranging from a diameter of 1 mm to 3 mm increasing in 0.5 mm steps, to give five different volume fractions to compare against. The layout of the sensor area within the program is shown in figure 3.21, detailing what each of the six electrode pairs are.

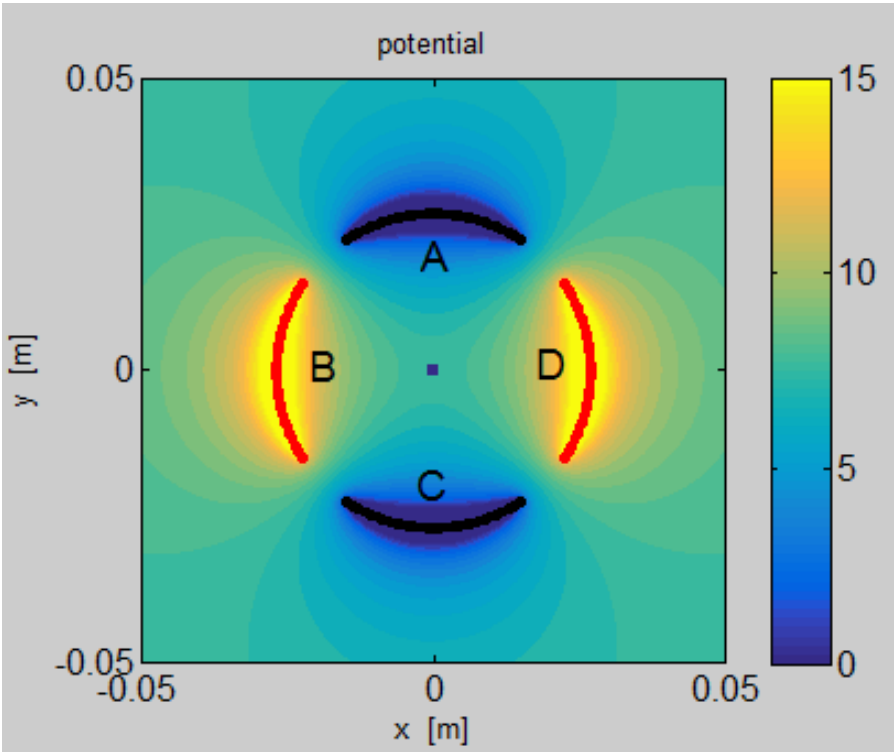


Figure 3-21 Location of the four electrodes, where AB = pair 1, BC = pair 2, BD = pair 3, AD = pair 4, CD = pair 5, and AC = pair 6.

The results of this test and a comparison to the three models are shown below in figure 3.22:

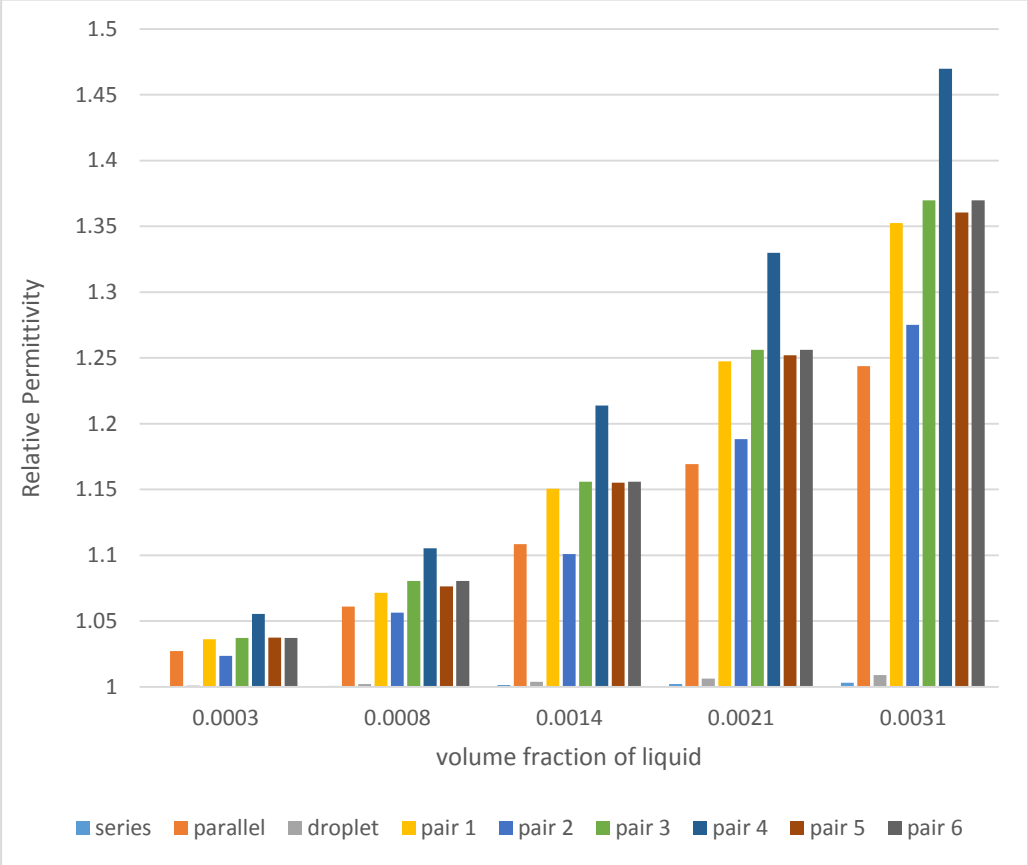


Figure 3-22 Comparison of the relative permittivity of different air and water mixtures calculated using the program against the relative permittivities predicted by the series, parallel and droplet model.

The graph demonstrates that there is poor correlation between the droplet and series model, as well as no significant difference between the parallel model and the predicted relative permittivity for all pairs except 2 and 4. The difference with pairs 2 and 4 was because as the area of high permittivity cannot be perfectly aligned to the centre of the grid, due the odd number of permittivity points in the x and y direction, causing a difference in the amount of permittivies being averaged for the two pairs. The pairs 3 and 6 being opposite pairs are not affected by the spatial positioning, they show a small difference that increases as the volume fraction of water becomes larger. This means that if the volume fraction is kept sufficiently low, then the

program is adequate to predict changes in relative permittivity that are not significantly different to the permittivity model.

This program is calculated mostly in 2D. The only 3D element is the length of the electrodes, which means the volume fraction of water is based upon the water as a column, not a droplet, therefore the next section details how a true 3D program is created.

3.5 Capacitance measurement program in a volume

The purpose of the true 3D program is to accurately measure the relative permittivity of mixtures containing a low volume fraction of water, as the last section showed how the program became inaccurate at higher volume fractions.

In order to achieve a 3D representation of the sensor, the permittivity must be mapped across the three dimensional domain, this is completed by utilising a rank 3 tensor to describe the permittivity of the scalar field within the 3D space. The tensor has the following structure:

$$\varepsilon_{space} = \begin{pmatrix} \begin{pmatrix} a1 \\ a2 \\ a3 \end{pmatrix} & \begin{pmatrix} b1 \\ b2 \\ b3 \end{pmatrix} & \begin{pmatrix} c1 \\ c2 \\ c3 \end{pmatrix} \\ \begin{pmatrix} d1 \\ d2 \\ d3 \end{pmatrix} & \begin{pmatrix} e1 \\ e2 \\ e3 \end{pmatrix} & \begin{pmatrix} f1 \\ f2 \\ f3 \end{pmatrix} \\ \begin{pmatrix} g1 \\ g2 \\ g3 \end{pmatrix} & \begin{pmatrix} h1 \\ h2 \\ h3 \end{pmatrix} & \begin{pmatrix} i1 \\ i2 \\ i3 \end{pmatrix} \end{pmatrix} \tag{3.18}$$

The equation 3.18 shows the levels of a grid made of 27 permittivity values, split over three layers for each letter. Each layer has the overall capacitance calculated per electrode pair in the same as the previous section using equation 3.17. In the same way that the capacitance for electrodes split in small sections is in parallel, the same applies for the layers of the grid stacked together, therefore the capacitance is calculated at each pair, for each slice and summed together. This gives the same capacitance values for

each electrode pair for known permittivies as shown in figure 3.20, thus the calibration is still valid, indicating the same sensitivity as the 2D program.

The electrodes were kept to the same length of 0.15 m, the capacitance was calculated for each slice of thickness 0.00075 m, giving 200 slices within the sensor. To test whether the accuracy had improved as predicted due to the lower volume fraction of water demonstrated from figure 3.21, the mixture permittivity was calculated by the program and compared to the three models, figure 3.23 shows the results of the test.

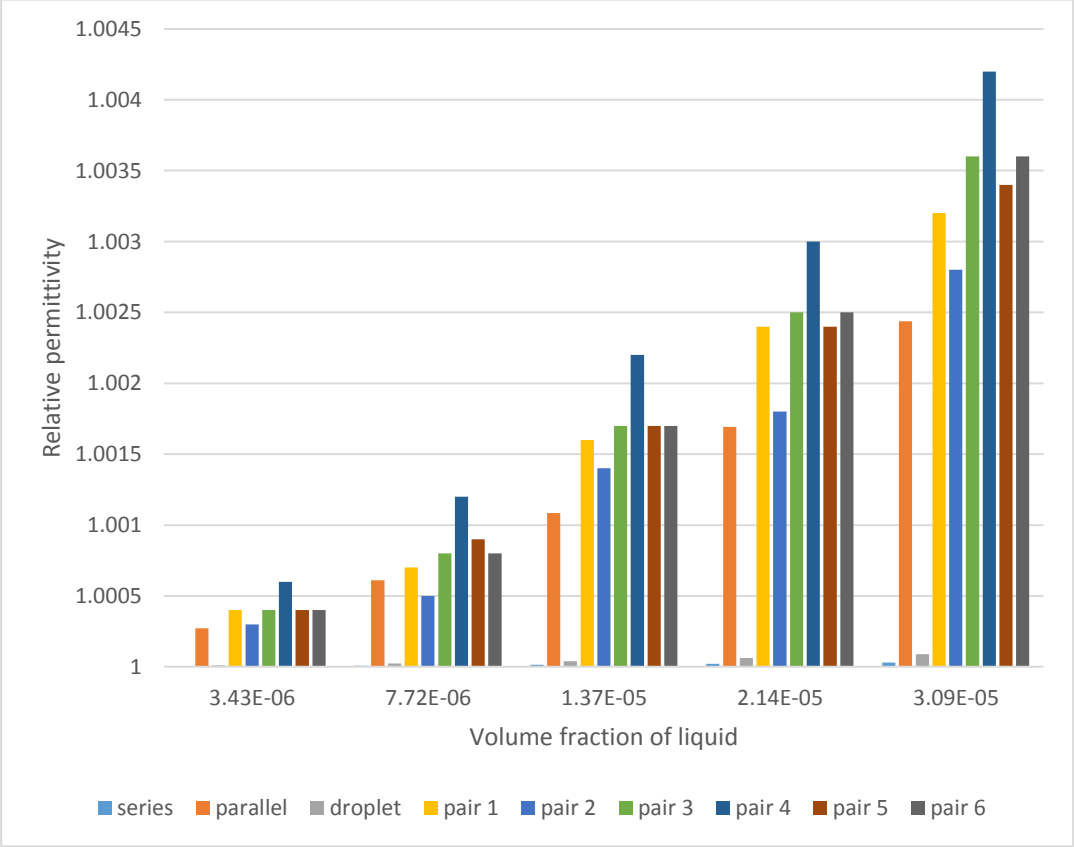


Figure 3-23 Comparison of the relative permittivity of increasing volume fractions of water within air calculated using the 3D program, against the relative permittivities predicted by the series, parallel and droplet model.

The trend of increasing inaccuracy is still apparent within figure 3.23, but the scale is significantly smaller, at these volume fractions the program is only 0.18% different to the parallel model for the largest capacitance pair, four, and as little as 0.03% different for the smallest pair, two.

A final addition to the program was to add the ability to monitor the relative permittivity within the sensor while droplets were falling. This was achieved using a 3D time varying scalar field and plotting the relative permittivity over time. As an example of this, figure 3.24 demonstrates four droplets with a diameter of 3mm falling through the sensor over 20 seconds, with each droplet having a total water volume fraction of 3.09×10^{-5} within the sensor. Further details of the program working and being tested against permittivities for water under different pressures and temperatures calculated using IAPWS-97, can be found in chapter 4 section 4.7.

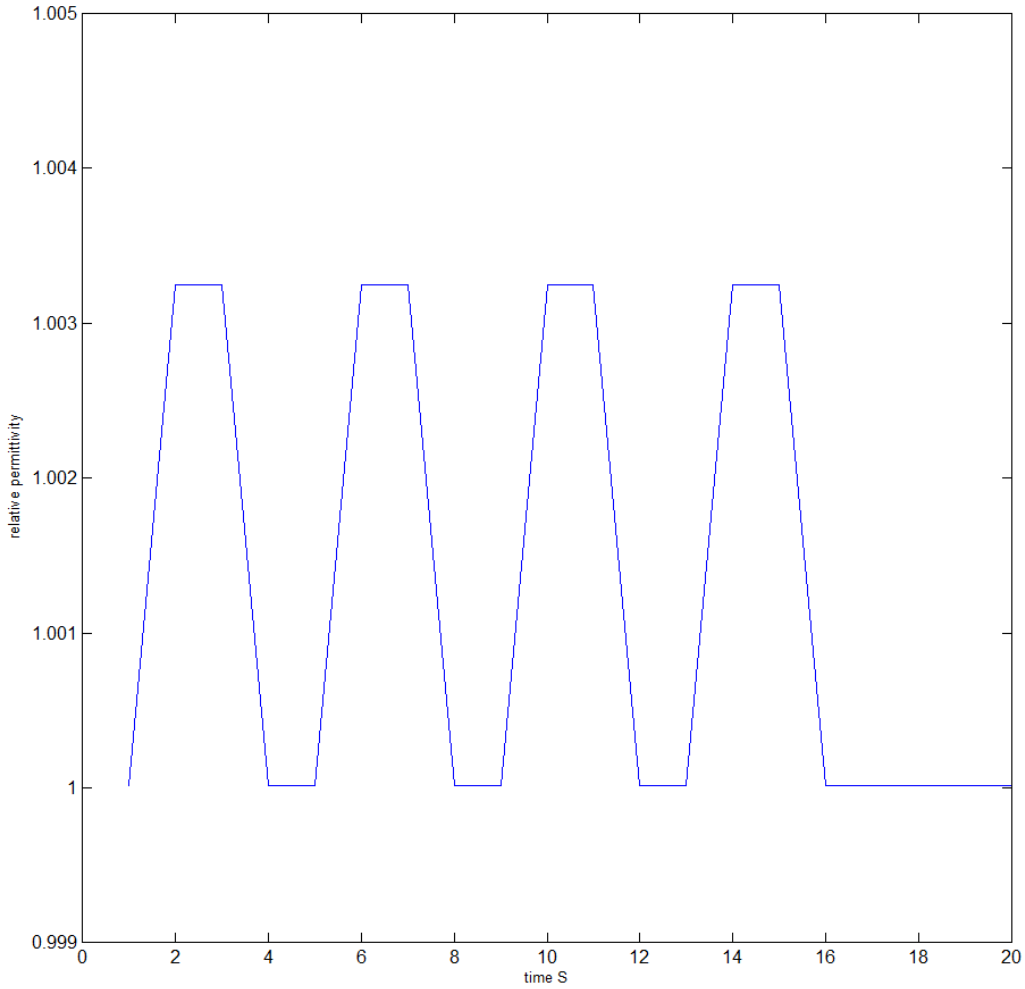


Figure 3-24 Plot of relative permittivity change over time for a volume fraction of 3.09×10^{-5} passing through the sensor four times, measured using electrode pair 1

The program shows water injection into the sensor over a period of time and can predict the mixture permittivity close to how it would be predicted using the parallel model. Apart from relative permittivity measurement the capacitance data, once calibrated to each electrode's sensitivity, can be used for cross sectional image reproduction. The next section will look into how this is achieved using linear back projection and what are the principles of the technique.

3.6 Principles of Linear Back Projection

The technique known as linear back projection referred to as LBP, is used to reconstruct a cross sectional image of a two phase flow within an electrical capacitance tomography sensor. An ECT system is assumed to have a linear relationship set by equation (3.6), if the equation is altered to describe how a system with *m* capacitance measurements can be calculated simultaneously, the following equation is assumed to describe the relationship:

$$C = SK \tag{3.19}$$

C is a column vector of the form (n x 1), K is a column vector of the form (p x 1), where is p is the number of relative permittivity measurements within the image, with each pixel in the image given a relative permittivity value, so for a square image of 40 x 40 pixels p = 1600. S replaces J from equation 3.6 and is a matrix of the form (n x p), called the sensitivity matrix.

The sensitivity matrix for a four electrode system will have six columns each with 1600 values. This matrix can be thought of as a combination of six sensitivity vectors, where each vector describes the sensitivity between each electrode pair. The numbers that make up the sensitivity matrix are a measure of how strongly a pixel will show a change in relative permittivity detected by an electrode pair. This means that for the four electrode system, each pixel will have six sensitivity values.

Each sensitivity vector is produced by using the electric field for the cross sectional area using equations (3.13) and (3.14). Using two electrodes, called i and j. First two 500 X 500 node matrices were created for the i electrode, one for electric field in x direction and one in y direction, this was repeated with the j electrode to give four matrices. To shrink this data down to 40 by 40 pixels, the average electric field from (3.13) and (3.14) was required per pixel in the x and y direction. This was taken by splitting the field in each of the four 500 X 500 matrices 1600 times, and averaging each of these areas to give each averaged electric field per pixel. Therefore every pixel has four values, the average electric field in the x direction for i Exi, the average electric field in the y direction for i Eyi, the average electric field in the x direction for j Exj and the average electric field in the y direction for j Eyj. These four values are made into the following two vectors:

$$\begin{bmatrix} Exi \\ Eyi \end{bmatrix} \begin{bmatrix} Exj \\ Eyj \end{bmatrix}$$

The dot product of these two vectors is then taken and then integrated over the area of each pixel to give a sensitivity value as shown by equation (3.20):

$$S = \iint \begin{bmatrix} Exi \\ Eyi \end{bmatrix} \cdot \begin{bmatrix} Exj \\ Eyj \end{bmatrix} dA \tag{3.20}$$

The 1600 sensitivity readings within the vector are then normalised between 0 and 1 to give the sensitivity vector which is a map for the electrode pair. This process only needs to be performed for one adjacent pair and one opposite pair, the other adjacent and opposite pairs can be found by rotating the respective vectors. Figure 3.24 shows the maps for the adjacent and opposite pair formed from their respective sensitivity vectors.

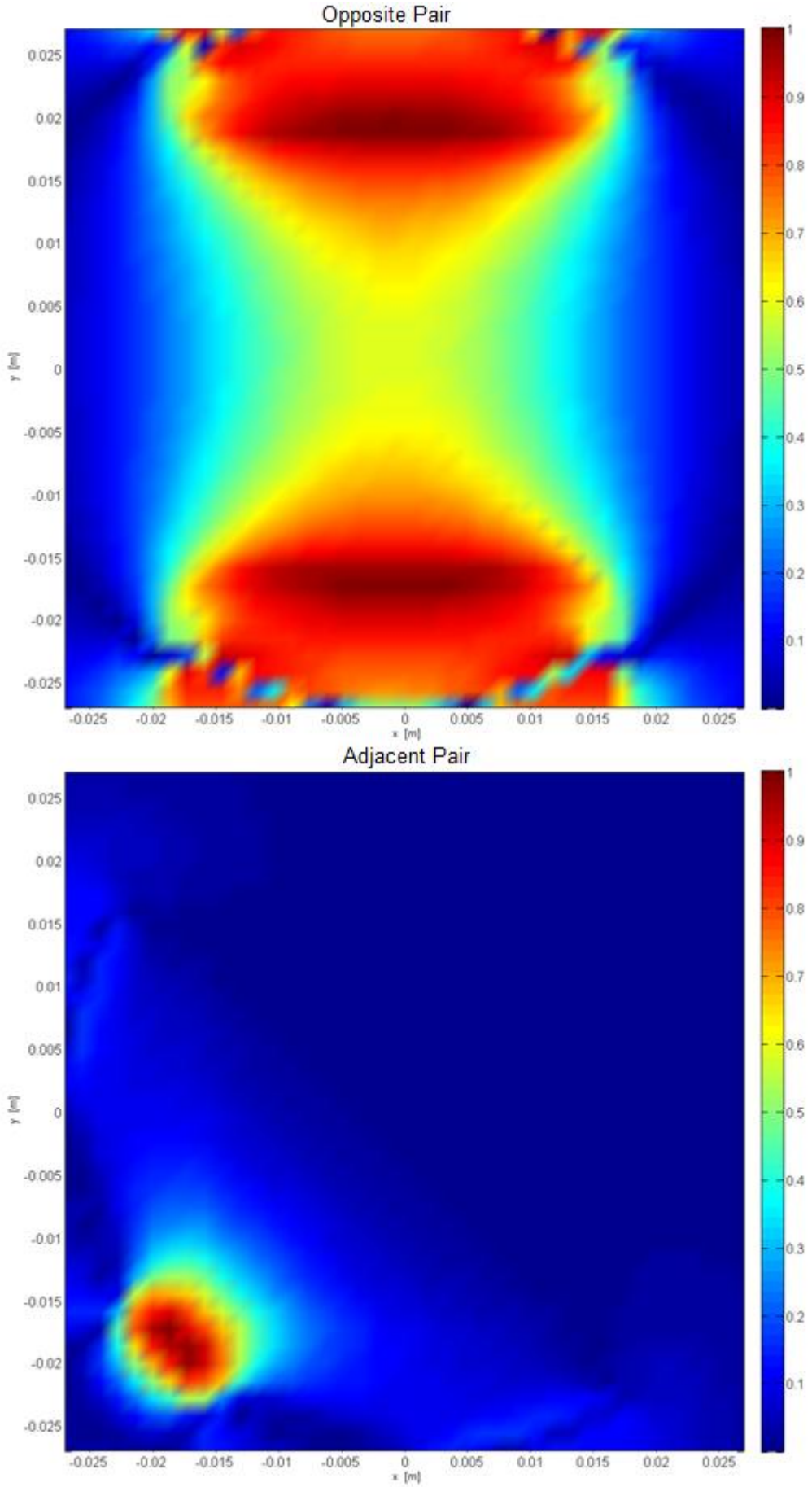


Figure 3-25 Electrode sensitivity maps

The six sensitivity vectors are then combined to give the full sensitivity matrix for the sensor. The shape of the matrix is not square this implies that equation 3.19 cannot be rearranged with the inverse sensitivity matrix to equal the relative permittivity vector, instead this is where linear back projection comes in to calculate K using the following relationship:

$$K = S^T C \tag{3.21}$$

The transpose of the sensitivity matrix S^T is used in LBP to calculate the normalised relative permittivity vector, along with the normalised capacitance vector C.

LBP using a low number of electrodes gives very blurred images, one way to improve upon this, is through iterative calculation, whereby the permittivity vector is recalculated though using a combination of equations 3.19 and 3.21. Barham (2013), used the following process to reiterate the image until there was minimal difference.

1. The normalised relative permittivity vector K is calculated using equation 3.21
2. Substitute K into equation 3.19 to calculate a new normalised capacitance vector called C_1
3. Calculate the difference between the vectors C and C_1 called ΔC vector
4. Use the ΔC vector to generate ΔK vector using equation 3.21
5. Subtract ΔK from K to give K_1 completing one reiteration step
6. Repeat steps 1 to 5 replacing K with K_1 use this to generate C_2, from this ΔC is calculated as the difference between C_2 and the original normalised measured values C
7. Repeat step 6 until the reiteration produces minimal difference

A further way to improve image quality is by using regularization, Yang and Peng (2003); explored different ways that LBP can be improved using different algorithms. A common method known as Tikhonov Regularization was explored in the literature. The process works by using the standard Tikhonov regularization procedure, if we have matrix A and vector B, whereby we wish to find vector x we have:

$$Ax = B$$

Using the standard Tikhonov regularization procedure the solution is demonstrated in equation 3.22:

$$\hat{x} = (A^T A + \Gamma^T \Gamma)^{-1} A^T B \tag{3.22}$$

The solution shown above works upon using a suitable chosen Tikhonov matrix Γ, in most cases this matrix is used in the form of a multiple of the identity matrix (aI). The Tikhonov Regularization is produced by solving equation 3.19 in the same process, in this way the solution for the permittivity vector becomes:

$$\widehat{K} = (S^T S + \mu I)^{-1} S^T C \tag{3.23}$$

The regularization parameter μ is chosen empirically to give the desired outcome. A small value of μ gives a good approximation to the original problem but can increase errors, whilst a large value of μ suppresses the data errors but increases the approximation error.

In the same way as before with the basic LBP method, reiteration will increase accuracy. Therefore reiteration of equation 3.23 using the steps from Barham (2013), by replacing equation 3.21 with equation 3.23 will allow for reiteration. The next section will utilise this method and integrate the process

and the Tikhonov Regularization into the 3D capacitance program to build images of water within the capacitance section.

3.7 Incorporation of the Tikhonov Regularization LBP method into the Capacitance measurement program

To incorporate the Tikhonov Regularization, the normalised capacitances had to be produced first. The 3D program demonstrated in section 3.5 calculated the capacitance within the sensor when it was filled with a material that had a relative permittivity of 2 at every point, this gave the full capacitance values for the six electrode pairs. The same procedure was repeated using a material with a relative permittivity of 1, this gave the empty capacitance values. The next stage was to use the formula from (Gamio *et al.,* 2004), to normalise capacitance values calculated from the six electrodes, this formula is given in equation 3.24:

$$\lambda_i = \frac{c_i - c_{i(empty)}}{c_{i(full)} - c_{i(empty)}} \tag{3.24}$$

From this stage, the cross sectional image is created using the process described in the previous section. As an example of this technique, a water droplet of 3 mm diameter will be inserted into the sensor in two different areas. Placed in the locations shown in figure 3.25, using a 2D map of the cross sectional potential difference. The LBP results using Tikhonov Regularization are shown in figure 3.26 for the two tests.

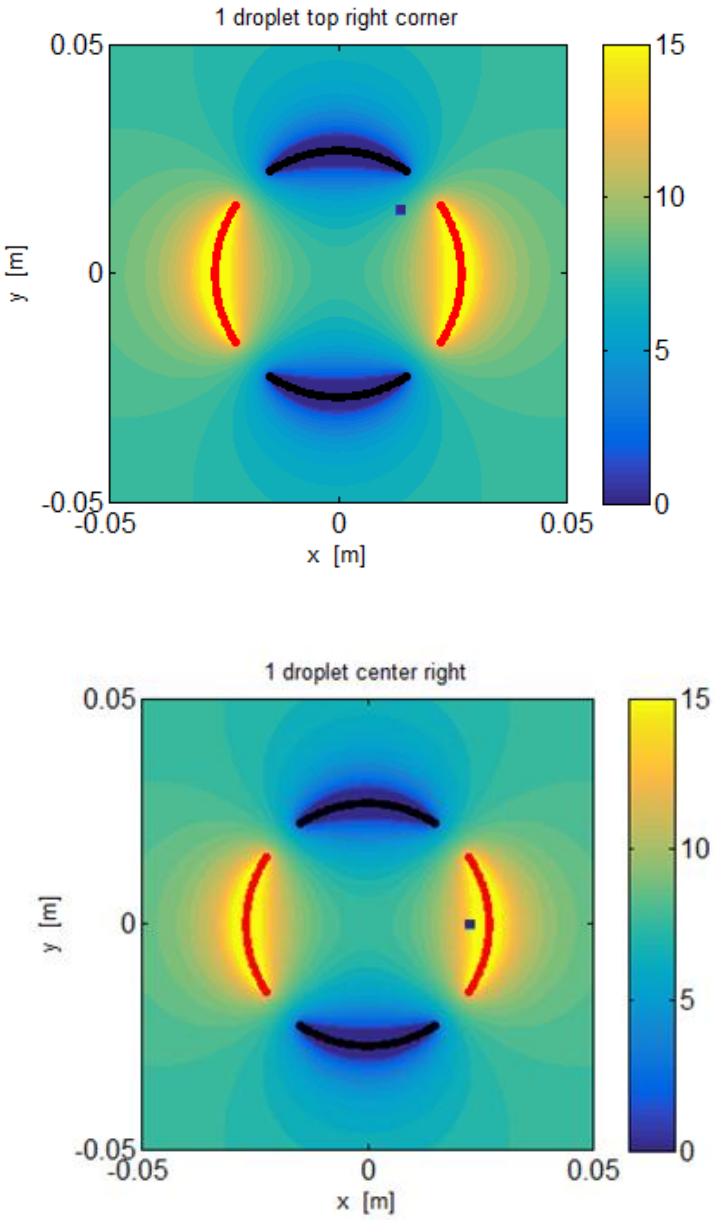


Figure 3-26 Potential difference maps showing where the water is located within the sensor. The bar to the right of the image is the potential difference.

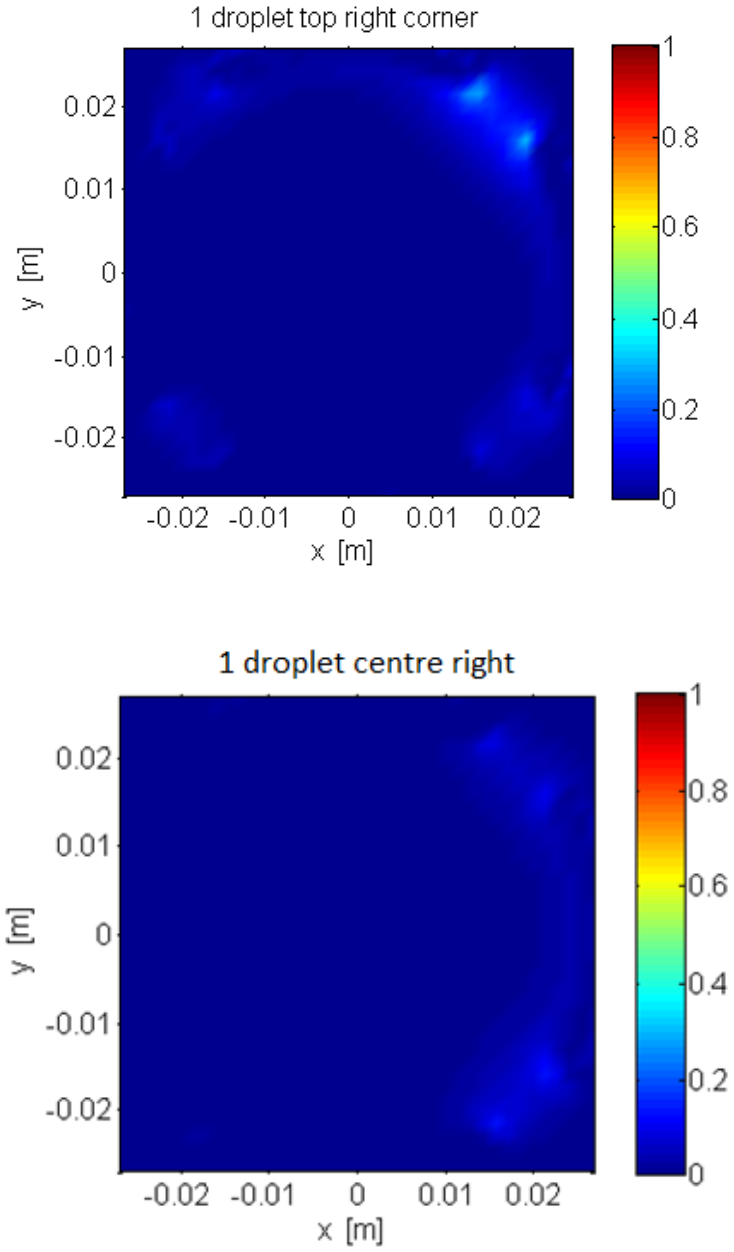


Figure 3-27 LBP using the Tikhonov Regularization for the two respective droplet locations

Due to the sensor having only four electrodes the resolution and accuracy of the images is low, this can be mitigated by increasing the amount of electrodes, if imaging the flow is a priority. Further examples of the LBP program being used can be found in chapter four section 4.7, where the LBP is applied to varying droplet injection patterns.

3.8 Conclusions

An overview of the ECT method was completed, along with a detailed analysis of the electronics system. This led to a review of Scott Barham's ECT sensor that showed that it was suitable to use for this research project. The state of the sensor from previous research highlighted that it would require extensive repairs and modifications to be usable again. The sensor was rebuilt using new materials to be used within a 200°C environment, this was necessary to be able to contain a static volume of superheated steam.

A program was developed that modelled the internal environment within the sensor filled with different substances, allowing for an analytical calculation of capacitance between each of the six pairs of electrodes, leading to a true 3D model that changes with time. This allowed for droplets to be modelled falling through the sensor, while measuring the capacitance and relative permittivity change.

A linear back projection method for producing images of a 2D cross section of the sensor was also developed. The principles of LBP were discussed and a suitable algorithm Tikhonov Regularization was selected to be used. The program was incorporated with the capacitance measurement program so that the effect of spatial positioning of water concentrations can be observed.

The next chapter will go to discuss the development of a suitable droplet injection system, which can deliver precise amounts of water into different regions of the sensor, to create a static volume of wet steam. In order to model the behaviour of the droplet injections within superheated steam at different pressures, the chosen droplet injection pattern will be incorporated into the capacitance and LBP program.

Chapter 4. Design, Construction and Analysis of the Droplet Injection System

Nomenclature

A Acceleration $[m/s^2]$

Bi Biot number

C_p Specific heat capacity $\left[\frac{J}{g\circ C}\right]$

E Energy in a droplet [kJ]

F Force [N]

g Gravitational force [N/kg]

h Heat transfer coefficient $\left[\frac{W}{m^2 k}\right]$

L Length of tubing [m]

k Thermal conductivity $\left[\frac{W}{mK}\right]$

$\dot{m}$ Mass flow rate of water [kg/min]

m Mass [kg]

Nu_{sph} Nusselt number

q Heat transfer rate [W]

Q Volumetric flow rate $[m^3/s]$

r Radius [m]

Re Reynolds number

S_a Surface area $[m^2]$

T_{final} Final temperature [°C]

T_{start} Starting temperature [°C]

v Velocity $[m/s]$

V Volume $[m^3]$

γ Surface tension [N/m]

η Viscosity [kg/ms]

Pr Prandtl number

θ_w Angle from the wall [rad]

ρ Density [kg/m^3]

ζ Dryness fraction

Sub script

d Droplet

D Drag force

f Flow

n Nozzle

s Steam

S Surface force

In order to control the amount and position of the moisture content within the static volume of wet steam, a droplet injection system was required. This system had to have multiple injectors to alter the position of the water to test to see how spatial positioning affected the measurement. A further requirement was to be able to control the mass flow rate, so that the same

volume of water per minute would pass through the sensor for each test.

Therefore it was imperative to access and learn how to calculate the diameter of droplets that could be produced from different gauge needles. To find the accuracy of the calculations, a novel technique of in time droplet diameter measurement was developed by using a Camsizer, to compare the predicted droplet sizes against the measured size.

The behaviour of the droplets within superheated steam was also investigated, by modelling how they were affected falling through the sensor. A means of delivering these droplets was then investigated. It was found that it was not possible to incorporate a design that included interchangeable needles. Therefore the final work used only droplets produced from 1/16th inch tubing.

This unintentional simplification of the design, meant that only one size of droplets could be investigated. Detailed below is the full investigation on all the variables involved in droplet production, how they are affected by superheated steam, the design, and the production of the droplet injection system. Furthermore there will be a discussion of how the droplet injection pattern is incorporated into the 3D model of the sensor.

This chapter is divided up into the following sections, where each outline and explain a key concept in the development of the final droplet injection system.

4.1 Droplet Diameter and Formation Time Analysis

Calculation of a droplet's formation time and diameter when produced from a needle with a given wall thickness and set mass flow rate. Accuracy of the calculations is determined by the novel technique for droplet diameter measurement.

4.2 The effects of Superheated Steam on a Droplet falling through the Sensor

Discussion and Analysis of how a droplet is affected by superheated steam as it travels through the sensor.

4.3 Initial Design of the Droplet Injector Manifold

Explanation of the process that went into producing the droplet injection manifold and the first rejected design

4.4 Overview of Vacuum Brazing for the Droplet Injection Manifold

A discussion of what vacuum brazing is and how it benefitted the construction of the manifold

4.5 Final Design of the droplet Injector Manifold using the 1/16th Tubes

Showing the final design of the injector manifold that could test the spatial positioning of water within the steam

4.6 Design and Construction of the Full Droplet Injection System

Showing how the full system was designed and constructed, what equipment was brought together and how the pipe layout was designed and constructed.

4.7 Incorporation of the Injection Pattern into the 3D Model of the Sensor

Explanation of how the injection pattern designed in section 4.5 was incorporated into the 3D model of the sensor.

4.8 Conclusions

4.1 Droplet Diameter and Formation Time Analysis

In order for the effect of spatial positioning to be determined, a repeatable amount of water must be able to be inserted into precise locations within the sensor. To create a repeatable amount of water, droplets must be produced that are the same size and can be made in a reasonable time. Therefore a prediction is required of what diameter droplets can be produced and the formation of them, from a needle with a given wall thickness and a set mass flow rate. The basis of the formulae were developed by Zheng *et al.,* (2012), the angle from the wall θ_w is defined in figure 4.1 where θ_C is the contact angle:

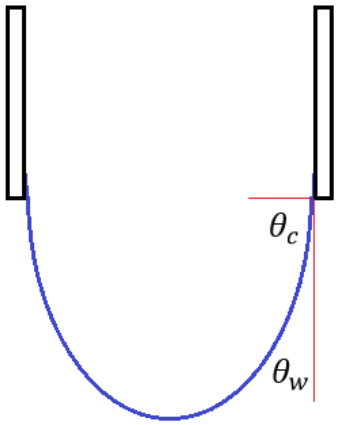


Figure 4-1 Demonstration of the angle from the inner wall of the needle.

Equation 4.1 describes the force at the surface on the end of the needle as:

$$F_s = 2\pi r_n \gamma \cos(\theta_w) \tag{4.1}$$

Only when the gravitational force is greater than the surface force does the droplet fall off the end of the needle $F_g > F_s$. Therefore the radius of the droplet can be calculated at the point of departure when the two forces are in equilibrium. The following situation arises shown in equation 4.2:

$$m_d g = 2\pi r_n \gamma \cos(\theta_w) \tag{4.2}$$

Due to density multiplied by volume is equal to mass, this can be substituted in to give:

$$\rho_d V_d g = 2\pi r_n \gamma \cos(\theta_w)$$

(4.3)

Rearranging equation 4.3 to be equal to the volume of the droplet and substituting in the formula to find the volume of a sphere gives equation 4.4:

$$\frac{4}{3}\pi r_d^3 = \frac{2\pi r_n \gamma \cos(\theta_w)}{\rho_d g}$$

(4.4)

Rearranging equation 4.4 gives the formula for the effective radius of the droplet as it is at the point of falling off the end of the needle:

$$r_d = \left(\frac{3 r_n \gamma \cos\theta_w}{2\rho_d g}\right)^{1/3}$$

(4.5)

Due to supply constraints only eight different types of needle were available. The sizes ranged from an internal diameter of 0.21 mm to 1.194 mm, these needles are shown in figure 4.1:



Figure 4-2 The eight needles used for testing, the G refers to the scale which is in the Birmingham gauge.

The dimensions of these needles were used to calculate their respective produced droplet size, the dimensions for the eight needles are shown in table 4.1:

Table 4-1 Dimensions of the eight needles that will be used for testing

gauge	outer diameter m	inner diameter m	area m^2	needle wall thickness m
27	0.0004128	0.00021	9.92E-08	0.0001014
25	0.0005144	0.00026	1.55E-07	0.0001272
23	0.0006414	0.000337	2.34E-07	0.0001522
21	0.0008192	0.000514	3.20E-07	0.0001526
19	0.001067	0.000686	5.25E-07	0.0001905
18	0.00127	0.000838	7.15E-07	0.000216
17	0.001473	0.001067	8.10E-07	0.000203
16	0.001651	0.001194	1.02E-06	0.0002285

The droplet diameter was then calculated using equation 4.5, where the density was set at 1000 kg/m^3.

The needle wall is set at 1.57 radians (90 degrees), the contact angle of stainless steel with water was measured at being 1.209 radians, and this means that the wall angle θ_w is set at 0.241 radians. Using these values and equation 4.5, the radius of the detached droplets were calculated as shown in figure 4.3:

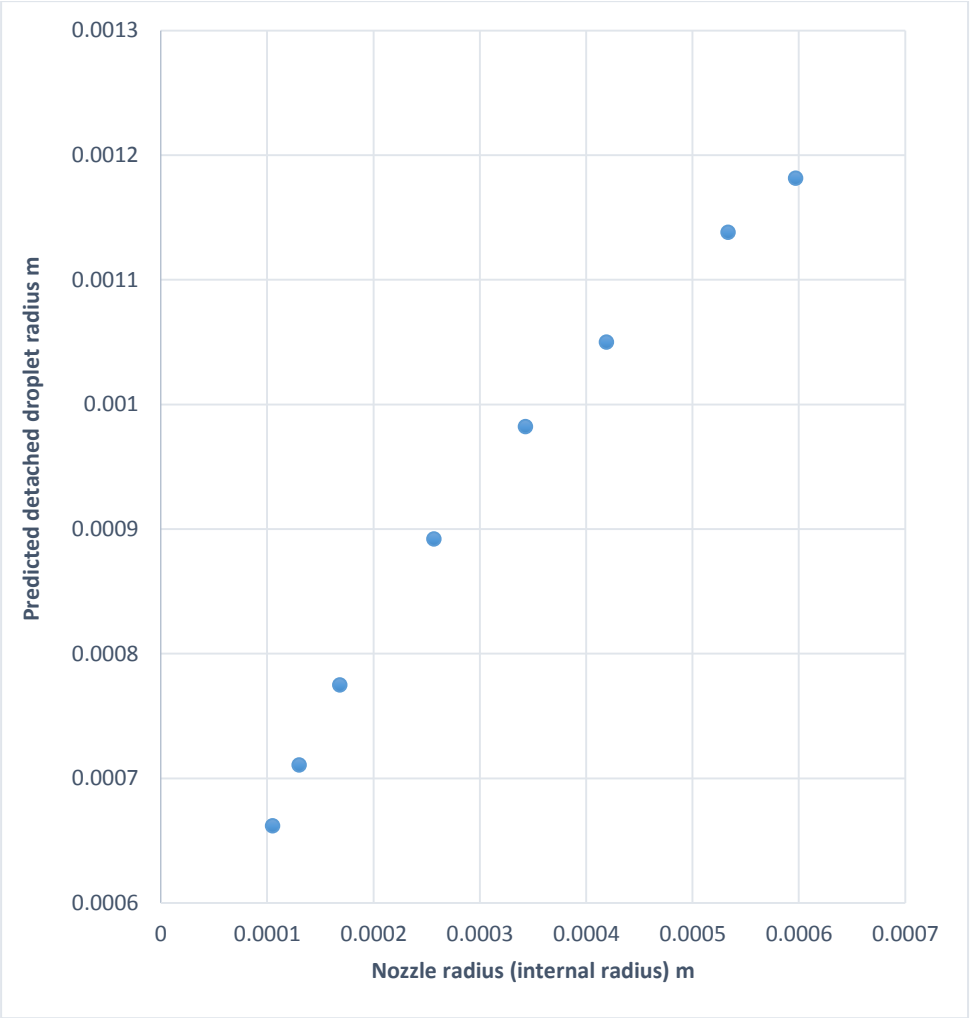


Figure 4-3 Predicted droplet radii, calculated from the nozzle radii (internal radius) for each needle

There is a clear trend that occurs as the nozzle radius increases. To verify that this correct, a recently developed technique of measuring droplet diameter was developed. This was achieved by using a piece of equipment called a Camsizer p4, which is normally used to measure fine dry particles such as milled coal. The machine can process 20000 frames per second and so is used to characterise the milled coal to determine the mean size of the particles and if there are any anomalies. By reprogramming the machine and removing the feeder area, the machine can measure the diameter of droplets and take still images of them as they are falling. Figure 4.4 shows the setup for the droplet diameter measurement procedure:



Figure 4-4 Droplet diameter measurement setup; 1. Is the Gilson pump, 2 is the needle holder, 3 is the pure water and 4 is the Camsizer.

By testing the needles shown in figure 4.1 using the setup shown in figure 4.4, the droplet diameter can measured. This measured diameter was converted to radius and plotted against the predicted droplet radii, the results are shown in figure 4.5:

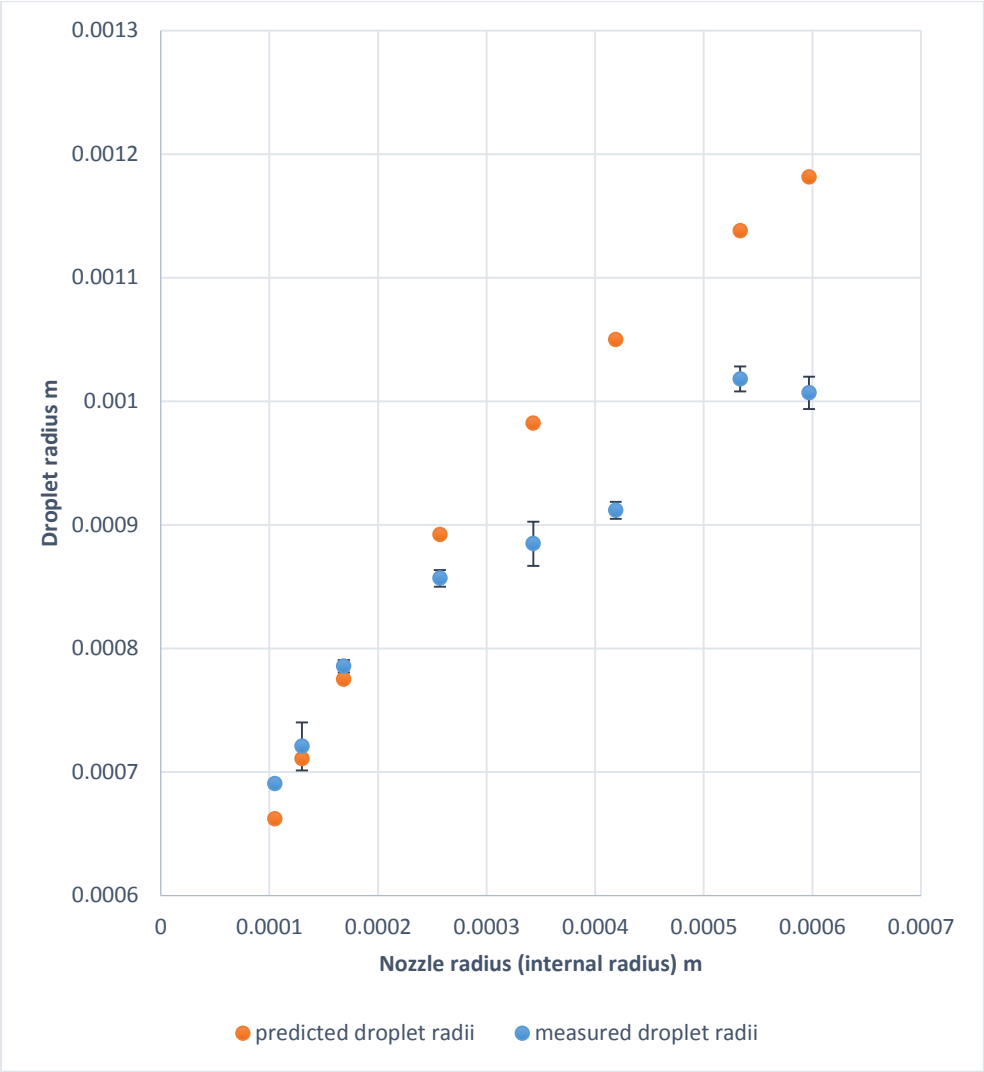


Figure 4-5 Predicted droplet radii plotted against measured droplet radii produced from the eight needles.

As the size of the nozzle radius increases the accuracy of equation 4.5 begins to decrease. Under a nozzle radius of 0.000257 m the equation increasingly under predicts the measured results as the nozzle radius decreases further. This indicates other variables are present that the model does not take into account.

The Camsizer was also able to capture still images of droplets as they fell through the sensor. Figure 4.6 shown on the next page clearly visualises the difference in size between a droplet produced from a 16g nozzle and one from a 27g nozzle.

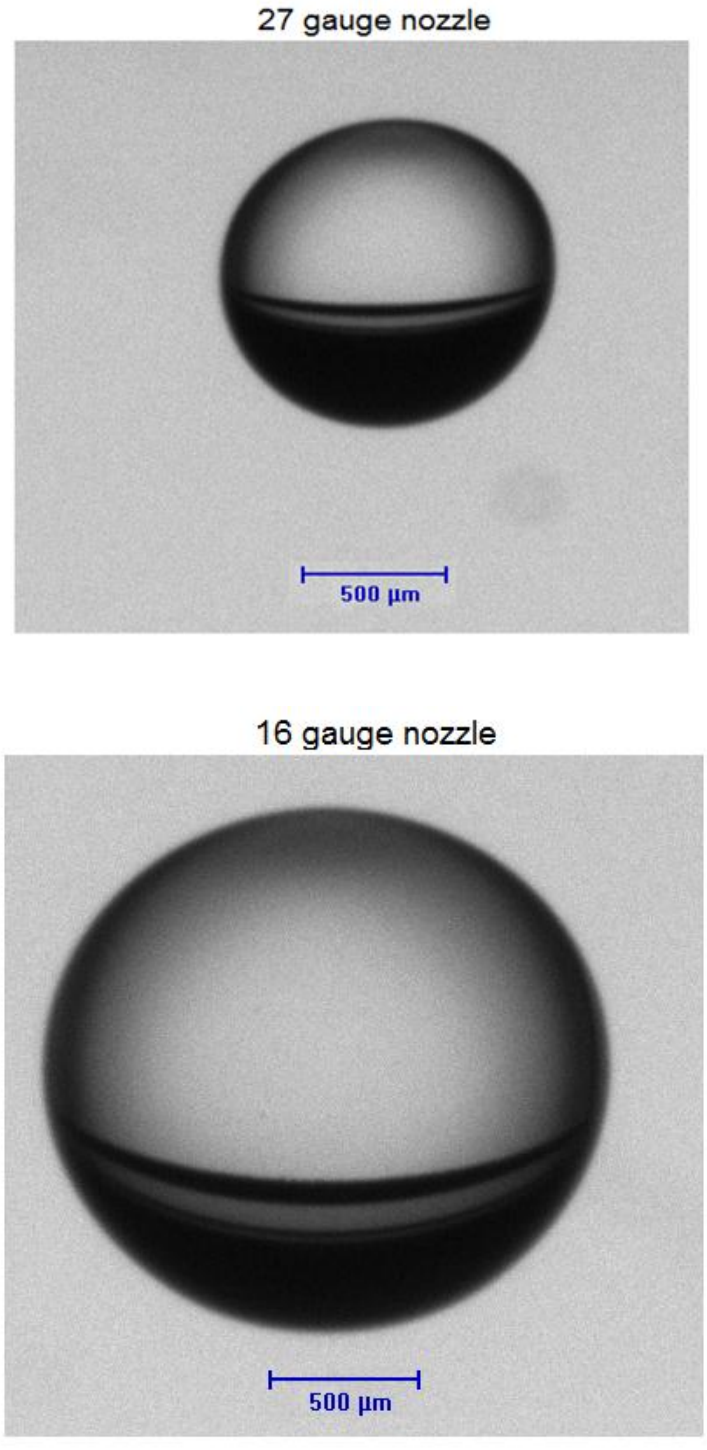


Figure 4-6 Still images captured using the Camsizer, showing a droplet produced from a 27g nozzle and a droplet produced from a 16g nozzle

The still images suggested that assuming the droplets were spherical was correct. For the rest of the project, droplets produced by any injector that is to be used on the final rig, will have the produced droplet diameter measured using the previously described Camsizer technique. The next section will examine the droplet behaviour as they are passing through the sensor filled with superheated steam.

4.2 The effects of Superheated Steam on a Droplet falling through the Sensor

An investigation was conducted to access whether droplets can survive intact while falling through a static volume of dry steam. This was a key part of the project, because if the droplets could not remain intact while falling, the spatial positioning could change. If they evaporated due to the heat, then there would be a cloud of saturated steam falling through sensor.

The first stage was to calculate the speed and the time the droplets would fall through the sensor. The sensor has electrodes of length 0.15 m, the room above the electrode to the top of the flange is 0.075 m, therefore for the purpose of this test, it is assumed that droplets are injected 0.02 m from the top of the flange. This gives a total distance of 0.205 m for the droplets to fall.

To measure the effect of viscosity on the droplets, the drag force had to be included within the calculation, due to there being a static volume of steam with droplets falling through the sensor. The Reynolds number is not assumed to be low to the point that there is no turbulent flow and the steam will pass the droplet in a laminar flow, therefore Stokes law cannot be used. This law is defined in equation 4.6:

$$F_D = 6\pi\eta_s r_d v_d \tag{4.6}$$

Therefore to calculate the acceleration of the droplet as it falls, equation 4.7 is used:

$$A = \frac{v_d^{n+1} - v_d^n}{\Delta t} \tag{4.7}$$

When the droplet is on the end of the injector, the velocity is 0 at t = 0, using this a starting point the acceleration is calculated. From this at t = 0.001, the new value of velocity is calculated. This process was then used calculate the total distance the droplet has travelled at every time step. When the distance is equal to 0.205 m, the corresponding time at that time step is the time taken for the droplet fall that particular distance.

The time to fall was calculated for each of the three steam conditions 10 Bara with a temperature of 181 C, 11 Bara with a temperature of 184 C and 12 Bara with a temperature of 190 C. The respective viscosities for each of the steam conditions was calculated using IAPWS – 97. Table 4.2 shows the time taken for the measured droplets, falling through each of the three different steam conditions.

Table 4-2 Mass flow rate per injector for 5, 10, 20, 40 and 80 injectors

		Time taken s to fall 0.205		
gauge	measured droplet radius m	10 Bara	11 Bara	12 Bara
27	0.00069	0.206	0.206	0.206
25	0.00072	0.206	0.206	0.206
23	0.00079	0.206	0.206	0.206
21	0.00086	0.206	0.206	0.206
19	0.00089	0.206	0.206	0.206
18	0.00091	0.206	0.206	0.206
17	0.00102	0.206	0.206	0.206
16	0.00101	0.206	0.206	0.206

Table 4.2 demonstrates that change in viscosity between steam at 10 11 and 12 Bara is so little that the change in the time for the droplet to fall is less than 3 decimal places.

Looking at the velocity change in depth at the smallest and largest measured droplets will tell how the range of droplets velocities changed as they fell, this will show whether the assumption for a low Reynolds number was correct. The velocities for a droplet produced by the 16G needle and the 27G needle were plotted as they fell through each of the three different steam viscosities. This graph is shown in figure 4.7:

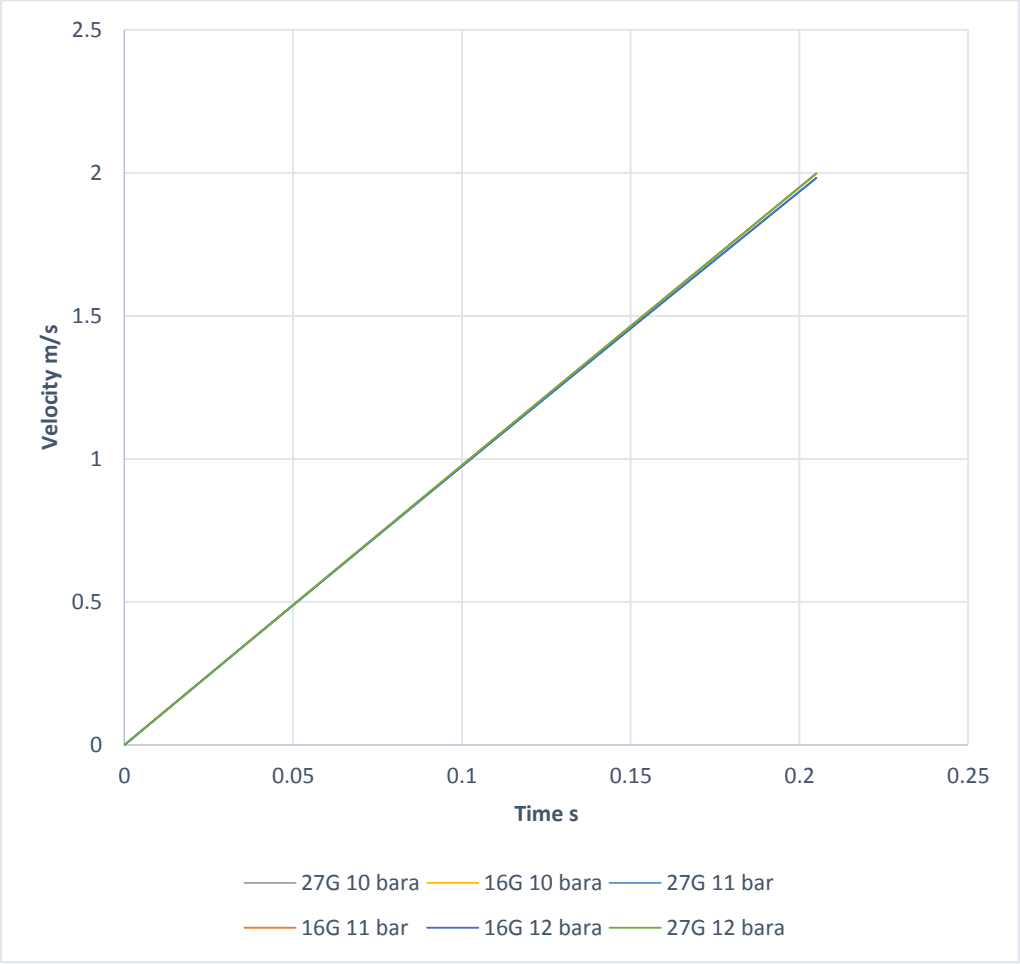


Figure 4-7 the velocity of the droplets as they fell through the three different steam conditions of 10 Bara 181°C, 11 Bara at 184°C and 12 Bara at 190°C

The velocity of the droplets as they fell can be seen to be quite similar until the droplets are half way through the sensor, at 10, 11 and 12 Bara the velocities are very close together.

Using the values of velocity, viscosity, droplet radius and the steam density, the change in the Reynolds number can then be calculated as the droplet falls. The Reynolds number is defined by equation 4.8

$$Re = \frac{\rho_s v_d 2r_d}{\eta_s} \tag{4.8}$$

Using equation 4.8 the Reynolds number can be plotted in the same as velocity, this is demonstrated in figure 4.7

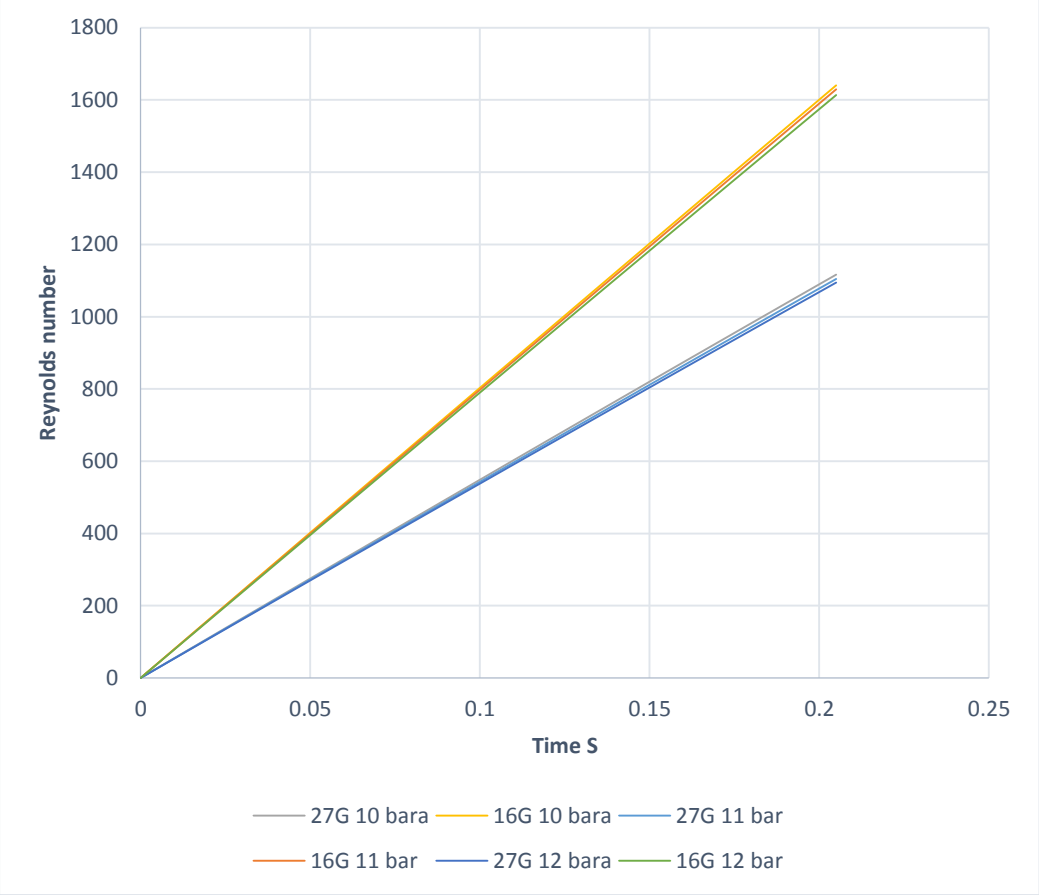


Figure 4-8 Reynolds number plotted over the time the droplet fell through the three different steam conditions of 10 Bara 181°C, 11 Bara at 185°C and 12 Bara at 190°C

Therefore as the different sized droplets fall through the steam they are creating a laminar flow.

4.2.1 Temperature rise in the droplets as they fall

The next problem with the droplets was if they would evaporate due to the steam temperature. In order to calculate the answer to this question, only the hottest steam temperature was required, therefore if the droplets can survive in 12 Bara of steam at 190°C, then they will be fine with the other conditions. The first step in the process was to calculate the Nusselt number, this is a measure of the ratio of convective heat transfer to conductive heat transfer at the boundary between the liquid water of the droplet and the dry steam environment. Assuming the droplet is spherical, then the correlation by Whitaker (1972) can be used, which describes the Nusselt number for a flow over a sphere, the equation is given by 4.9:

$$Nu_{sph} = 2 + \left[0.4Re^{1/2} + 0.06Re^{2/3}\right]Pr^{0.4}(\eta_s/\eta_d)^{1/4} \tag{4.9}$$

The Prandtl number is the ratio of momentum diffusivity to thermal diffusivity. This dimensionless number tells if heat conduction is dominant if Pr< 1, rather than if convection is dominant Pr > 1. For steam at 190°C under 12 Bara, the Prandtl number is 1.005, meaning heat conduction is more significant, therefore thermal diffusivity is dominant.

Using the Nusselt number for a sphere the heat transfer coefficient is calculated for the droplet passing through the steam, it is calculated by equation 4.10:

$$h = \frac{Nu_{sph}k_s}{2r_d} \tag{4.10}$$

The heat transfer coefficient allows for the calculation of the heat transfer rate from the steam to the droplet. This tells how much energy is going into the surface of the droplet every time step, showing a greater rate of transfer is occurring leading to a faster heating time, which indicates the droplet will heat up quicker. Equation 4.11 gives the heat transfer rate for the droplet using Newton's law of cooling:

$$q = hA\left(T_{final} - T_{start}\right) \tag{4.11}$$

Looking at the change in energy each time step, for the droplet to heat up the energy going into the droplet should increase, then decrease as the droplet reaches its boiling point. Figure 4.8 demonstrates this effect occurring for the minimum and maximum droplet size from heating a droplet at 20°C.

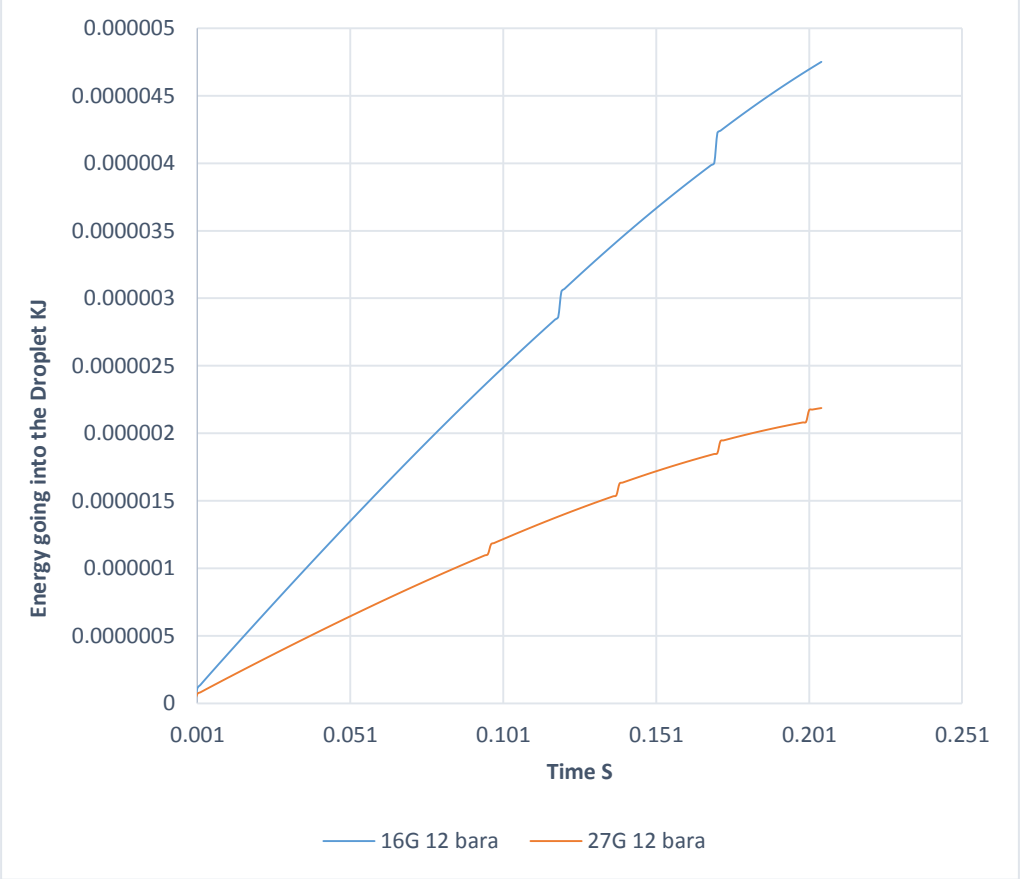


Figure 4-9 Amount of energy required to heat the droplet at each time step till the droplet reaches the bottom of the sensor

To calculate the final temperature of the droplet at each time step, the following equation 4.12 must be rearranged, which describes how to calculate the energy to heat up a droplet:

$$E = C_p m(T_{final} - T_{start})$$

(4.12)

Rearranging 4.12 to give the final temperature at the end of the time step gives:

$$T_{final} = (E + m_d C_p T_{start})/m_d C_p$$

(4.13)

The temperature increase as the droplet falls through the sensor over a distance of 0.205 m was then calculated using equation 4.13 at every time step. Figure 4.10 shows that temperature increases for the two different sized droplets over the time it took them to fall.

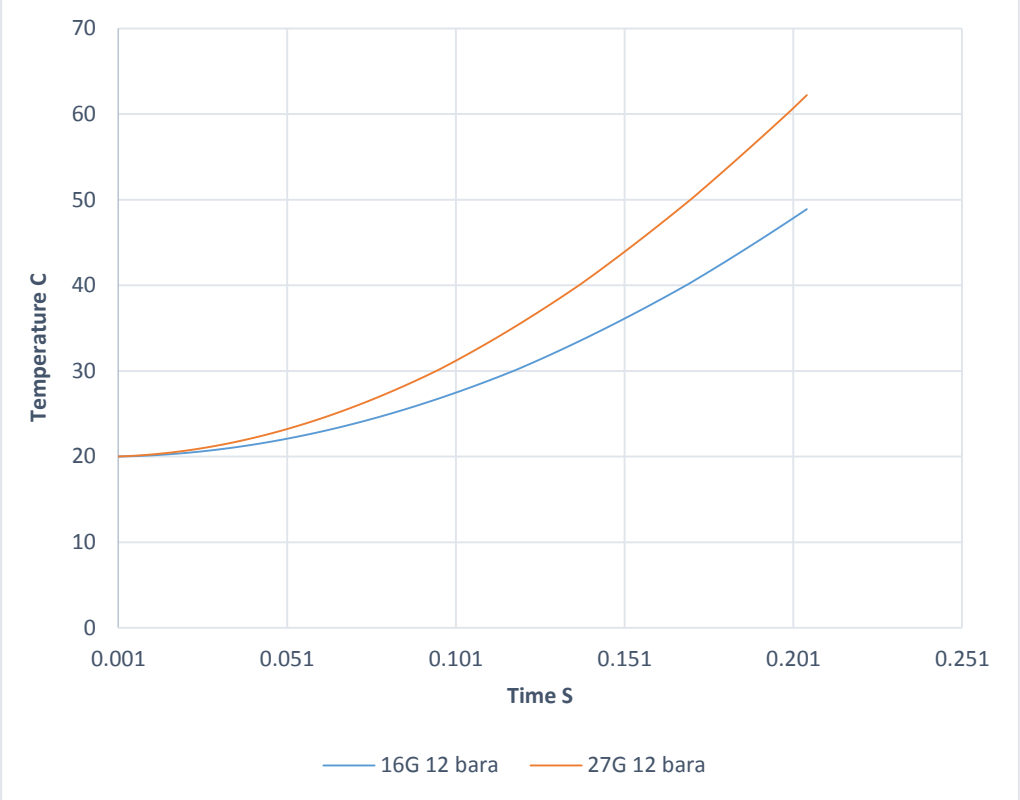


Figure 4-10 Temperature increases of the different size droplets over 0.205 S

The droplets heat up quickly over the short space of time, however they are still liquid by the time they reach the bottom of the sensor. If the water is heated first, then this will increase the time it takes to heat them as they are nearer the boiling point of water, as shown by figure 4.10.

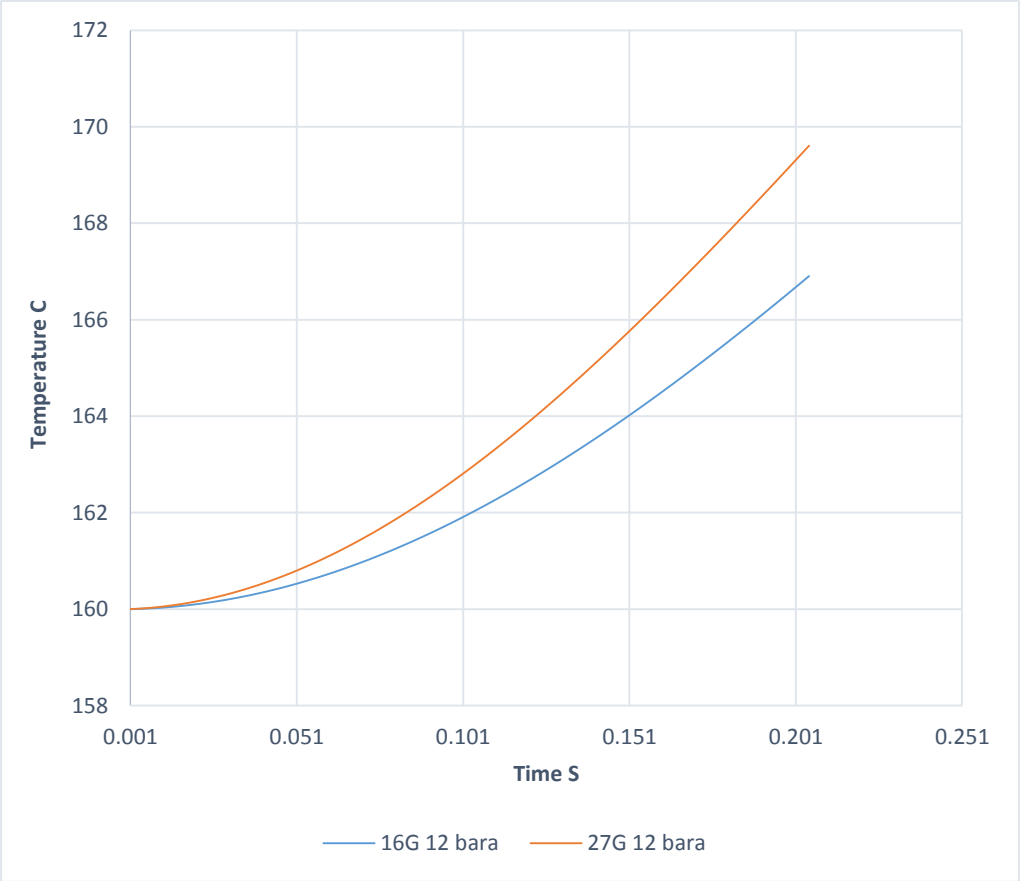


Figure 4-11 Temperature change as droplets are injected into steam at 160°C

As the droplets are injected at the increased temperature, the correct behaviour is observed. This implies that the droplets will not evaporate within the sensor before reaching the bottom, instead they would evaporate after 0.8 seconds. This means that the drops will not evaporate and cause a loss in the mass of liquid water falling through the sensor. The next section will move onto the stability of the droplets as they fall and will consider how the Weber and the Biot number changes with the time they are within the steam.

4.2.2 Droplet Stability analysis

The next factor to consider with the droplets behaviour, is whether they will break apart due to the flow of steam pushing against them. To determine whether this will happen the Weber number must be calculated for the droplets as they pass through the steam at the three different pressures.

The Weber number is a measure of how likely in a two phase flow the liquid phase can be entrained within the vapor flow. The critical value where entrainment can start is when the Weber number is greater than one. Therefore as the droplets fall, for them to be stable the Weber number should be less than one throughout their journey. The Weber number is calculated using equation 4.14:

$$We = \frac{\rho v_d^2 (2r_d)}{\gamma} \tag{4.14}$$

The Weber number will also determine how stable the droplets are, as a high Weber number will indicate that the droplets are becoming deformed and are breaking apart. Figure 4.11 demonstrates the change in Weber number over the time it takes them to fall through the steam at the three different pressures.

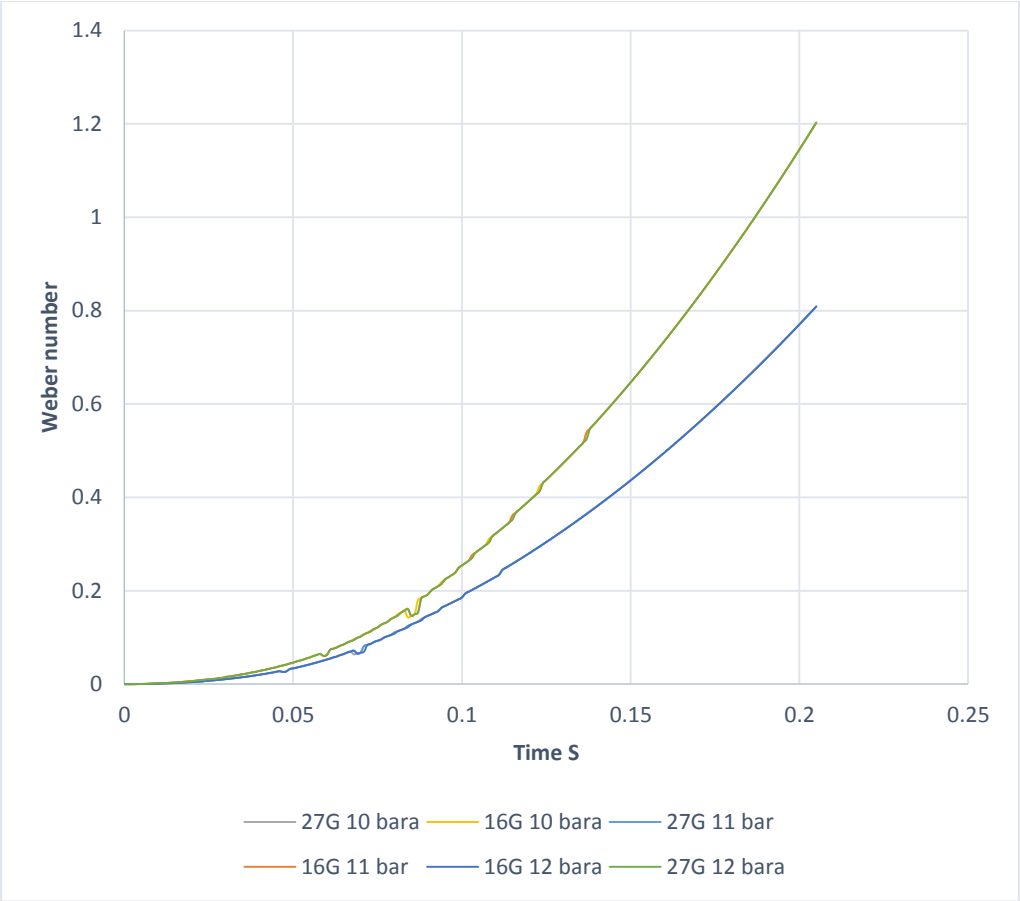


Figure 4-12 Weber number for droplets produced by the 16G and 27G nozzle traveling through steam at 10, 11 and 12 Bara

Within the time it takes the droplet to boil of 0.85 seconds, the Weber number is less than 0.3 indicating stable droplets that won't break apart and entrain within the superheated steam vapour.

The final factor to consider is whether the droplets heat up uniformly or if the surface of the droplet heats up quicker than the interior, to calculate this the Biot number is used. The Biot number is calculated using equation 4.15:

$$Bi = \frac{(V_d/S_a)h}{k_d} \tag{4.15}$$

The equation calculates the ratio between the convective and the conductive heat transfer to an object. If the object is thick, has a high volume

to surface area ratio then the convective heat transfer to the object will be larger than the conductive heat transfer, resulting in a large Biot number.

The biot number was calculated at every time step as before like the previous dimensionless numbers. Figure 4.12 shows the change in Biot number as the droplets fall through the sensor with a steam temperature 190°C.

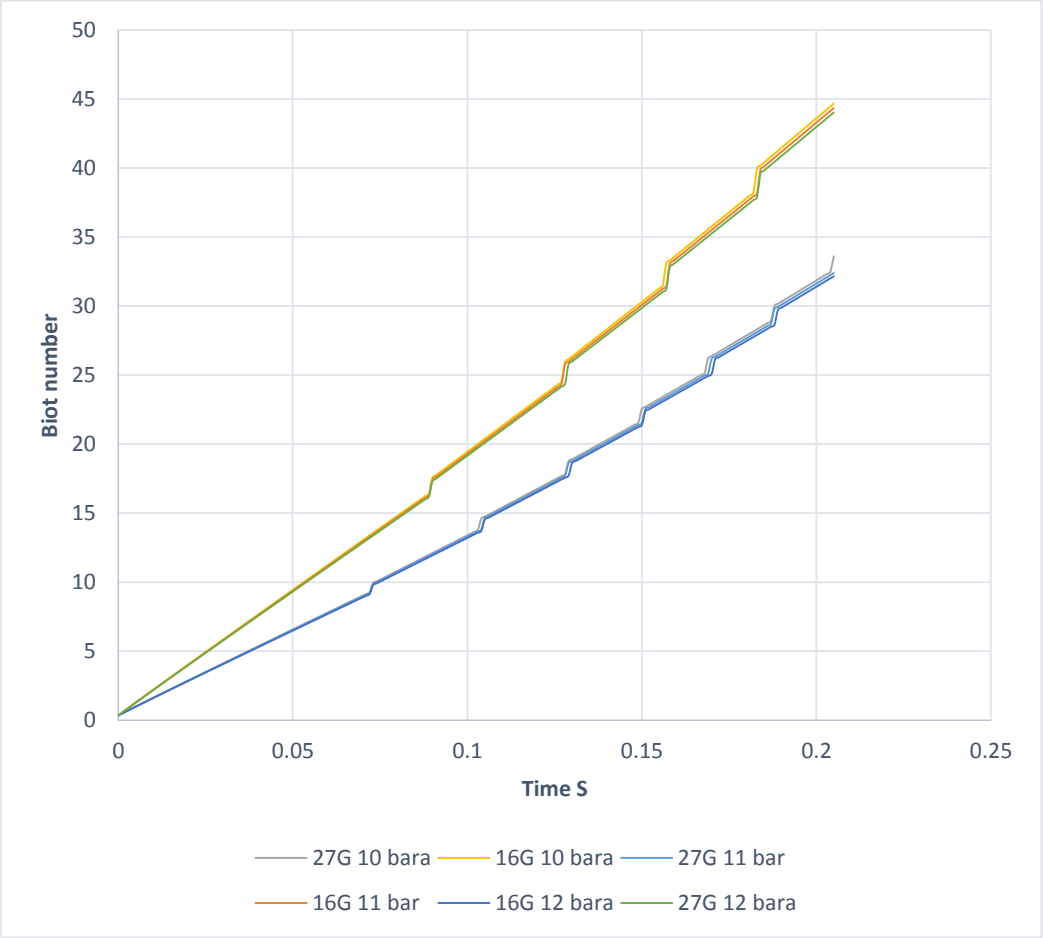


Figure 4-13 Biot number plotted for every time step of 0.001 seconds for a droplet within 10, 11 and 12 Bara of superheated steam

The Biot numbers shown indicate that the convective heat transfer is greater than the conductive heat transfer, resulting in a slower heating time. Therefore the droplets are liquid throughout the sensor as shown in figure 4.9. The stability of droplets is fine, they are shown to not break apart, this means the volume of liquid can be injected into precise regions of the sensor

4.3 Initial Design of the Droplet Injector Manifold

To inject the droplets into precise regions of the cross section of the sensor, a manifold was required that could hold different sized injectors. This would allow for changing amounts of different sized droplets to be injected precisely, thus controlling the volume fraction of the liquid and controlling the spatial positioning of the liquid.

The first step in the design was to see how different amounts of droplets produced at the sizes shown in table 4.2, could affect the steam wetness of the volume of steam contained within the sensor. The mass flow rate of water to each injector tip is required, where there will be a constant mass flow rate from the pump.

A Gilson pump with a maximum mass flow rate of 10 ml/min was acquired for the droplet injection system. Converting the mass flow rate to the volumetric flow rate gives $1.67 \times 10^{-7}\ m^3 s$. The flow velocity is found by rearranging equation 4.16:

$$Q = \pi {r_n}^2 v_f \tag{4.16}$$

This gave a flow velocity of 0.85 m/s. To calculate that the flow was laminar, equation 4.8 was used by replacing the 2r with the diameter of the pipe D. This gave a Re of 423.76. The flow is laminar and therefore the pressure drop for a laminar flow can be calculated using equation 4.17 Poiseuille's law:

$$\Delta P = \frac{128 \eta_f L Q}{\pi {D_n}^4} \tag{4.17}$$

The Darcy friction factor is calculated from f = 64/Re, this gave a friction factor of 0.15. From the pressure drop was then calculated using

equation 4.17 this gave a pressure drop over 1 m of 1/16th inch tubing of 109035 N/m^2.

As long as the lengths of tubing connecting each injector are equal the pressure drop will be equal as well. Dividing the total mass flow rate by the number of injectors gives the mass flow rate at each injector, table 4.3 shows the mass flow rate at each injector for a total of 5, 10, 20 and 80 injectors.

Table 4-3 Mass flow rate per injector for 5, 10, 20, 40 and 80 injectors

Injectors	mass flow rate per injector kg/s
5	3.33E-05
10	1.67E-05
20	8.33E-06
40	4.17E-06
80	2.08E-06

If the droplet production time is shorter than the time it takes for a droplet to fall through the sensor, then it will be possible for two droplets to be within the sensor which will affect the volume of liquid present. In order to complete this calculation the velocity profile within the nozzle must be known. Equation 4.8 showed the flow was laminar, this means the following velocity profile is present within the nozzle:

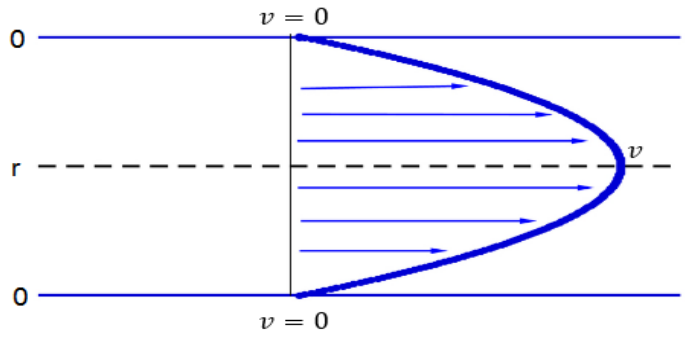


Figure 4-14 The 2D velocity profile within the nozzle

Using equation 4.16, it can be seen that as the mass flow rate is reduced by the number of injectors, the volumetric flow will decrease, this in turn will decrease the velocity going to each injector. The velocity at each injector is further reduced by the diameter of the nozzle. Figure 4.14 shows the velocity change for each injector as the size and the number are altered.

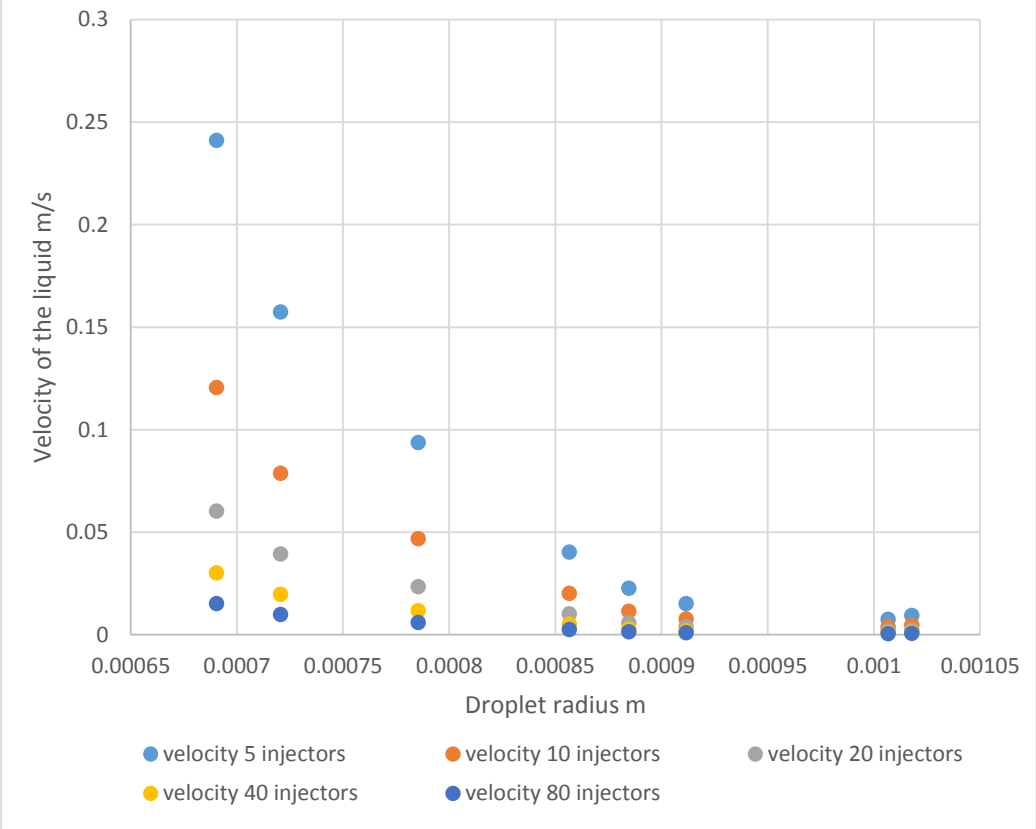


Figure 4-15 Velocity change as the nozzle size and the number of injectors increases.

The velocities shown in figure 4.14 can then be used to calculate the droplet formation time using the following equation 4.19:

$$t_{form} = \frac{V_d}{\int_0^r v_f(r_d) 2\pi r_d \, dr} \tag{4.19}$$

Integrating for the velocity profile shown in figure 4.14, where r is the radius of the pipe, gives the final equation for the formation time of a droplet:

$$t_{form} = \frac{V_d}{v_f \pi {r_d}^2}$$

(4.20)

Figure 4.15 demonstrates the droplet formation times for the measured droplet sizes using different number of injectors from 5 to 80.

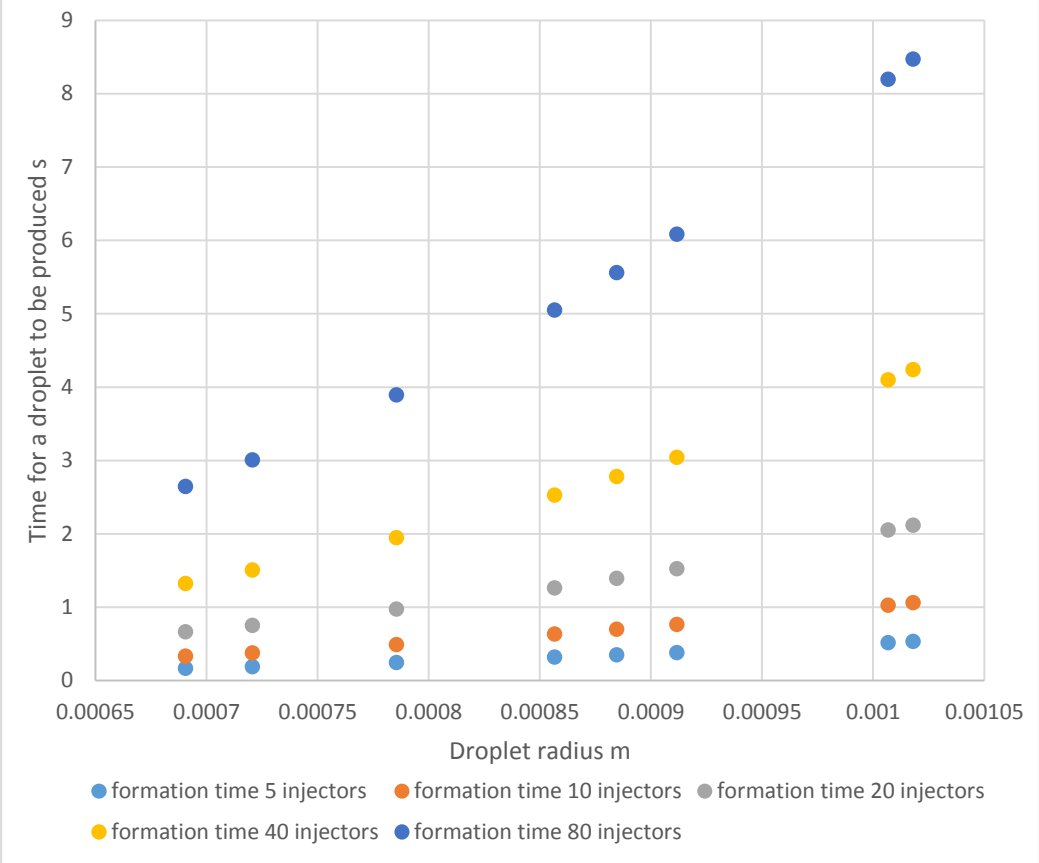


Figure 4-16 Droplet formation times for the measured droplet diameters using 5, 10, 20, 40 and 80 injectors.

Only droplets produced from the 27g and 25g nozzles using 5 injectors will be produced fast enough to allow for more than one droplet from one injector to be in the sensor at any time. Furthermore figure 4.16 demonstrates that the droplets with a formation time of more than 0.7

seconds will evaporate on the end of the needle within the superheated steam environment.

Controlled amounts of water can be injected into the test section, if the steam is superheated then the water will boil on the ends of the needles for the larger droplets and the longer formation times. If the steam becomes saturated then the droplets will not boil and will fall through the sensor.

Thus the final variable that requires calculation for the design is how much the percentage wetness will change as different volumes of liquid water are injected. From previous calculation for the majority of injections, only one droplet per injector will be evaporated into the total mass of steam within the sensor at any time, therefore the percentage wetness within the sensor can be calculated for a plane of droplets being added from the previous numbers of injectors.

The total volume within the sensor is $0.000354\ m^3$. By calculating the total mass within the sensor for 10, 11 and 12 Bara of dry steam, and knowing the total mass of liquid water injected, the dryness fraction can be calculated using equation 4.21:

$$\zeta = \frac{m_s}{m_s + m_d} \tag{4.21}$$

Over a second the pump delivers 167 µl of water to the sensor, if all that water is continually evaporated, then the dryness fraction after a second of injection is shown in table 4.4:

Table 4-4 Dryness fraction after one second of water injection

Pressure Bara	specific volume dry steam	mass	Dryness Fraction
10	0.194	0.001824742	0.917
11	0.177	0.002	0.923
12	0.163	0.002171779	0.929

The underlying principle in superheated steam is that due to the droplets evaporating as soon as they are injected, water is not collected on the end of the needle and falls through in larger or smaller amounts based upon the size of the nozzle. Instead the water evaporates as soon as it reaches the end of the nozzle and causes a constant change in wetness, based upon the overall mass flow rate.

As soon as water is injected it evaporates and saturates the steam within an area the active injectors are covering. Once this saturation occurs the droplets won't evaporate any more and instead will decrease the dryness of the steam depending upon the total mass of the droplets present within the sensor. Therefore for a constant flowrate, the more injectors that are used there will be a larger change in dryness fraction and due to figure 4.15 this change will occur less often as the droplets take longer to form, this change is shown in figure 4.16 for the maximum amount of dry steam within the sensor at 12 Bara.

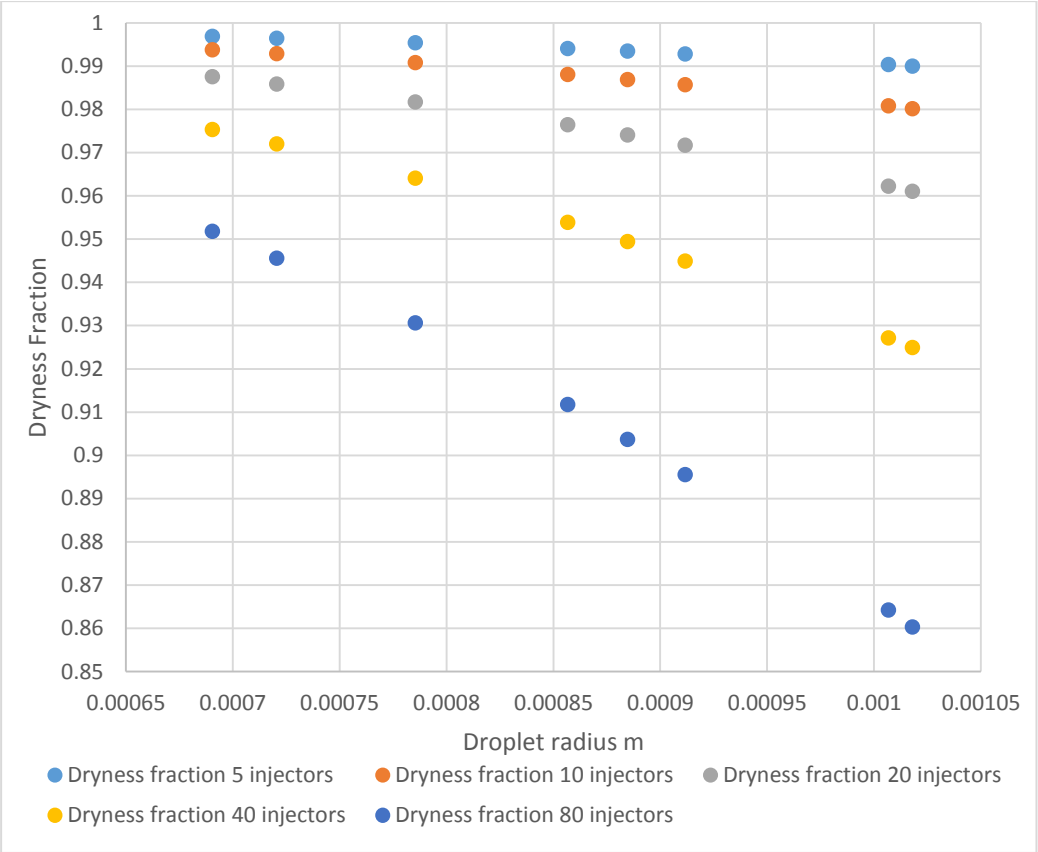


Figure 4-17 Dryness fractions produced by 5, 10, 20, 40 and 80 droplets of different radii injected into steam with a pressure of 12 Bara

The sensor that was discussed in the last section can detect changes in wetness of 1% in 11 Bara of steam, therefore using 20 or more injectors would be ideal for seeing changes with the larger diameter droplets. With the smaller diameter droplets 40 or more injectors would be more sufficient. The next section takes these calculations and shows how they were applied to the design of the manifold, and why certain designs were rejected.

4.3.1 Rejected Injector manifold design

The design of the manifold needed to be cost effective, practical and allow precise steam wetness control within specific regions of the sensor. To this end the first design was cheap in the cost of materials and was very flexible, allowing for different nozzles to fit to the manifold. The basis of the design was a DN 100 blind flange that could be connected to the top of the sensor. The injection lines had to go through this flange, this would be achieved by wielding 1/8th inch to 1/16th inch adaptors into the flange plate.

The downside to this was that the total number of injectors was limited to 17, with four injectors per quadrant of the sensor and one central injector. Underneath the blind flange, luer lock adaptors would be connected to each injector line, whereby different luer lock fitting nozzles, such as those shown in figure 4.2 could be connected. Figure 4.18 shows the design and all the components.

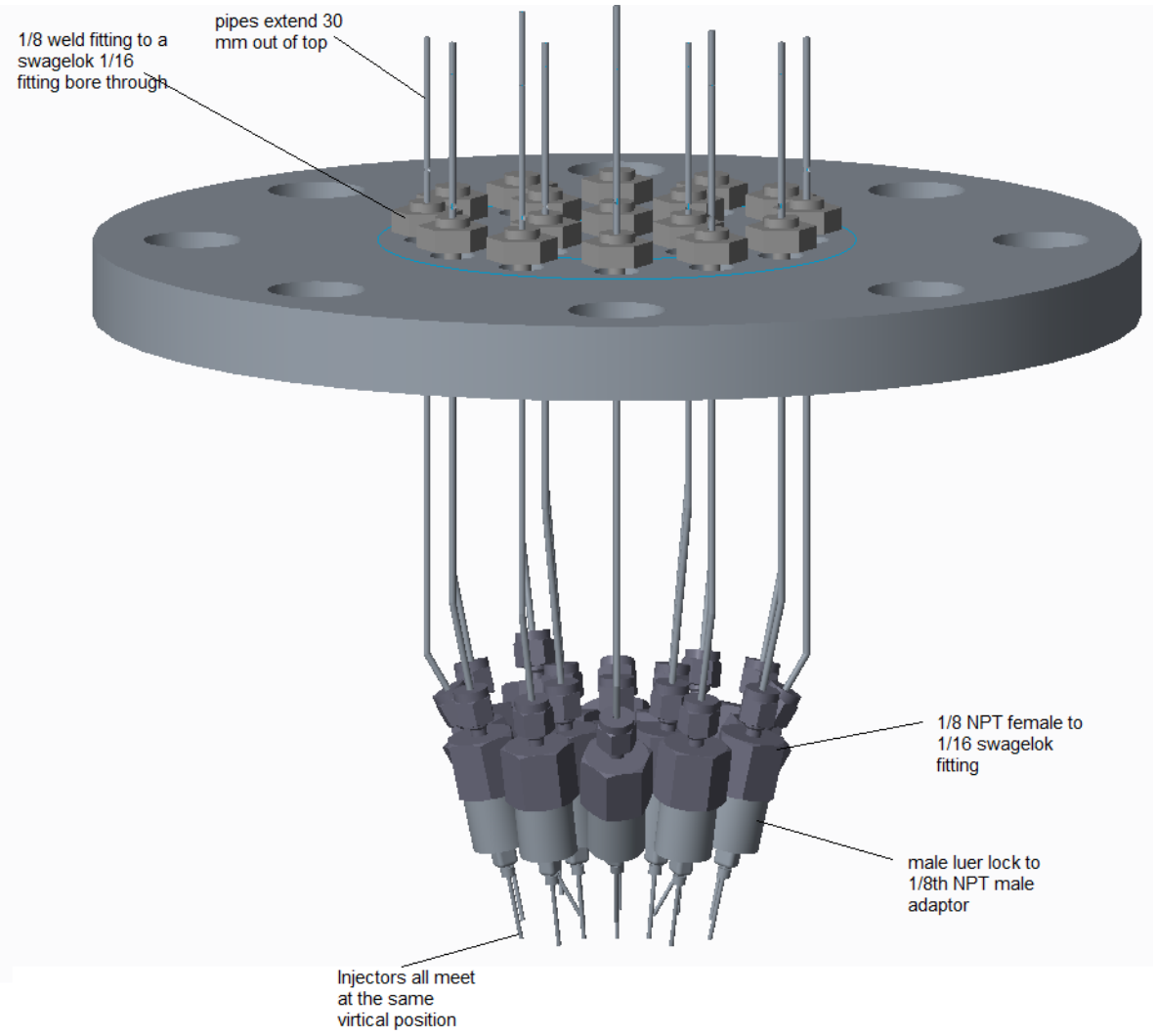


Figure 4-18 The first design for the droplet injection manifold

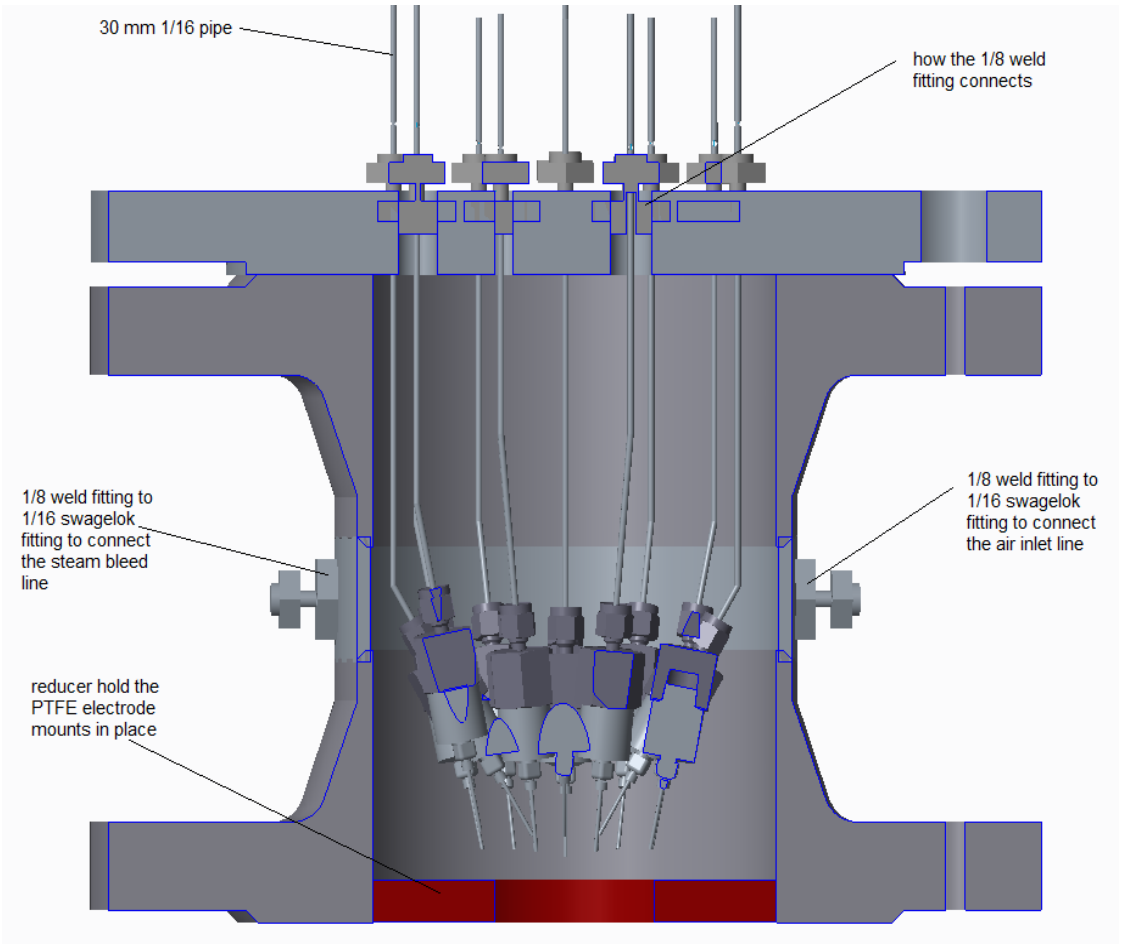


Figure 4-19 How the droplet injection manifold connected to the sensor

The design shown in figures 4.18 and 4.19, meets all the criteria, however it was rejected due to needing a DN50 pipe which would have meant a larger oven would have been needed, this would have placed construction cost outside of the budget. Secondly the amount of pipe exposed to the superheated steam would have caused evaporation within the tubes creating jets of wet steam vapor, this would have reduced spatial positioning control. To move forward, a design was required that could overcome the problem caused by using welded adaptors, and would be simplified where it would have one non-interchangeable nozzle size fitted.

4.4 Incorporation of Vacuum Brazing into the Design of the Droplet Injector Manifold

To overcome the problem of a reduction in space caused by having to weld fittings to the blind flange, a new technology was investigated which would allow for the pipes to be fitted through the blind flange and fixed in place. The technique is called vacuum brazing and works upon the principle of normal brazing whereby a filler material with a lower melting point is melted between the parts of metal to be joined together, this technique is then performed in a vacuum, which allows for the filler material to be drawn between the metal parts, while keeping the area clear of any contamination. The advantage of the technique is that as long as the brazing joint is complete the resistance to pressure will be the same as the joining materials. This means that for the 316 stainless blind flange, it would be able to take upwards of 30 bar, for a health and safety perspective this makes the technique ideal.

The strength of the joint depends upon the thickness of the gap between the two metals that are to be joined. As the gap increases the tensile strength decreases, ideally for vacuum brazing a gap of less than 0.1 mm is required, which can decrease depending upon the material used for brazing (Handy and Harman 2001). Figure 4.20 demonstrates this principle.

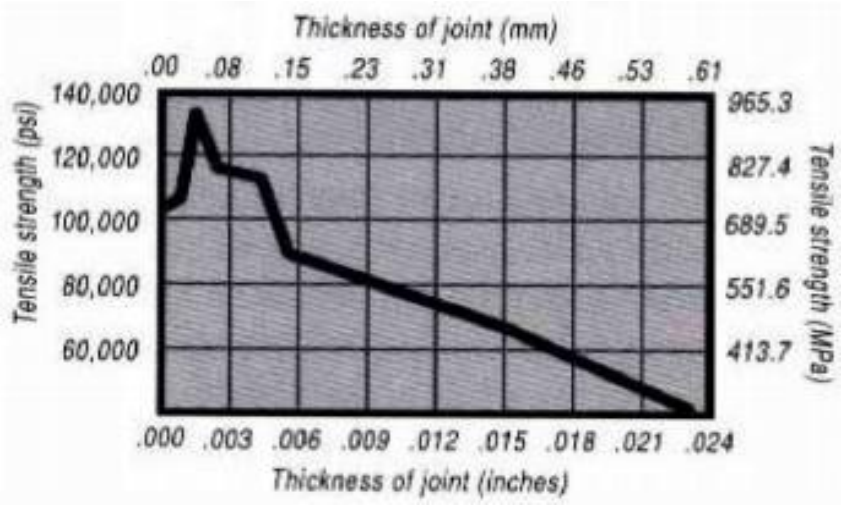
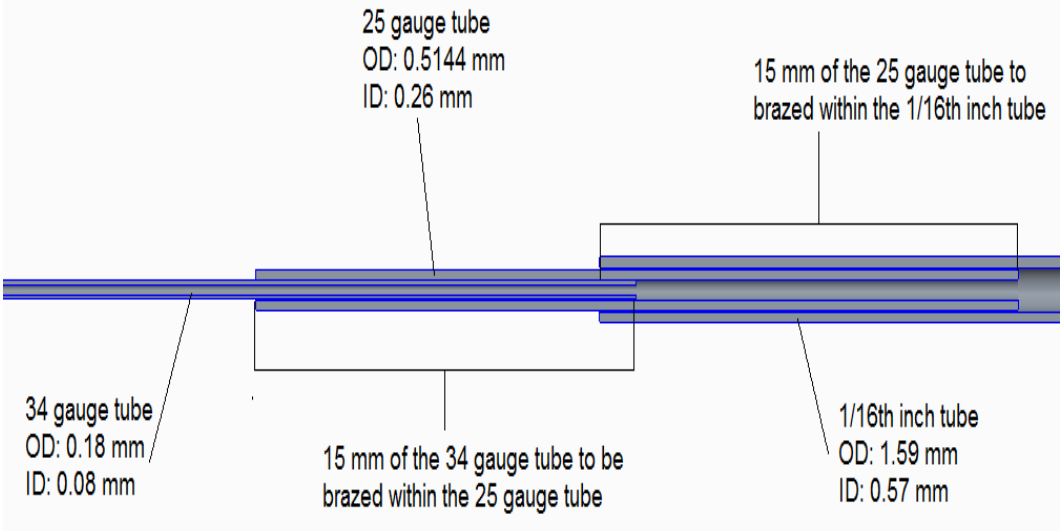


Figure 4-20 How the tensile strength of a joint changes with thickness (Handy and Hardman 2001)

Using this new technique it was found to be possible to braze custom diameter pipes into a 1/16th inch tube to create smaller nozzle diameters that could be used for smaller mass flow rate injections. Figure 4.21 shows the design of one of these custom injection nozzles showing the ability to use



even smaller 34 gauge nozzles.

Figure 4-21 Design of a custom 34 gauge tube injector that could be made using vacuum brazing

These custom made nozzles could be directly vacuum brazed to the blind flange, enabling up to 73 injectors to be used with a low mass flow rate. Using equation 4.5, theoretical droplet diameters of 0.0012 m could be produced with this setup.

To see if it was possible to produce smaller than 1 mm droplets, the technology was combined with laser cutting, whereby a 25 gauge rod of 316 stainless could be drilled out from one end, and then at the droplet production end the laser would cut a 10 µm hole 100 mm to end of the drilled part of the rod. This custom made injector could be vacuum brazed to the 1/16th tube as shown in figure 4.21. This setup would be ideal if a fine mist flow was required, however the cost of the manufacture of each injector and

the durability of them meant that this was impractical and beyond the scope of the project.

The multi-tube design shown in 4.21 was also impractical and too costly due to the brazing costs as well as the rough cost of the amount of valves and adaptors to connect the system up. Therefore it was concluded that the simplest and most effective way to inject the liquid was to use 1/16th tubes as the injectors, by directly vacuum brazing them to holes drilled through the blind flange. Due to the requirement of their needing to be a 0.1 mm gap between the outer diameter of the tube and the hole wall, it was calculated that a maximum of 29 injectors could be fitted onto the flange, whereby seven would be in each quadrant and one central injector. Figure 4.22 shows the final hole layout for the blind flange.

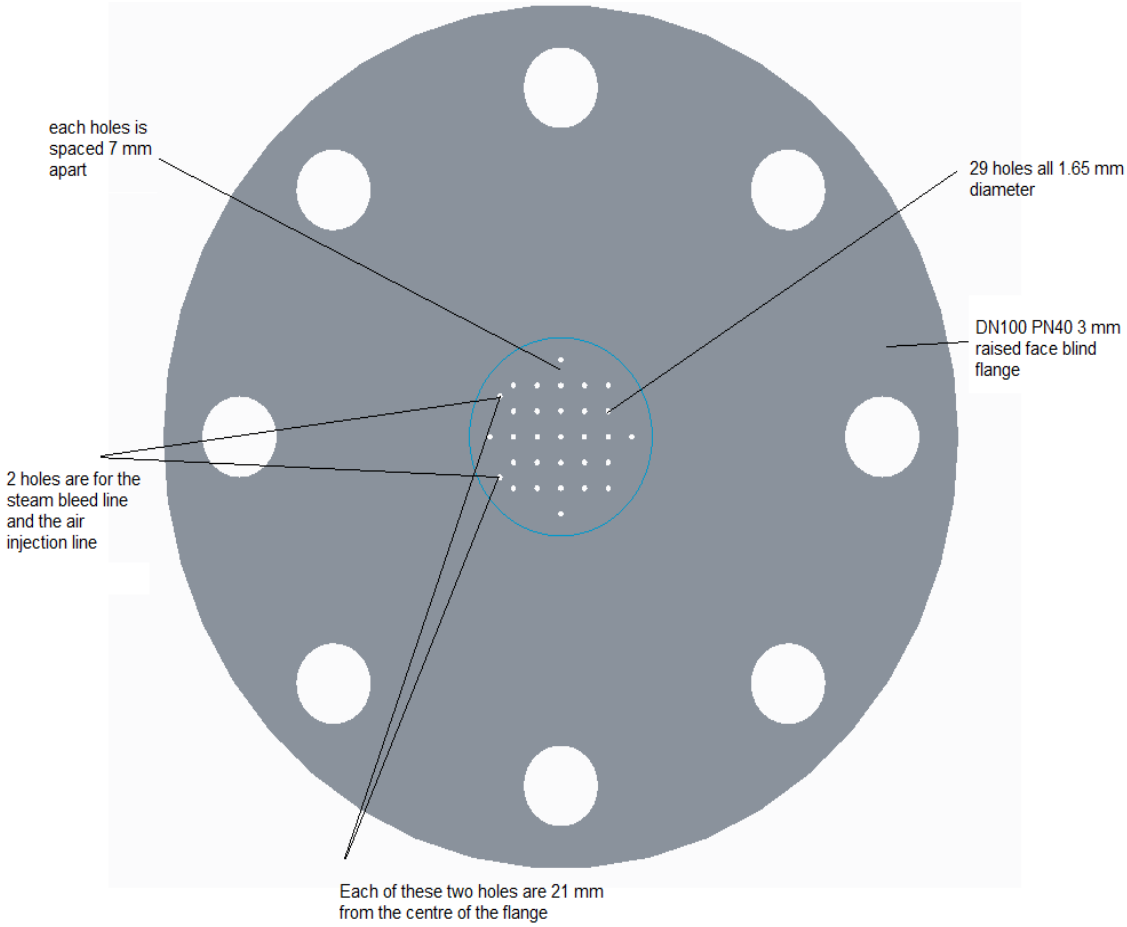


Figure 4-22 Layout of the holes for the blind flange utilising vacuum brazing

4.5 Final Design of the droplet Injector Manifold using the 1/16th inch Tubes

Before the final design was mapped out, a final investigation of what droplet sizes would be produced from the 1/16th tube was carried out using the droplet measurement procedure in section 4.1. Figure 4.23 shows the measured average diameter droplets produced from the tube compared to the average droplet size produced from the nozzles.

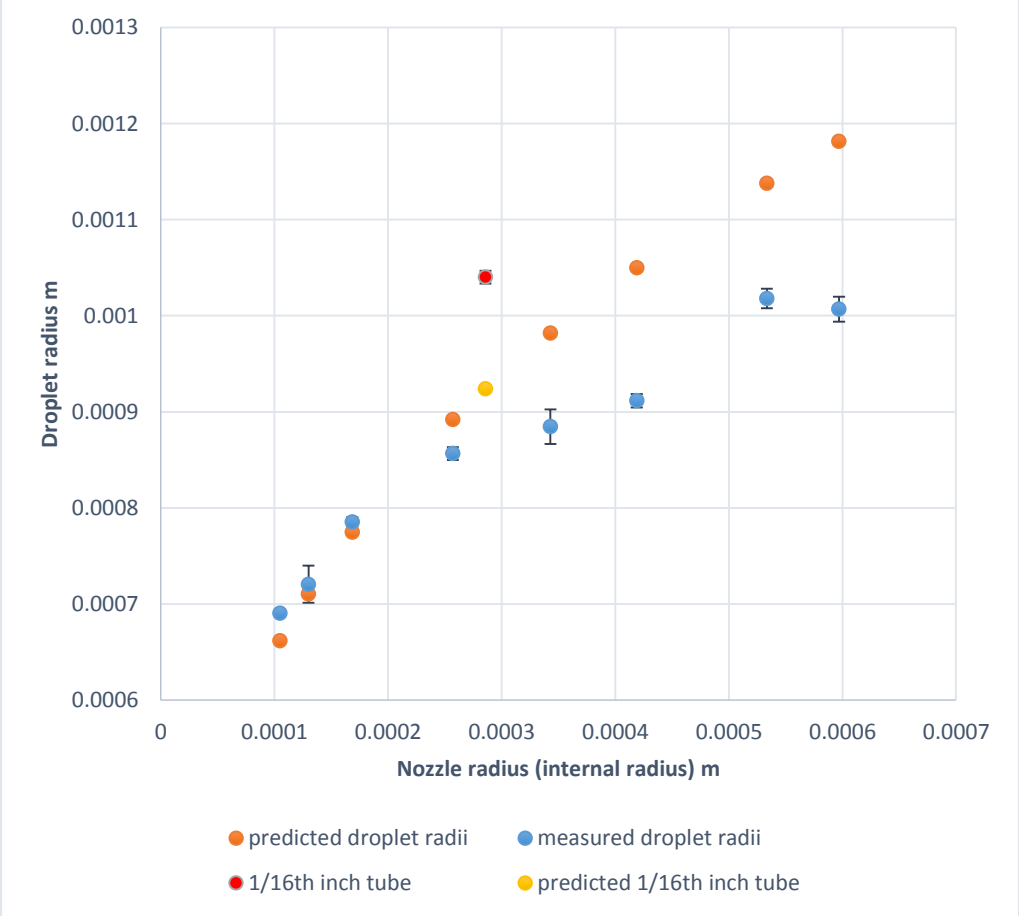


Figure 4-23 Measured droplet radius produced from the 1/16th inch tube shown in red against the predicted radius shown in yellow

The diameter of the droplet was measured at being on average a diameter of 2.08 mm. This is slightly larger than the droplet diameter produced from the 16G gauge nozzle. From figure 4.23 it can be seen that wall thickness must be taken into account when calculating the diameter of the produced droplets, as the inner radius of the 1/16th tube was less than

half the inner radius of the 16G nozzle, but the thickness of the 1/16th inch tube was over twice the thickness of the 16G nozzle. Due to the size of the error bar for the produced droplets, variation in the droplets produced is negligible, therefore the average produced size can be used for further calculations.

Because the diameter of the droplet is larger than one produced by the 16G nozzle, this will mean the droplet will have more mass and hence will heat up slower than the 16G droplet in figure 4.9 and 4.10. For the stability because the droplet diameter is larger by less than 100 µm the change to the Weber number and Biot number is trivial and so the droplet will behave the same as the one produced by the 16G nozzle.

The design for the holes to be drilled within the blind flange allows for a maximum of seven injectors to be in every quadrant of the sensor and one injector within the centre. Instead every seven injectors are grouped together, this gives combinations between 1, 7, 14, 21 and 28 injections. Table 4.5 gives the formation times for 1, 7, 14, 21 and 28 droplets from 1/16th inch tubes if a tube length of 1 m is assumed and flow rate 10 ml/min is given. The final tube lengths for each injector were measured and the final formation times are given in section 4.6

Table 4-5 Formation times for 1, 7, 14, 21 and 28 droplets from 1/16th inch tubes

Number of injectors	mass flow rate per injector kg/s	volumetric flow rate m^3/s	formation time [s]
1	1.67E-04	1.67E-07	0.11
7	2.38E-05	2.39E-08	0.79
14	1.19E-05	1.19E-08	1.58
21	7.94E-06	7.95E-09	2.37
28	5.95E-06	5.96E-09	3.16

The long formation times are not a problem as long as the steam becomes saturated. Therefore the droplets should fall through the sensor in a plane. Figure 4.24 shows the changes in dryness fraction using the amounts of droplets in table 4.5 for 10 Bara, 11 Bara and 12 Bara of steam.

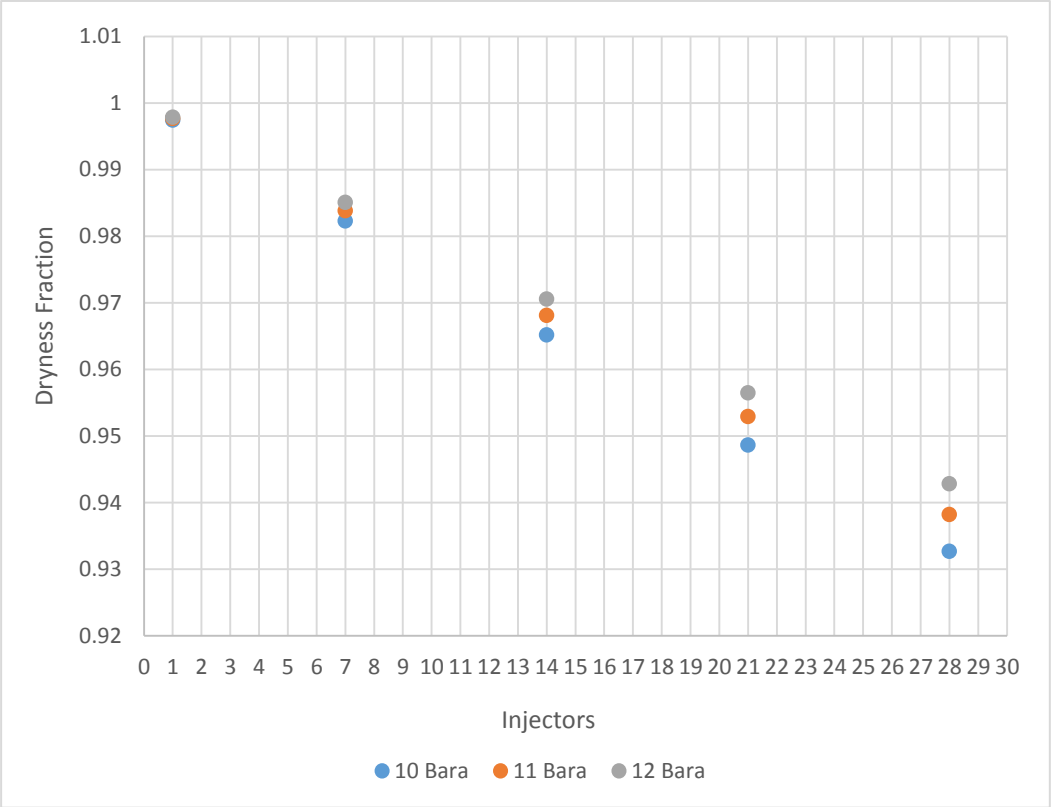


Figure 4-24 Dryness fraction for a plane of droplets produced by 1, 7, 14, 21 and 28 injectors using 1/16th inch tubes

This tells that in the ideal situation where all the pipes are 1 m long, it will not be possible for the sensor to detect a difference in wetness between the same amounts of droplets injected at two different pressures, because the difference in wetness is less than 0.5%.

Figure 4.24 also demonstrates that injecting 7 droplets into a quadrant gives enough change in dryness fraction to be detectable, therefore this design should be able to show differences in permittivity measurement between electrodes which would correspond to the change in dryness fraction for 7 droplets injected.

Every seven injectors will be grouped together, therefore figure 4.19 demonstrates the following four injection quadrants in relation to the position of the electrodes. The two holes in black are marked for the steam bleed line and the air injection line, more information on these components is explained in detail in chapter 5.

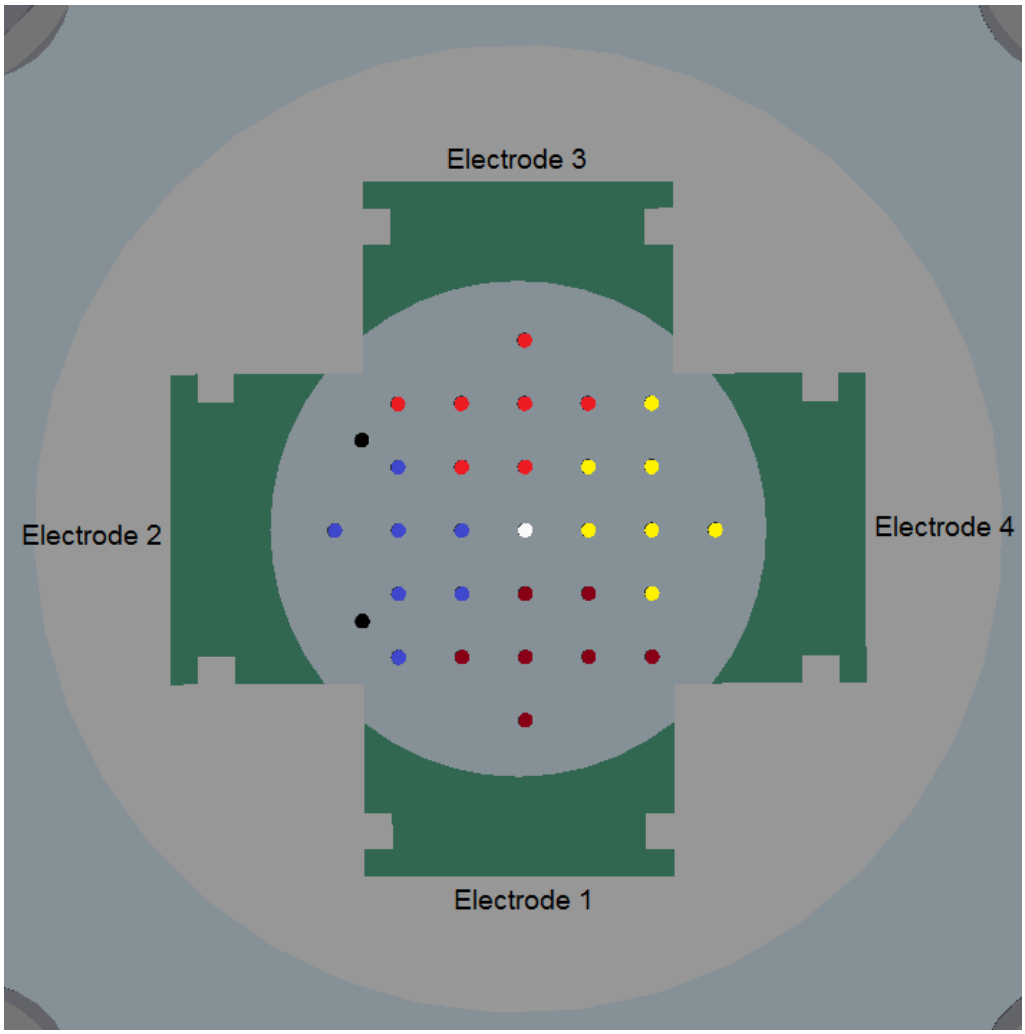


Figure 4-25 View looking directly down upon the sensor, quadrant A is red, quadrant B is blue, quadrant C is brown and quadrant D is yellow. The steam bleed line and air line are shown in black.

Once the quadrants had been marked out and their respective injectors grouped together, the final task was to work out how long the injector tubes inside the test section would be. The calculations in section 4.2 demonstrate that the droplets will not boil quickly therefore it was not imperative to have them as close to the electrodes as possible. Instead the

problems comes from insuring the water is liquid all the way to end of the tube, and when lowering the flange onto the test section, the tubes have to be short enough so that they don't catch and bend, but not too short so that they cannot be straightened.

The original calculated length of 20 mm was ideal, as this allowed for the tubes to be manipulated, and as water flows through the tubes through the testing period the pipes will be gradually cooled, so that water boiling in the tubes was not a problem after water had been initially pumped through. Figure 4.26 shows the completed droplet injection manifold.

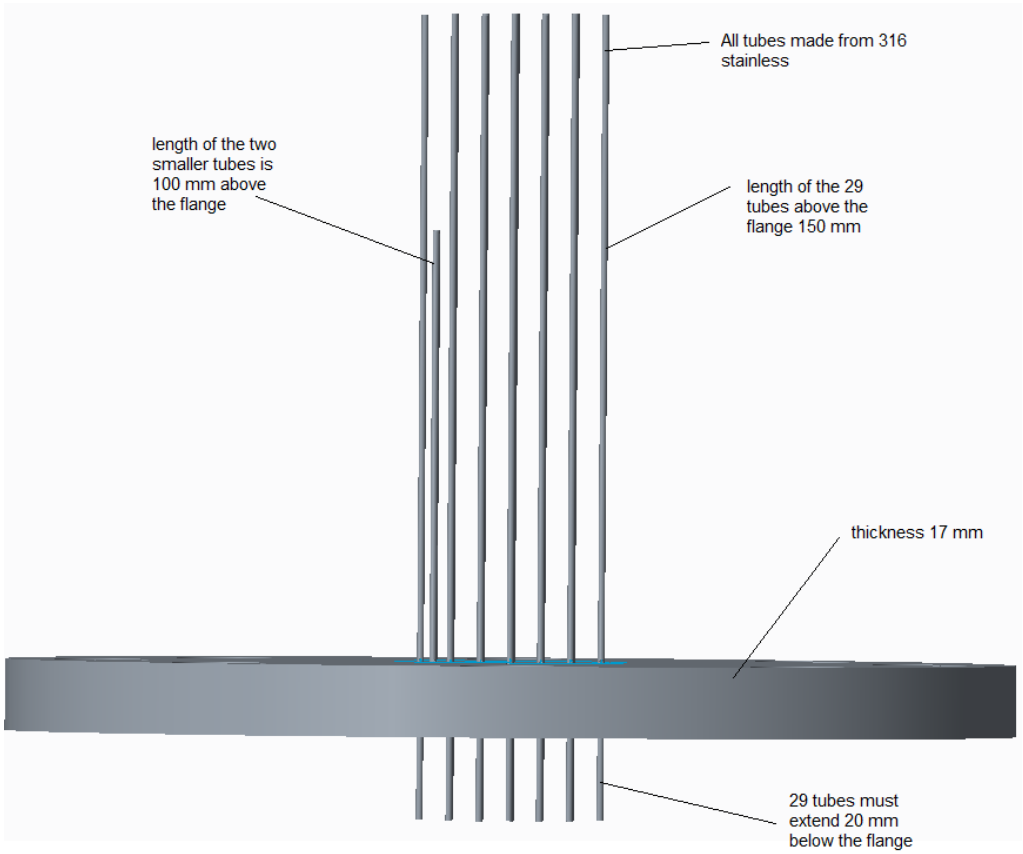


Figure 4-26 Sideways view of the final design of the droplet injection manifold

The next section discusses the steps that went into designing the water supply injection system, and how the injection lines were built and connected to the droplet injection manifold to form the droplet injection complete system.

4.6 Design and Construction of the Full Droplet Injection System

The final part of the process was to design and build the layout of the water injection tubes. The main point at this stage was to ensure that the volumetric flow rate was distributed as evenly as possible to each injector line. This work was carried out in parallel to the work in chapter 5.

The first option was to use five and seven way ball valves to evenly distribute the flow. Whereby a five way ball valve would split the flow between quadrants A, B, C, D or the central line. Then at the terminus at each of those lines except the central one, a seven way ball valve would allow for the flow to be distributed between each of the seven injectors present in each quadrant.

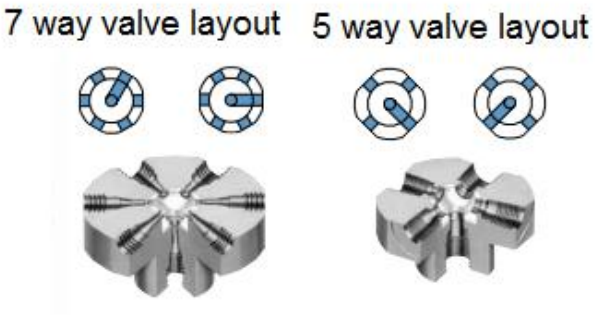


Figure 4-27 Layout of the seven and five way ball valves (Swagelok)

There were two major problems with this setup; firstly the ball valves would only allow water down one line at a time, this meant only tests involving one droplet injector would have been possible. Secondly due to the sensitivity of sensor this amount of water may not have been picked up, as figure 4.18 shows that for one droplet the change in dryness fraction would be less than 0.5%

Therefore the best option to allow for different amounts of water to be injected was to use a combination of two way on-off ball valves and four

way union connectors. This would mean that within the quadrants all seven injectors would have to be used to together, but different combinations of quadrants could be used interchangeably, and the central injector could still be used independently. To achieve this and to reduce material costs an effective design was utilised. The design was split into two parts, the initial quadrant/central line split, and secondly the feeder lines to each quadrant, which are made to be four identical copies. The overall line layout of the design with one copy of the feeder lines is shown in figure 4.28.

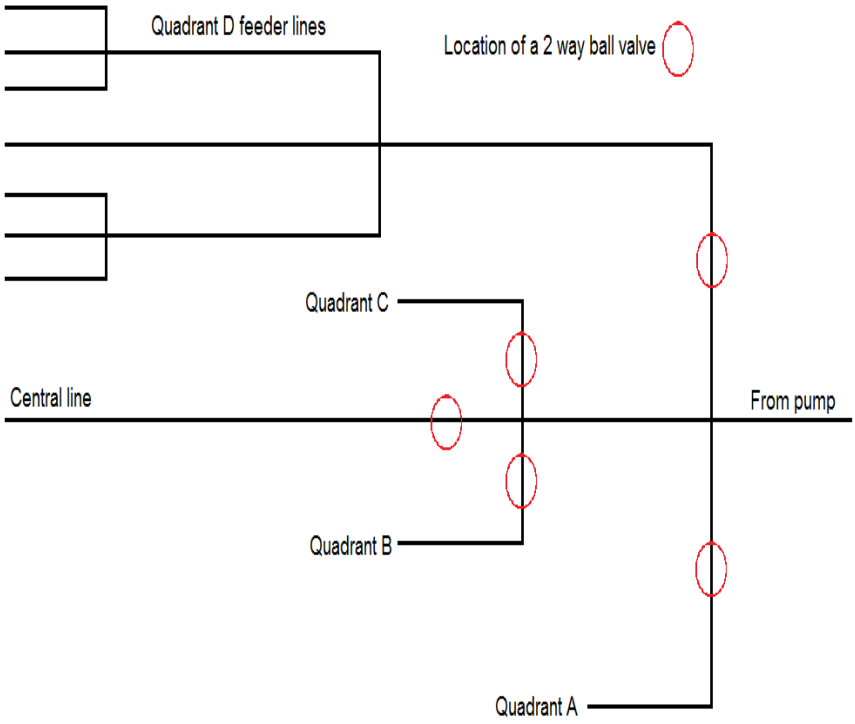


Figure 4-28 Line layout showing feeder system for quadrant D and location of the 2 way ball valves

With the resources available, this was the most cost effective design that allowed for multiple amounts of droplets to be injected. The only apparent problems is that the central line will have a greater volumetric flow rate than any of the other lines, and that for each quadrant 1/3 of the volumetric flow to that quadrant will go to one line assuming equal length. Finally when all four quadrants are tested together, quadrants B and C will have 1/6 of the flow rate each while A and D will have 1/3 each. This means in

reality six droplets can be injected together instead of seven for each quadrant, and when all the quadrants are tested together 12 droplets will be injected not 24. Therefore for this design the maximum amount of droplets that can be injected together is twelve. The higher flow rate line in each quadrant will be connected to an injector closest to an electrode to maintain the symmetry of each quadrant.

Ways to make the flow rates as close as possible such as changing the length of the tubes with the higher flow rate to reduce the flow were reviewed. It was concluded that with the space within the oven and the tubing available it was not possible to achieve this. It was not feasible to solve the problem by using a combination of 5 way and 7 way unions, due to the total cost of the parts.

Therefore the design in figure 4.22 became the final design for the droplet injection line layout. To address the problem of the unequal flowrate when all four quadrants are injecting at once, needle valves were added to the design to slow the flowrate on quadrants A and D to the same rate as B and C. Figure 4.29 shows these valves added to the schematic.

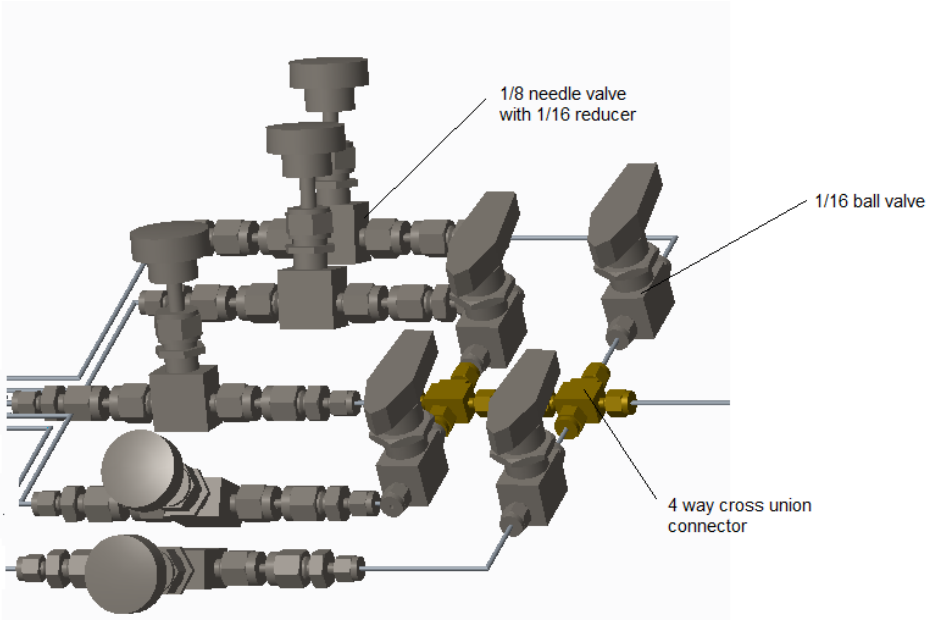


Figure 4-29 CAD drawing of the initial quadrant flow splitter with the added needle valves.

The needle valves were included on all the lines to balance out any unequal flow rates. Before this section a check valve was added to stop any back flow to protect the pump. The full design with two lines for demonstration is shown below.

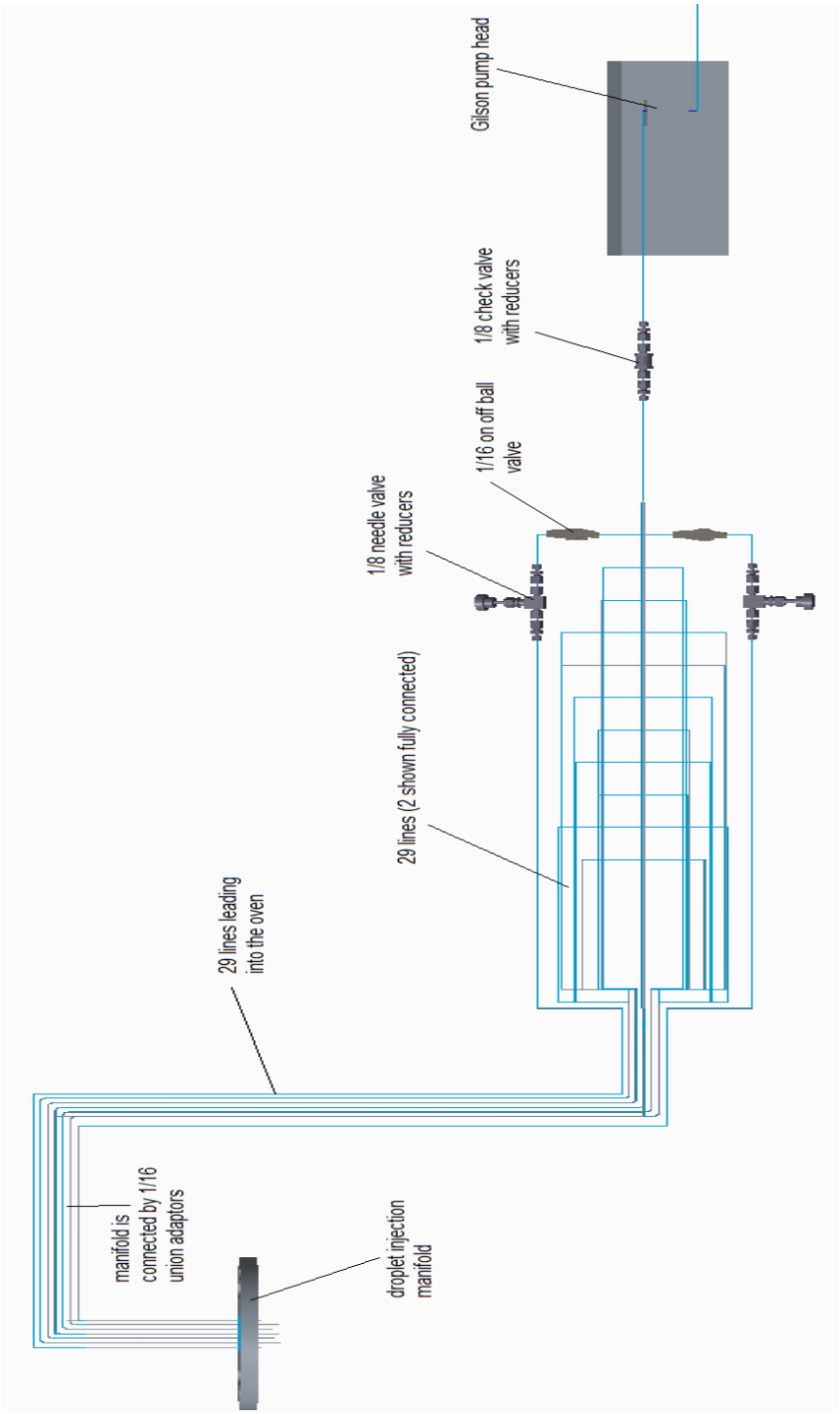


Figure 4-30 Full design of the droplet injection system

The lines were then constructed to the specification of figure 4.28 and 4.29, whereby the splitter components were built onto a board to hold them in position while the on-off valves are turned. Figure 4.31 shows the constructed control section.

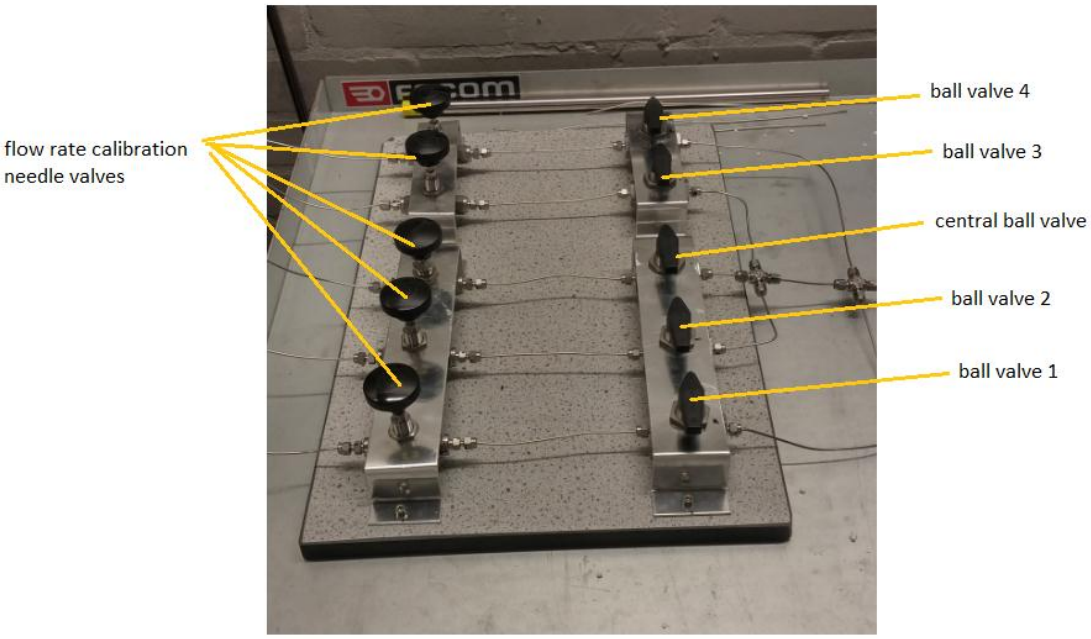


Figure 4-31 Constructed initial flow rate splitter, where 4 controls quadrant D, 3 controls quadrant C, 2 controls quadrant B and 1 controls quadrant A.

To ensure the system was working correctly and the needle valves were able to restrict the flow rate, the total mass flow rate coming out of the injectors over a minute was measured for each quadrant combination, while all the needle valves were tightened ¾ quarters of the way. The results of this test are shown in figure 4.32:

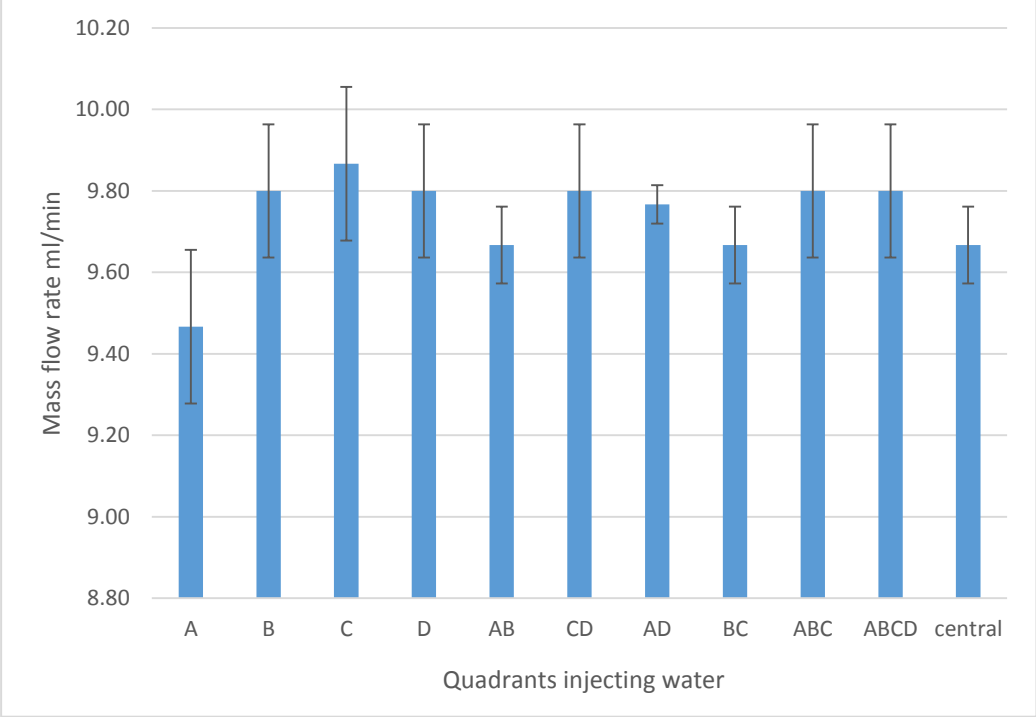


Figure 4-32 Measured mass flow rate over 1 minute for the quadrants and the central injector with the needle valves ¾ tightened

The results demonstrate that the needle valves did not work, the cause was found to be because the strength of the pump kept the flow rate up. The pump could not be changed so for the rest of the project the needle valves were left untightened, as any tightening of them would not make any difference to droplet injection rates, and would give an undetermined flowrate.

The final piece of information required is the flow rate for each line to truly determine how many droplets are being injected at once. In the droplet injection system, the following measurements that were given for each tube to be cut for the feeder system, shown in figure 4.33:

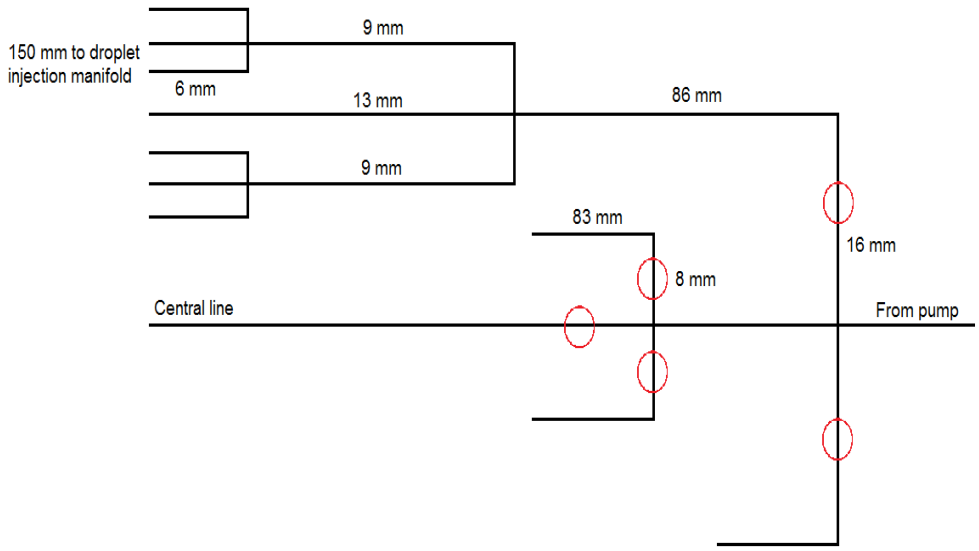


Figure 4-33 Tube length measurements for the water injection system

Actual measurement of the system after construction showed differences with each injector line of length of ±7 mm with an average of 284 mm. In a parallel system such as this the pressure drop on each branch line due to Poiseuille's law must be equal, so when the pipe diameters are equal only the change in length will alter the flow rate at each line. If it had been possible to attach a flow meter to the central line, then an accurate calculation of volumetric flow rate could have been calculated at each line, using the known ratio of length to flow rate. The problem is shown in equation 4.21 for two branch lengths of pipe:

$$\frac{128\eta_f L_1 Q_1}{\pi D_n^4} = \frac{128\eta_f L_2 Q_2}{\pi D_n^4}$$

Which cancels down to:

$$\frac{L_1 Q_1}{L_2} = Q_2$$

(4.22)

Since Q_1 could not be determined with the available resources, a different approach was performed to calculate the estimated flow rate. By

treating all the tube lengths as equal, the flow rate at each branch could be split equally. Therefore the mass flow rates were calculated as they would be from 1, 2, 3 and 4 quadrants injecting simultaneously. Figure 4.28 shows the flow rates from quadrants A, AB, ABC, and ABCD.

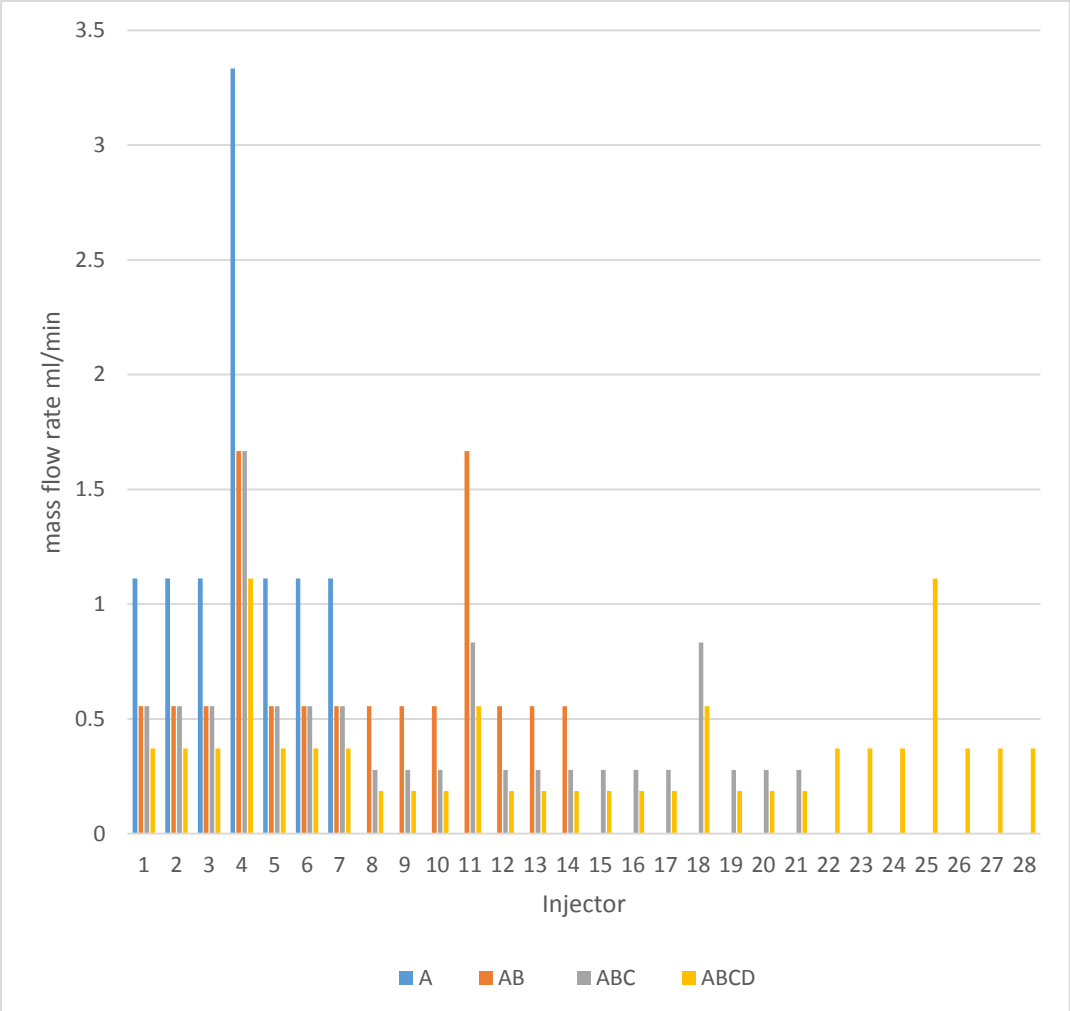


Figure 4-34 Calculated mass flow rates ml/min for each injector assuming equal flow rate split.

These flow rates can then be converted into volumetric flow rates, but to answer how many droplets could be injected at once the volumetric flow rates then need to be converted to formation times. Figure 4.29 shows the formation times for the mass flow rate for each injector.

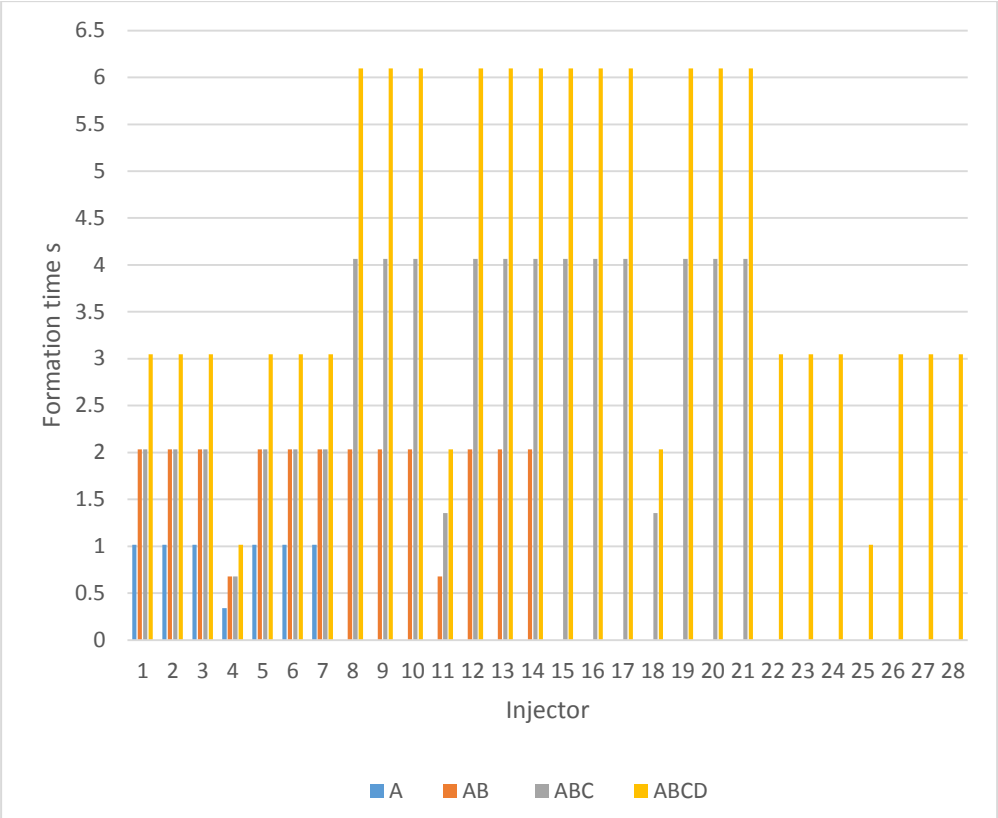


Figure 4-35 Formation times for each injector assuming equal division of the volumetric flow rate

This means that from the formation times of the droplets from each injector it can be seen that a maximum of 12 droplets can be dropped simultaneously for all the quadrants together, for one quadrant a maximum of six droplets can be dropped together. This situation was fine to test for spatial positioning with as the change in dryness fraction due to six droplets being injected is detectable with the sensor. For injecting into more than one quadrant, a maximum of 12 droplets is fine as it will be enough for the sensor to detect different injection patterns. If the droplets fall together, the opposite electrode pairs will be able to distinguish the different steam wetness produced for 6 and 12 droplets being injected. The four lines that had the largest flow rate in each quadrant were connected to the four injectors nearest to the centre of each electrode, to maintain an equal quadrant size for each test.

4.7 Incorporation of the Injection Pattern into the 3D Model of the Sensor

Because the droplet injection system has been designed and constructed, it is now possible to add the location of all 29 droplet injectors into the program. To model this, each droplet was represented as a cubic volume of liquid that was assumed to fall straight through the sensor. Since the model area is 1000 by 1000 nodes which takes up a real world space of 0.1 m then the gap between every node is 0.0001 m. Therefore because the diameter of a droplet produced by a 1/16th inch tube is 2.08 mm, then 20 X 20 nodes will represent the droplet in 2D. For the 3D component the sensor is divided into 200 slices with each slice having a thickness of 0.00075 m therefore 3 slices will give an approximate depth of 0.00225 mm to the droplet. The programmed layout of the droplets is shown in figure 4.30, taking into account the amount of droplets that can be injected simultaneously from the previous section.

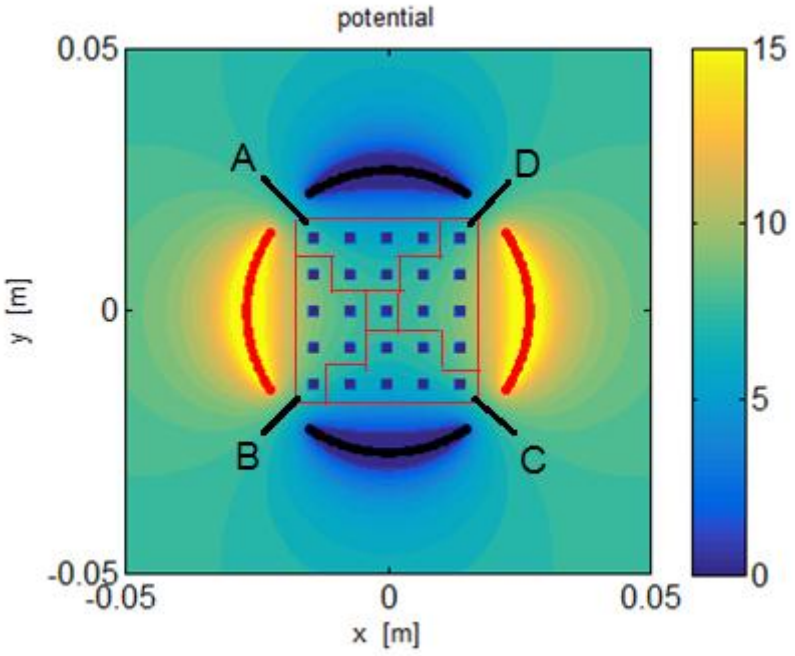


Figure 4-36 Droplet injection pattern into the model for a maximum of six droplets being injected into each quadrant

This layout when applied to the 3D still and to the 3D permittivity change with time programs, can be controlled to allow for the droplets to fall in their respective quadrants together. To give an example of this functioning figure 4.37 shows six droplets being injected in each of the four quadrants A, B, C and D discussed earlier.

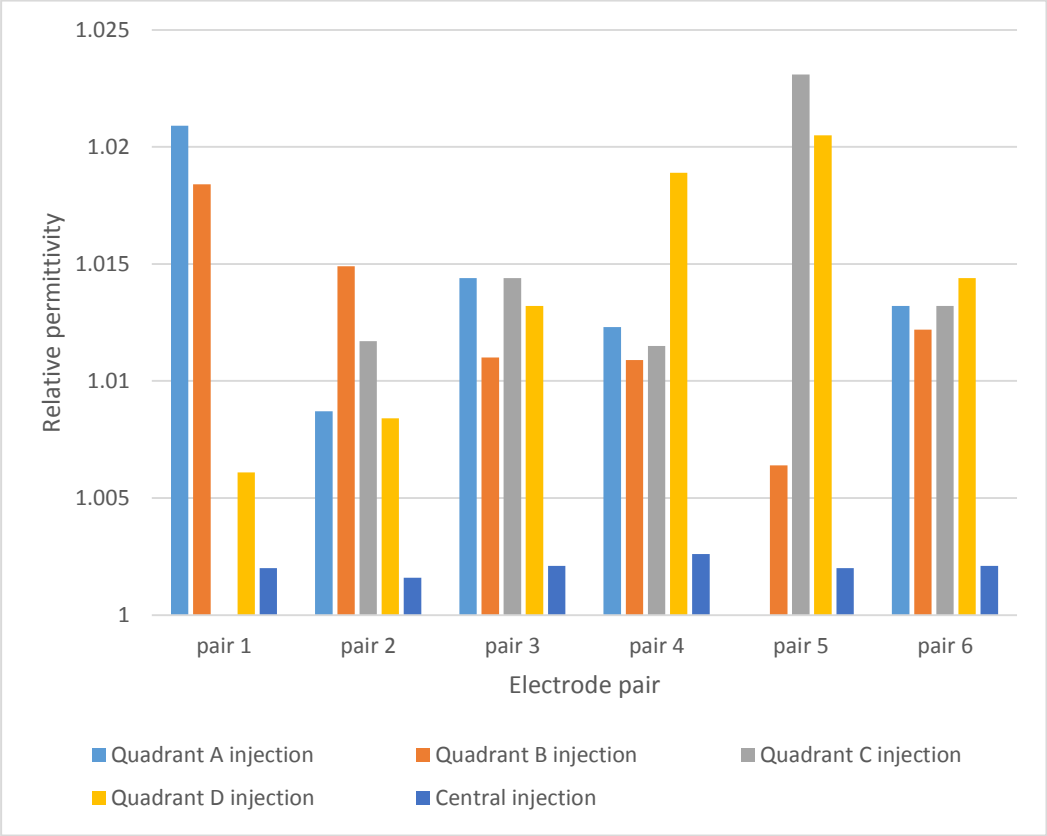


Figure 4-37 Six droplets injected in steam into each of quadrants A, B, C and D as well as the central injector

The results show that the model strongly responds to the spatial positioning of the droplets within the sensor, the results are not as clear for injections within B and D due to the location of where the droplets have been injected, further showing that spatial positioning is affecting the results. This is only a preliminary explanation of the program, the full testing and analysis of droplets being injected in steam and air, will be discussed in chapter 6.

4.8 Conclusions

Based upon the brief and the design goal, a novel technique of measuring the diameter of droplets was developed by utilising the Camsizer P4, the technique demonstrated that the selected way of predicting droplet diameter from the available parameters was inaccurate, and so the measured droplet diameters were used for all further calculations, measurements and experiments.

A study was completed on the behaviour of droplets falling through a steam environment and whether different diameter droplets could survive intact. It was found that they heated slowly over a falling time of 0.205 seconds over a distance of 225 mm. The only initial problem was found by their formation time, as at first the droplets would evaporate before falling off the end of the needle, but this would saturate the steam and prevent any further evaporation, hence allowing the droplets to fall intact.

Vacuum brazing was utilised to fit the maximum amount of injectors onto the blind flange, this however meant that only one droplet size using $1/16^{th}$ inch tubes could be used due to the cost of making multiple manifolds.

The full droplet injection system was then designed to allow for equal amounts of water to be fed to each injector on the manifold. Due to mounting costs with the system a design using ball valves and union crosses was used to direct the flow. Needle valves were included as well to control the flow rate, this proved to be ineffective and so they were not used in the final testing. Therefore the built injection system was what could be afforded, not what was ideal for the final testing.

The designed droplet injection pattern from the droplet injection manifold was incorporated into the 3D capacitance measurement program. It was shown by initial tests, that spatial positioning is affecting the capacitance measurement. The full testing of spatial positioning will be covered in depth within chapter 6, with a comparison of the results from the test rig to the 3D capacitance model.

Chapter 5. Design and Construction of the Test Rig

Nomenclature

P Pressure [Bara]

L Length [m]

k Thermal conductivity $\left[\frac{W}{mK}\right]$

R Gas constant

r Radius [m]

T Temperature [°C]

V Volume $[m^3]$

ρ Density $\left[\frac{kg}{m^3}\right]$

Subscript

S Specific volume of dry steam

a Thermal conductivity of the pipe

b Thermal conductivity of the insulating material

This chapter details the design and construction of the experimental test rig facility that was used to house the ECT sensor and the droplet injection system. The work detailed within chapters 3, 4 and 5 was completed simultaneously as the droplet injection system in chapter 4 and the sensor in chapter 3 were designed to fit within the layout which will be discussed here.

Within the literature, there were few previous examples of test rigs involving superheated steam, and even fewer that fully explained how the rig was constructed. However an excellent example was produced by Veiga *et al.,* (2009). This test rig was used to test how gaskets leaked under different pressures and temperatures with superheated steam. The core of their test rig was used as the basis of this one, thereby improving the safety aspect of the rig by using a design that has already been shown to succeed.

The rig was not the cheapest design, but it was considered the best, as it mitigated the problem encountered by Barham (2013), where a film of water would build up on the electrodes. This film had to be removed as it could invalidate the capacitance measurement by changing the spatial positioning of water within the sensor. The other novel design will be discussed in this section, however it was not practical due to the aforementioned reason.

Construction of the final design introduced faults, as the valves had to be setup in different positions to how they were designed. This introduced longer lengths of pipes which produced condensation problems. This chapter will discuss all of these faults and their solutions, and show how in the end they actually improved the working of the rig.

This chapter is split up into the following sections:

5.1 Initial Test Rig Designs

Detailing the principles behind the test rig's design and a discussion of the final two designs, where one is based upon the work by Veiga *et al.,* (2009), and the second uses the same principles but with a cheaper method.

5.2 Final Experimental Test Rig Design

Overview of the final design that was selected to be the experimental test rig, detailing all the components needed in the construction of the rig.

5.3 Construction of the Test Rig

How the experimental test rig was built and a discussion on how the rig was modified for efficiency and to comply with health and safety

5.4 Steam Control within the completed Test Rig

An overview of how the amount of steam required for the different pressures was calculated, as well as a discussion on the problems with steam condensation outside the test section

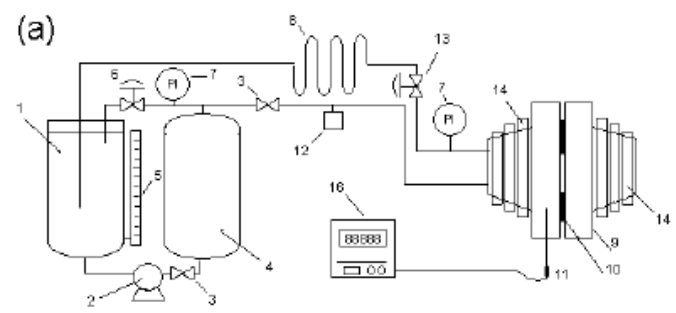
5.5 Conclusions

5.1 Initial Test Rig Designs

The test rig was required to hold a volume of superheated steam under different pressures and temperatures. The design parameters of the test rig are as follows:

- Must be able to hold a volume of superheated steam within the sensor;
- The steam contained must be static;
- The rig must contain a pressure transducer;
- The rig must contain a thermocouple as close to the sensor as possible;
- A pressure relief valve has to be equipped;
- The steam must be allowed to condense safely to be reused or to be removed as waste water;
- Allow for the ECT measurement recording equipment and injection pumping system to be a safe distance from the pressurised sensor.

Taking these parameters into account, due to safety concerns it was advised that the best way to design the rig was to base the schematic upon a previous test rig that performed a similar function, and featured the same equipment onboard. For these reasons, the previously mentioned rig by Veiga *et al.,* (2009) was ideal for this purpose, as it was actually performing the same function and following almost all of the parameters above apart from not using ECT equipment as they were testing gasket failure. This rig is laid out in the following way, shown by the design in figure 5.1 below:



Test rig components:

1- Water Vessel.
2- Water Feed Pump.
3- Check Valve.
4- Pressure Vessel.
5- Calibrated Glass Sight Gauge.
6- Pressure Regulator.
7- Pressure Gauge.
8- Condenser.
9- Flange Set.
10- Test Gasket.
11- Temperature Sensor.
12- Pressure Controller
13- Relief Valve.
14- Heating Tapes.
15- Oven
16- Temperature Controller.

Figure 3 - Schematic of the Superheated Steam Test Rig with heating element tapes.

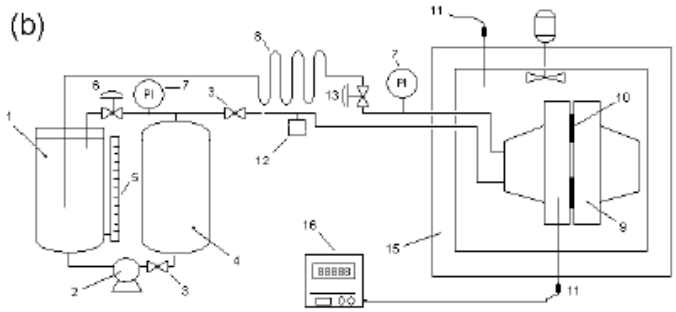


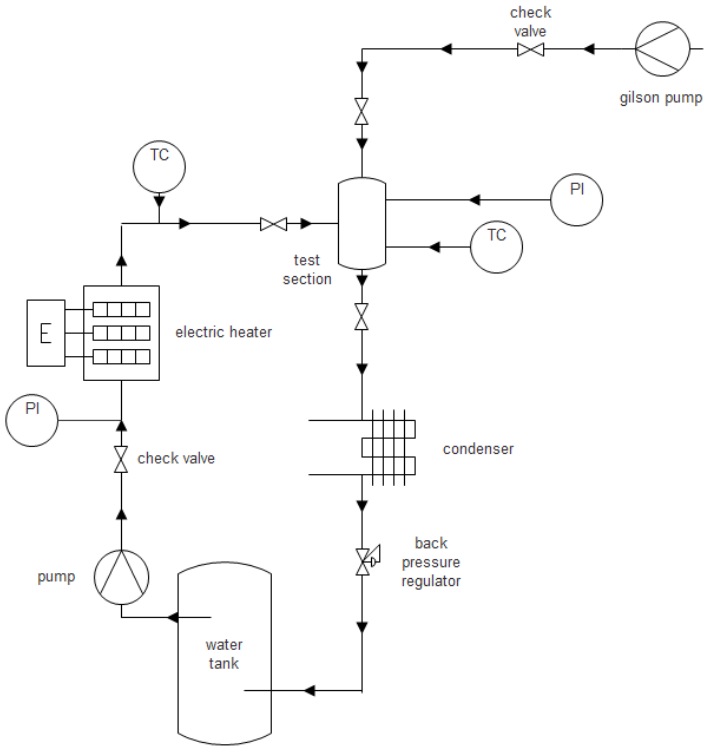
Figure 4 - Schematic of the Superheated Steam Test Rig with oven heating.

Figure 5-1 Designs of the gasket failure test rig using an oven or heating tape by Veiga et al., (2009)

The rig works by pumping pressurised water into the gasket, which is heated by the oven increasing the pressure until the gasket fails. If the pressure goes beyond a certain point the relief valve opens and the steam is condensed and fed back into the water tank.

This setup is advantageous due to the following reasons. The design does not include a steam generator, which lowers the total cost significantly. The static volume of superheated steam is maintained due to being contained within the oven, so if this technique was applied it would not be possible for a film of liquid to develop on the electrodes. Finally their design has a condenser, would be useful as an additional safety feature to remove excess steam and to prevent wastage within the system.

From the design shown in figure 5.1 two final schematics were developed that could fit the design parameters and complied with all health and safety regulations, the first of these designs utilised heating tape and blankets to trap the heat within the test section the outline of this design is



shown below in figure 5.2:

Figure 5-2 Initial design using electric heating tape and blankets

The original purpose of the above design was to test supercritical water, the design was changed by wrapping the test section up in a heating blanket. The water is first pumped into the heater at 12 bar, due to the pressure the water needs heating to 190 degrees C to boil, at this point the steam travels along to the test section. When the pressure inside the test section is equal to 12 bar the valves are closed and no more water is allowed in. To stop the steam condensing on the walls the section will be wrapped in a heating blanket that needs to produce more than 200 C while the tests are being carried out. Like the design by Veiga *et al.,* (2009) if the pressure

becomes too high or the experiment ends the relief valve will open allowing the steam to pass into the condenser, a back pressure regulator makes sure the pressure is low enough when it enters the water tank.

For this research it is more important that the film is shown to be 100% removed when taking measurements, the way the section is heated could allow for a cold area, even if it is only slightly below the saturation point a film could form on an electrode and invalidate the results. For this reason the design was rejected in favour of one that had the test section heated by an oven. A full discussion of this final design is detailed in the following section.

5.2 Final Experimental Test Rig Design

The final design was based upon the schematic shown in figure 5.1 with heavy modification on the layout to include the droplet injection system shown in chapter 4. Also included was a way to fill the test section with pressurised air, this system will be detailed later in the chapter.

The system would have two main inputs into the test section, the water injection lines and the air injection line. The droplet injection system will be used to initially inject cold water to become the superheated steam, thus removing the need for a separate water injection line. There will be two main outputs from the test section, a steam removal line and a water removal line. A further output will be the bleed valve to draw steam up towards the top of the test section prior to testing. The schematic for this system is shown below in figure 5.3, detailing all the components and inputs/outputs.

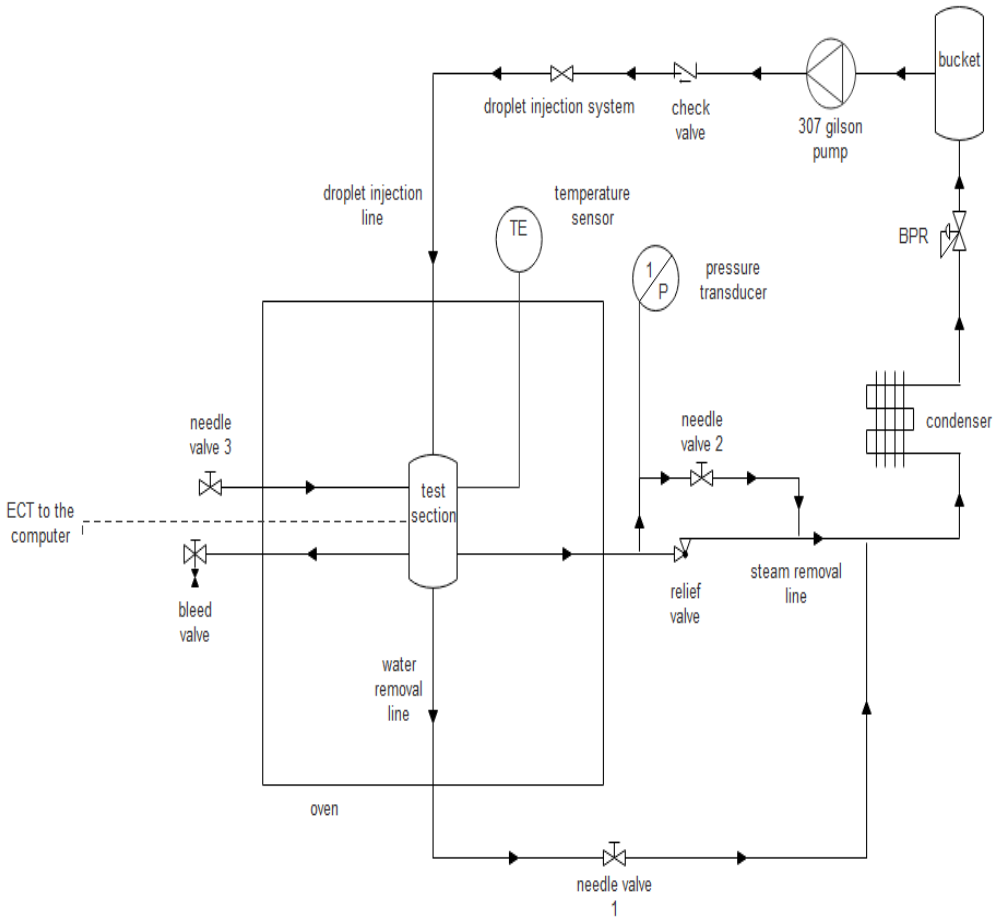


Figure 5-3 Final schematic for the droplet injection test rig

Each of the input and output lines are clearly labelled in figure 5.3, the valve outline for the droplet injection system detailed in chapter four has been simplified for understanding. Using a testing pressure of 12 Bara the system works by injecting a set volume of water into the test section, the valves are then closed and the testing section is heated steadily by an oven temperature of 208°C. When the thermocouple reads a temperature of 190°C inside the test section, the volume of water added would be superheated steam of a pressure of 12 bar. This volume of steam would be static and contain no film as the walls of the section would be hotter than the boiling point of water at 12 bar. If the pressure goes above 13 Bara the relief valve will open. If the experiment is finished valve two can be opened allowing the steam to flow to the condenser.

The condenser allows vented and removed steam to be cooled down to a liquid where the back pressure regulator (BPR) can be used to slowly remove the pressure from the liquid entering the bucket.

The other half of the testing procedure requires the ECT measurement of droplets being injected into a pressurised air environment with the same density as superheated steam. To allow this, the test rig has the ability to be filled with pressurised air; a more detailed discussion on using the system with air is discussed in the next subsection.

5.2.1 Air Input system

For air testing, needle valve 3 can be opened allowing air into the test section up to the required pressure. The air would be fed from a gas bottle with a regulator allowing for pressures up to 10 Bara. To calculate the required air pressure within the test section for the three different pressures, so that the density of the air is the same as the density of the steam at 10, 11 and 12 Bara the ideal gas law is used. The law is rearranged to the form shown in equation 5.1, to calculate the required pressure of air for a given steam density.

$$P = \frac{\tilde{R}T\rho}{molecular\ weight} \tag{5.1}$$

The temperature would be measured before air testing from the thermocouple situated within the test section, to provide an accurate calculation of the required air pressures. At the end of testing, the air can then be vented through use of needle valve one or two; if the pressure goes above 13 Bara then the relief valve will remove the air.

To accurately record the pressure within the test section as well as attach the three aforementioned valves, a pipe section was developed that could be fitted to the bottom of the test section.

5.2.2 Water removal section

The connection section required had to be custom made so that it was compact enough to be able to fit inside an oven along with the ECT section and the droplet injection lines. The pipe section was fitted to the ECT section by a DN 100 to DN 50 converter pipe, whereby the section was attached to the DN 50 end. Figure 5.4 demonstrates the pipe section fitted to the test rig:

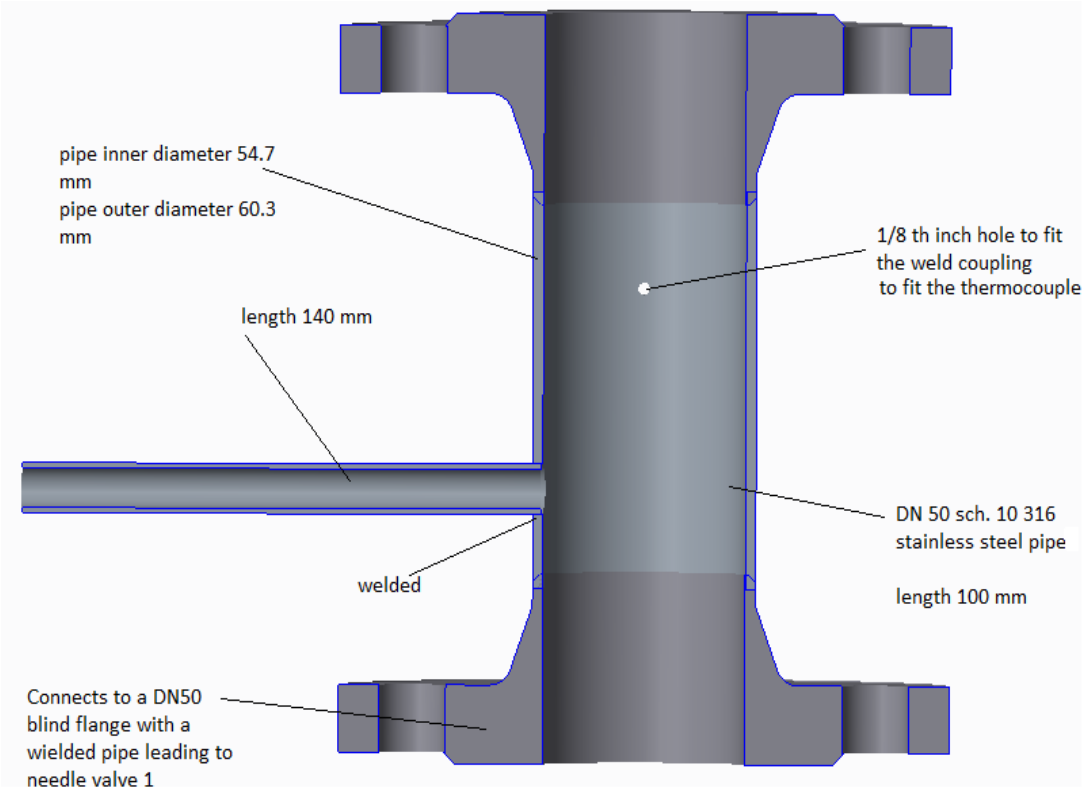


Figure 5-4 Cross section of the water removal section

The thermocouple was to be inserted into the water removal section by the 1/8th inch hole and bent upwards so that the sensor is taking temperature readings directly below the test section inside the pipe.

The layout of the pipes leading to the relief valve and needle valve two had to be carefully designed so that the pressure transducer could be included within the pressurised section as well as being outside the oven, to avoid breaking the sensor due to the long heating periods. The pipe layout is shown on the next page, detailing all important components.

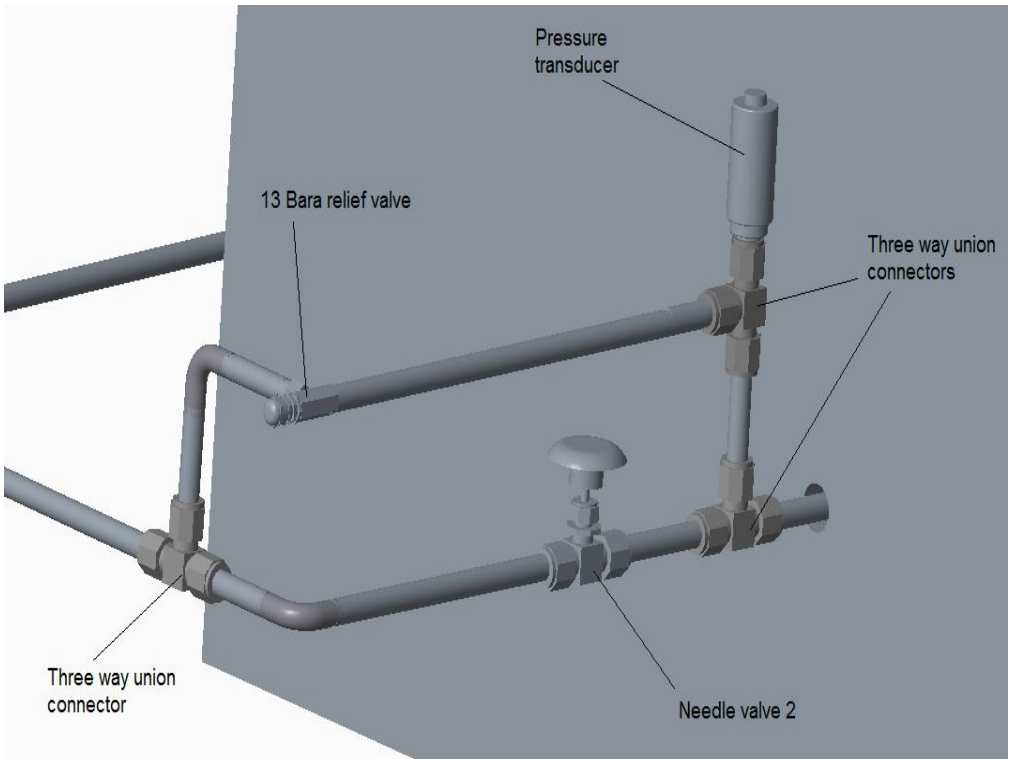


Figure 5-5 3D layout of the relief valve, pressure transducer and needle valve two

This layout was then incorporated into the final 3D CAD of the test rig that details the layout of all the main components. The final CAD drawing is discussed within the next section.

5.2.3 3D layout of the Test Rig

The schematic shown in figure 5.5 was converted into a 3D CAD model that could show the entire layout of the test rig and what additional components were required to make the rig safe and easy to operate. The model was also required to give an idea of how the piping system would be connected in the real world, and where problems might develop. This 3D CAD model is shown in figure 5.6 detailed on the following page, this is an ideal view of what the test rig should have looked like, as modifications were made when the rig was built which are detailed in section 5.3.

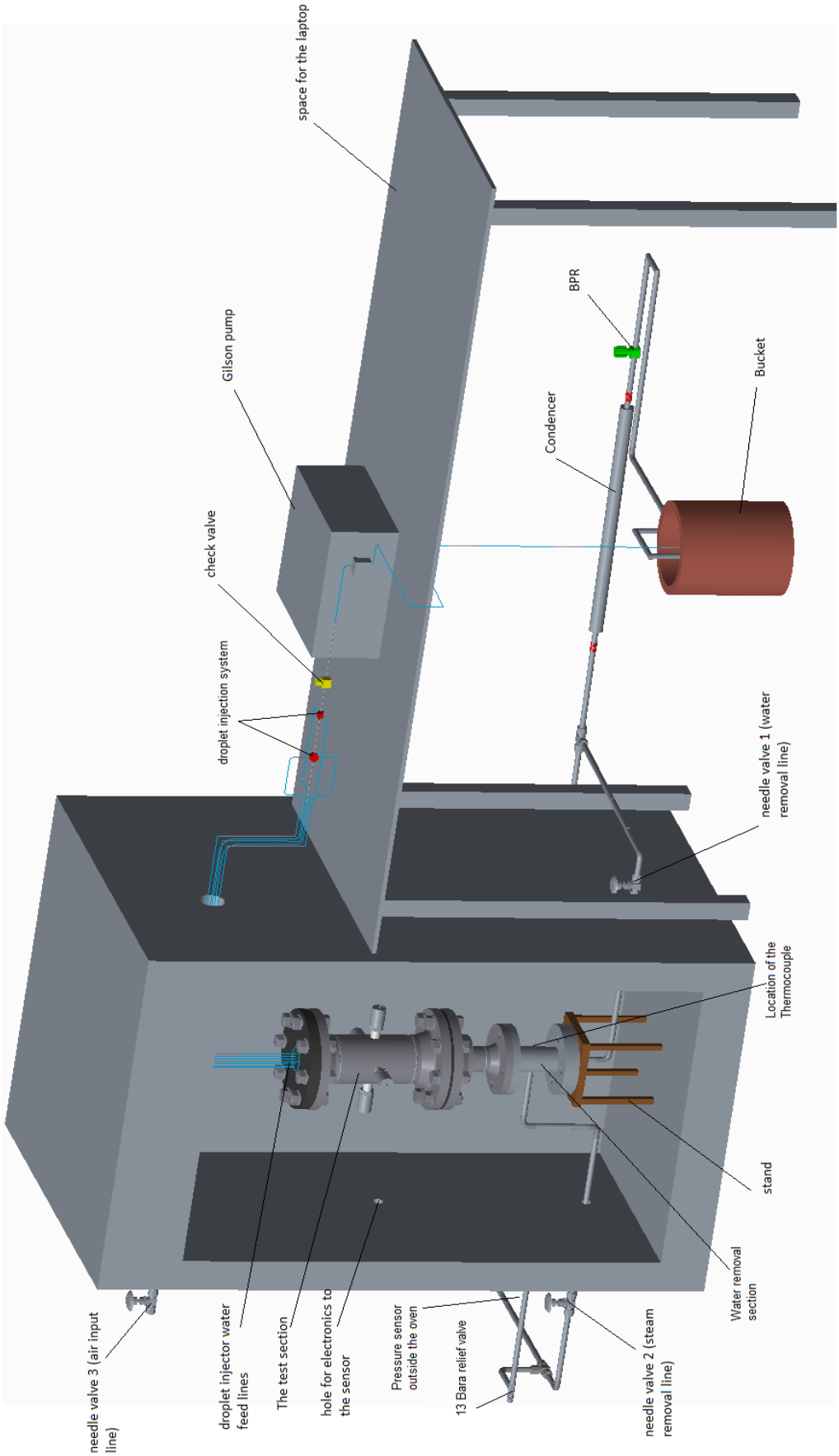


Figure 5-6 3D CAD model of the test rig, laid out in the ideal way

5.3 Construction of the Test Rig

The first step in the construction of the test rig was the selection of the oven. As it was the main component of the rig it would have to house the test section, droplet injection and the water removal system stacked on top of each other being over 400 mm in height. It would have to be able to maintain different heat cycles over long periods of time that would be suitable for different testing procedures. The oven would also have to have the ability to have holes fitted through the sides shown in the positions in figure 5.6. Due to these reasons the Nabertherm TR450 oven was selected, it had a largest interior with an internal height of 1100 mm and width of 580 mm, the oven had a computer built in where different heating cycles could be programmed, and finally the company Nabertherm gave the option to modify the oven, so that holes could be placed in specific locations. A CAD drawing of the oven along with the hole position options is detailed in figure 5.7 below:

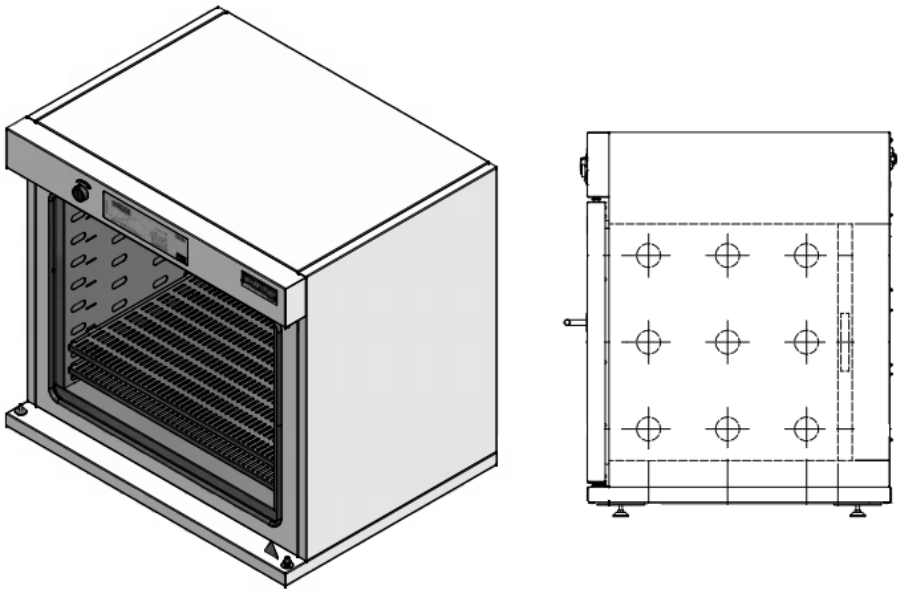


Figure 5-7 Outline of the selected Nabertherm oven with the selectable hole positions for each side (Nabertherm 2018)

This oven was then set up in the corner of the lab with a large workbench table alongside the oven in the same way as figure 5.6, to give enough space for the Gilson pump to be set up at one end and the laptop to

be positioned at the other end of the table. With the basic shape of the test rig in place the next step was to install the water removal system inside the oven as a platform for the test section to be connected onto. From the drawing shown in figure 5.4 the two pieces of the section were constructed from 316 stainless steel, these are shown in figure 5.8:

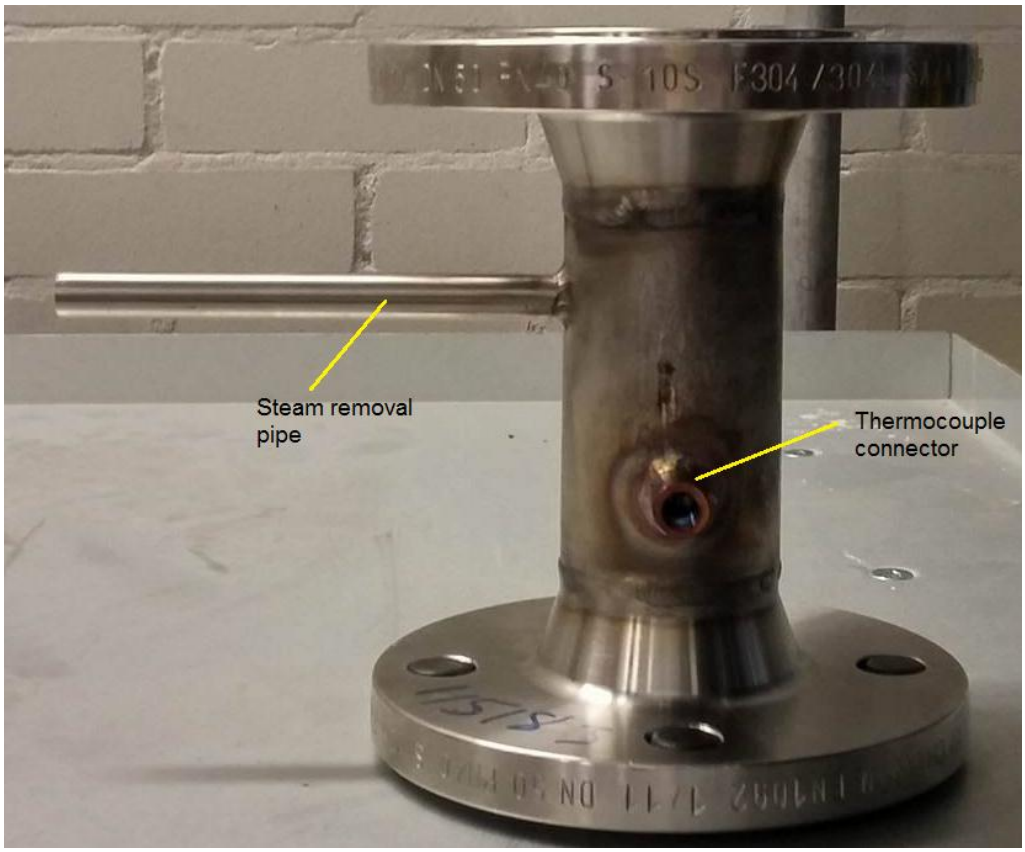


Figure 5-8 Water removal section constructed

This piece was fitted by attaching it to the blind flange and placing the attached pieces on top of a stand within the oven, which allowed for a pipe to go directly out of the bottom of the blind flange towards needle valve one.

5.3.1 Construction of the steam and water removal lines

With this in place the steam and water removal lines were fitted next. It was at this point that it was apparent that the layout of the steam removal line had two problems; firstly health and safety was an issue as having the steam let out by needle valve two did not allow for a controlled amount of steam to be released, this in turn would have made it difficult to have the

right amount of superheated steam present within the test section. Secondly because needle valve two would be in use while the system was under pressure, it had to be in an easily assessable location. Due to this, the valve would have had to have been placed too far from the oven which would have caused the steam to condense without the use of insulation.

To rectify this issue, the effect of how the amount of insulation causes a difference in the time it takes the steam to condense was investigated. The basic model for a non-insulted pipe is shown below for a cross section of a 1 m pipe:

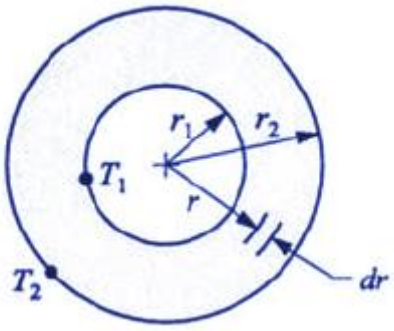


Figure 5-9 A non-insulated pipe where r1 is the radius from the centre of the pipe to the inner wall, r2 is the radius of the centre of the pipe to the outer wall, T1 is the temperature inside the pipe and T2 is the temperature on the outside of the pipe (Engineers Edge 2018).

The heat transfer rate is therefore calculated as being:

$$q = \frac{2\pi kL(T_1 - T_2)}{\ln(r_2/r_1)} \tag{5.2}$$

This equation would be sufficient to calculate heat transfer rate of water within the 0.5 inch steam pipe. However due to the pipe requiring insulation the heat transfer problem becomes more complicated so the following situation is present shown in figure 5.10:

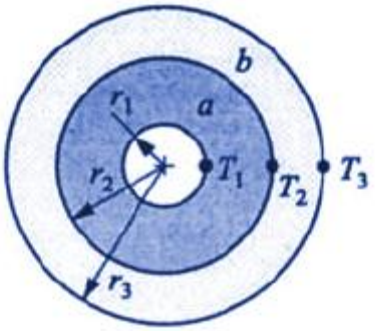


Figure 5-10 Insulated pipe where T3 is the temperature on the outside of the pipe and r3 is the radius of the pipe through all the insulating material. (Engineers Edge 2018).

The equation to calculate the heat transfer rate in the situation shown in figure 5.10 is given by equation 5.3:

$$q = \frac{2\pi L(T_1 - T_3)}{(1/k_a)\ln(r_2/r_1) + (1/k_b)\ln(r_3/r_2)} \tag{5.3}$$

For the steam removal pipe it has a length of 1.5 m an internal diameter of 0.01 m, a thickness of 0.0009 m and an outer diameter of 0.012 m. With steam under 12 Bara, the temperature inside the pipe is 189 C and the outside temperature is 21 C. To test the importance of insulation in this equation, the insulating layer thickness will be increased (r3), showing the change in heat transfer rate as the thickness is increased. The results of this calculated test are demonstrated in figures 5.11 and 5.12 on the next page.

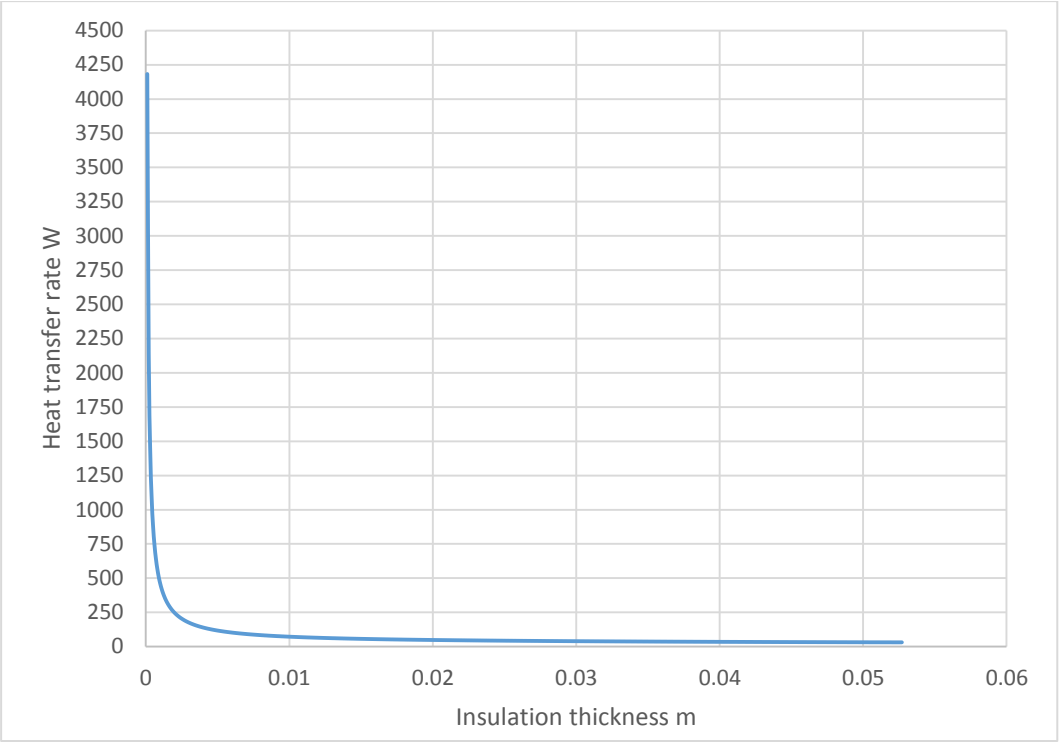


Figure 5-11 Heat transfer rate as the insulation thickness increases

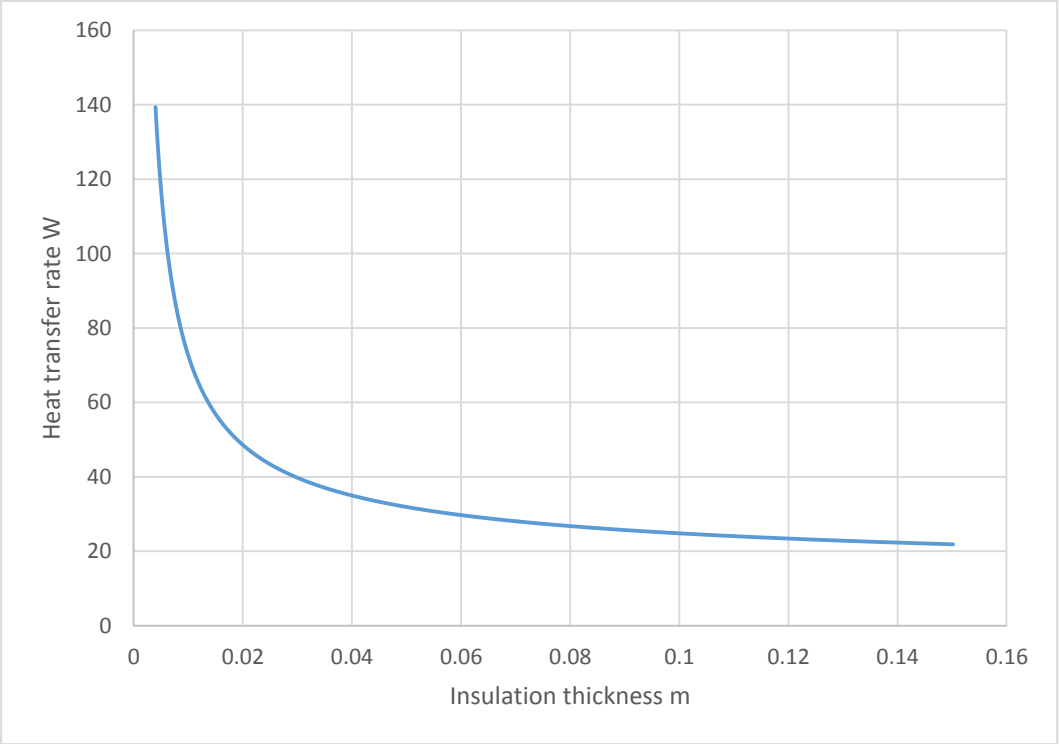


Figure 5-12 Zoomed in change in insulation against heat transfer rate starting with an insulation thickness of 0.004 m.

The evidence shows that a wall thickness of more than 50 mm will be sufficient for the 1.5 m steam pipe outside of the oven.

With this issue covered, in order to further reduce the length of pipe required the condenser was removed from the design and needle valve 2 was replaced with the BPR. This meant steam could slowly be released at the end of testing into the bucket, without the need to recycle the water it did not need condensing and instead would collect in the bucket. Needle valve two was instead used to remove condensed water collecting in the lowest point of the steam removal line after testing had finished. The runoff pipes from needle valve two and needle valve one were connected together and fed to a drain.

Needle valve three had an air bottle attached as explained in section 5.2.1. Figure 5.13 details all the parts located on the left side of the oven in their fully constructed state.



Figure 5-13 Left side of the oven with the steam removal and the injection sections shown

5.3.2 Final Assembly

The test section after being fully connected and heat proofed as detailed in chapter 3, was bolted to the steam and water removal section with a DN50 to DN 100 adaptor pipe. The droplet injector manifold detailed in chapter 4 was then bolted on top of the test section. At this point, each of the droplet injector lines were connected onto the manifold, along with the steam bleed line and the air injection line. This completed the fully assembled test section, the layout of the assembly is shown below in figure 5.14 detailing all the components.

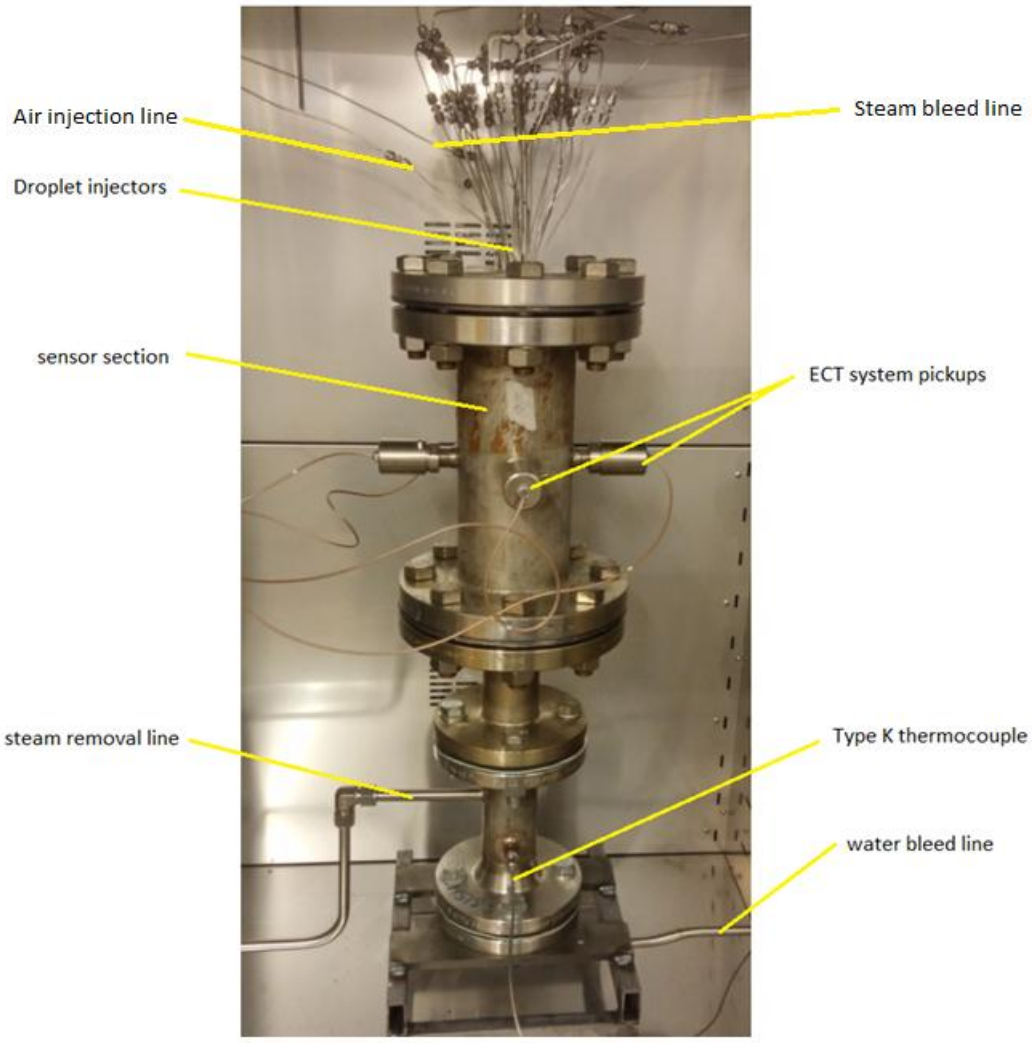


Figure 5-14 Fully assembled rig inside the oven with the ECT system, droplet injection system, air injection system and the water/steam removal section fitted together.

The final components to be detailed are the layout of the completed measurement and recording systems located on the workbench, along with the droplet injection system control valves and the Gilson pump, these are shown in figure 5.15:



Figure 5-15 Test rig workbench setup showing each of the components

5.4 Steam Control within the completed Test Rig

After the test rig had been completed, it was time to calculate the amount of water that the Gilson pump would be injecting initially to produce the correct steam pressure. Due to condensation loss from the steam removal pipe this amount of water would need to be periodically topped up. Therefore the initial water mass required will be calculated from just the total volume including the test section and the steam/water removal section. This gives a total volume of 0.000943 m^3 within the combined sections. Using the target of producing steam under 12 Bara of pressure as an example. The specific volume of steam for 12 bars is 0.163 m^3/kg this means that 1 kg of steam will take up a space of 0.163 m^3 and since 1 kg of water will make 1 kg of steam and the total volume of the test section is 0.000943 m^3, and then the following equation 5.4 will calculate the amount of water required.

$$m = \frac{V}{V_s} \tag{5.4}$$

Therefore the water required inside the test section is 5.79 grams to create a volume of dry steam under 12 Bara of pressure. The following table shows the different masses of water that will initially be required for the three different pressures.

Table 5-1 Different initial masses of water to achieve 10, 11 and 12 Bara of steam pressure

steam pressure (Bara)	Specific volume	mass of water required kg
10	0.194	0.00486
11	0.177	0.00533
12	0.163	0.00579

Since the initial amounts of water for each of the steam pressures will not be enough to reach the required pressure due to condensation within the pipe wall outside the oven, further amounts of liquid will be injected at intervals when it can be seen on the pressure monitor that the pressure has levelled off. The steam pressure can then be further controlled by letting excess steam out using the back pressure regulator to reach the exact pressure required.

5.5 Conclusions

The work in this chapter was developed alongside the work detailed in chapters 3 and 4, and represents the unification of the ECT system with the droplet injection system inside the previously explained test rig.

Different designs of the test rig were investigated where two different heating systems were presented. It was shown that heating the testing section with heating tape or keeping it hot with a heating blanket was impractical and increased the risk of non-uniform heating, leading to the production of a film of liquid on the electrodes. To prevent this, the heating system selected was to use an oven that would heat the entire section continuously, making film production not an issue.

The rig was built to specification with the test section pressure tested to 20 Bara to comply with European health and safety for pressure vessels. This meant the rig was safe to use for testing steam and water mixtures up to 12 Bara of steam pressure.

It has been shown that the issue of steam condensing in the pipe outside the oven is not a problem, as it was investigated and found that 50mm of insulation would slow the condensation to the point where the steam pressure could be maintained.

The test rig was now able to begin major testing, this work and an explanation of the testing procedure are detailed in the following chapter.

Chapter 6. Results, Analysis and Comparisons

Nomenclature

f_s Sampling rate (samples/sec

N Number of time samples

t_n Nth sampling instant (sec)

T Sampling interval (sec)

ω_k Kth frequency sample (rad/sec)

ω Angular frequency

$X(\omega_k)$ Spectrum of x, at different frequencies

$x(t_n)$ Input signal amplitude

X_k Discrete Fourier Transform

ε_0 Vacuum permittivity

ε_1 Permittivity of water

ε_2 Permittivity of steam

ε_s Static relative permittivity

ε_∞ Absolute relative permittivity

ε'' Loss factor

τ Relaxation time

This chapter details the results using the test rig that was discussed within chapters 4 and 5. An overview of how the tests were carried out is discussed. Highlighting the problems that arose from the testing, and how these problems showed which results could be used in the final statistical analysis.

The tests were all carried out using the ECT sensor in chapter 3, whereby the results given are for a four electrode system, which when the reversed electrode pair measurements are included e.g. (1, 2) and (2, 1), gives a total of 12 electrode pair measurements. This allowed for further analysis to see if the results don't change between reversed electrode pairs.

It was discovered after testing that some of the capacitance signals from electrode pairs had a small amount of random fluctuations. Attempts to find the frequency of the noise were explored using the Fast Fourier Transform (FFT) technique were unsuccessful, but they did yield evidence that there was no underlying signal producing the noise, and that all the results have a DC signal.

The data for the opposite electrode pairs will be compared against the parallel and droplet model to demonstrate that in keeping with previous

experimental observations the steam and water results show good correlation to the parallel model, while the air and water results correlate more to the droplet model, when seven droplets of water is injected into the same area of the sensor. It is important to note however, that at this stage the correlation is inconclusive as it cannot be guaranteed that the correct number of droplets fell at once through the sensor, it could only be guaranteed that the amounts fell in the same section. Therefore the tests will also be repeated with a set volume of liquid using only one droplet. If it is found that the results are better predicted by the droplet model then there is an indication that the spatial positioning of water within the steam is affecting the relative permittivity measurement between opposite electrode pairs.

The results were compared against the relative permittivity calculated from the 3D capacitance program, the model showed poor correlation between the predicted change in relative permittivity and the change for one droplet injected.

The images matched well the predetermined areas of high water concentration. This gave further evidence that the spatial positioning of the water was having an effect on the measurement for adjacent electrode pairs.

The chapter is broken down into the following sections:

6.1 The Testing Schedule

Overview of the testing procedure with an explanation of how each stage of the testing will be carried out.

6.2 Calibration of the ECT sensor

Discussion on how the ECT sensor was calibrated, the problems that arose and how they were dealt with.

6.3 Raw Capacitance measurements

Details of how the raw data was laid out for the results of each test and an explanation of the evidence showing how results from electrode pairs (1, 4), (2, 4) and (3, 4) was corrupted.

6.4 Fast Fourier Transform of the Data

Analysis of the raw capacitance data from each test using the Fast Fourier Transform (FFT) to determine if there was any noise present within the signal.

6.5 Linear Drift Correction

Explanation of how the capacitance data was converted to relative permittivity, taking into account the drift over the testing days

6.6 Analysis of the linearly corrected relative permittivity results

Details of the statistical analysis of the relative permittivity results from the uncorrupted electrode pairs (why steam is close to the parallel model, average results, integral results).

6.7 Comparison of relative permittivity measurements to the Parallel and Droplet models

Overview of how the experimental data for a droplet injected in the centre and areas A, B, C, and D compares to the predicted results using the droplet and parallel model.

6.8 Comparison to the results from the 3D Capacitance Program

Discussion of the results from the 3D capacitance program and how they compare to the experimental data for one droplet injected in the centre and areas A, B, C, and D.

6.9 Spatial Position Imaging

Images of the spatial positioning tests produced using the linear back projection program.

6.1 The Testing Procedure

The testing procedure is to determine the effect of the spatial positioning of the water on the relative permittivity measurement between electrode pairs, when droplets are injected into different regions of the sensor. Figure 4.25 shows the defined regions of the sensor, whereby equal amounts of droplets can be injected.

In order to allow the regions labelled A, B, C and D to show the effect on opposite pairs and adjacent electrode pairs, droplets must be injected into single and combinations of regions. The total number of combinations with four regions that is required is 10 with an 11^{th} central injection test, this will allow for five different amounts of droplets to be injected into the sensor, as well as being able test the effect of the moisture content being placed in each quarter of the sensor and the moisture content being placed in different halves of the sensor. Figure 6.1 demonstrates the 11 different injection patterns that will be used for the testing.

The injection patterns shown in figure 6.1 on the next page do not include testing in regions AC or BD; this is because there are already enough combinations to determine the effect of spatial positioning on adjacent electrode pairs. As for the opposite electrode pairs, the effect of spatial positioning can be shown by comparing between injecting in AB and in injecting BC, or vice versa with AD and CD.

Therefore the goal with this testing is to show that the relative permittivity measurement between electrode pairs does not change as the same amount of water is injected into different regions of the sensor, thus showing that spatial positioning does not affect the measurement. This measurement is crucial because if the relative permittivity measurement changes for adjacent electrode pairs and does not change for opposite electrode pairs, then it means that the cross section of the two phase flow can be imaged and the volume fraction and hence the wetness can be determined accurately with the opposite electrode pairs.

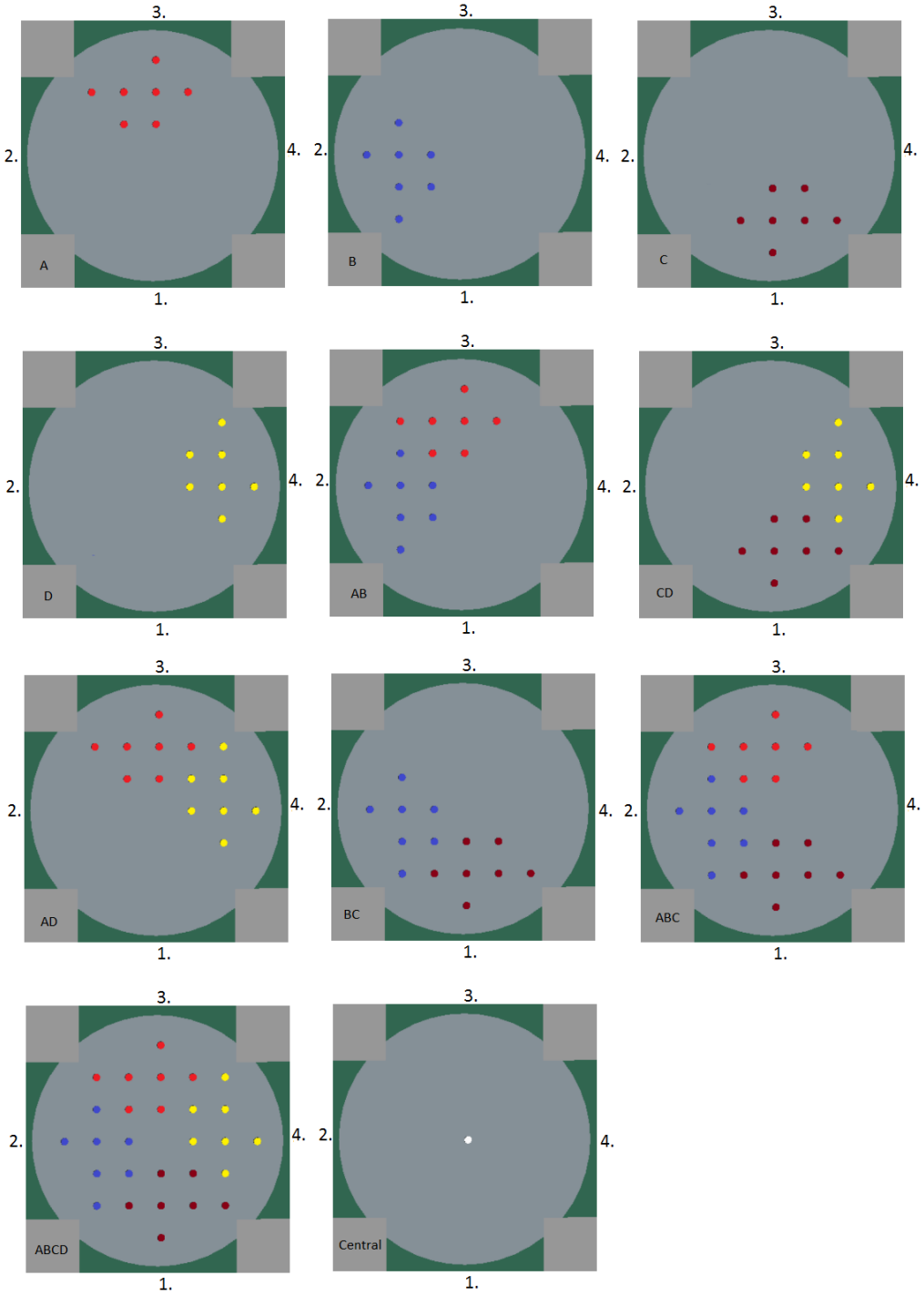


Figure 6-1 The 11 different injection patterns, red denotes region A, blue denotes region B, brown denotes region C and yellow denotes region D.

Once the injection pattern for each of the different tests was determined, a testing time was required. Each test was set to last 1 minute to negate the effect of drift on the rate of change. The first 20 seconds are used to determine a baseline by just having superheated steam within the test

section, this is so linear drift between tests can be accounted for by setting the average relative permittivity of the baseline to the calculated relative permittivity of the superheated steam, this will be explained more in section 6.5. The next 20 seconds of the tests will consist of the injection time, this will show on the trace as a clear area of time where droplets were injected. For the final 20 seconds the pump will be stopped, allowing for the droplet to come to a halt. Details of the testing process will be discussed in depth with example data in section 6.3. The next step is to calibrate the sensor by expanding upon the principles discussed in section 3.1.3. This will be explained within the following section.

6.2 Calibration of the ECT sensor

During the testing period, the calibration of the ECT sensor took place on the testing rig. The standard method of calibration is to fill the sensor with air and read the capacitance to give a baseline value for a relative permittivity of 1; then the sensor is filled with the high permittivity material water giving the maximum capacitance reading. Using the linear relationship shown in equation 3.6, any recording of capacitance in testing can then be linearly converted to a value of relative permittivity.

For this testing procedure two problems were apparent; it was not possible to fill the sensor with water and secondly, due to the extremely small values of the relative permittivity of superheated steam to maintain accuracy the high permittivity material had to have a relative permittivity less than 2. To overcome these problems linear regression modelling was used to build a picture of the relationship between the change in capacitance and the change in relative permittivity.

Compression of the PTFE could force some electrodes closer together while other might become further apart. Therefore this calibration procedure also checks and determines the sensitivity of each of the electrode pairs, as the electrode pairs might not be as similar as they appear.

The first step in forming a regression model for each electrode pair is to decide what variable to change in the testing material, that will only increase or decrease the relative permittivity steadily over time. Using IAPWS – 97, the relative permittivity of superheated steam could be easily determined from measurements of the steam's pressure and temperature, therefore this testing material was ideal to use, as the test rig could manipulate the steam pressure or temperature as desired. For the control variable, ether temperature or pressure could be changed, however it first had to be determined that the changes caused by either of these variables were detectable by the sensor, by the change being larger than the RMS noise calculated in chapter 3. Figure 6.2 and 6.3 shows the modelled changes in relative permittivity of steam by changing temperature and pressure respectively.

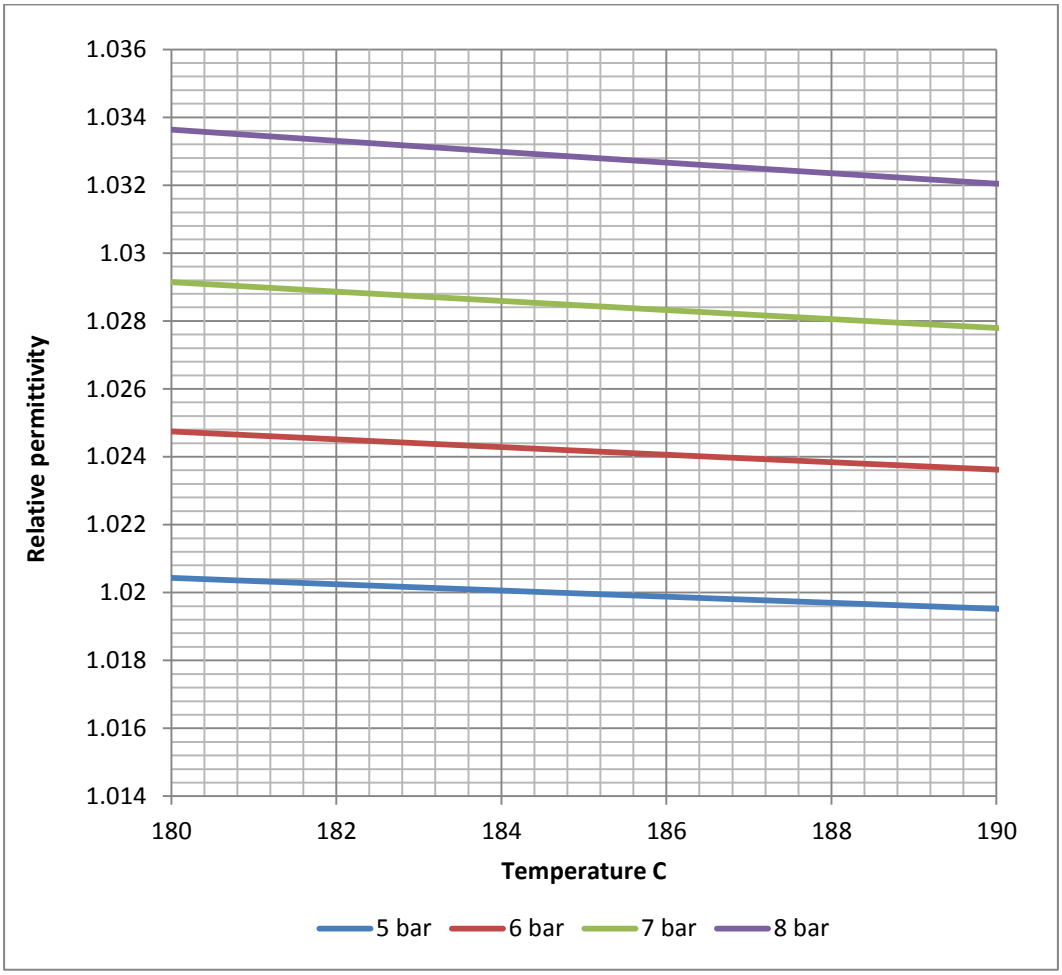


Figure 6-2 Relative permittivity change with temperature at constant pressures

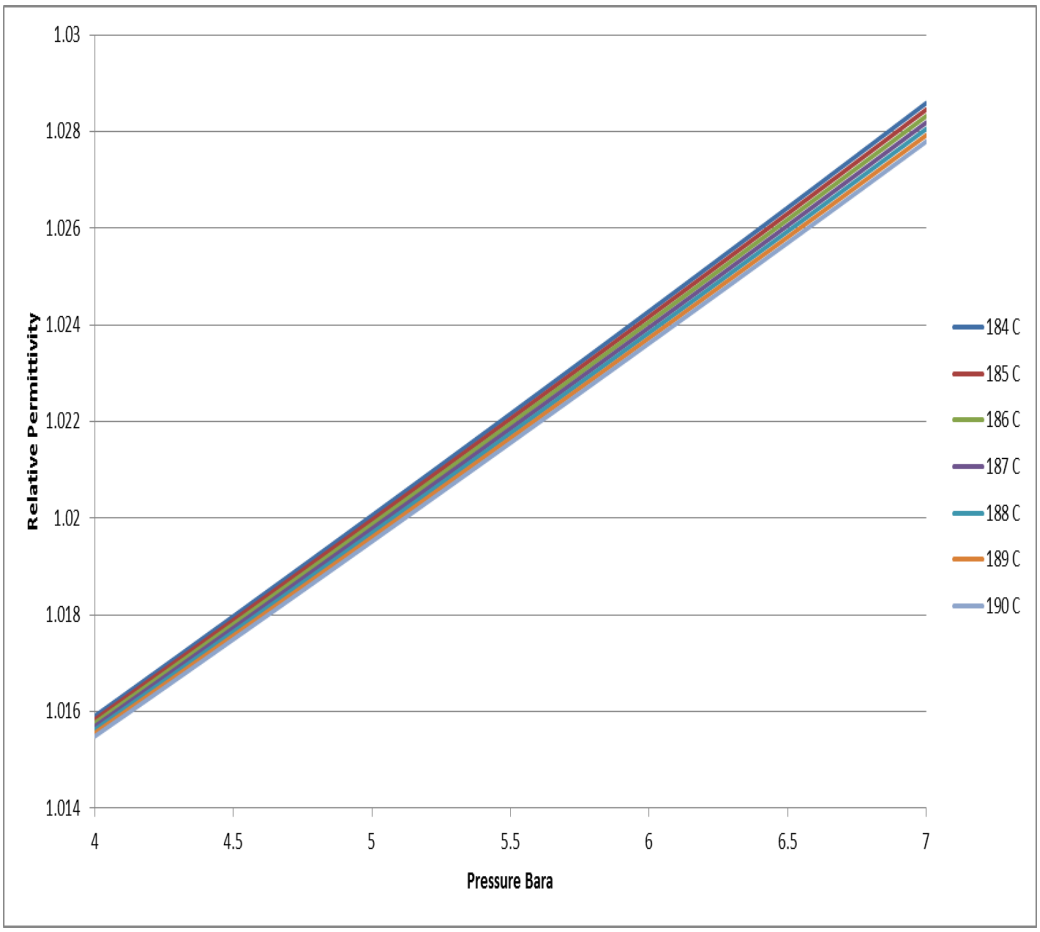


Figure 6-3 Relative permittivity change with pressure at constant temperature

The graph figure 6.3 demonstrates the change in relative permittivity if just temperature is changed, varies by less than 0.001, but if just pressure is changed the variation is under 0.01. Due to pressure change being easier to detect, this was the control variable that was selected.

To recreate this pressure change on the actual rig, superheated steam at 185°C was contained within the sensor under 7 Bara, then the steam was allowed to condense within the pipe outside the oven leading to the back pressure regulator. Two of the tests were run with the steam dropping purely due to the condensation. However on the other two tests the back pressure regulator was required to control the pressure drop, the results from those

have been included to demonstrate the differences and what effect this had on the regression modelling.

This side effect was only apparent during calibration as in normal testing the steam is heated within the test rig throughout the day and is not released until the end of testing. While in calibration steam is released after each test, and this means water has to be reinjected to build the pressure back up. After a few cycles the steam in the unheated pipe is not hot enough to maintain pressure for very long without condensing and so the pressure drops quicker. Figure 6.4 shows the pressure change recorded every second for the four tests.

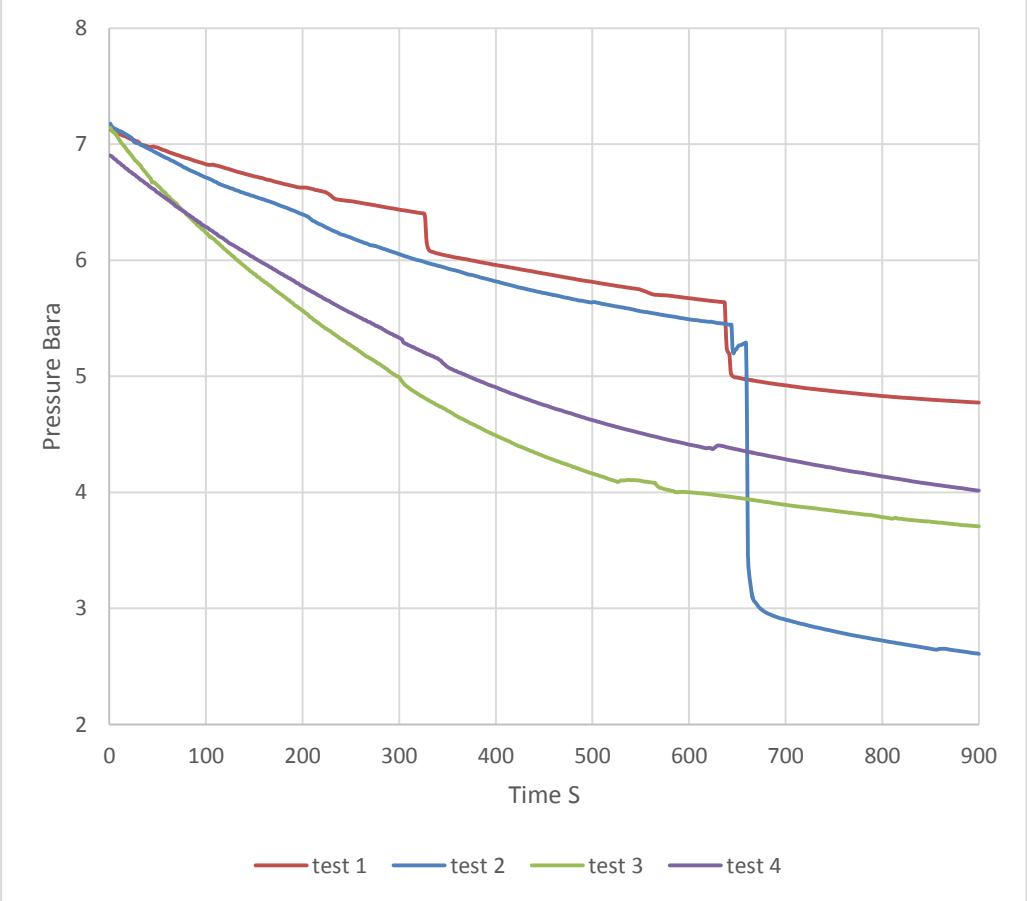


Figure 6-4 Pressure change during testing, where test 1 and 2 are the ones where the back pressure regulator was used and 3 and 4 are where the steam was left to condense

Using the sensor a recording rate of 1000 Hz was chosen due to previous testing (Barham 2013) showing that recording at the maximum rate of 5000 Hz increases the noise. Against the pressure and temperature, the capacitance was recorded over a 15 minute period for the four tests.

It was discovered at this point that there were high amounts of noise with electrode pairs that included electrode 4, this will be discussed in more detail within the next section. Concentrating on the unaffected pairs figure 6.5 shows the recorded capacitances for the opposite electrode (1, 3).

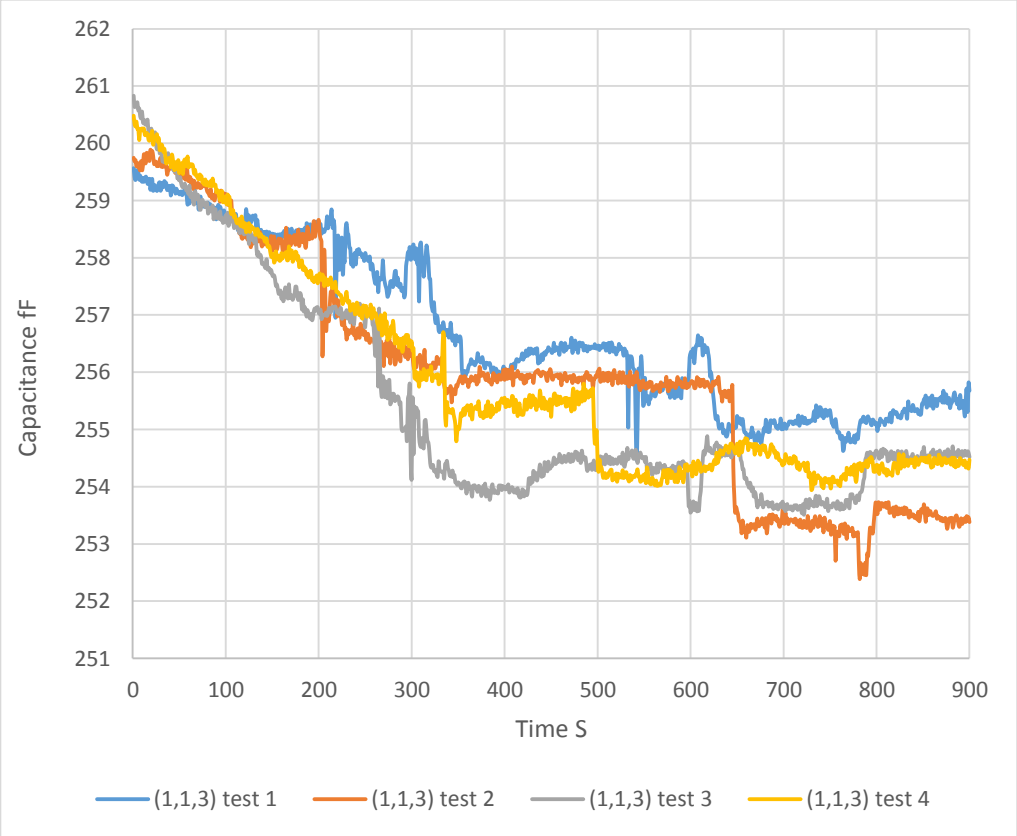


Figure 6-5 Capacitance recording for the four tests using electrode pair (1, 3), where the first number denotes the circuit used in the recording system

The trace shown above shows the small difference between the capacitances recorded over 15 minute test period. Test 1 and test 2 indicate the sudden drop in pressure due to opening the pressure relief valve. Tests 3 and 4 have a moderate amount of noise but have very similar traces as the

steam was slowly condensed, figure 6.6 shows the capacitance recordings from the adjacent electrode pair (2, 3).

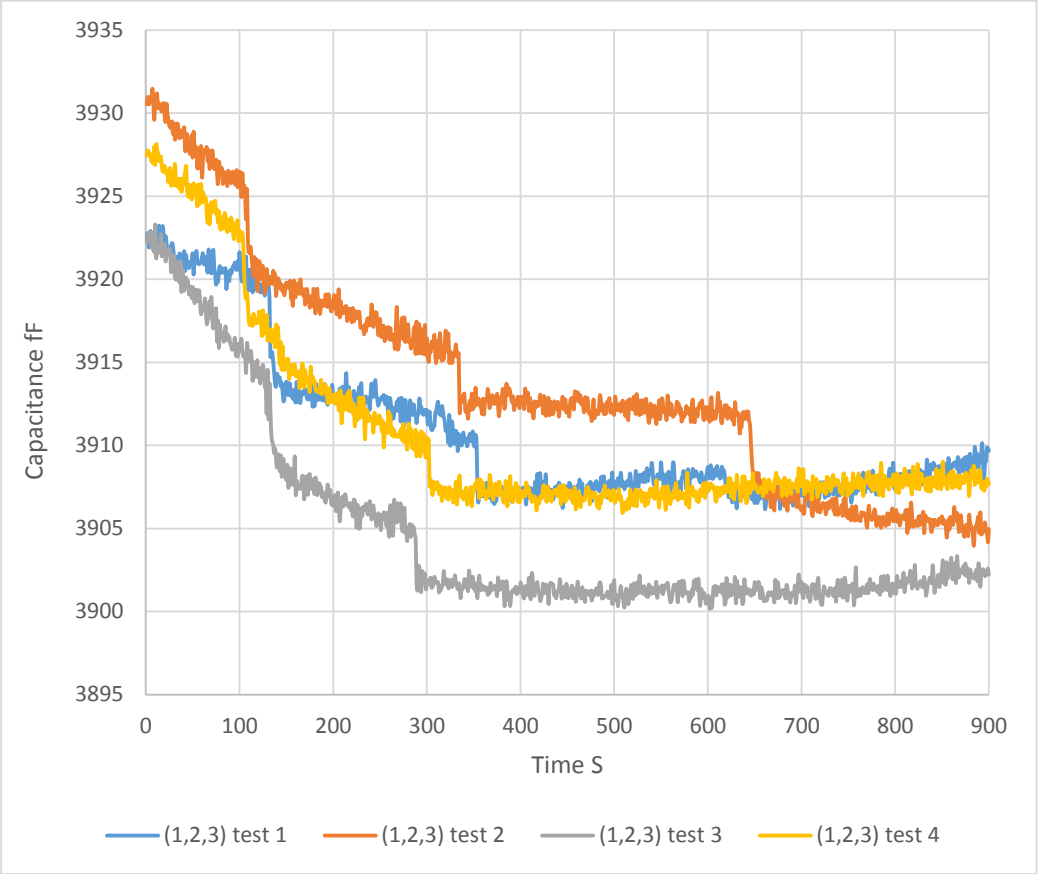


Figure 6-6 Capacitance recording for the four tests using electrode pair (2, 3)

In this trace the differences between the two groups of tests are more apparent than before. The patterns observed on the opposite electrode trace can be seen with less noise and there is less variation in the capacitance over 300 seconds.

In total 12 capacitance traces (one for each of the electrode pairs) were produced for each test, two of these were given as examples in figures 6.5 and 6.6. The relative permittivity of the superheated steam over the 15 minute testing period for each test was derived from the pressure and temperature recorded every second. Therefore the calculated relative permittivities could be plotted against the capacitance measured every second for each electrode pair. On the next pages in figures 6.7 and 6.8 is an example using test 3, of the capacitance plotted against the relative

permittivity for all 12 electrode pairs. The plots for the other 3 tests can be found in the appendix.

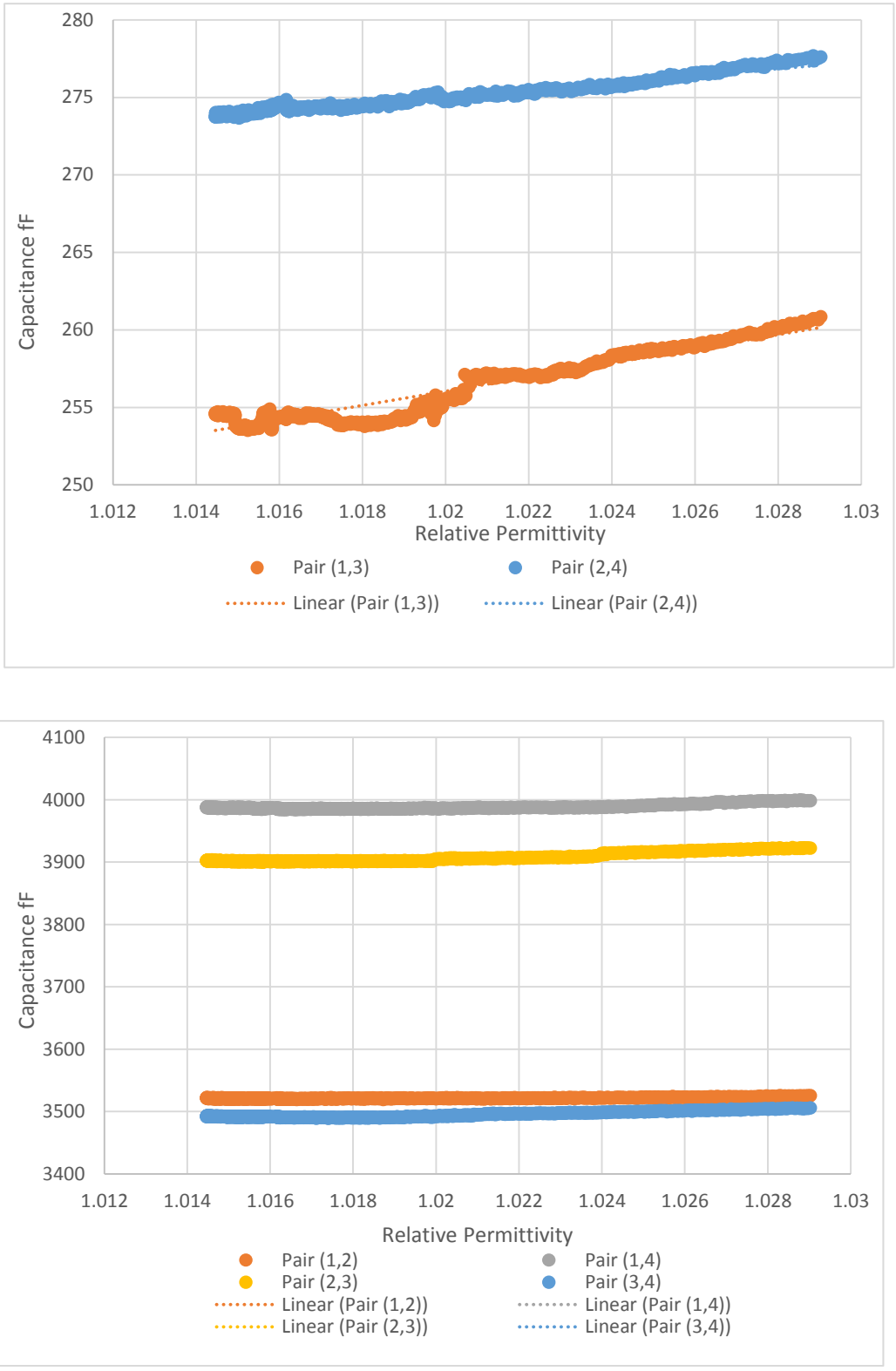


Figure 6-7 Capacitance plotted against calculated relative permittivity for non-reversed opposite and adjacent electrode pairs using IAPWS -97

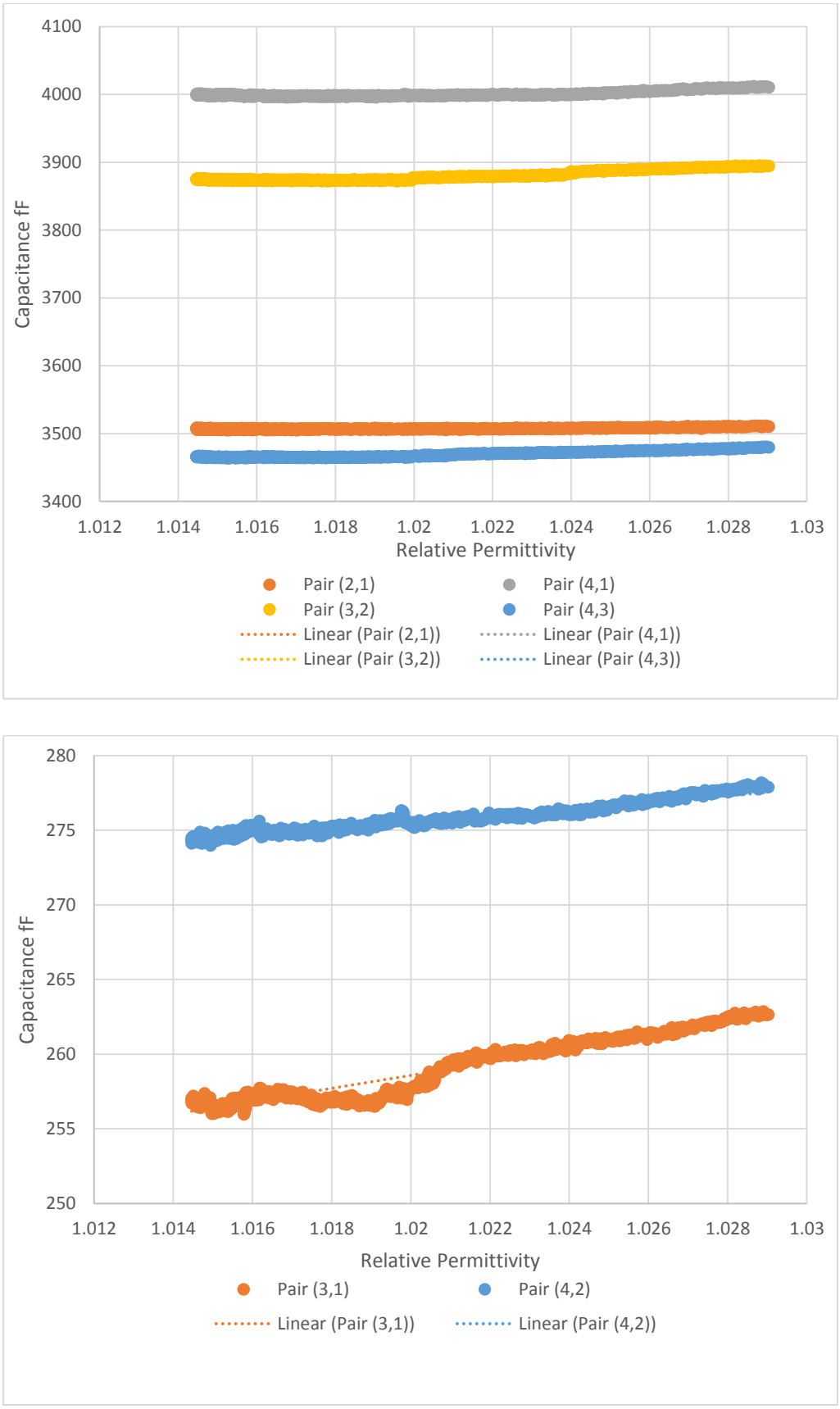


Figure 6-8 Capacitance plotted against calculated relative permittivity for reversed opposite and adjacent electrode pairs using IAPWS -97

For each of the plots shown in appendix 2 and figures 6.7 and 6.8 a linear regression curve was constructed that modelled how much the relative permittivity changed relative to capacitance change. Table 6.1 details the gradients of the models for each electrode pair and table 6.2 details the y intercept.

Table 6-1 Gradients for each regression model for each electrode pair

Test	(1,2)	(1,3)	(1,4)	(2,3)	(2,4)	(3,4)
1	8.5407	426.45	330.32	1154.3	207.87	719.17
2	445.22	293.48	577.29	958.97	262.44	670.66
3	190.98	456.16	568.46	1374.8	224.65	896.43
4	-11.275	527.57	11.881	1503.1	205.11	899.65
Test	(2,1)	(3,1)	(3,2)	(4,1)	(4,2)	(4,3)
1	49.967	458.02	1106.1	353.16	218.73	727.66
2	422.3	382.21	719.03	616.86	262.34	719.03
3	197.6	433.7	1327.5	545.56	214.65	916.11
4	9.9338	489.51	1477.5	107.81	207.37	874.46

Table 6-2 Y intercepts for each regression model for each electrode pair

Test	(1,2)	(1,3)	(1,4)	(2,3)	(2,4)	(3,4)
1	3517.5	-179.81	3656	2729.3	62.91	2762.7
2	3073.9	-43.655	3406.3	2934.8	7.3905	2815.7
3	3326.6	-209.24	3408.2	2504.2	45.911	2580.3
4	3536.7	-282.18	3894.3	2375.8	65.94	2581.2
Test	(2,1)	(3,1)	(3,2)	(4,1)	(4,2)	(4,3)
1	3460.6	-209.26	2750.8	3644.4	52.463	2727.2
2	3083.2	-131.22	2904.6	3377.4	8.0887	2740.7
3	3305.6	-183.79	2524.7	3443.5	56.65	2534.1
4	3501.4	-240.59	2375.8	3894.3	64.211	2581.2

The important part at this stage is to determine how repeatable the curve is, hence the most important aspect is the gradient as that will tell the sensitivity of the electrode pair and if it is repeatedly that sensitive.

Performing an F test on the gradients shown in table 6.1, showed the variance between the gradients and if any were significant differences to the rest. For most of the electrode pairs test 2 gave gradients that were significantly different from the rest of the results, indicating that the large drop in pressure caused by opening the back pressure regulator had affected the calibration for that test.

For all the electrode pairs the most outlying result was removed, then combining the average gradient and the average y intercept from the 185 C range tests gave the average regression model that controlled how capacitance is converted to relative permittivity. Table 6.3 below shows the final regression model equation for each electrode pair.

Table 6-3 Regression model equation for each electrode pair

(1,2)	(1,3)	(1,4)	(2,3)	(2,4)	(3,4)
158.366x + 3363.675	425.915x - 178.721	371.988x + 3591.2	1247.793x + 2636.025	225.0175x + 45.538	796.478x + 2684.975

(2,1)	(3,1)	(3,2)	(4,1)	(4,2)	(4,3)
169.95x + 3337.7	440.86x - 191.215	1157.533x + 2638.975	405.848x + 3589.9	225.773x + 45.353	809.315x + 2645.8

These final regression models take into account the variation due to noise between each test and the fluctuating sensitivity on each electrode pair. Drift is not important for this calibration as the readings were taken over a short space of time where the effect of drift would have been negligible. It was not required to repeat the procedure on different days as rate of change is repeatedly accurate with the ECT sensor. The absolute capacitance values would have altered but it is only the rate of change that is required.

The equations for each electrode pair will be used in the final testing to convert the capacitance to relative permittivity. The next section will now discuss the raw capacitance testing data.

6.3 Raw Capacitance Measurements

Before the data is converted to a trace in the change in relative permittivity using the equations in table 6.3, an overview of the raw capacitance data is required to determine if the testing procedure went to plan and if any consistent errors are present. At this stage measurements from different electrode pairs cannot be compared against each other, since they have not been converted to relative permittivity the measurements will still be biased by the sensitivity of their respective electrode pairs. An example of a raw capacitance trace using electrode pair (2, 3) for droplets being injected into section A in shown in figure 6.9, detailing the different sections of testing.

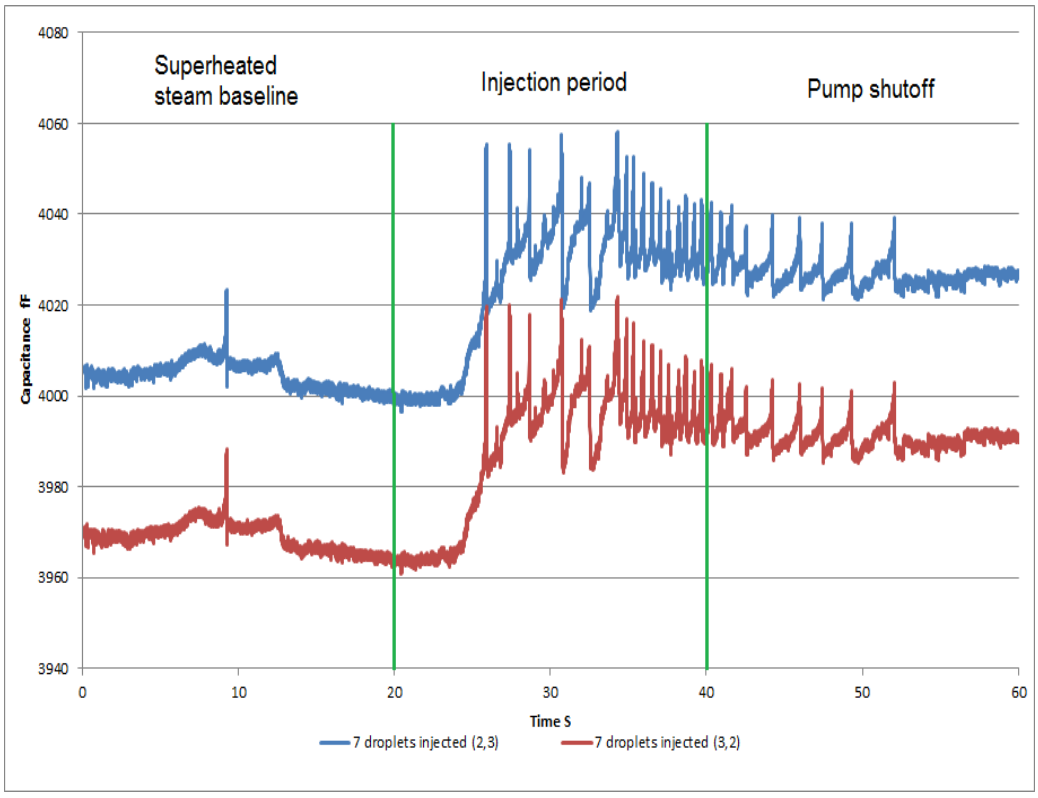


Figure 6-9 Capacitance measurement trace for electrode pair (2, 3) and (3, 2), for droplets injected in section A into superheated steam under 10 Bara, detailing the three parts of the tests.

This example clearly defines where injection started and how long it took the droplets to stop dripping after the pump was turned off. It also

demonstrates the time it takes for the water to start injecting into the test section, which was approximately 5 seconds.

The baseline section shown in figure 6.9 is a typical result from electrode pairs (1, 2), (1, 3), (2, 3) and the reversed pairs, (2, 1), (3, 1) and (3, 2). However for the other six electrode pairs of which all of them included electrode 4, their baseline and results had moderate noise present in a few of the results, notably these this was mostly found on electrode pairs (1, 4) and (4, 1). Figure 6.10 gives an example of the noise present in one of the tests for these electrode pairs, shown by the large variation in the baseline.

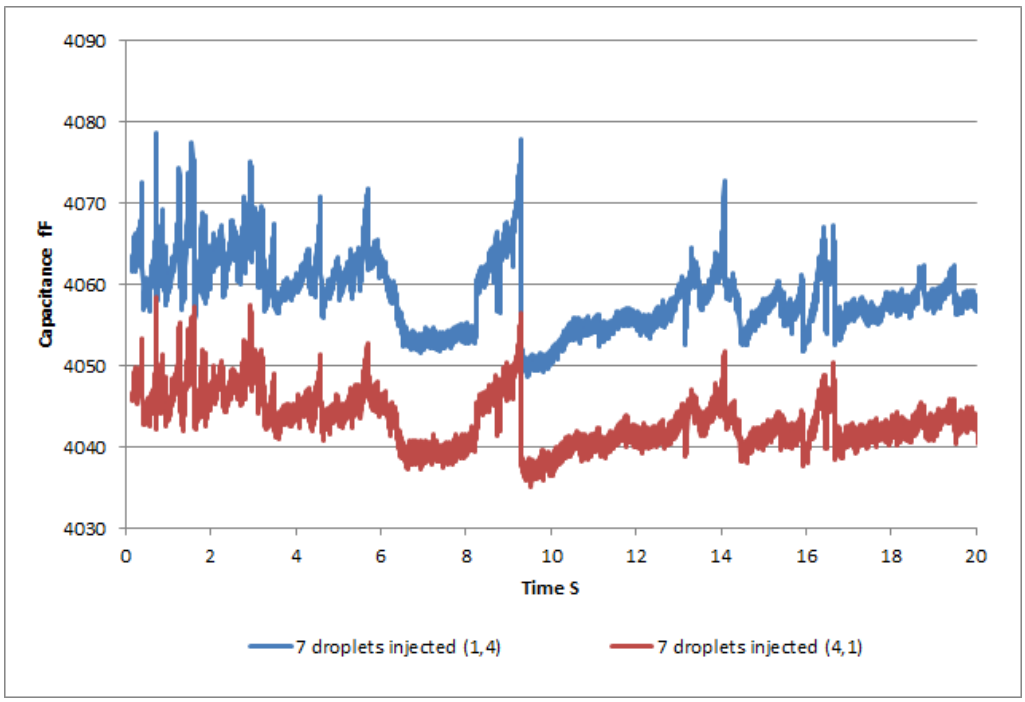


Figure 6-10 Corrupted capacitance measurement example using the result from electrode pair (1, 4) and (4, 1) for droplets being injected into section A in 10 Bara

To investigate if this problem was present in all the tests for these electrode pairs, the variance of the baseline was measured for all tests at all three pressures. The results are shown in figure 6.11 on the next page, with the error bars being the standard deviation of variance.

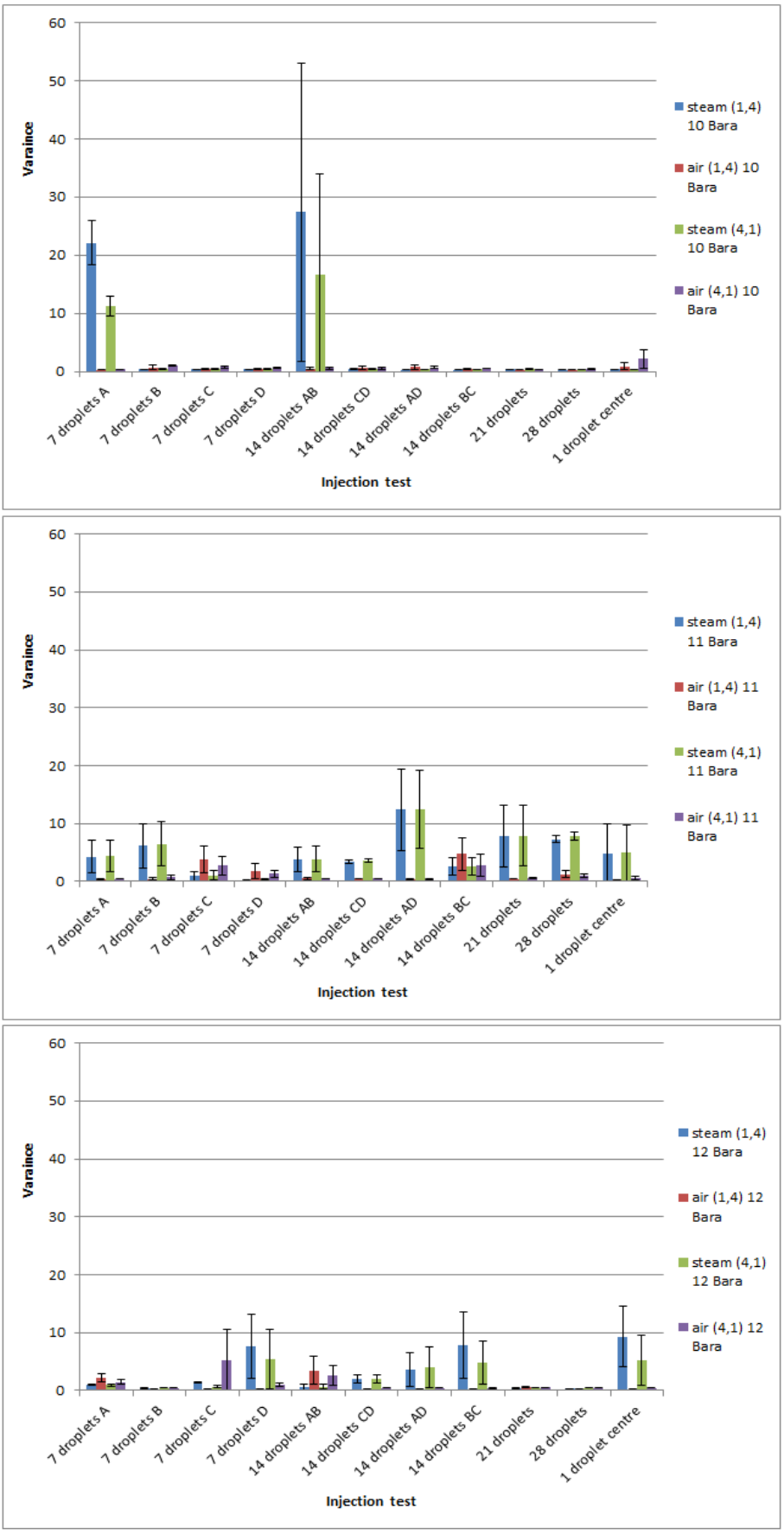


Figure 6-11 Variance for electrode pairs (1, 4) and (4, 1) baseline

The high variance for the electrode pairs is only in 2 tests under 10 Bara. Two theories were thought to be the route of the problem, firstly a faulty ball valve could be letting water into other injection areas, or secondly there was an underlying signal of noise within the measurement that could be removed. The first theory was shown to be incorrect, as the ball valves were tested and found not to be malfunctioning. The second theory required a more detailed analysis, this is discussed in the next section.

6.4 Fast Fourier Transform of the Data

The fast Fourier Transform is a useful tool to analyse the components of a composite signal to find the frequencies of the component signals. The basic continuous Fourier transform is described by equation 6.1:

$$F(\omega) = \int_{-\infty}^{\infty} f(x) e^{-i\omega x}\, dx$$

(6.1)

When the equation is discrete and periodic, the discrete Fourier transform is used instead, called the DFT. The DFT uses a finite summation, this removes the infinite integral. The discrete Fourier transform is given by equation 6.2:

$$X(\omega_k) = \sum_{n=0}^{N-1} x(t_n) e^{-i\omega_k t_n} \qquad k = 0, 1, 2, \ldots \ldots N-1$$

(6.2)

This can be simplified down to become:

$$X_k = \sum_{n=0}^{N-1} x_n e^{-\frac{2\pi i}{N} nk} \qquad k = 0, 1, 2, \ldots \ldots N-1$$

(6.3)

The fast Fourier transform is a quicker way of calculating the DFT. The most common algorithm of the FFT is called the Cooley-Tukey FFT algorithm

(Heckbert 1998). This algorithm splits the DFT into two rational parts each of size N/2. This method of the algorithm called the radix-2 decimation in time (DIT) rearranges the split DFT into one part even numbered indices $n = 2m$ and one part of odd number indices $n = 2m + 1$. Therefore equation 6.4 shows the split DFT in the new form of the radix-2 decimation DIT.

$$X_k = \sum_{m=0}^{N/2-1} x_{2m} e^{-\frac{2\pi i}{N/2}mk} + e^{-\frac{2\pi i}{N}k} \sum_{m=0}^{N/2-1} x_{2m+1} e^{-\frac{2\pi i}{N/2}mk}$$

(6.4)

By simplifying further where the even part is represented by E_k and the odd component is represented by O_k the final form of the FFT algorithm is obtained as shown by equation 6.5.

$$X_k = E_k + e^{-\frac{2\pi i}{N}k} O_k$$

(6.5)

What makes the FFT so quick is that at the same time as X_k is calculated $X_{k+N/2}$ can also be calculated simultaneously, this is calculated using equation 6.6:

$$X_{k+N/2} = E_k - e^{-\frac{2\pi i}{N}k} O_k$$

(6.6)

On Matlab, the Cooley-Tukey FFT algorithm is computed using equations 6.5 and 6.6, as is located in a pre-made program called FFT. This program was used to check the raw capacitance data for any component signals with a given frequency that could be adding noise to the data. Using the signal shown in figure 6.8 as an example, a zoomed in 2 second plot of the baseline is shown in figure 6.12 below. It appears that there is no natural harmonic to the data and that the raw capacitance varies by a random amount every frame.

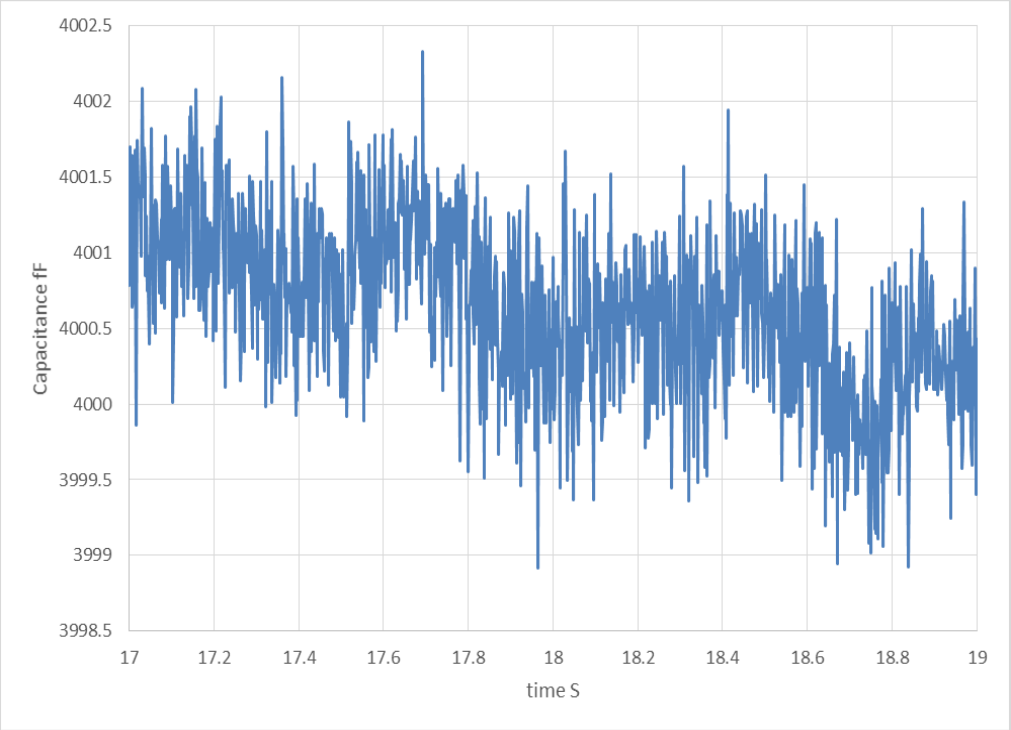


Figure 6-12 baseline for steam under 10 Bara for pair (2, 3) for 2 seconds

To test that the FFT code is working fine, an example signal is required with a known output. Using the example from matlab as a guide, the following signal is produced.

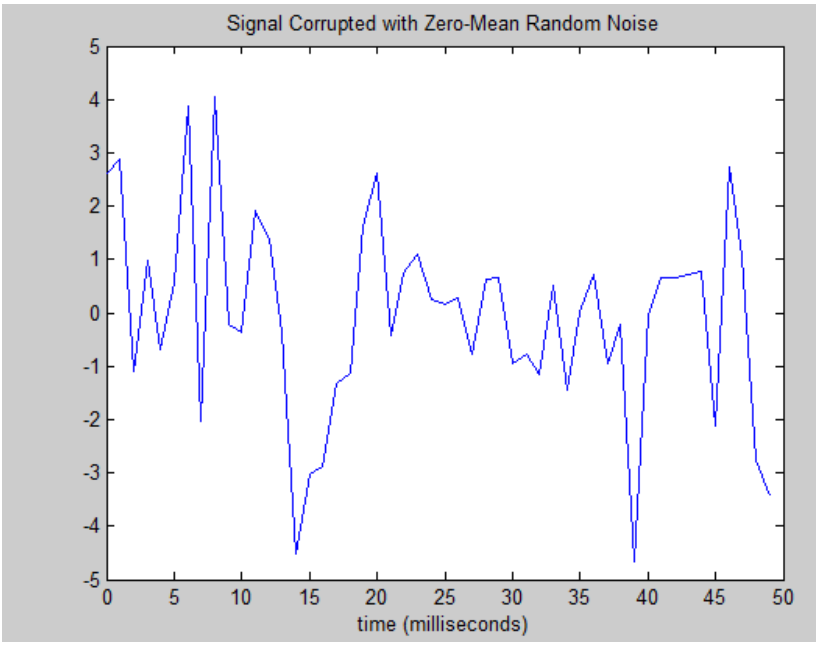


Figure 6-13 Example signal containing a 50 Hz sinusoid of amplitude 0.7 and a 120 Hz sinusoid of amplitude 1 with random noise added

The Fourier transform of the signal shown in figure 6.14 clearly shows where the two sinusoid waves are found.

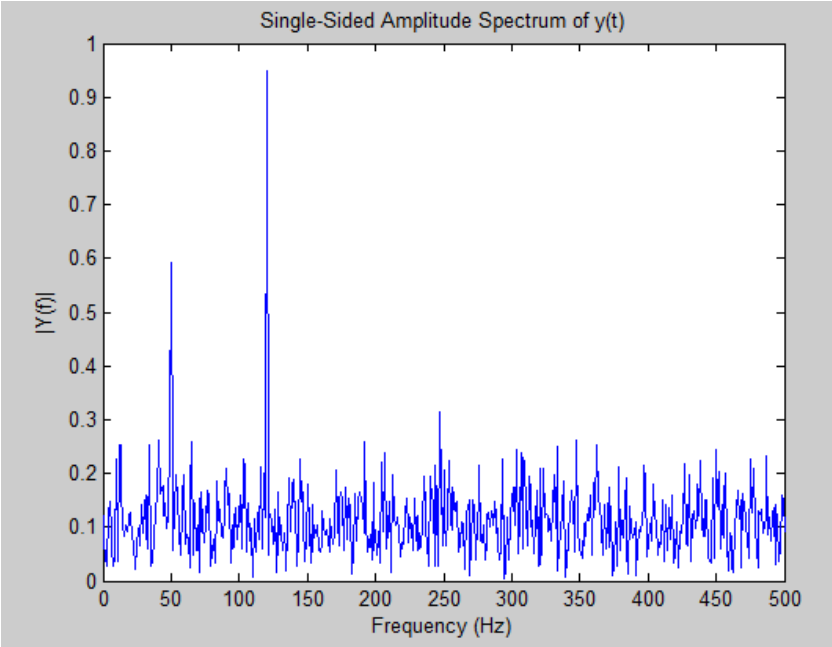


Figure 6-14 FFT of the signal in figure 2, showing the two waves at frequency of 50 Hz and 120 Hz

The code can then be adapted to show the reliability, this time a 50, 120 340 and 450 Hz sinusoid waves were added together with random noise, the amplitudes were 0.9 and 1 for the added waves respectively.

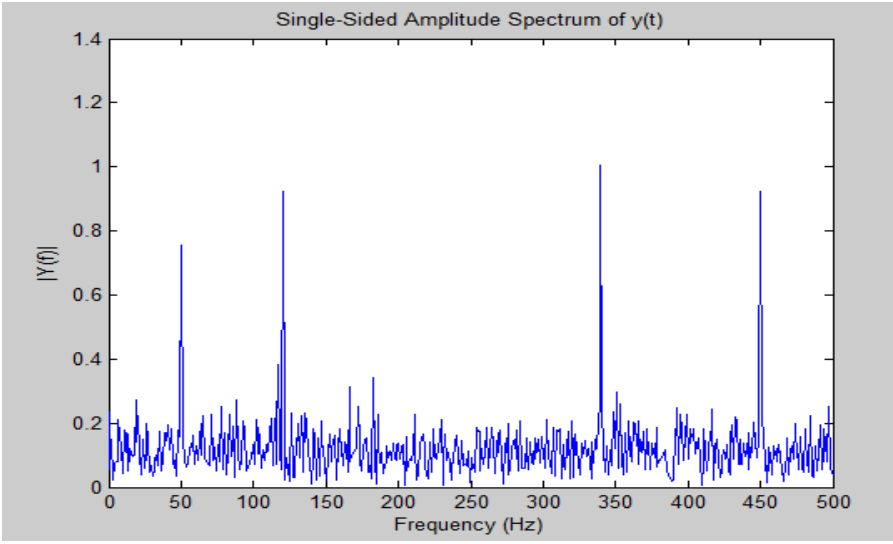


Figure 6-15 FFT of the modified signal with the additional sinusoidal waves at 340 and 450 Hz.

The final point to test is the modification of N, which gives the number of sampling points. The effect of changing N from 1000 to 100000 is given in figure 6.16.

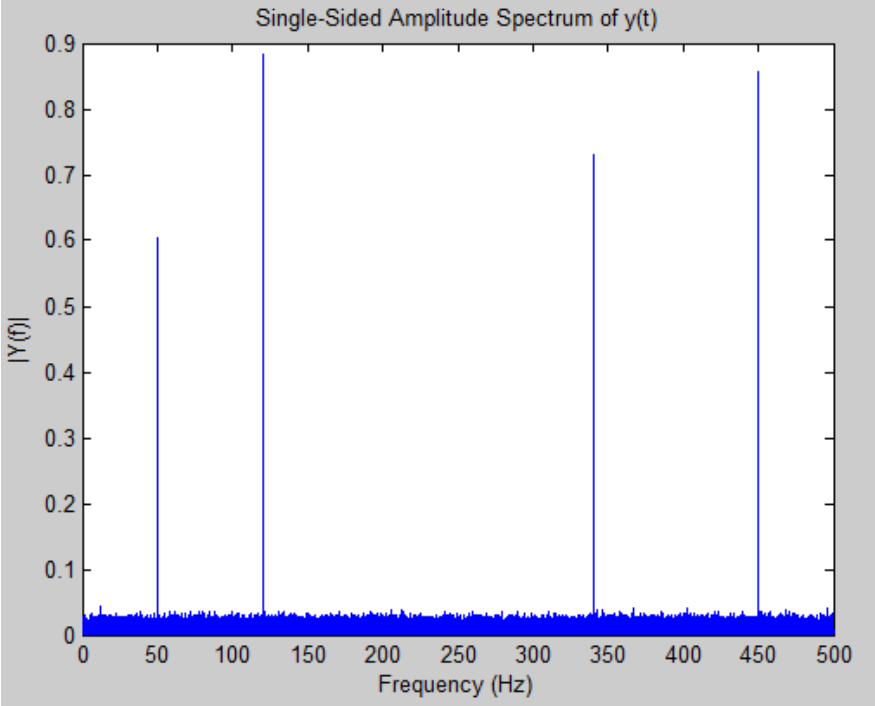


Figure 6-16 FFT of the signal with an increased number of sampling points caused by increasing N to 100000

The results shows that by increasing N improves the FFT clarity, and that the code produces repeatable, correct results of artificial data. The code was then used on all the data to if any noise was present. The results of this work showed that in all the tests there was no underlying noisy signal, the fluctuations seen in figure 6.9 were due to random noise. An example of the FFT result that was common for all the tests is shown in figure 6.17, using the signal from figure 6.7.

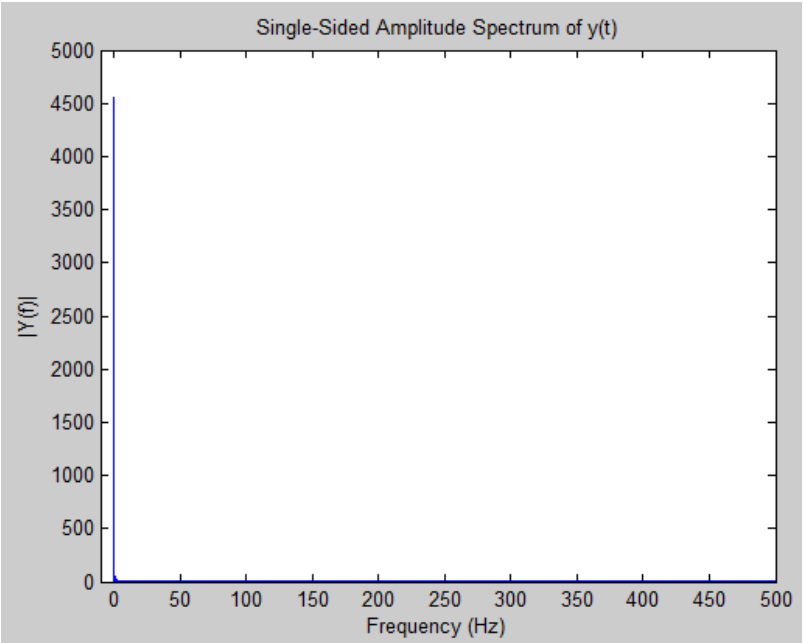


Figure 6-17 FFT result from the raw capacitance data of 7 droplets injected into section A under 10 Bara

There is a single spike at 2 Hz and no harmonic frequencies within the data. To test this is the case, a sinusoidal wave as noise with a frequency of 400 Hz and an amplitude of 3000 will be introduced. The FFT of this result is shown below in figure 6.18.

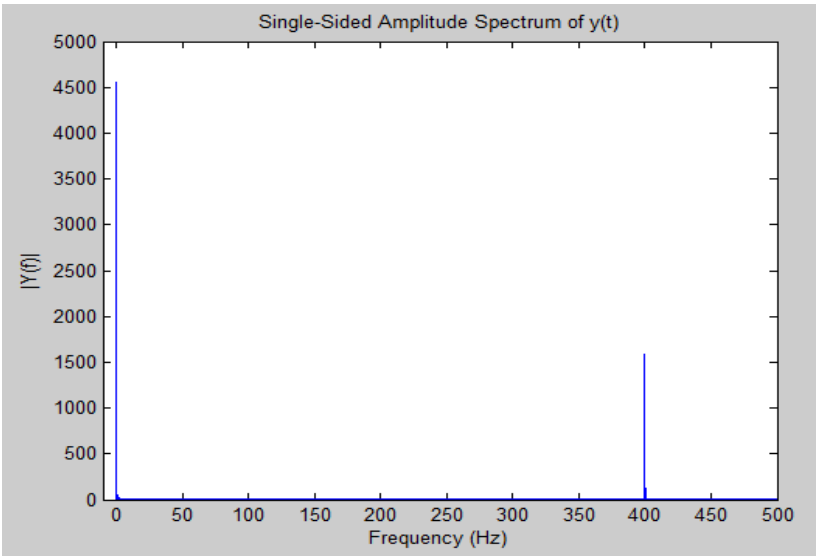


Figure 6-18 FFT of the raw data with an added sinusoidal wave of 400 Hz, to see if it is detected on the FFT

The FFT detected the added wave that had been introduced to the data. Therefore if there were any sinusoidal waves in the data to begin with they would have shown up on the FFT. This indicates that the fluctuations are random noise and hence cannot be removed. Furthermore, the signal spike present in all the FFT's indicates a purely DC signal, with no harmonic frequencies.

With the signals checked for noise, and deemed adequate, the next step was to convert the raw capacitance data to relative permittivity. These steps are discussed in the following section.

6.5 Linear Drift Correction

The equations developed at the end of section 6.2 displayed in table 6.3 detail the linear regression model for each electrode pair. By rearrangement of each of these equations so that the input is the raw capacitance data, the output becomes the relative permittivity trace over time. As an example of this figure 6.19 shows the data from figure 6.8 converted to relative permittivity.

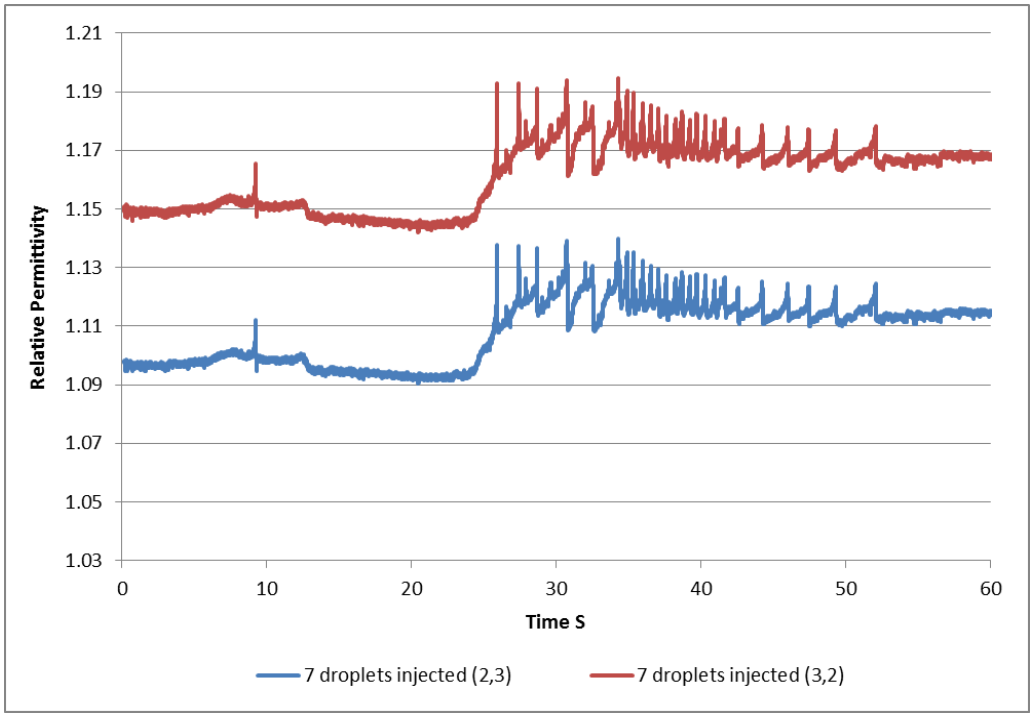


Figure 6-19 Relative permittivity measurement against time for electrode pair (2, 3) and (3, 2), not linearly corrected

To linearly correct the results, the following procedure, demonstrated in figure 6.20 is used, a full explanation is found on the following page.

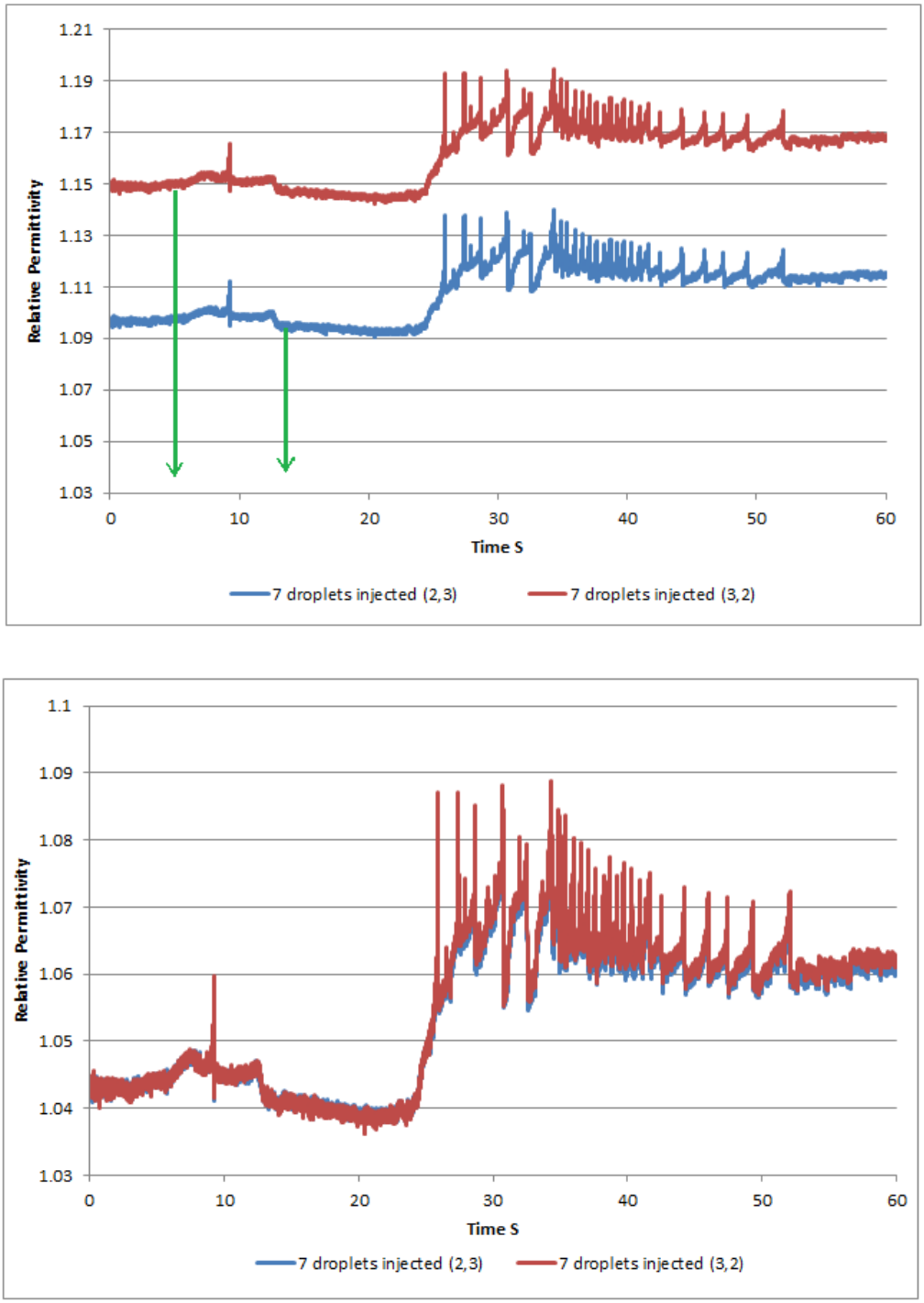


Figure 6-20 The procedure for linearly correcting each of the test results using the known relative permittivity of superheated steam from the baseline.

The baseline section is used to determine an accurate measurement of the relative permittivity of the superheated steam for the first 20 seconds. The relative permittivity is calculated from the pressure and temperature of steam using IAPWS – 97. The difference between the average of the non-linearly corrected baseline and the calculated relative permittivity is determined, then every relative permittivity measurement for the whole test is adjusted by this difference, fixing the baseline to the correct relative permittivity.

The level of drift observed was tracked throughout the day. Figure 6.21 shows the drift throughout a typical day when the oven is switched on and the test section is heated up for two of the electrode pairs.

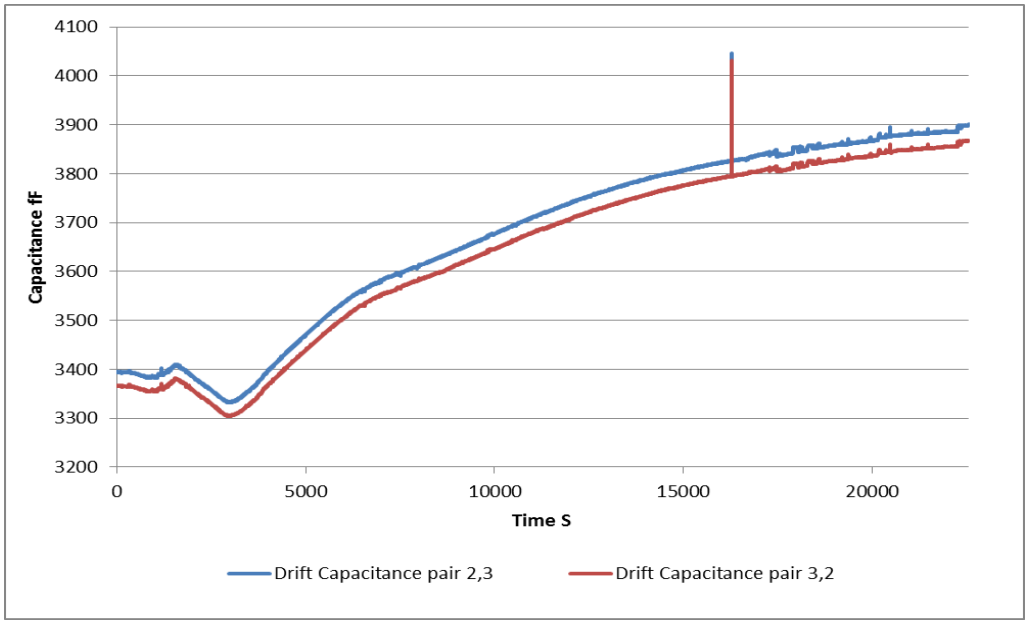


Figure 6-21 The measurement drift of the electronics over 6 hours for electrode pairs (2, 3) and (3, 2)

The drift differs between electrode pairs and is never consistent. It was hypothesised that the drift was being caused by the equipment being heated and pressurised over the day. The drift was significantly greater than when the TFL was used in the past (Barham 2013) and (Byars 2009). However because of the introduction of the baseline and the short testing period, the drift can be removed for every test causing no problems.

6.6 Analysis of the linearly corrected relative permittivity results

The first step in analysing the results was to determine if the effect of the high flowrate injector in each quadrant detailed in chapter 4 section 4.7 could affect the results. In order to see if this is true, a comparison was required between injecting six droplets and injecting one droplet at the respective flowrate they would come out if they were all together. These tests were completed and analysed before any other testing was started, in order to confirm that the fault in the droplet injection system shown in chapter 4 would not cause problems.

The droplet injection setup detailed in chapter 4 was altered for the duration of the test. Therefore the injectors from quadrants C and D were plugged off, the injectors were reconfigured for quadrant B so that the flowrate could be equal for only six injectors while the 7th was plugged. Finally for quadrant A all the injectors were plugged except the outer one. Therefore, the following two injection patterns were tested, shown in figure 6.22.

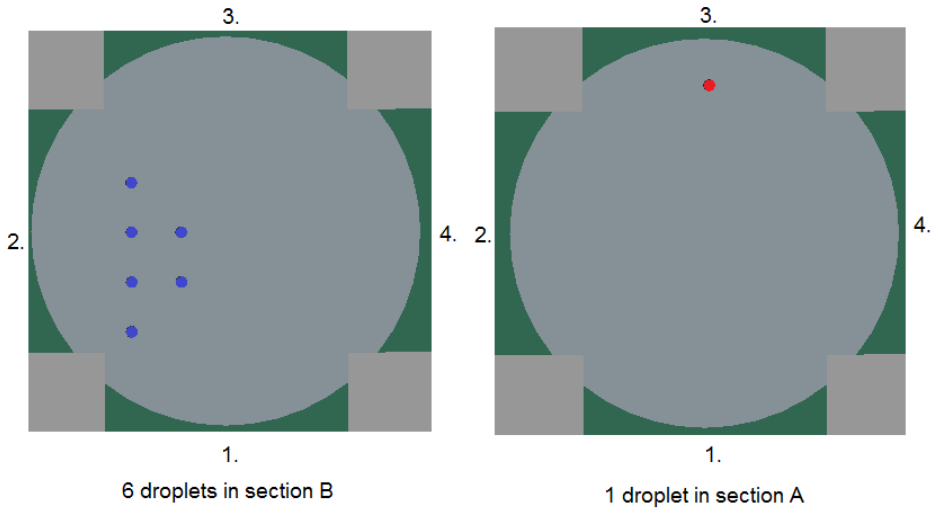


Figure 6-22 Extra two injection patterns to test the effect of the high flowrate injector

The results from these injection tests were compared in two ways; firstly, the results for each electrode pair for the six droplets injected in section B were compared against seven droplets injected in B, to see if the

extra droplet made a difference. Secondly, the results for each electrode pair for one droplet injected in A were compared against the results for one droplet injected in the centre; this was to see if the position made a difference and if the extra flow rate in the centre was allowing more than one droplet in the sensor at a time. The results for these comparisons are shown below in figure 4.23:

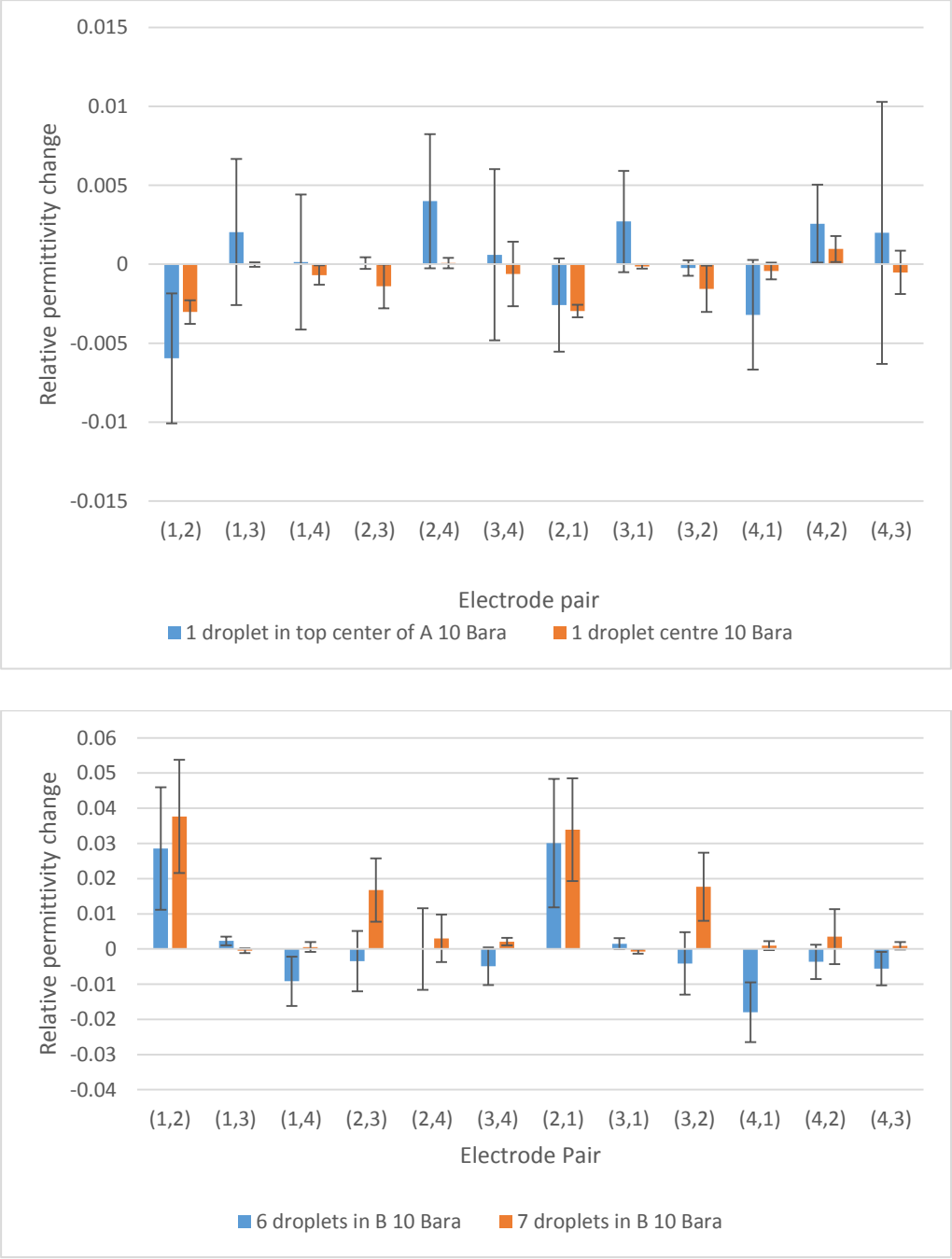


Figure 6-23 Results of the comparative tests to determine the effect of the higher flow rate injector

The results shown in figure 6.23 indicate that when one droplet is injected in the position shown in figure 6.22 compared to a droplet injected in the centre, due to the overlap of error bars, there is no significant difference. For the second test a significant difference is shown between the standard injection with seven droplets and injecting six droplets for electrode pairs (2, 3) and (1, 4) as well as their reversed pairs. For the closest electrode pair to the injection (1, 2) and (2, 1), there is no significant difference.

Overall this means that the position of one droplet should not affect the results as shown by the lack of significant difference in test 1, however by reducing the amount from seven to six in test 2 it is shown to have an effect on the change in relative permittivity in nearby adjacent pairs and a non-detectable change for the closest electrode pair to injection. Based upon these tests and results, the injection pattern was kept the same; this would increase the chance of having an uneven amount of droplets but the change in relative permittivity will be more detectable.

6.6.1 Average relative permittivity change comparison

Detailed here is the first way the results were analysed. This was completed by comparing each linearly corrected test's average change in relative permittivity between the baseline and the injection period. The tests were repeated three times for each of the 11 droplet injection patterns, with the maximum amount of droplets in each injection detailed in chapter 4 section 7. These droplets were injected at three pressures of 10, 11 and 12 Bara. These results are compared against droplets dropped into air at the same three densities of the steam tests. To obtain the closeness in density the steam density was used with the room temperature of the rig on the testing day to calculate the required pressure of air.

The results shown in figure 6.24 and 6.25 detail the comparison between the results of droplets being dropped into steam at 10, 11 and 12 Bara and droplets being dropped into air at 4.27, 4.68 and 5.08 Bara, with the steam and air both having the same average density of 5.17, 5.5 and

6.13 kg/m^3 respectively. The results are from electrode pairs (1, 2) and (2, 1), showing the response from the example adjacent pairs, the results for the other adjacent pairs are detailed in appendix 1. Figure 6.25 details the results for the opposite electrode pairs (1, 3) and (3, 1).

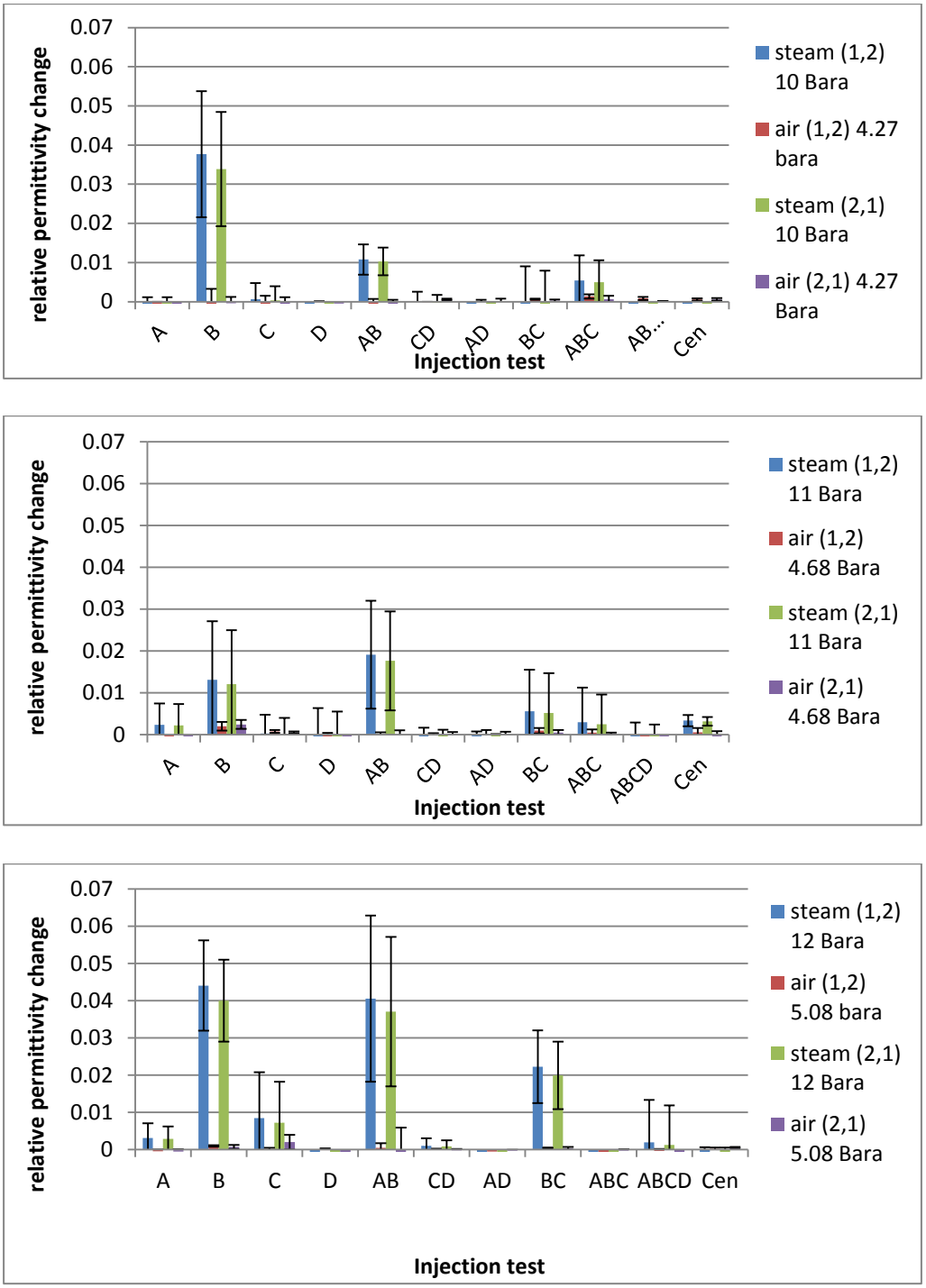
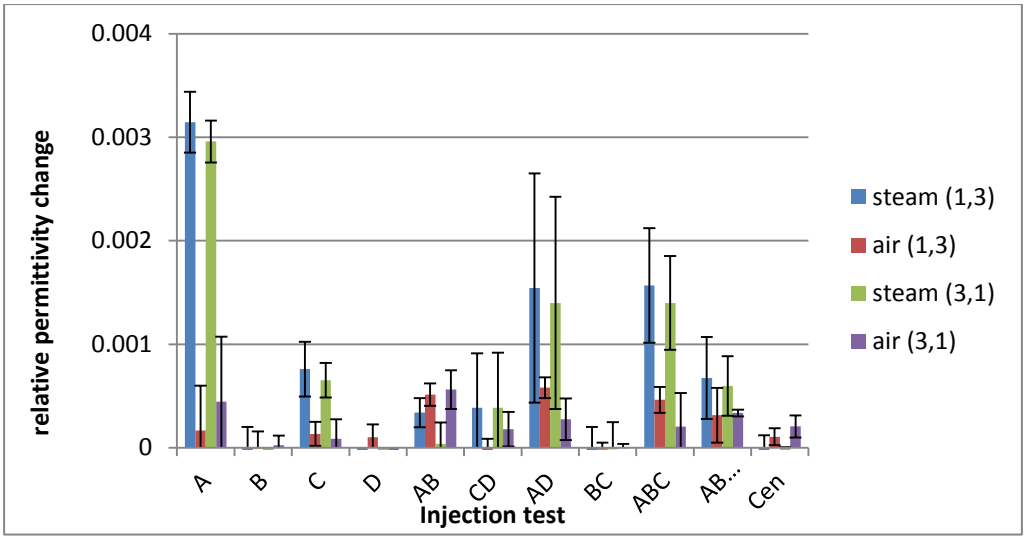
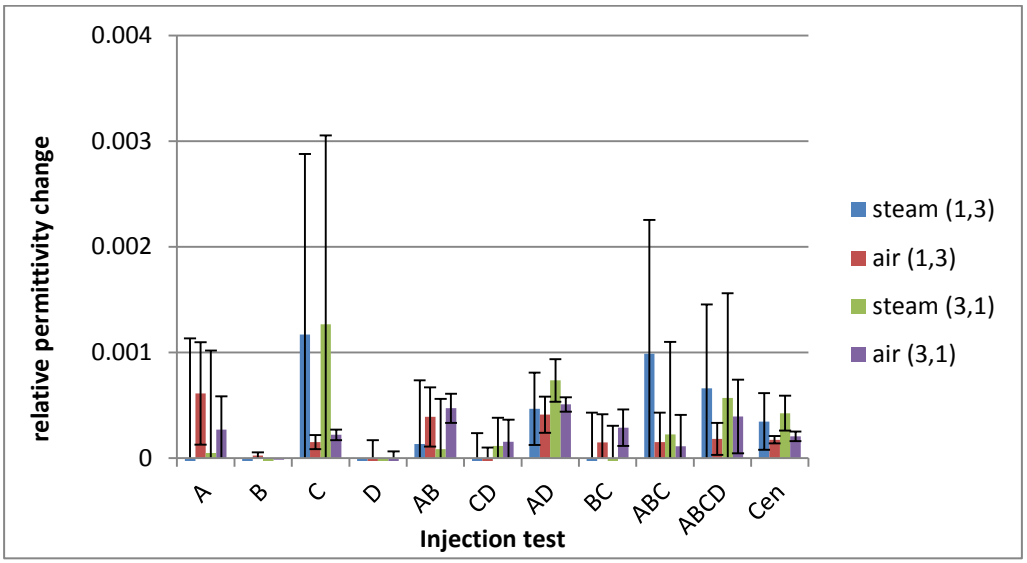


Figure 6-24 comparison of the average change in relative permittivity for electrode pairs (1, 2) and (2, 1) for droplets injected in steam at 10, 11 and 12 Bara and air at 4.27, 4.68 and 5.08 Bara.





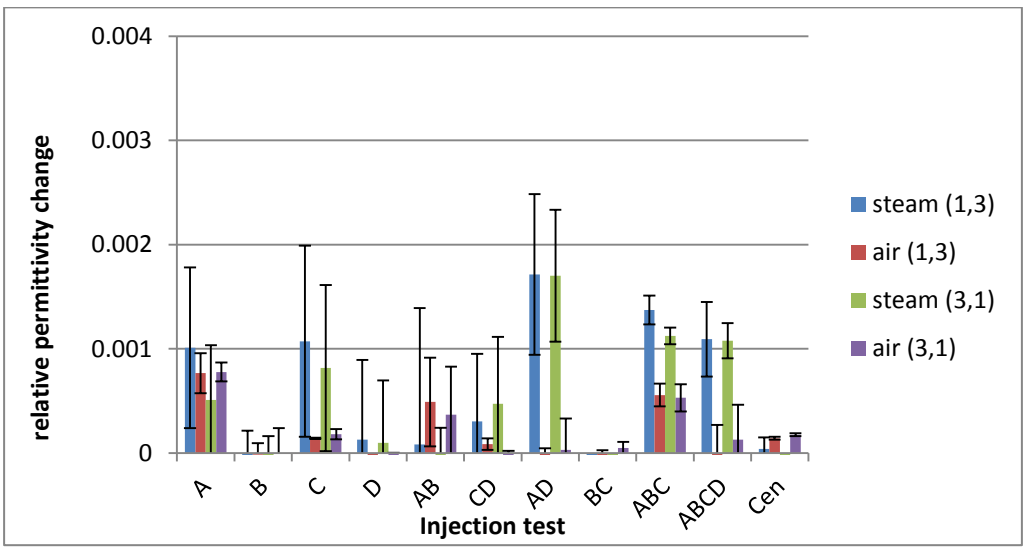


Figure 6-25 Comparison of the average change in relative permittivity for electrode pairs (1, 3) and (3, 1) for droplets injected in steam at 10, 11 and 12 Bara and air at 4.27, 4.68 and 5.08 Bara

First observations of the results for adjacent electrode pairs such as the examples in figure 6.23 and the results in the appendix 1 within chapter 9, show an inconclusive pattern in which droplets that are injected near to the measurement electrode pair have the highest change in relative permittivity. At these points the error bars do not overlap with the air test results, indicating a significant difference.

The opposite is shown with the opposite electrode pairs shown in figure 6.24 and in appendix 3, where there is no pattern visible in the averages. However some of the steam results at 10 Bara for injection patterns A and C show a significant difference, but not at the higher pressures, this is interesting as it could mean the spatial positioning is affecting the results, however this is unlikely due to the absent pattern from the rest of the recorded data for the opposite pairs.

For measuring steam wetness in the setup, this can only be done by comparing between injections in one quadrant and injections in multiple quadrants with the opposite electrode pairs shown in figure 6.25. A significant change in wetness was not observed, this suggests the sensitivity isn't sufficiently high.

Another two interesting observations; firstly is the significant difference between the air and steam results that is measured for adjacent electrode pairs closest to the water injection, and secondly the lack of behaviour change between air and steam results for opposite electrode pairs. To see if these measurement trends extend throughout all the data, the results for each electrode pair was analysed with ANOVA using an F test and T test to determine if there was an actual significant difference between average relative permittivity change for steam and air. If the F result was higher than the F critical or the T result was lower than the significant p value of 0.05, then a significant difference was recorded. This will tell four possibilities; that the results for steam and air are not significantly different at all, significantly different for all tests for when droplets are injected, significantly different due to an unknown variable causing a random pattern

of significance, or are significantly different only when droplets are injected near to the high sensitivity region of the measuring electrode pair. The results of this statistical test are shown in figure 6.26, 6.27 and 6.28.

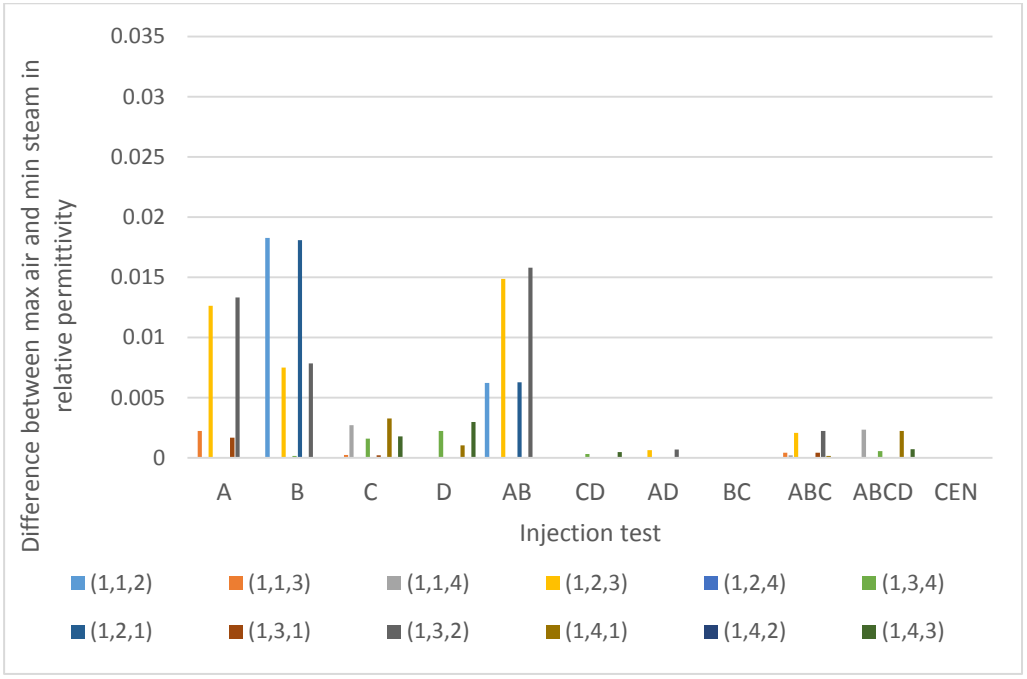


Figure 6-26 Significant differences 10 Bara steam vs 4.27 Bara air, same density

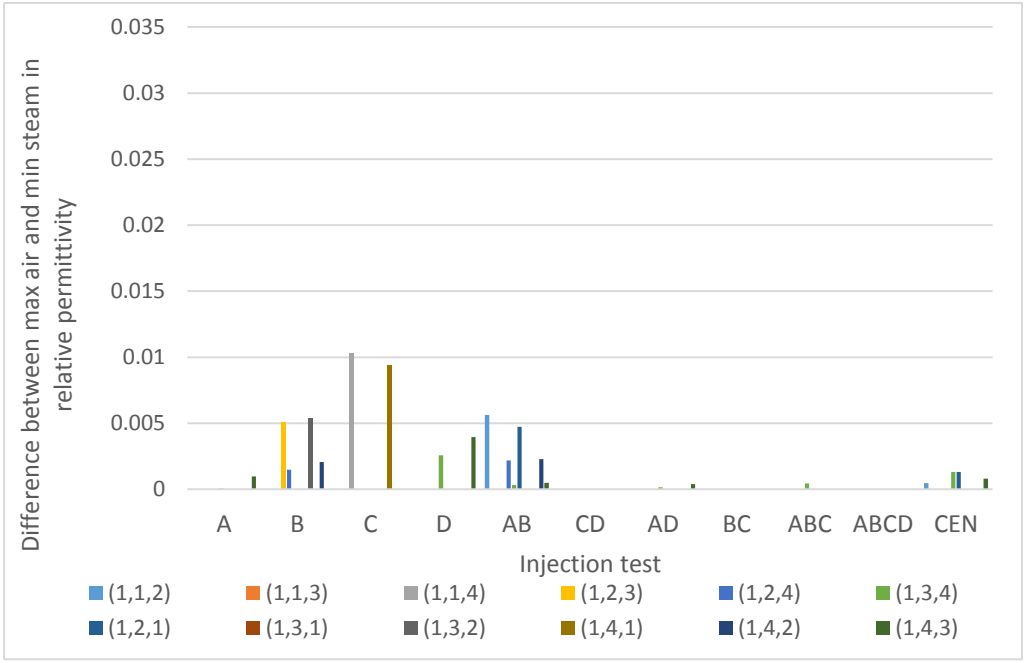


Figure 6-27 Significant differences 11 Bara steam vs 4.68 Bara air, same density

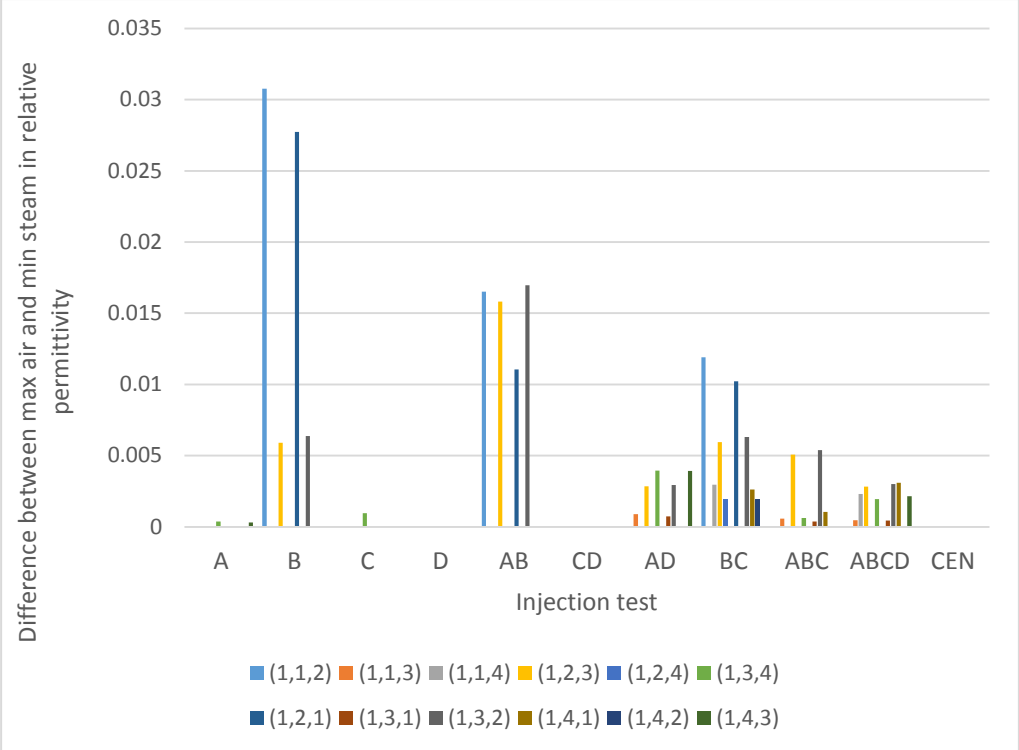


Figure 6-28 Significant differences 12 Bara steam vs 5.08 Bara air, same density

For the adjacent electrode pairs there is a definite pattern at 10 and 11 bar, that when 7 droplets are injected into region A, B C, or D, the nearest electrode pair gives a significant difference. At higher amounts of droplets being injected this pattern breaks down across all three pressures and the significant difference drops, due to more droplets falling non-uniformly as explained in chapter 4.

There is evidence of a significant difference between droplets being injected into air and steam. However this significant difference appears partially random and becomes more chaotic as more droplets are injected, this was hypothesised to be because of the earlier issue that the droplets were not falling uniformly, and so it cannot be determined how many droplets are within the sensor at any one time.

The insensitivity of the results shown from figures 6.24 and 6.25 for droplets injected into air where the change is less than 0.001 would mean that injecting one droplet into air using the current sensor would not show a

noticeable difference from the average baseline. It is therefore recommended that to investigate this observation further, that a separate study is performed with a more sensitive ECT sensor to see if there is a behaviour difference between steam water and air water mixtures when measuring with opposite electrode pairs, this is detailed in the further work section.

As the available ECT sensor can detect changes in the water content accurately, the focus of the work will now narrow down on further studying the effect of the spatial positioning in steam using a controlled amount of water, this is detailed in the next section.

6.6.2 Change in relative permittivity for single droplets injected into the sensor regions in steam

The sensor is theoretically capable of detecting one droplet injected into dry steam, therefore with the rig modified to inject one droplet in each corner of the sensor into the highest sensitivity region for an adjacent electrode pair, therefore the effect of spatial positioning of the water in dry steam can be determined with a known amount of liquid.

It was initially decided to analyse the data in the same way as before by looking at the average change over the injection period. However by injecting one droplet with a mass flowrate of 2.5 ml/min it meant that 1 droplet was being produced every 0.45 seconds. This means that there will be longer periods where a droplet is not within the sensor so the average will be smaller and not as accurate. Instead it was decided to measure the maximum change in relative permittivity within the injection period. The theory behind this is that the electrode pair closest to the injection will give the largest maximum change.

By injecting one droplet into the corner of A, B, C, and D individually and comparing the maximum change in relative permittivity to one droplet injected in the centre the following results are produced, detailed on the next page in figure 6.29.

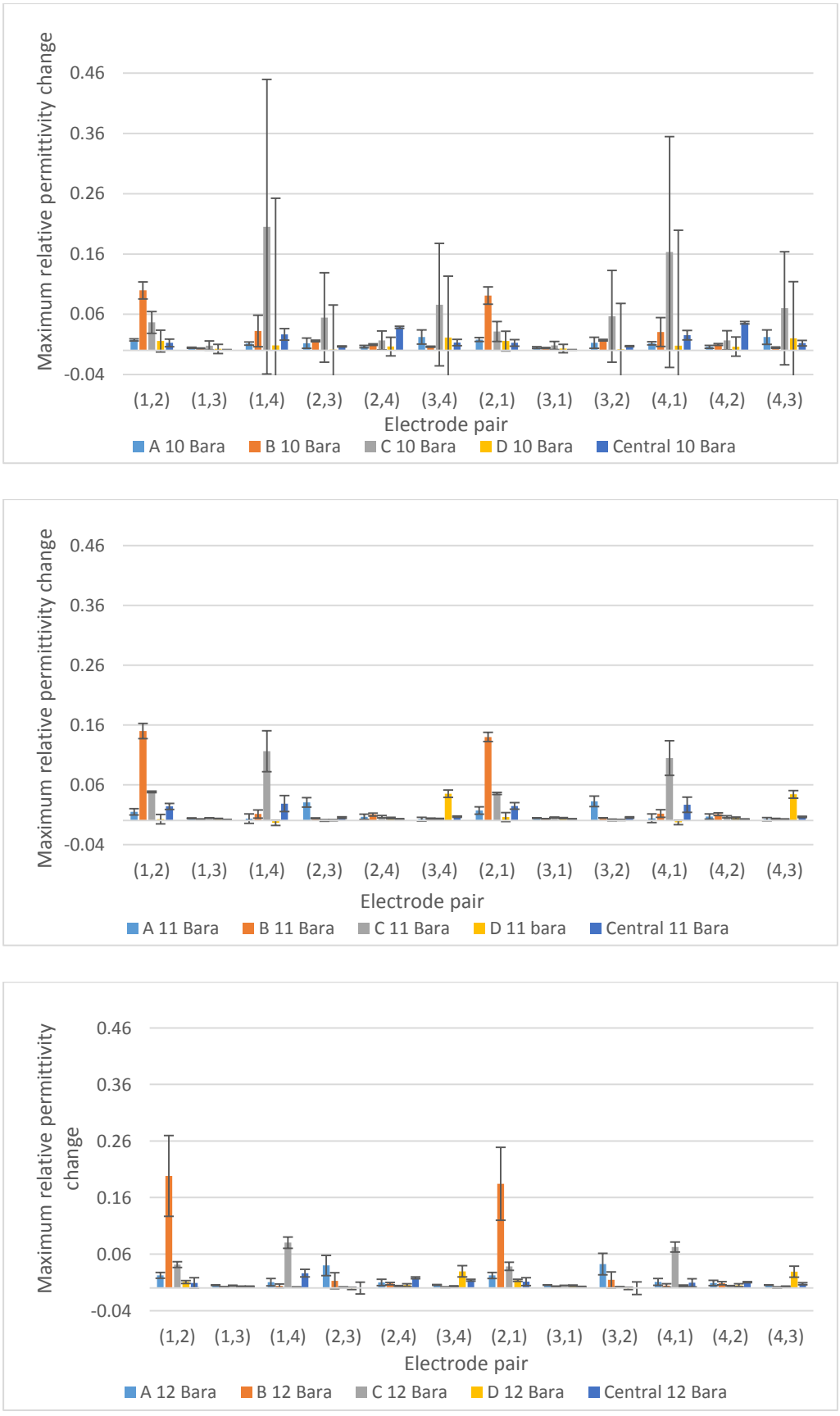


Figure 6-29 Maximum relative permittivity change for 1 droplet injected in section A, B, C, D, and central at 10, 11 and 12 Bara.

The results show that at 10 Bara, the electrode pairs are not susceptible to the positioning of the droplet and the maximum change in relative permittivity changes considerably no matter where the droplet is injected with no significantly different results due to the size of the error bars. The opposite is shown for the measurements at 11 and 12 Bara, where the closest measurement pair to the injection gives the largest maximum change. From this limited evidence, assuming the change was caused by a droplet being injected, then at 11 and 12 Bara the spatial positioning of the water in the steam strongly affects the measurement for adjacent electrode pairs.

For the opposite electrode pairs (1, 3), (2, 4), (3, 1) and (4, 2), the evidence suggests that spatial positioning is not affecting the measurement. However this could be because the electrodes are further apart and have a lesser sensitivity. To confirm that the droplets are producing the measured maximums and the measured insensitivities of the opposite electrode pairs; a further study needs be carried out which is proposed in the further work section of this thesis.

Spatial positioning could therefore alter the measurement of the relative permittivity of wet steam, making modelling the relative permittivity of a steam water mixture harder as the spatial positioning of the phases has to be taken into account. To understand the effect of spatial positioning on the parallel and droplet model detailed in chapter 3, two questions needed answering, firstly do single droplets injected in the centre follow the mixture permittivity predictions of the parallel or droplet model without the effect of spatial positioning? Do single droplets injected into the high sensitivity areas follow the mixture permittivity predictions of the parallel or droplet model? These questions will be answered in the following section.

6.7 Comparison of relative permittivity measurements of the opposite electrode pairs to the Parallel and droplet models

The parallel and droplet models explained in chapter 3, can be used to predict the mixture permittivity of wet steam based upon the water fraction. The relative permittivity measurement of wet steam has been inconclusively shown to follow the parallel model (Barham, 2013) for opposite electrode pairs, which have been predicted to have low sensitivity to spatial positioning. Evidence of this pattern was shown by Cimorelli & Evangelisti, (1967); Jaworek et. al, (2004) and Zunft & Bissinger, (1999); although it was not discussed in any depth.

The results presented so far have indicated that wet steam mixtures are affected by spatial positioning with adjacent electrodes and the measurement is not susceptible to spatial positioning with opposite electrodes. To see the effect of spatial positioning on how accurate the models predict the maximum change for the opposite electrode pairs; the accuracy of the models will be determined first for the relative permittivity of the wet steam with one droplet injected in the centre, this will give the accuracy of the model without the effect of spatial positioning. Secondly the accuracy will be determined for one droplet injected into each corner of the sensor, giving the accuracy when the effect of spatial positioning is included. A comparison between the tests will tell the effect of spatial positioning on the models and which is the more accurate for the results presented. The results of this comparison at 10, 11, 12 Bara which focuses on electrode pairs (1, 3), (2, 4), (3, 1) and (4, 2) is demonstrated in figures 6.30 to 6.32 on the following page.

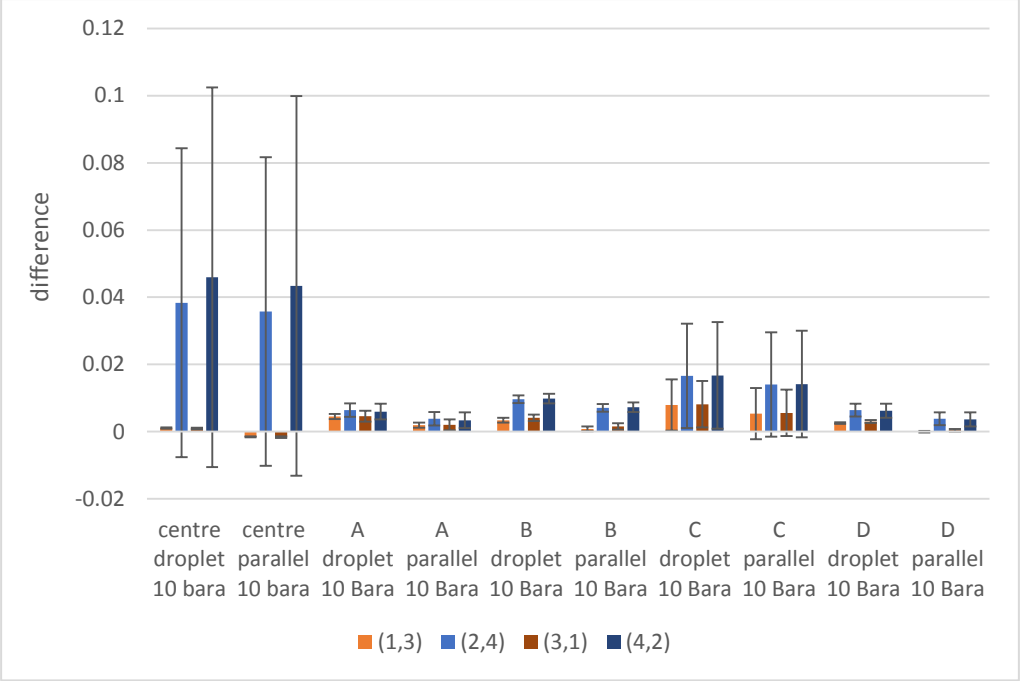


Figure 6-30 Difference between the maximum change within the injection time for the centre, A, B, C, and D against predicted by the droplet and parallel models for 10 Bara.

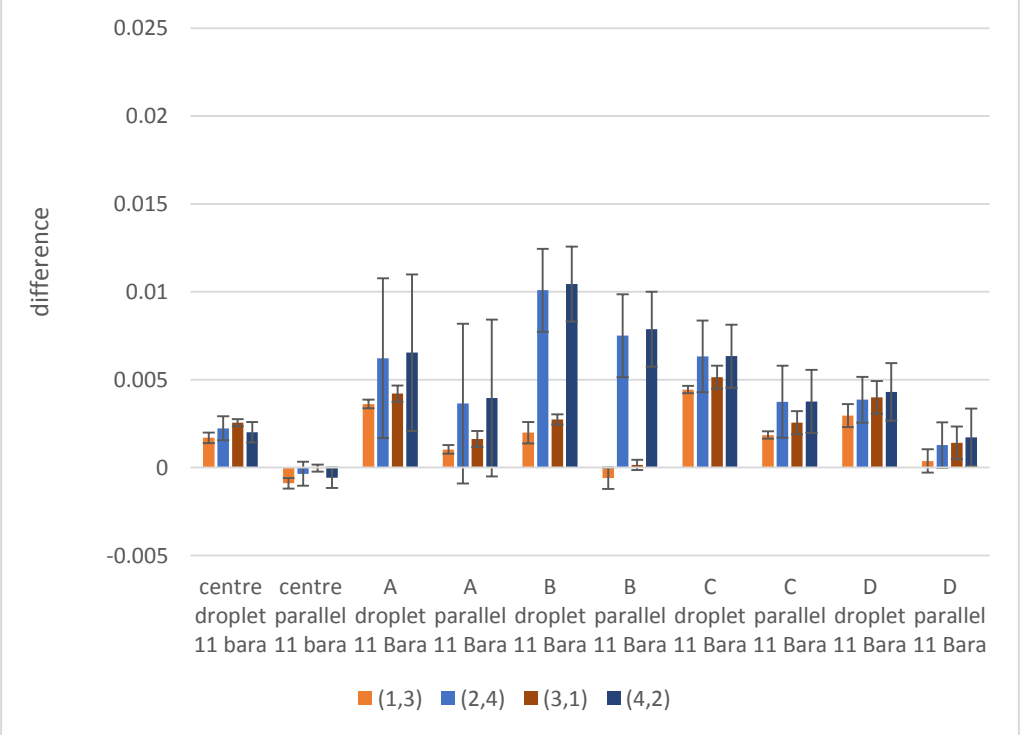


Figure 6-31 Difference between the maximum change within the injection time for the centre, A, B, C, and D against predicted by the droplet and parallel models for 11 Bara.

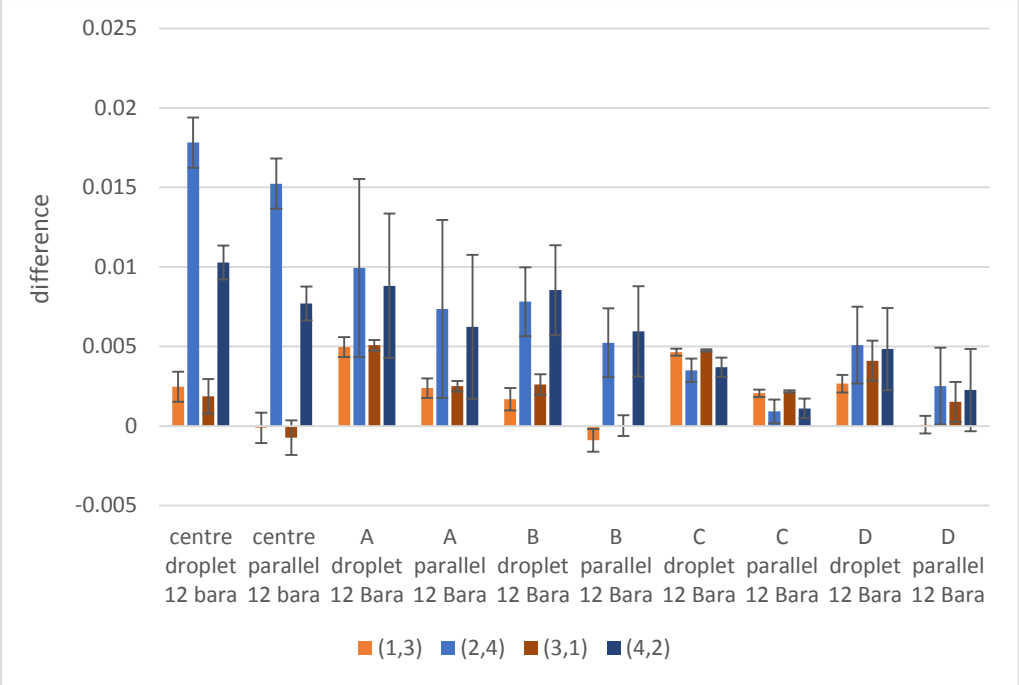


Figure 6-32 Difference between the maximum change within the injection time for the centre, A, B, C, and D against predicted by the droplet and parallel models for 12 Bara

The results of this comparison between the models and the measured data using the opposite pairs, indicates that there is no significant difference to the accuracy of the model between the predicted change for the droplet injected in the centre, and the droplet injected into a corner of a section for the parallel and the droplet model. This means that there is evidence the spatial positioning of 1 droplet within the steam is not affecting the measurement of opposite pairs.

The outcome also gives limited evidence that the water steam mixture is following closer the predictions of the parallel model instead of the droplet model. This is an interesting point because the previous study using the ECT sensor (Barham, 2013) also gives inconclusive evidence that the parallel model was the most accurate. Since the difference between this study and the previous one was the amount of liquid and the control over the spatial positioning, the evidence points towards the positioning of the water phase within the steam is not having an effect on the measurement.

There is however one unknown, in the previous study the exact time of injection was known, in this one the results are based upon a maximum change within the 20 second injection time.

The reason for the observed large change in permittivity for the maximums being greater than the parallel model was investigated. Previous studies have suggested water slugs forming a continuous path of water, this is not possible with this setup, nor can any film be present. Therefore after extensively investigating the literature, the most plausible explanation was due to the Maxwell-Wagner-Sillars Polarization shown by equation 6.7, occurring at the low measurement frequency of 2.5 MHz, causing separation of charges with the strong dipole behaviour of the steam and water:

$$\tau_{Mw} = \varepsilon_0 \frac{\varepsilon_1 + \varepsilon_2}{\sigma_1 + \sigma_2}$$

(6.7)

To calculate this the conductivity of steam σ_2 at the three pressures will have to be known. This is calculated using equation 6.8:

$$\sigma_2 = \varepsilon_0 \varepsilon^{"} \omega$$

(6.8)

Using the Debye equation (Onimisi *et al.,* 2015) shown in equation 6.9 the absolute relative permittivity can then be used to calculate the loss factor $\varepsilon^{"}$

$$\varepsilon^{"} = \frac{(\varepsilon_s - \varepsilon_\infty)\omega\tau}{1 + \omega^2\tau^2}$$

(6.9)

The absolute relative permittivity ε_∞ is calculated for steam at 10, 11 and 12 Bara, using the reflective index for steam from 100°C to 225°C given as $n = 1.004$ (Schiebener *et al.,* 1990). The dielectric constant at the reflective index frequency ε_∞ is calculated by the square of the reflective index giving

1.008 as the absolute relative permittivity. The problem occurs because the relaxation time τ is not able to be calculated as the relaxation frequency of steam at 10, 11 and 12 Bara is unknown. Therefore if the relaxation frequency can be measured, the polarization time can be calculated and if this is less than the measurement frequency, then the hypothesis that separation of charges at the interface is occurring can be used to conclude as the reason the large change in relative permittivity appears in the results.

The remainder of this chapter will now focus of the development of the 3D capacitance program for developing another way to predict the relative permittivity change. As well as review how well the sensor can image the water steam mixture and identify the different phases.

6.8 Comparison to the results from the 3D Capacitance Program

The capacitance program that was developed and discussed within chapter 3 section 5 and expanded upon in chapter 4, allows for different amounts of water to be placed anywhere within the simulation of the sensor and to record the resulting capacitance measurement. This program was originally intended to be compared against all the experimental data, however the previous results have shown that injections with more than 1 droplet cannot guarantee a uniform droplet injection from all the injectors in a given area. Therefore the capacitance program was compared against experimental results for one droplet injected into the centre and the high sensitivity region of areas A, B, C and D.

The aim of this comparative analysis is to determine the accuracy of the program for a known amount of droplets injected and hence validate the predictive capability of the program at this prototype stage. The program only gives results for electrodes (1, 2), (1, 3), (1, 4), (2, 3), (2, 4) and (3, 4), and not any of the reversed pairs, hence only results from these electrode pairs were compared against the program. The results for the program were compared against results at pressures 10, 11 and 12 Bara, and are detailed in figures 6.33, 6.34 and 6.35 respectfully.

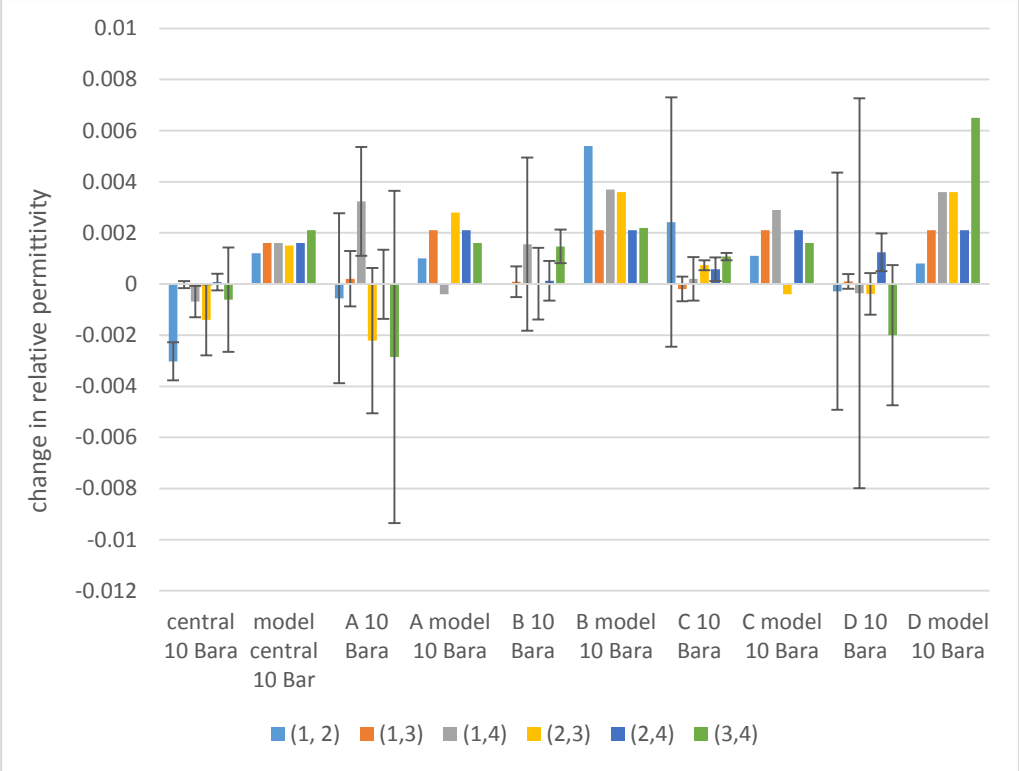


Figure 6-33 Change in relative permittivity for a single droplet injected in each region at 10 Bara compared to the results calculated by the program

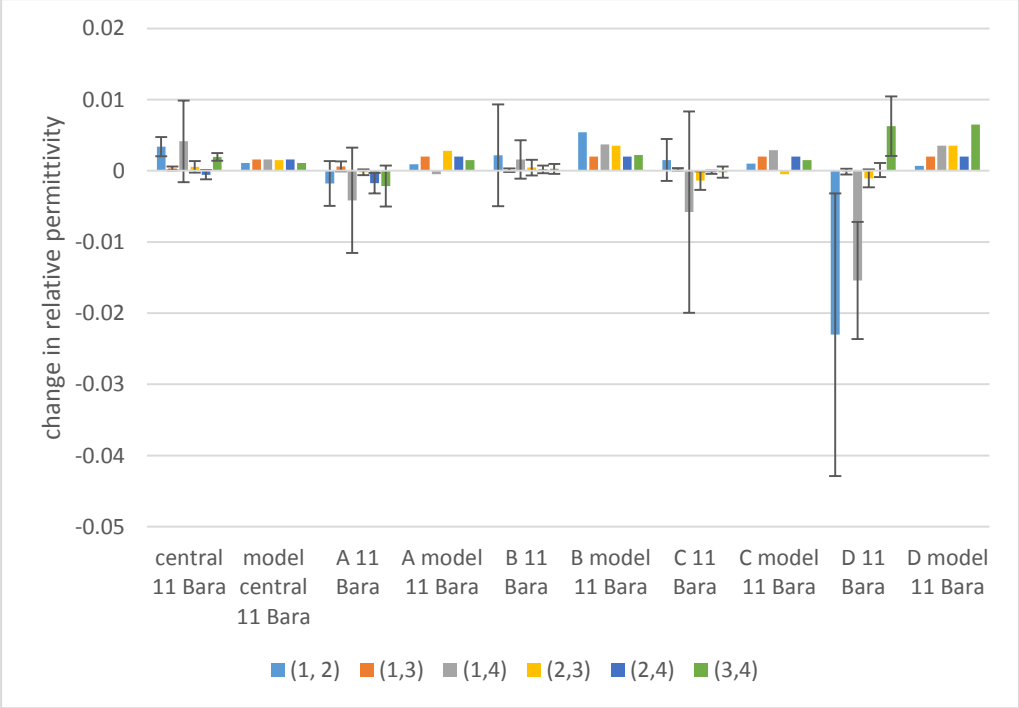


Figure 6-34 Change in relative permittivity for a single droplet injected in each region at 11 Bara compared to the results calculated by the program

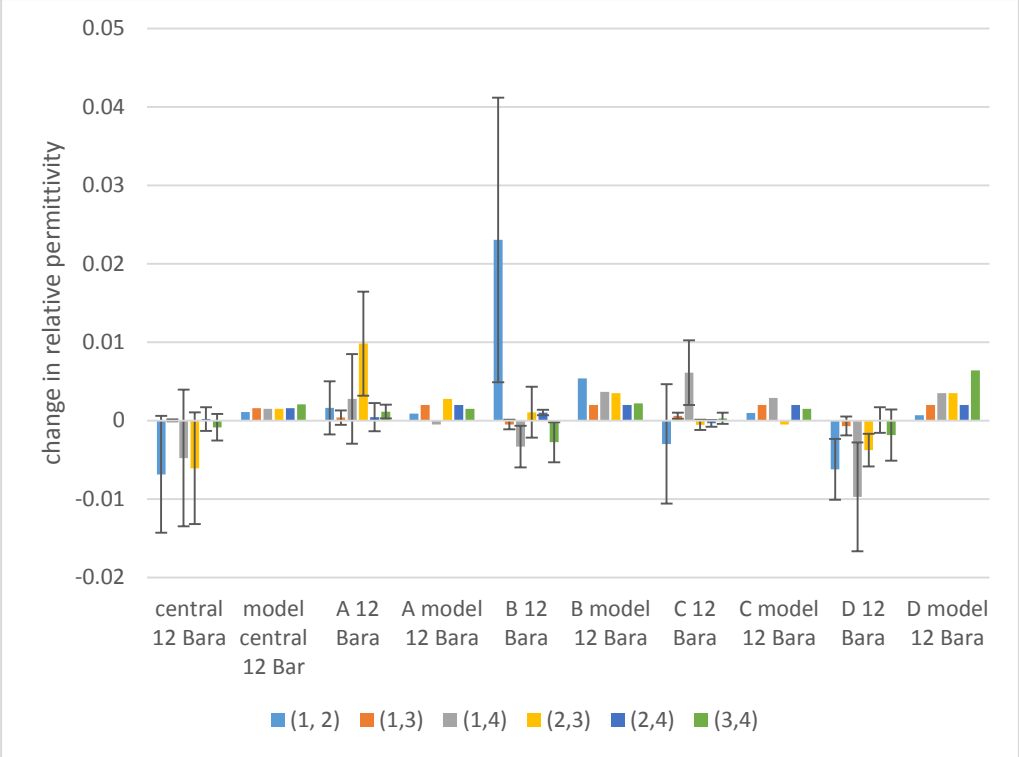


Figure 6-35 Change in relative permittivity for a single droplet injected in each region at 12 Bara compared to the results calculated by the program

The outcome of the comparison on the previous pages shows that the change in the relative permittivies predicted by the capacitance program are highly significantly different for the majority of the comparisons. Firstly the inaccuracy is caused because of comparing average change in relative permittivity instead of the exact change caused by one droplet at one time. It was investigated whether to compare to the maximum change data as shown in section 6.6.2, these results are shown in appendix 3. The outcome of the maximums was that the predicted results were even more inaccurate, due to them being predicted lower than the parallel model.

Secondly in chapter 3 the program was shown to predict changes in relative permittivity that closely matched the parallel model to within 0.18%, this meant that although the previous section has shown the parallel model to be the most accurate for opposite pairs it was still highly inaccurate, so the average change in relative permittivity from the results would definitely not line up with the changes predicted by the program.

To conclude, this is only a limited testing of the program against the available data and was run as a side project to the main work. The main goal of this was to provide a platform where the full understand of the workings of an ECT system and the measurement process can be shown. The end objective beyond this study is to eventually have a program that can accuracy predict the change in relative permittivity for different spatial positions of water. This links back to the previous section whereby if this program was validated, then it would be able to predict the effect of size and distribution of the water droplets and how they could form a bridge of high conductivity at any pressure.

The results so far have shown that spatial positioning affects the measurement of the adjacent pairs, therefore an imaging program should be able to visualise the different phases, this work is detailed below.

6.9 Spatial Position Imaging

In chapter 3 section 3.7, the process of linear back projection was discussed, and a program was built that could produce images from the electrode pairs capacitance readings. This program was used to produce cross sectional images for the final results, to show the droplets being injected into the different sections detailed in 6.1.

The images produced have a low resolution due to the small amount of electrode pair, but it is still possible to determine where the injection occurred as long as the measurement is affected by the spatial positioning of the water. It would be possible to produce an image of every frame of the measurement, however due to running time of the program it is quicker to produce a single image for each result at an optimum point in time where there is the highest chance of seeing a clear image of where the droplets were injected, this is where the closest electrode pair to the injection has its highest capacitance reading.

This process of section was completed for all the results, the first observation is that there is little change in visualisation of the injection area at

the higher pressures. This is demonstrated in figure 6.36, where 7 droplets were injected into section C, at 10, 11 and 12 Bara.

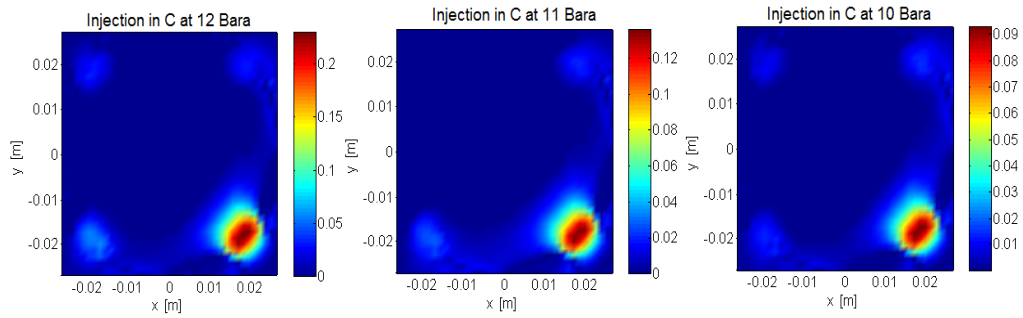


Figure 6-36 7 droplets injected into section C at 10, 11 and 12 Bara

The most defined image is at 12 Bara, while 10 and 11 Bara have lower normalised relative permittivities. Using the 12 Bara results, an example for each test is shown on the next page in figure 6.37:

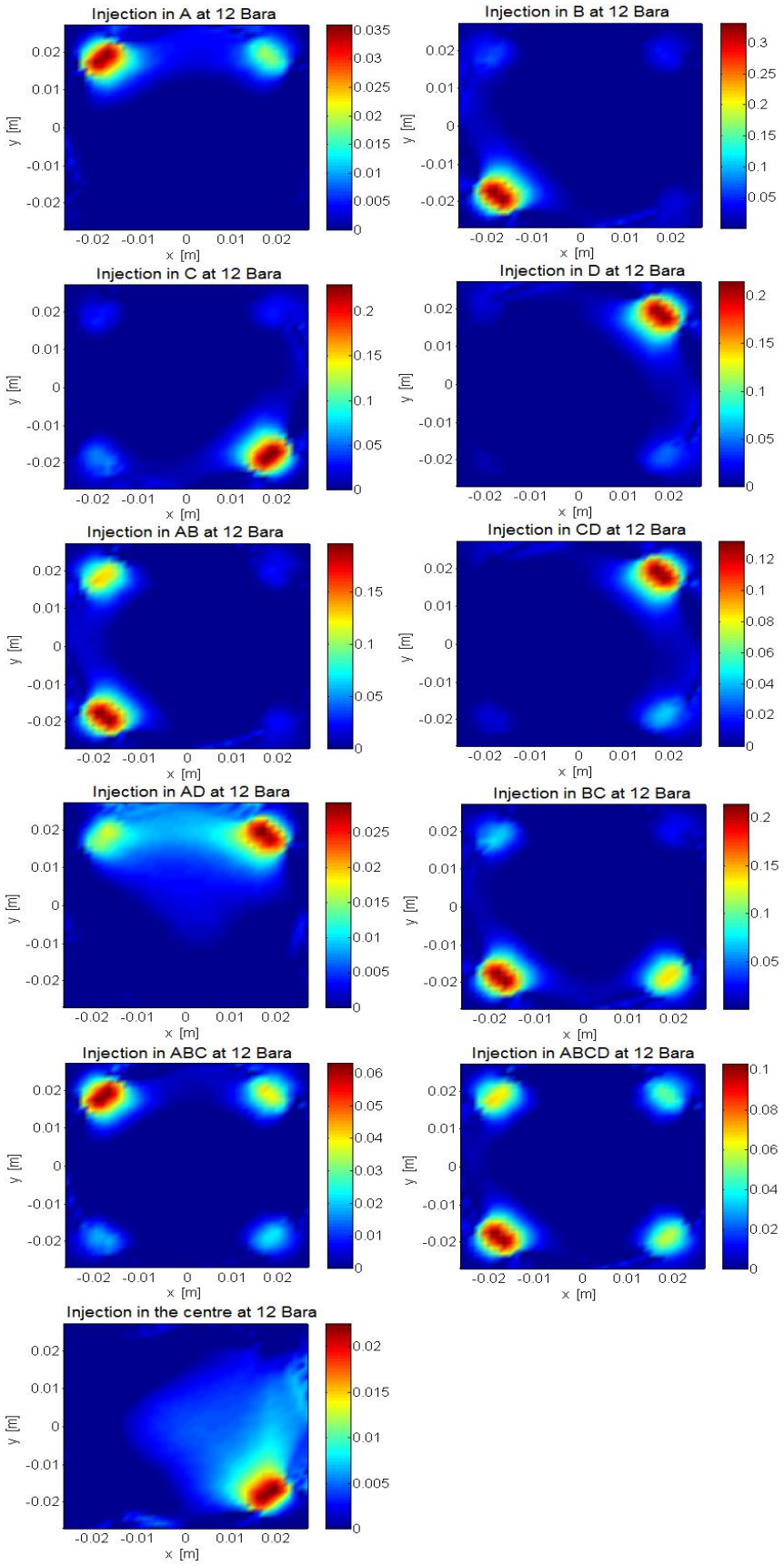


Figure 6-37 LBP of each of the 11 injection patterns into steam at 12 Bara

The images in figure 6.30 clearly show the most defining time frame for each test, giving a clear indication of where droplets were injected when two or less injection sites are used. This is evidence to show that the measurement of the wet steam mixture can be affected by spatial positioning to the point where the area of injection can be rebuilt from the difference in relative permittivity between electrode pairs and their respective sensitivity maps.

In this regard the prototype four electrode sensor is able to gather enough relative permittivity measurements to see roughly where the area of injection is located and hence capturing spatial positioning. The sensor does not have enough electrodes to determine any further detail. This clearly demonstrates that spatial positioning is affecting the measurement correctly for cross sectional visualisation, however future research should concentrate on increasing the length of the electrodes further, while decreasing the width to maintain the same surface area, allowing for more electrodes to be fitted together.

Chapter 7. Conclusion

This project sought to build upon the work by Scott Barham in measuring the moisture content of a high quality wet steam flow, that has less than 1% steam wetness at 70 Barg as found in a nuclear power station. Scott's work showed that with electrical capacitance tomography (ECT) it was possible to measure the steam wetness. However unpredicted behaviour differences in measuring wet steam when compared to measuring an air water mixture were found, which highlighted that ECT was more sensitive to changes in moisture content in a water steam mixture, and that the spatial positioning of the water phase does not affect the capacitance measurement when using opposite electrode pairs. This study therefore designed and built a novel testing platform that could test for these behavioural changes between air water and steam water mixtures, and could test to see what effect the spatial position of the water phase had on the measurement.

To keep the steam dry within the ECT sensor for as long as needed, the sensor needed to be housed within a large oven. In order for the ECT equipment to survive for long periods of time within the extreme heat, the sensor was modified by replacing the plug in ports with direct connection cables that ran straight from the electrodes to the signal processing unit outside the oven. As well as this, the use of PTFE within the sensor was reviewed, it was found that using PEEK (Poly ether ketone) would improve the lifespan of the sensor and make it more resistant to pressure / temperature damage. Unfortunately the cost of replacing the PTFE with PEEK was half the budget and was unacceptable due to the need to build the test rig, therefore a simpler and cheaper solution was used where the most damaged PTFE components were remade and the sensor electronics were repaired in house. These repairs worked as the recorded noise was an average of 600 aF.

The second part of the test rig, the novel droplet injection system, had a design proposed that would allow for single or groups of droplets to be injected in 29 different locations. This design worked upon the principle that

different radii pipes produced different sized droplets and so having multiple manifolds with different sized pipes attached would allow for different concentrations of liquid to be injected into the same place. Initial experiments were conducted to determine what size pipe could produce a certain droplet size, this lead to the creation of a novel method of droplet diameter measurement using a Camsizer. This method was able to measure different droplet sizes from 27 gauge needles to 1/16th inch pipes, and could photograph the droplets as descended checking the premise that they were spherical.

Due to the costs and time required, only the simplest design of manifold using the 1/16th inch tubes could be vacuum brazed. An appropriate water feed system was designed and constructed that could feed water to each of the 29 injection lines in four groups of 7 and one central droplet injection.

Full testing of system was conducted by injecting water in 11 different spatial positioning patterns and seeing what changes in the measurement of relative permittivity from each electrode pair were between tests. It was found that there was significant behaviour changes between the measurement of the average relative permittivity of a water steam mixture and a water air mixture; specifically the larges changes were found for adjacent electrode pairs where the water phase was nearest.

Further investigation looking at where the significant differences were found, indicated that adjacent electrode pairs that have the water phase nearest to them had the largest significant difference in the majority of cases. There were few significant differences between the measurements with the opposite electrode pairs. It was concluded that it could not be guaranteed that seven droplets were falling at once, therefore the amount of water producing the result is not known. Secondly it was decided that to accurately see if there is a difference one droplet would have to be injected. This is fine for a water steam mixture, but the results suggested that for air water mixture the change in relative permittivity would have been below the RMS

noise for the sensor. Therefore a more sensitive ECT system is required before accurate behaviour differences between air and steam mixtures with one droplet injected can be recorded and repeated.

The one droplet idea was taken forward and used by injecting one droplet into the system into the high sensitivity region between each adjacent electrode pair, giving a total of four additional tests that would have a controlled amount of liquid within the system. The results of this testing showed that adjacent electrode pairs are very susceptible to the spatial positioning of the water phase and that opposite electrode pairs showed evidence that they are not susceptible to spatial positioning of the water phase. Further testing is required with larger droplets and in more areas than what has been allowed to confirm the non-susceptibility.

Due to the known volume fraction within the system at the time of injection, the parallel and droplet models were used to determine which could better predict the relative permittivity change as a droplet falls through for an opposite electrode pair. The predicted change was compared against the maximum measured change within the injection time, whereby the maximum change is assumed to be because of a droplet falling through. The results indicated that the maximum changes were better predicted by the parallel model.

A novel 3D capacitance measurement program was developed alongside the test rig that could replicate the process of relative permittivity measurement of the four electrode sensor. This program was found to predict relative permittivity differences for small amounts of water with a difference of 0.18% to the parallel model.

The ECT system was also used to generate images of the spatial position patterns of injection. The images were created using four electrodes and showed good correlation to the actual injection pattern, with the most accurate images being when the droplets were injected into a corner of the sensor.

Within this work the author has analysed and tested in a novel way the effect of spatial positioning of water within steam at pressure and reviewed if steam water mixtures behave differently to air water mixtures. The results are inconclusive but do show that steam water mixtures are more susceptible to spatial positioning with adjacent electrode pairs and that opposite electrode pairs are not susceptible to spatial positioning. Previous work in the literature has also shown evidence to suggest that the behaviour of the permittivity change is different between air and steam and that the parallel model is the more accurate in predicting relative permittivity changes. This is important as the novel work thus far suggests that measurements with wet steam with opposite electrode pairs would be sensitive to changes in wetness and not sensitive to the position of the moisture content.

7.1 Future work

The work carried out within the thesis highlighted the need for additional testing that would be able to push the experimental analysis further and validate assumptions. This testing could not be completed with the current rig setup due to the lack of time and the additional funds required. The further testing would also require the use of a new more sensitive ECT sensor, the modifications to achieve these goals are detailed below:

Improving the sensitivity of the ECT sensor

To lower the RMS noise of the sensor and to improve the ability to detect changes in relative permittivity that are less than 3 decimal points. The electrodes could be made longer or the diameter of the sensor could be made wider allowing for larger electrodes to be fitted, increasing the sensitivity.

Installing a droplet detection system

Such a system could be developed to detect when a droplet is released from the manifold and run alongside the ECT measurement recording. This would allow for the exact time of injection to be

located on the trace any resulting spike in the measurement could be accuracy shown to be because of a droplet being injected.

Different manifolds

A future project could have different manifolds for different tests with varying sized injectors, it would even be possible using this system to inject droplets less than 100 µm diameter.

Installing a superheated steam generator

The last change to the hardware of the rig would be to add a superheated steam generator. In this project it was not an option due to cost but in future work installing this system would allow for higher pressures to be tested and greater flexibility in the pressure testing.

With these changes implemented, single droplet measurement comparison between air and steam would be possible and highly accurate. It would also allow for fine tuning of the rig to inject multiple droplets at the same and have the evidence to say the droplets fell through the sensor together.

Chapter 8. References

Abdul W., Y., Ahmad, M. A., Abdul Rahim, R., & Fazalul Rahiman, M. H. (2011). Application of transmission-mode ultrasonic tomography to identify multiphase flow regime. International Conference on Electrical, Control and Computer Engineering (INECCE), Kuantan, Malaysia.

Abouelwafa, M. S. A., & Kendall, E. J. M. (1980). The measurement of component ratios in multiphase systems using alpha -ray attenuation. Journal of Physics E: Scientific Instruments. 13(3), 341.

Agmon, N. (1995). The Grotthuss Mechanism. Department of Physical Chemistry and the Fritz Haber Research Center, the Hebrew University, Jerusalem 91904, Israel. Chemical Physics Letters 244 456-462

Areeba Shafquet & I. Ismail. (2012). Measurement of Void Fraction by Using Electrical Capacitance Sensor and Differential Pressure in Air-Water Bubble Flow. Electrical and Electronic Engineering Department, University Teknologi PETRONAS, Malaysia.

Arai & Crawford. (2009). Chapter 2 Neutron Sources and Facilities. Neutron Scattering Applications and Techniques. Springer

Asher, R. C. (1983). Ultrasonic Sensors in the Chemical and Process Industries J. Sci. Instrum. Phys. E: UK: The Institute of Physics. 16: 959-963.

Barham. S. (2013). High Quality Steam Measurement in power Station pipework. Ph.D. University of Nottingham.

Barthel, F. Bieberle, M. Hoppe, D. Banowski, M. Hampel, U. (2015). Velocity measurement for two-phase flows based on ultrafast X-ray tomography. Flow Measurement and Instrumentation. 46, Part B: 196-203.

Baumgardner, D. & M. Spowart. (1990). Evaluation of the Forward Scattering Spectrometer Probe. Part III: Time Response and Laser Inhomogeneity Limitations. Journal of Apmospheric and oceananic technology 7(5):666-672

Belz, R. A. & R. W. (1979). Menzel. Particle Field Holography At Arnold Engineering Development Center, SPIE.

Bereznai. (2005). Nuclear Power Plant Systems and Operation. School of Energy Systems and Nuclear Science University of Ontario Institute of Technology Oshawa, Ontario

Bieberle, M. & U. (2006). Hampel Evaluation of a limited angle scanned electron beam X-ray CT approach for two-phase pipe flows. Measurement Science and Technology. 17(8): 2057.

Bieberle, M. Schleicher, F. Fischer, D. Koch, H.-J. Menz, H.-G. Mayer, U. Hampel, (2010). Dual-plane ultrafast limited-angle electron beam X-ray tomography. Flow Measurement and Instrumentation. 21(3): 233-239.

Bieberle, M. Barthel, F. Hoppe, D. Banowski, M. Wagner, M. Lucas, D. Stürzel, T. Hampel, U. (2012). Ultrafast electron beam X-ray computed tomography for 2D and 3D two-phase flow imaging. 2012 IEEE International Conference on Imaging Systems and Techniques Proceedings. Manchester, United Kingdom.

Bieberle, A., Hans-Ulrich Härting, Swapna Rabha, Markus Schubert and Uwe Hampel. (2013a). Gamma-Ray Computed Tomography for Imaging of Multiphase Flows. Chemie Ingenieur Technik. 85(7), 1002–1011

Bieberle, A., Nehring, H., Berger, R., Arlit, M., Härting, H.-U., Schubert, M., & Hampel, U. (2013b). Compact high-resolution gamma-ray computed tomography system for multiphase flow studies. Review of Scientific Instruments. 84(3):033-106 With the permission of AIP Publishing.

Bieberle, A. T. Frust, M. Wagner, M. Bieberle, U. Hampel (2015). Data processing performance analysis for ultrafast electron beam X-ray CT using parallel processing hardware architectures. Flow Measurement and Instrumentation.

Bin Hu, Sven Nuland, Morten Langsholt, Peter Andersson, Chris Lawrence. (2011). A fast X-ray tomography system in multiphase pipe flow measurement Department of Process and Fluid Flow Technology Institute for Energy Technology, Kjeller, 2027, Norway.

Bosdas, I. Mansour, M. Kalfas, A. & Abhari, R. (2016). "An optical backscatter probe for time resolved droplet measurements in turbomachines." Measurement Science and Technology. 27(1): 015204.

Brenguier, J., T. Bourrianne, A.A. Coelho, J. Isbert, R. Peytavi, D. Trevarin, & P. Weschler (1998). "Improvements of Droplet Size Distribution Measurements with the Fast-FSSP (Forward Scattering Spectrometer Probe)." Journal of Atmospheric and Oceanic Technology. 15(5): 1077-1090.

Brook W. Abegaz, Nathan T. Dick & Satish M. Mahajan. (2014). Measurement and Characterization of Fluid Flow Profile using Electrical Capacitance Tomography. Department of Electrical and Computer Engineering, Tennessee Technological University, Cookeville, Tennessee, USA.

Buford Randall Jean. (2008). A Microwave Sensor for Steam Quality. *IEEE Transactions on Instrumentation and Measurement.* vol. 57, no. 4, pp. 751-754

Byars, M. (2009). ELECTRICAL CAPACITANCE TOMOGRAPHY SYSTEM Vol 1: Fundamentals of ECT (Issue 1). Process Tomography Ltd. Retrieved from http://www.tomography.com/pdf\Fundamentals of ECT.pdf

Cai, T. Ning, F. Niu, G. Wu, Y. Song. (2009). "Investigation of wet steam flow in a 300 MW direct air- cooling steam turbine. Part 1: Measurement principles, probe, and wetness." Proceedings of the Institution of Mechanical Engineers, Part A: Journal of Power and Energy. 223(5): 625- 634.

Chason, E., & Mayer, T. M. (1997). Thin film and surface characterization by specular X-ray reflectivity. Critical Reviews in Solid State and Materials Sciences. 22(1), 1-67.

Chien, S.-F., & Ibele, W. (1964). Pressure Drop and Liquid Film Thickness of Two- Phase Annular and Annular-Mist Flows. Journal of Heat Transfer. (1964). 86(1), 89-96.

Cimorelli, L., & Evangelisti, R. (1967). The application of the capacitance method for void fraction measurement in bulk boiling conditions. International Journal of Heat and Mass Transfer, 10(3), 277–288. doi:http://dx.doi.org/10.1016/0017-9310(67)90145-7

Clayton C. G., Clarke W. E., & Ball A. M. (1960). The accurate measurement of turbulent flow in pipes using radioactive isotopes and the effect of some restrictions on optimum operation. Symposium on flow measurement in closed conduits. National Engineering Laboratory.

Clifford A. Moses and Gilbert D. Stein. (1977). On the Growth of Steam Droplets formed in a Laval Nozzle using both Static Pressure and Light Scattering Measurements. Northwestern University, Department of Mechanical Engineering and Astro nautical Sciences. Evanston Illinois

Coelho, A.A., J. Brenguier, and T. Perrin. (2005). "Droplet Spectra Measurements with the FSSP-100. Part I: Low Droplet Concentration Measurements." Journal of Atmospheric and Oceanic Technology 22(11): 1748-1755

Coney, M. W. E. (1973). The theory and application of conductance probes for the measurement of liquid film thickness in two-phase flow. Journal of Physics E: Scientific Instruments. 6(9), 903.

Cooper I. (2016). Doing Physics with Matlab. School of Physics, University of Sydney.http://www.physics.usyd.edu.au/teach_res/mp/mphome.htm. Accessed 23/03/2018

Cristiano Bigonha Tibiriçá, Francisco Júlio do Nascimento, Gherhardt Ribatski. (2010). Film thickness measurement techniques applied to micro-scale two-phase flow systems. Experimental Thermal and Fluid Science 34 463–473 (reorder).

Cui, Z. Wang, H. Chen, Z. Xu, Y. Yang, W. (2011). "A high-performance digital system for electrical capacitance tomography." Measurement Science and Technology **22**(5): 055503.

Cui, Z., Yang, C., Sun, B., & Wang, H. (2014). Liquid Film Thickness Estimation using Electrical Capacitance Tomography Measurement Science Review. Vol. 14, pp. 8.

Daisuke Ito, Yasushi Saito & Yuji Kawabata. (2014). Hybrid two phase flow measurements in a narrow channel using neutron radiography and liquid film sensor. Research Reactor Institute, Kyoto University, 2-1010 Asashiro-nishi, Kumatori, Sennan, Osaka 590-0494, Japan.

Damsohn, M., & Prasser, H. M. (2009). High-speed liquid film sensor for two-phase flows with high spatial resolution based on electrical conductance. Flow Measurement and Instrumentation. 20(1), 1-14.

Dyakowski, T., Laurent F.C. Jeanmeure, Artur J. Jaworski. (2000). "Applications of electrical tomography for gas–solids and liquid–solids flows — a review." Powder Technology **112**(3): 174-192.

Dye, J. E. and D. (1984). Baumgardner "Evaluation of the Forward Scattering Spectrometer Probe. Part I: Electronic and Optical Studies." Journal of Atmospheric and Oceanic Technology. 1(4): 329-344.

Franks F. (1972). Introduction-water, the unique chemical, in water a comprehensive treatise, Vol 1, Ed. F. Franks (Plenum Press, New York) pp 1-20

Fischer F, Hoppe D, Schleicher E, Mattausch G, Flaske H, Bartel R and Hampel U. (2008). An ultra-fast electron beam X-ray tomography scanner. Institute of Safety Research, Forschungszentrum Dresden-Rossendorf. Fraunhofer Institute of Electron Beam and Plasma Technology (FEP).

Fischer F. and U. Hampel. (2010). Ultra-fast electron beam X-ray computed tomography for two-phase flow measurement. Nuclear Engineering and Design. 240(9): 2254-2259.

Fukano, T. (1998). Measurement of time varying thickness of liquid film flowing with high speed gas flow by a constant electric current method (CECM). Nuclear Engineering and Design. 184(2–3), 363-377.

Gamio J. C., C. Ortiz-Alemán and R. Martin. (2005). Electrical capacitance tomography two-phase oil-gas pipe flow imaging by the linear back-projection algorithm. Instituto Mexicano del Petróleo, México, D. F., México. Geofísica Internacional, Vol. 44, No. 3, pp. 265-273

Gardner, G. C. (1963). "Events Leading to Erosion in the Steam Turbine." Proceedings of the Institution of Mechanical Engineers. 178(1): 593-601.

Gardiner, J. A. (1964). 'Measurement of the drop size distribution in water sprays by an electrical method', Instrum. Pract. 353

Gonzalez-Nakazawa A, Gamio J C and Yang W Q. (2005). Transient processes and noise in a tomography system: an analytical case study IEEE Sensors J. 5 321–9

Gyarmathy, G., (1963). "Kondersationsstoss-Diagramne für WasserdampfStrömungen," Forsch. Ing. Wes Vol. 29, (p. 105. 14.)

Gyarmathy, G., and H. Meyer. (1965). "Spontane Kondensation (VDI Forsch.-Heft 508)," Dusseldorf, VDI Verlag,

Halls, B. R., Theodore J. Heindel, Alan L. Kastengren, Terrence R. Meyer. (2014). Evaluation of X-ray sources for quantitative two- and three-dimensional imaging of liquid mass distribution in atomizing sprays. International Journal of Multiphase Flow. 59: 113-120.

Haller, K. K., Ventikos, Y., Poulikakos, D. and Monkewitz, P. (2002). Computational study of high-speed liquid droplet impact. Journal of Applied Physics 92, 2821. doi: 10.1063/1.1495533

Hampel, U., M. Speck, D. Koch, H.-J. Menz, H.-G. Mayer, J. Fietz, D. Hoppe, E. Schleicher, C. Zippe, H.-M. Prasser. (2005). Experimental ultra-fast X-ray computed tomography with a linearly scanned electron beam source. Flow Measurement and Instrumentation. 16(2–3): 65-72.

Han, H., Zhu, Z., & Gabriel, K. (2006). A study on the effect of gas flow rate on the wave characteristics in two-phase gas–liquid annular flow. Nuclear Engineering and Design. 236(24), 2580-2588.

Handy & Harman Brazing Book. (2001).

Hary, Charles P. (1959). Steam Quality Measurements using a radioactive tracer. Monterey, California: U.S. Naval Postgraduate School. http://hdl.handle.net/10945/14608.

Heckbert, P. (1998). Fourier Transforms and the Fast Fourier Transform (FFT) Algorithm

Herzog W. G., Cotton K. C., & Schofield P. (1972). ASME Steam Turbine Code Test Using Radioactive Tracers. Winter Annual Meeting of American Society of Mechanical Engineers. New York: ASME.

Hewitt, (2018). Gas-Liquid Flow. http://www.thermopedia.com/content/2/ Accessed 10/04/2018

Hewitt, G. F. and D. N. Roberts. (1969). Studies of two-phase flow patterns by simultaneous X-ray and flast photography. Atomic Energy Research Establishment, Harwell, United Kingdom.

Hoyle, B. S. (1996). Process Tomography Using Ultrasonic Sensors. Measurement Science Technology. 7:272-280.

Industrial Process Gamma Tomography. (2007). Final report of a coordinated research-project-2003-2007. http://wwwpub.iaea.org/MTCD/publications/PDF/te_1589_web.pdf.

Ismail I, Areeba Shafquet and Mohd Noh Karsiti. (2011). Void Fraction Estimation by Using Electrical Capacitance Tomography and Differential Pressure in an Air-Water Co-Current Bubble Column. Electrical and Electronic Engineering Department, University Teknologi PETRONAS, Malaysia.

Jamaludin, J. Zawahir, M. Rahim, R. Yunus, F. Ayob, N. Muhammad, Aw, S. Fadzil, N. Zakaria, Z. Rahiman, M. *(2013). A review of Tomography System. Journal Technology Sciences and Engineering. 64:5 47-51*

Jaworek, A., Krupa, A., & Trela, M. (2004). Capacitance sensor for void fraction measurement in water/steam flows. Flow Measurement and Instrumentation, 15(5-6)-317–324. Retrieved from http://www.sciencedirect.com/science/article/pii/S095559860400023

Jiang, Y. & Rezkallah, K. S. (1993). An experimental study of the suitability of using a gamma densitometer for void fraction measurements in gas-liquid flow in a small diameter tube. Measurement Science and Technology. 4(4), 496.

Kachuriner, Y. Y. and V. G. Orlik. (2007). "Specifics of initial steam condensation and its influence on corrosion damage in turbines." Thermal Engineering. 54(2): 118-122.

Kirby, K. R. (1956). Thermal Expansion of Polytetrafluoroethylene. Journal of Research of the National Bureau of Standards Vol. 57, No 2. Paper 2696

Klausner, J. F., Zeng, L. Z., & Bernhard, D. M. (1992). Development of a film thickness probe using capacitance for asymmetrical two-phase flow with heat addition. Review of Scientific Instruments. 63(5), 3147-3152.

Kleitz, A. and J. J. Courant. (1989). "Probes for industrial particle measurement: Application for water droplet sizing in wet steam turbines." Journal of Aerosol Science. 20(8): 1477-1480.

Kleitz, A. and J. M. Dorey. (2004). "Instrumentation for wet steam." Proceedings of the Institution of Mechanical Engineers, Part C: Journal of Mechanical Engineering Science. 218(8): 811-842.

Li, J., Chen, Q., Dong, X., & Liu, S. (2005). Electrical capacitance tomography measurement of flow patterns and film thickness in a thermosyphon. Journal of Thermal Science. 14(1), 81-86.

Li, W., and B. S. Hoyle. (1997). Ultrasonic Process Tomography Using Multiple Active Sensors for Maximum Real-Time Performance. Chemical Engineering Science. 52: 2161 -2170

Liu, Y., Qinxue, P., Chunguang, X., Xianghui, G., & Kai, P. (2013). Immersion ultrasonic reflection tomography by annular array system. Far East Forum on Nondestructive Evaluation/Testing: New Technology & Application (FENDT), Jinan, China.

Liu, W., Tamai, H., & Takase, K. (2013). Pressure Drop and Void Fraction in Steam-Water Two-Phase Flow at High Pressure. Journal of Heat Transfer. 135(8), 081502-081502.

London South Bank Unversity. (2017). Water and Microwaves. Available at http://www1.lsbu.ac.uk/water/microwave_water.html [Accessed 8 March 2018]

Lu, Q., Suryanarayana, N. V. and Christodoulu, C. (1993). Film thickness measurement with an ultrasonic transducer, Experimental Thermal and Fluid Science 7. 354–361.

Lynnworth, L. C., & Liu, Y. Ultrasonic flowmeters: Half-century progress report, 1955–2005. Ultrasonics, 44, Supplement(0). e1371-e1378.

Malhotra, A., & Panda, D. M. R. (2001). Thermodynamic properties of superheated and supercritical steam. Applied Energy. 68(4), 387-393.

Martínez F, Velázquez M, Martínez A, Silva F, Montes S and Chávez O. (2011). "Theoretical and Numerical Analysis of the Mechanical Erosion in Steam Turbine Blades. Part I," *Energy and Power Engineering*, Vol. 3 No. 3, pp. 227-237. doi: 10.4236/epe.2011.33029.

Mohd Hafiz Fazalul Rahiman, Ruzairi Abdul Rahim, Herlina Abdul Rahim and Nor Muzakkir Nor Ayob. (2012). Design and Development of Ultrasonic Process Tomography. University Malaysia Perlis (UniMAP) University Teknologi Malaysia (UTM).

Morala EC, Cheong D, Wan PT, Irons GA, Chang JS. (1983). Ultrasonic wave propagation in a bubbly gas–liquid two-phase flow. In: Proc. 3rd multiphase flow and heat transfer international symposium.

Mor I, Vartsky D, Bar D, Feldman G, Goldberg M. B, Katz D, Sayag E, Shmueli I, Cohen Y, Tal A, Vagish Z, Bromberger B, Dangendorf V, Mugai D. b , Tittelmeier K, Weierganz M. (2009). High Spatial Resolution Fast-Neutron Imaging Detectors for Pulsed Fast-Neutron Transmission Spectroscopy. Physikalisch-Technische Bundesanstalt (PTB). 38116 Braunschweig, Germany.

Miles J. (1957). On the generation of surface waves by shear flows, Department of Engineering, University of California, Los Angeles.

Mishima, K., Hibiki, T., & Nishihara, H. (1997). Visualization and measurement of two-phase flow by using neutron radiography. Nuclear Engineering and Design. 175(1–2), 25-35.

Mishima, K., & Hibiki, T. (1998). Development of high-frame-rate neutron radiography and quantitative measurement method for multiphase flow research. Nuclear Engineering and Design. 184(2–3), 183-201.

Nagpurwala, Q. H. Steam Turbines. Ramaiah School of Advanced Studies

Oliveira, F. S. d., Yanagihara, J. I., & Pacífico, A. L. (2006). Film thickness and wave velocity measurement using reflected laser intensity. Journal of the Brazilian Society of Mechanical Sciences and Engineering. 28, 30-36.

Onimisi, M. Y. & Ikyumbur, J. T. (2015). Comparative Analysis of Dielectric Constant and Loss Factor of Pure Butan-1-ol and Ethanol. American Journal of Condensed Matter Physics. 69-75 DOI: 10.5923/j.ajcmp.20150503.02

Özgüt, M. R., Chen, J. C., & Eberhardt, N. (1973). A capacitance method for measurement of film thickness in two-phase flow. Review of Scientific Instruments. 44(12), 1714-1716.

Pedersen, P. C., Cakareski, Z., & Hermanson, J. C. (2000). Ultrasonic monitoring of film condensation for applications in reduced gravity. Ultrasonics. 38(1–8), 486-490.

Pląskowski, A., Beck, M. S., Thorn, R., & Dyakowski, T. (1995). Imaging Industrial Flows: Applications of Electrical Process Tomography. Bristol: Institute of Physics Pub. Retrieved from http://books.google.com/books?id=1p-G0rfJZI0C

Roshani, G. H., Nazemi, E., Feghhi, S. A. H., & Setayeshi, S. (2015). Flow regime identification and void fraction prediction in two-phase flows based on gamma ray attenuation. Measurement. 62(0), 25-32.

Rouleau J. F., Goyrtte J. and Bose T. K. (2000). “Performance of a microwave sensor for the precise measurement of water vapor in gases”, IEEE Transactions on Dielectrics and Electrical Insulation, Vol.7, pp.825-831

Ruzairi Abdul Rahim, Mohd Hafiz Fazalul Rahiman, Ng Wei Nyap and Chan Kok San. (2004). On Monitoring of Liquid/Gas Flow using Ultrasonic Tomography. Journal Teknologi, 40(D) Jun. 2004: 77–88 Process Tomography Research Group (PROTOM), Control & Instrumentation Engineering Department, Faculty of Electrical Engineering, University Teknologi Malaysia, 81310 UTM.

Ryzhenkov, Lebedeva, and Mednikov. (2011). Erosion wear of the blades of wet steam turbine stages: present state of the problem and methods for solving it. Thermal Engineering 58:713

Schiebener P., Straub J., Levelt Sengers J. M. H. and Gallagher J. S. (1990). Refractive Index of Water and Steam as Function of Wavelength, Temperature and Density. J. Phys. Chem. Ref. Data, Vol. 19, No.3, 1990

Seeger, A., Affeld, K., Goubergrits, L., Kertzscher, U., Wellnhofer, E., & Delfos, R. (2002). X-ray-Based Flow Visualization and Measurement. Annals of the New York Academy of Sciences. 972(1), 247-253.

Shafquet, A., Ismail, I., & Karsiti, M. N. (2010). Study of Void Fraction Measurement in a Two Phase Flow by Using Differential Pressure and Electrical Capacitance Tomography. Fourth Asia International Conference on Mathematical/Analytical Modelling and Computer Simulation (AMS), Kota Kinabalu, Malaysia.

Shu-e, Z. and L. cLu. (2010). The error analysis and improvement of microwave resonant cavity method in steam turbine exhaust wetness measurement.

Sillars, R. W. (1937). The properties of a dielectric containing semiconducting particles of various shapes. Wireless Section, Institution of Electrical Engineers-Proceedings of the, 12(35), 139–155.

St-Arnaud J. M, Bose T. K, Okambawa II and Ingrain D. (1992). "Application of the permittivity measurements to study the influence of the small quantities of water vapor on the compressibility factor of methane", Int. J, Thermophys. Vol. 13, pp. 6855697

Stürzel, T. Bieberle, M. Laurien, E. Hampel, U. Barthel, F. Menz, H. J. Mayer, H. G. (2011). Experimental facility for two- and three-dimensional ultrafast electron beam X-ray computed tomography. Review of Scientific Instruments. 82(2): 023702.

Takenaka, N., & Asano, H. (2005). Quantitative CT-reconstruction of void fraction distributions in two-phase flow by neutron radiography. Nuclear Instruments and Methods in Physics Research Section A: Accelerators, Spectrometers, Detectors and Associated Equipment. 542(1–3), 387-391.

Tarelin, A. A. (2014). "Electrization of a wet steam flow and its influence on reliability and efficiency of turbines." Thermal Engineering 61(11): 790-796.

Teflon from - 1900 to +3000 C. Journal of Research of the National Bureau of Standards. Vol. 57, No. 2,

T.E. Mason, T.A. Gabriel, R.K. Crawford, K.W. Herwig, F. Klose, and J.F. Ankner. (2000). The Spallation Neutron Source: A Powerful Tool for Materials Research. SNS Project, 701 Scarboro Rd. Oak Ridge.

Tianming Chen, John R. Bowler and Nicola Bowler. (2014). Analytical solution for capacitance calculation of a curved patch capacitor that conforms to the curvature of a homogeneous cylindrical dielectric rod. Applied Physics Letters 104, 032901.

Thorpe, A. D. and Wood, M. R. (1967). Coarse Water Distribution within the Low Pressure Stages of a 350 MW Steam Turbine. Proceedings of the Institution of Mechanical Engineers 1967-69. Vol 182 Pt 3 H

Theodore J. Heindel, Terrence c. Jensen and Joseph N. Gray. (2007). Visualizing Fluid Flows with X rays. Department of Mechanical Engineering Centre for Non-destructive Evaluation Iowa State University Ames, Iowa 50011-2161. 5th Joint ASME/JSME Fluids Engineering Conference July 30-August 2, 2007 San Diego, California USA.

Theodore J. Heindal, Jeremy L. Hubers, Terrence C. Jensen, Joseph N. Gray and Alexander C. Striegal. (2005). Using X rays for Multiphase Flow Visulization. ASME Fluids Engineering Division Summer Meeting and Exhibition Houston Texas

Thwaites, G. R., Kulov, N. N., & Nedderman, R. M. (1976). Liquid film properties in two-phase annular flow. Chemical Engineering Science. 31(6), 481-486.

Thwaites G. R., (1973). Ph.D. Thesis, Cambridge

Tomographic Image Reconstruction. (2015). Ultrasound. (2006). http://courses.washington.edu/bioen508/Lecture6US.pdf. Accessed 13/01/2017

Utaka Y, Tasaki Y and Okuda S. (2004). Micro-liquid–layer behaviour and heat transfer Characteristics of boiling in a micro-channel vaporizer, in: Proceedings of the 10th Brazilian Congress of Thermal Science and Engineering – ENCIT, Rio de Janeiro, Brazil. Paper 0798,

Vernon, Kris (2014) A photographic probe for wet steam. EngD thesis, University of Nottingham.

Veiga, J., Cipolatti, C. and Furtado, A. (2009). Superheated Steam Test Rig for Compressed Non-Asbestos Gaskets Evaluation. Proceedings of the ASME 2009 Pressure Vessels and Piping Division Conference. PVP2009-77466

Wada, S., Kikura, H., & Aritomi, M. (2006). Pattern recognition and signal processing of ultrasonic echo signal on two-phase flow. Flow Measurement and Instrumentation. 17(4), 207-224.

Whitaker, S. (1972). Forced Convection Heat Transfer Correlations for Flow in Pipes, Past Flat Plates, Single Cylinders, Single Spheres, and for Flow in Packed Beds and Tube Bundles. Department of Chemical Engineering University of California

Wuqiang, Y. (2010). "Design of electrical capacitance tomography sensors." Measurement Science and Technology **21**(4): 042001.

www.nabertherm.com. (2018). Nabertherm 240L. GmbH, D-28865 Lilienthal/Germany

Yamada N., & Lindberg G. (2008). Tracer Measurement Technique and its Application to onsite Feed Water Calibration and Performance Analysis of Nuclear Power Plants. AIST / SP Workshop on Flow Measurements in Nuclear Power Plants. Tokyo, Japan: Alstom Power.

Yamashita, F. Mori, Y. Fujita, S. (1979). Sizes and size distributions of bubbles in a bubble column comparison between the two point electric probe method and the photgraphic method. Journal of Chemical Engineering of Japan 12(1): 5-9.

Yang, W. Q., Chondronasios, A., Nattrass, S., Nguyen, V. T., Betting, M., Ismail, I., & McCann, H. (2004). Adaptive calibration of a capacitance tomography system for imaging water droplet distribution. Flow Measurement and Instrumentation. 15(5–6), 249-258.

Yang, W. Q. and Peng, L. (2003). Image reconstruction algorithms for electrical capacitance tomography. Meas. Sci. Technol. 14 R1

Yang, W. Q. and York T. A. (1999). "New AC-based capacitance tomography system." IEE Proceedings - Science, Measurement and Technology **146**(1): 47-53.

Yongqian Li, Junchao Zhao, Shu'e Zhang, Zhi Yang and Hua Zhao. (2006). A Microwave Cavity Resonator Based System for Wetness Measurement in Steam Turbine. Department of Electronics and Communication Engineering North China Electric Power University, Baoding, 071003, Hebei, China

Yu, S. C. M., Tso, C. P., & Liew, R. (1996). Analysis of thin film thickness determination in two-phase flow using a multifiber optical sensor. Applied Mathematical Modelling. 20(7), 540-548.

Zboray, R., & Prasser, H. M. (2013). Measuring liquid film thickness in annular two-phase flows by cold neutron imaging. Experiments in Fluids. 54(9), 1-15.

Zboray, R., Mor, I., Dangendorf, V., Stark, M., Tittelmeier, K., Cortesi, M., & Adams, R. (2014). High-frame rate imaging of two-phase flow in a thin rectangular channel using fast neutrons. Applied Radiation and Isotopes. 90, 122-131.

Zboray, R., Dangendorf, V., Mor, I., Bromberger, B. and Tittelmeier, K. (2015). Time-resolved fast-neutron radiography of air-water two-phase flows in a rectangular channel by an improved detection system, Paul Scherrer Institute, PSI Villigen, 5232, Switzerland, Physikalisch-Technische Bundesanstalt (PTB), Braunschweig, 38116, Germany, Soreq NRC, Yavne, 81800, Israel.

Zhao, Y., Bi, Q., & Hu, R. (2013). Recognition and measurement in the flow pattern and void fraction of gas–liquid two-phase flow in vertical upward pipes using the gamma densitometer. Applied Thermal Engineering. 60(1–2), 398-410.

Zheng, Y., Zhang, Y,. Junqiang Hu and Wenle Gao. (2012). Pulsatile Drug Delivery System Based on Electrohydrodynamic Method. Department of Mechanical Engineering, Columbia University, New York, NY 10027

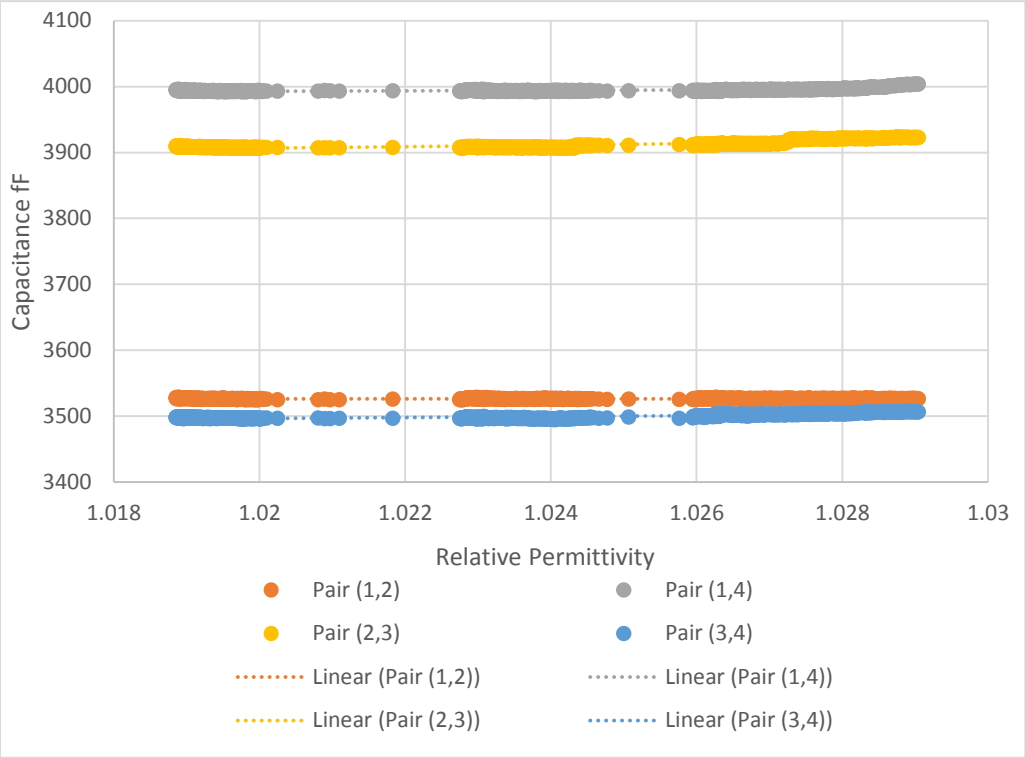
Zhu, I. P, Matthews and A. H. Samuel. (1996). "Quantitative measurements of analyte gases in a microwave spectrometer using a dynamic sampling method", Rev. Sci. Instrum, Vol. 67, no 7, pp, 2496-2501

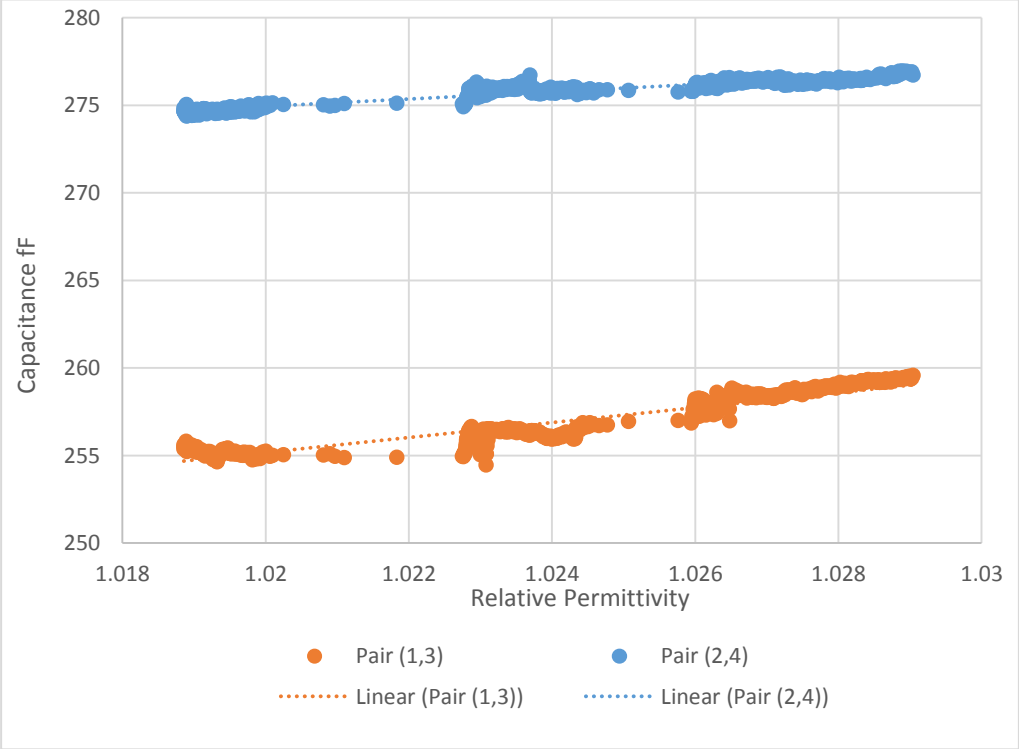
Zunft, S., & Bissinger, N. (1999). Measurement of steam quality for the control of steam-generating collectors. Le Journal de Physique IV, 09(PR3), Pr3–501–Pr3–506.doi:10.1051/jp4:199937

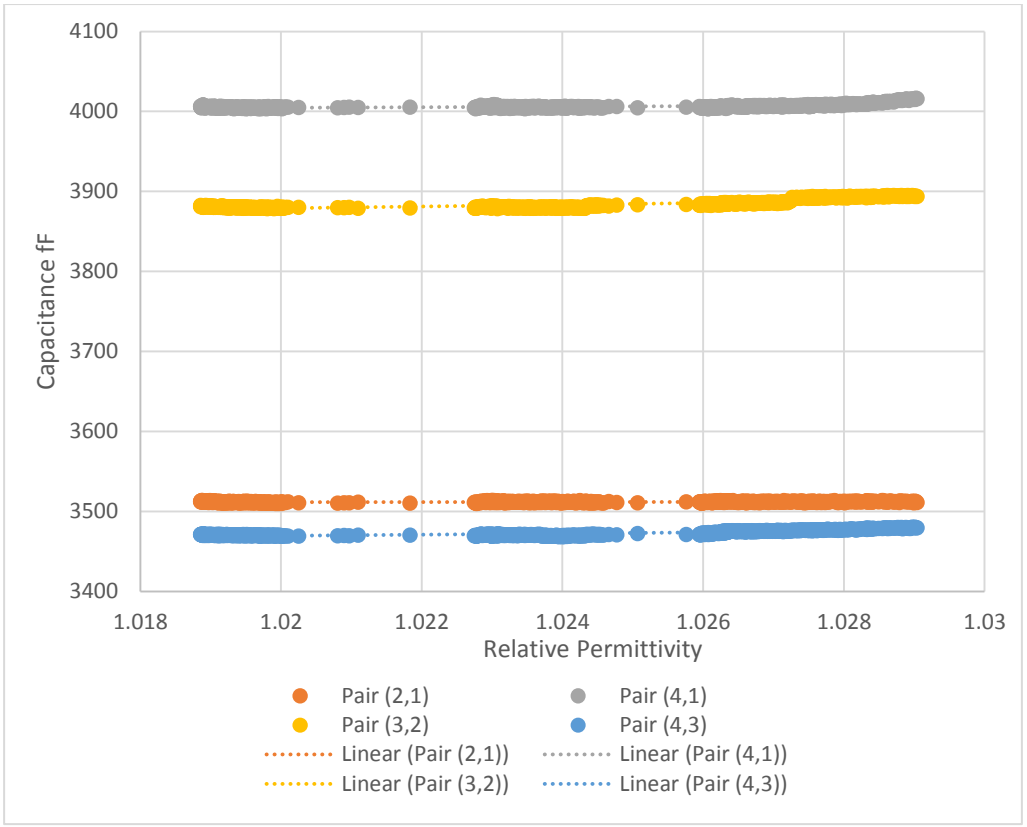
Chapter 9. Appendix

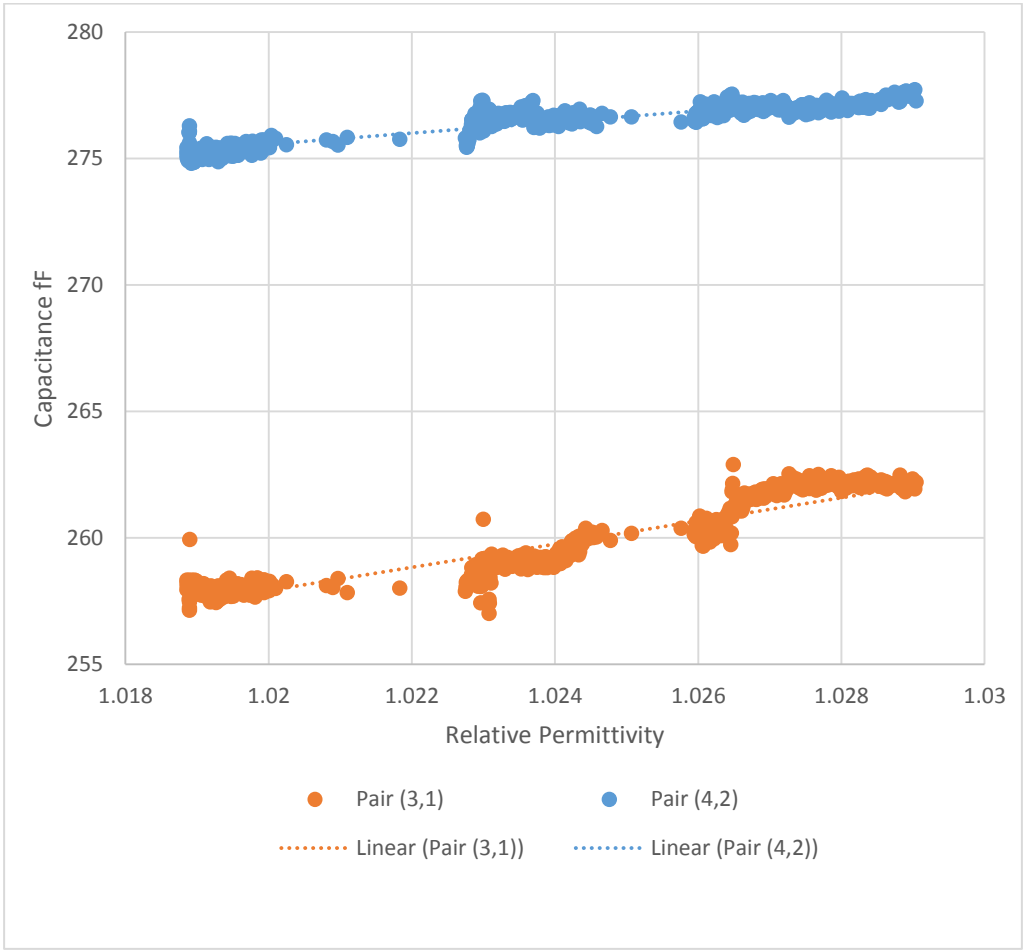
Calibration capacitance against relative permittivity (back pressure regulator used)

Test 1

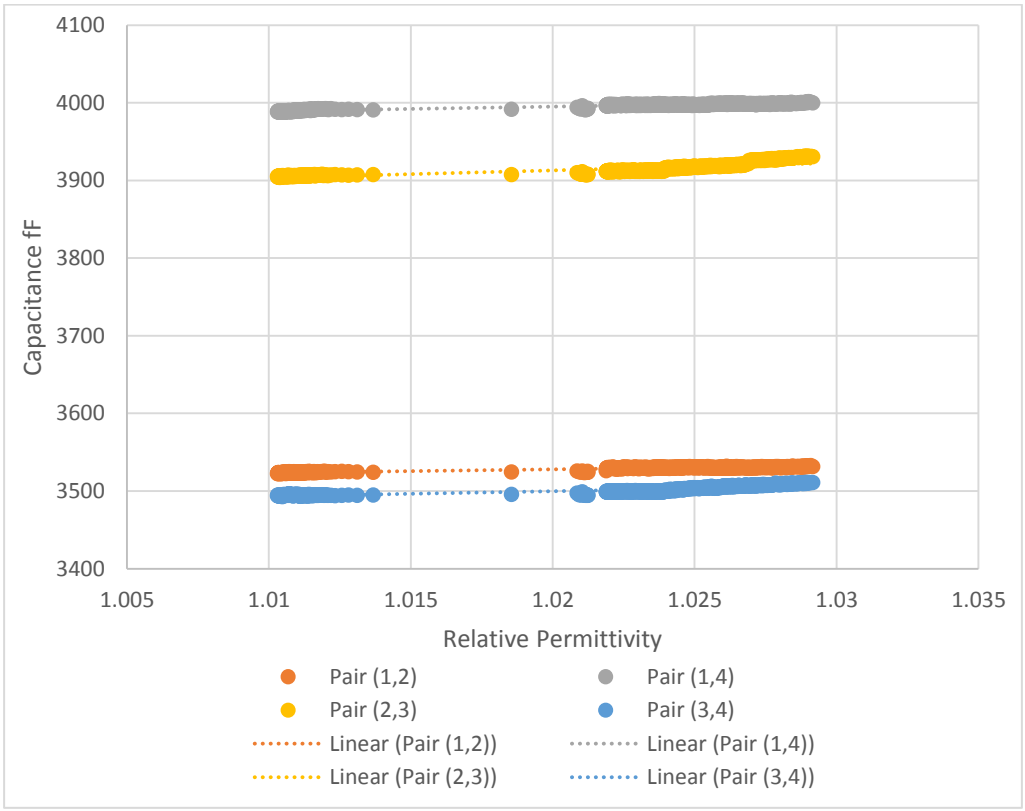


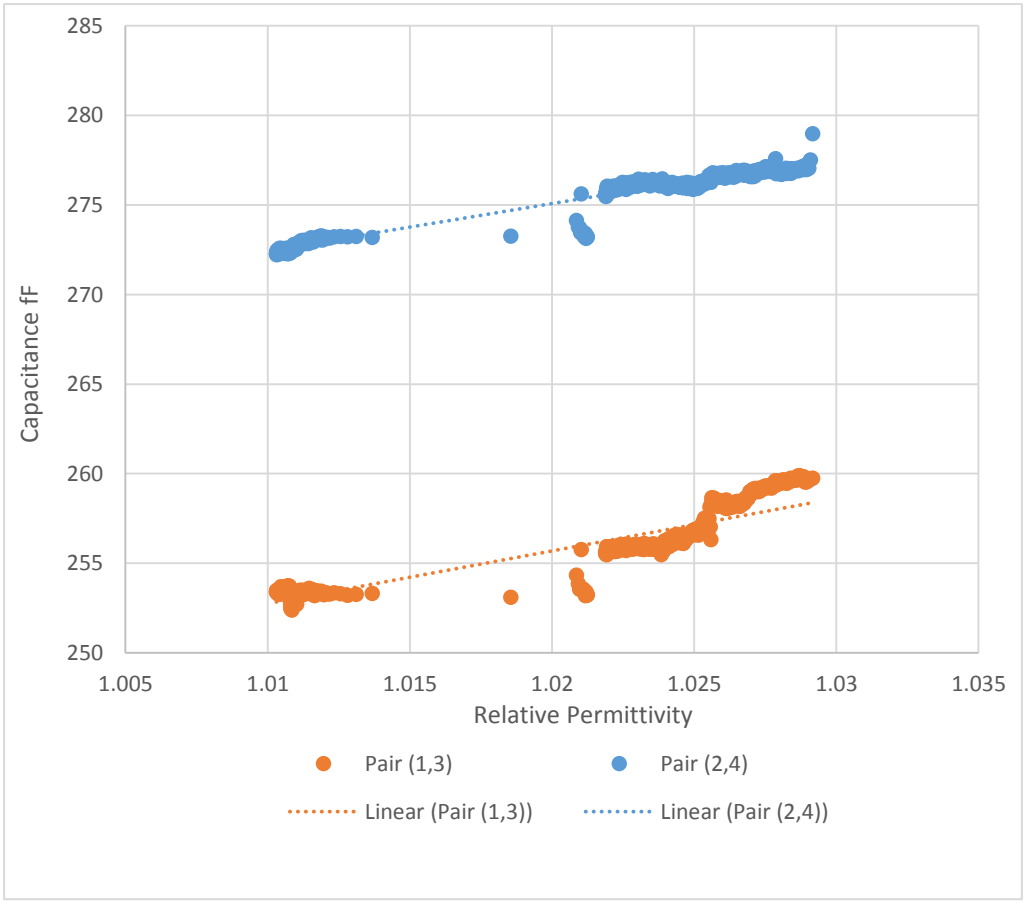


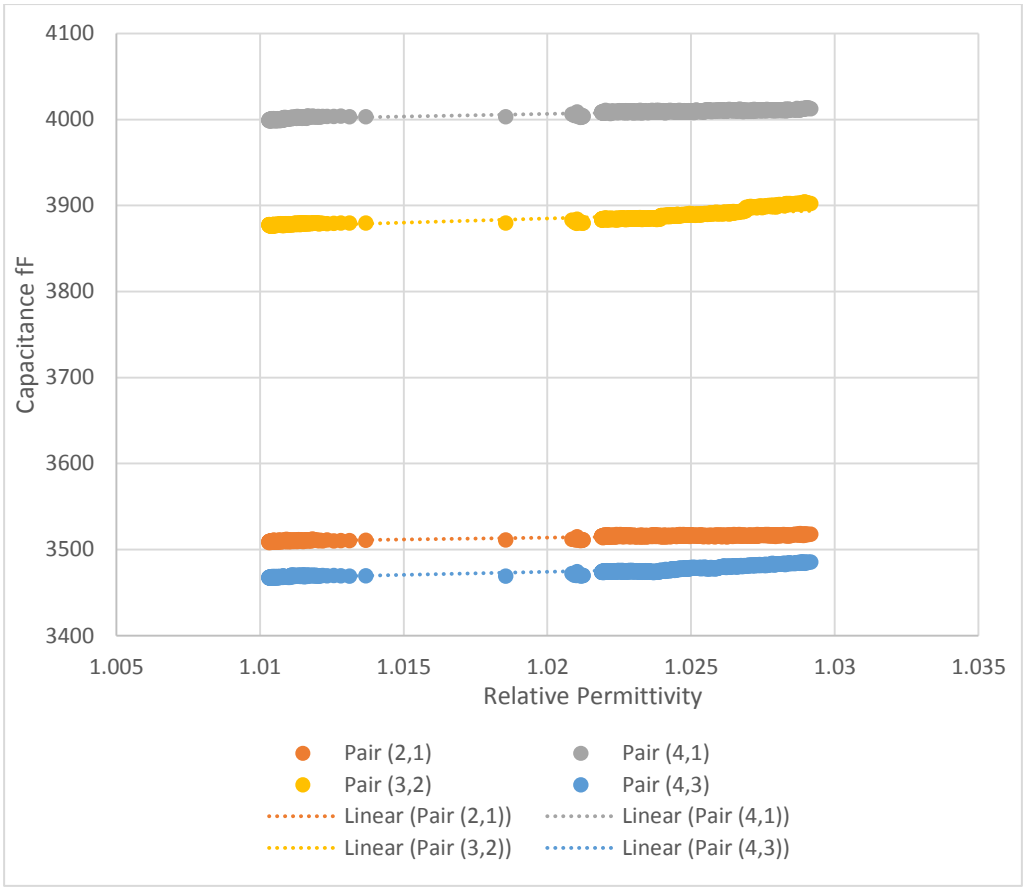

4100
4000
3900
3800
3700
3600
3500
3400
Capacitance fF
1.018
1.02
1.022
1.024
1.026
1.028
1.03
Relative Permittivity
Pair (2,1)
Pair (4,1)
Pair (3,2)
Pair (4,3)
Linear (Pair (2,1))
Linear (Pair (4,1))
Linear (Pair (3,2))
Linear (Pair (4,3))

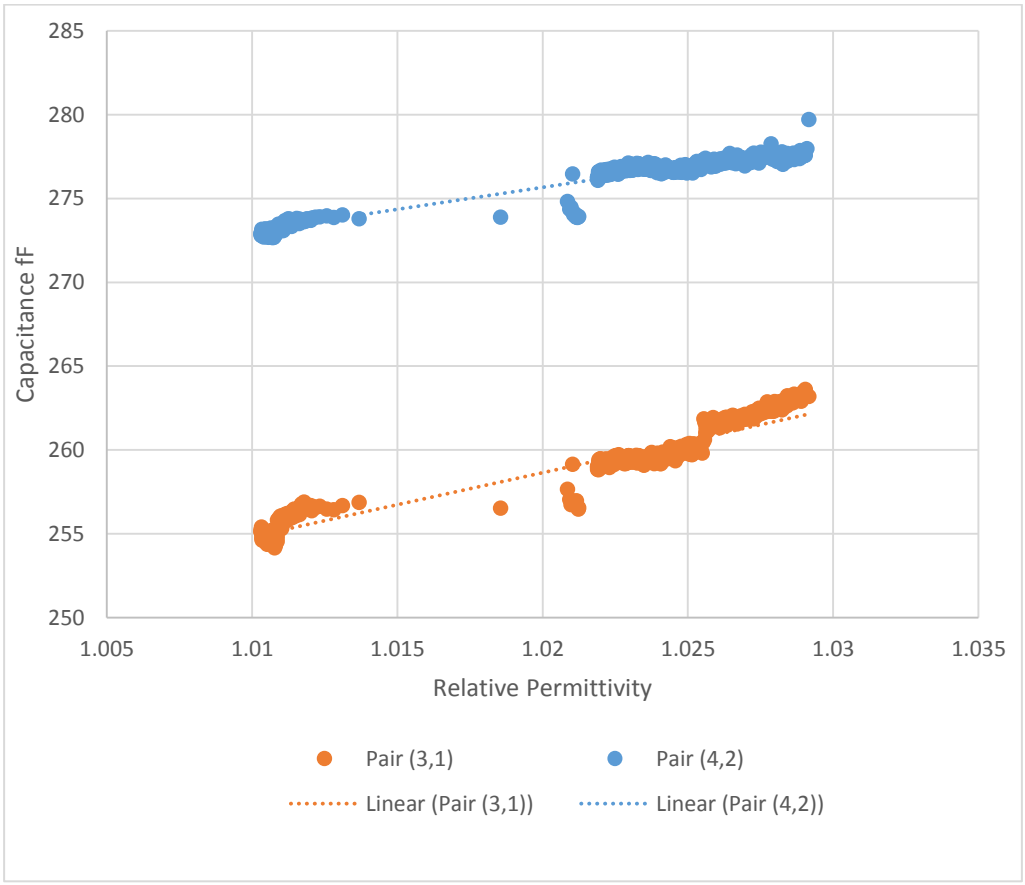

280
275
270
265
260
255
Capacitance fF
1.018
1.02
1.022
1.024
1.026
1.028
1.03
Relative Permittivity
Pair (3,1)
Pair (4,2)
Linear (Pair (3,1))
Linear (Pair (4,2))

Test 2

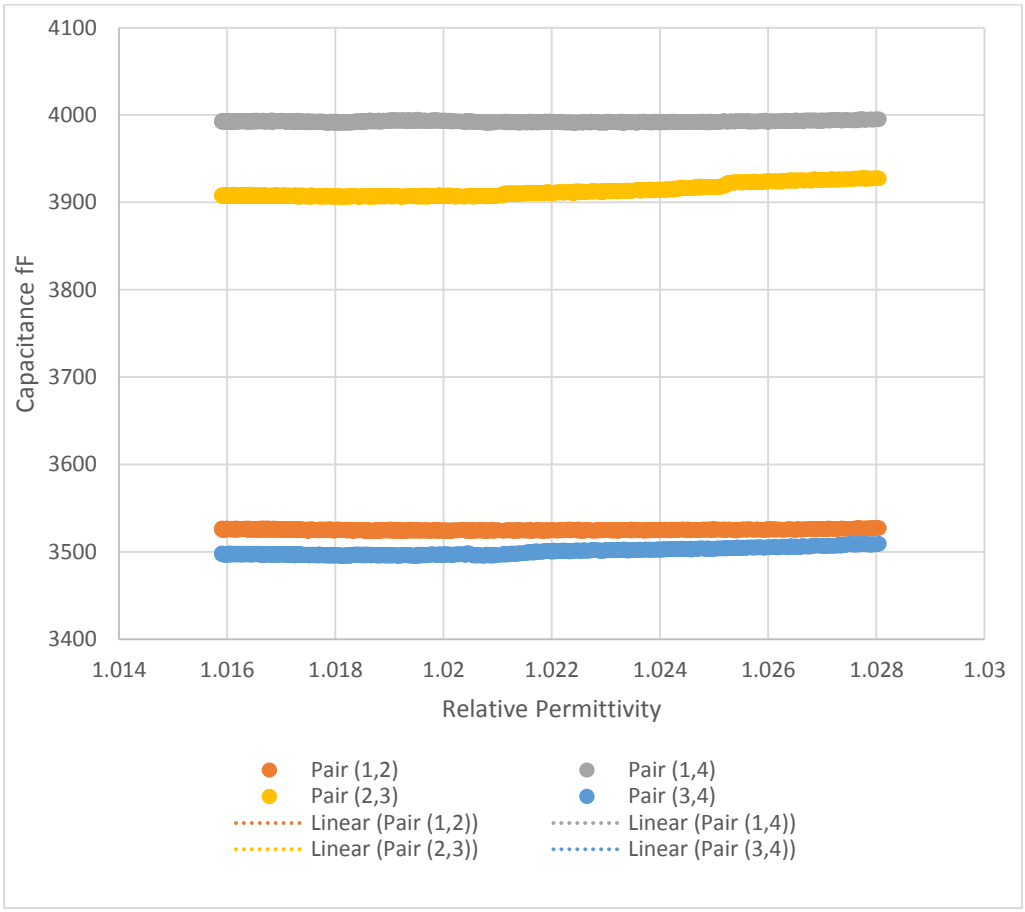

4100
4000
3900
3800
3700
3600
3500
3400
Capacitance fF
1.005
1.01
1.015
1.02
1.025
1.03
1.035
Relative Permittivity
Pair (1,2)
Pair (1,4)
Pair (2,3)
Pair (3,4)
Linear (Pair (1,2))
Linear (Pair (1,4))
Linear (Pair (2,3))
Linear (Pair (3,4))

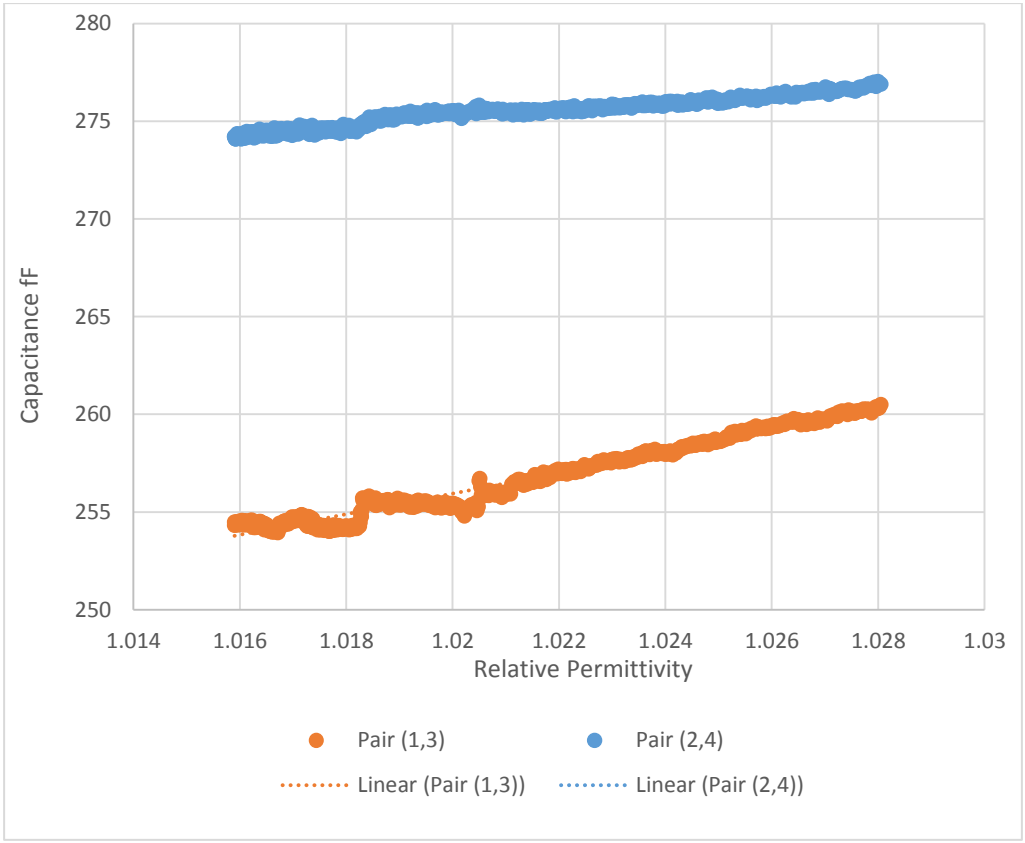

285
280
275
270
265
260
255
250
Capacitance fF
1.005
1.01
1.015
1.02
1.025
1.03
1.035
Relative Permittivity
Pair (1,3)
Pair (2,4)
Linear (Pair (1,3))
Linear (Pair (2,4))

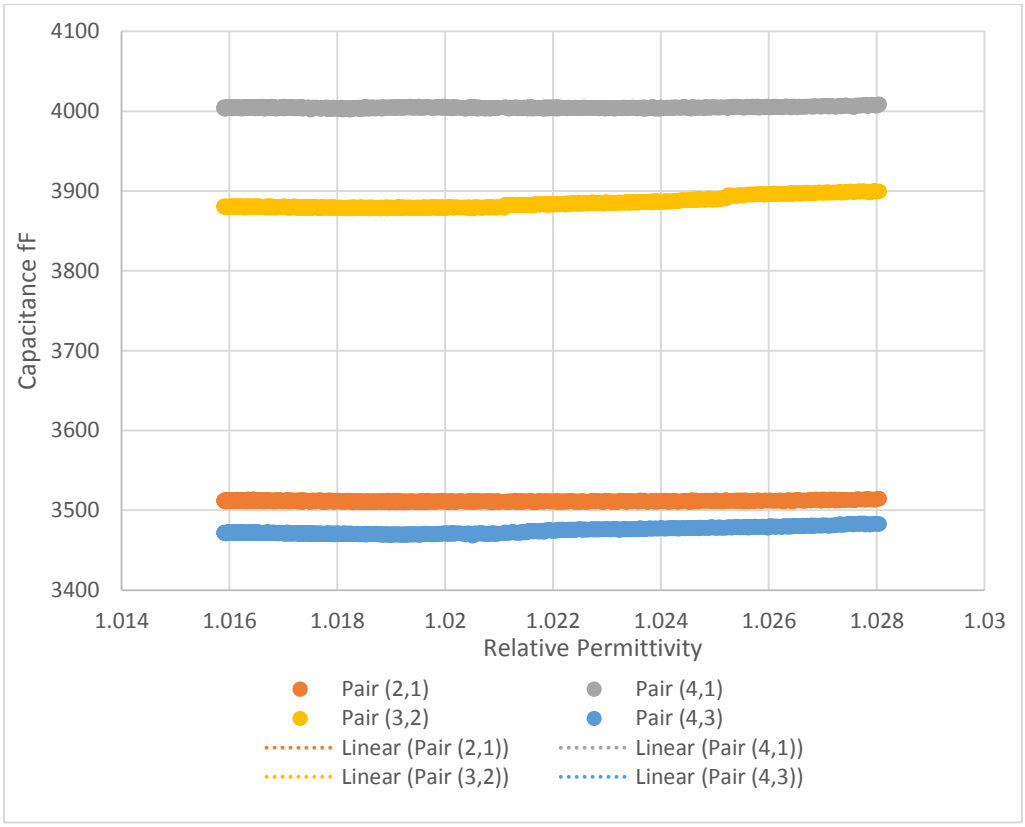

4100
4000
3900
3800
3700
3600
3500
3400
Capacitance fF
1.005
1.01
1.015
1.02
1.025
1.03
1.035
Relative Permittivity
Pair (2,1)
Pair (4,1)
Pair (3,2)
Pair (4,3)
Linear (Pair (2,1))
Linear (Pair (4,1))
Linear (Pair (3,2))
Linear (Pair (4,3))

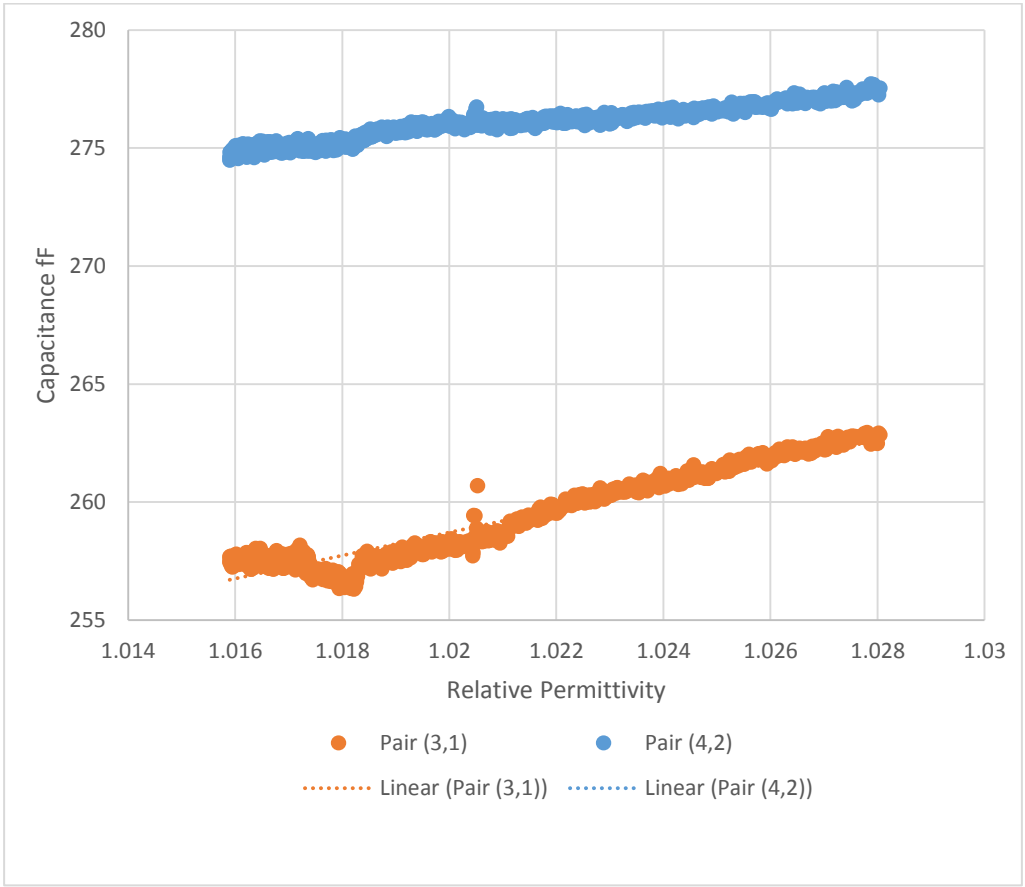

285
280
275
270
265
260
255
250
Capacitance fF
1.005
1.01
1.015
1.02
1.025
1.03
1.035
Relative Permittivity
Pair (3,1)
Pair (4,2)
Linear (Pair (3,1))
Linear (Pair (4,2))

Test 4 (back pressure regulator not used)



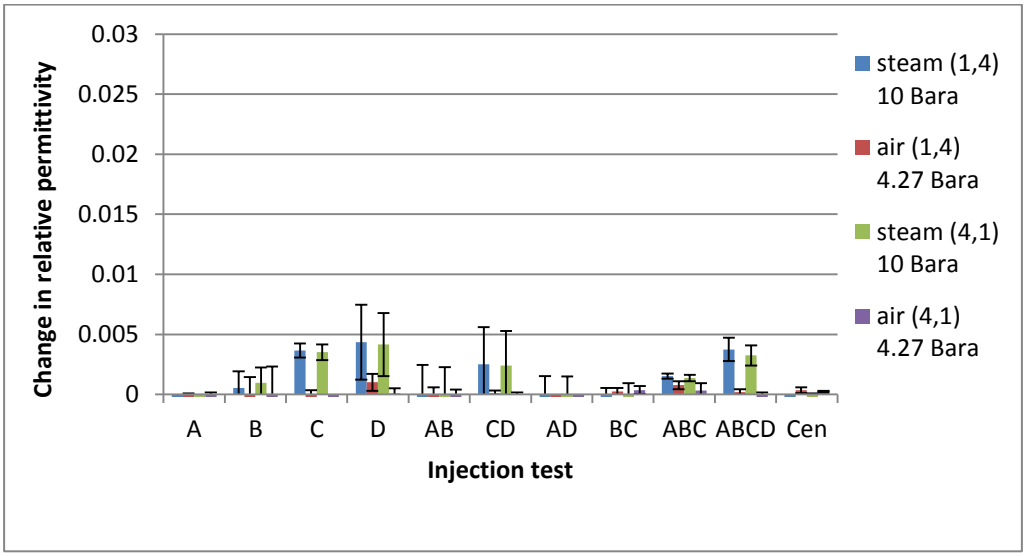


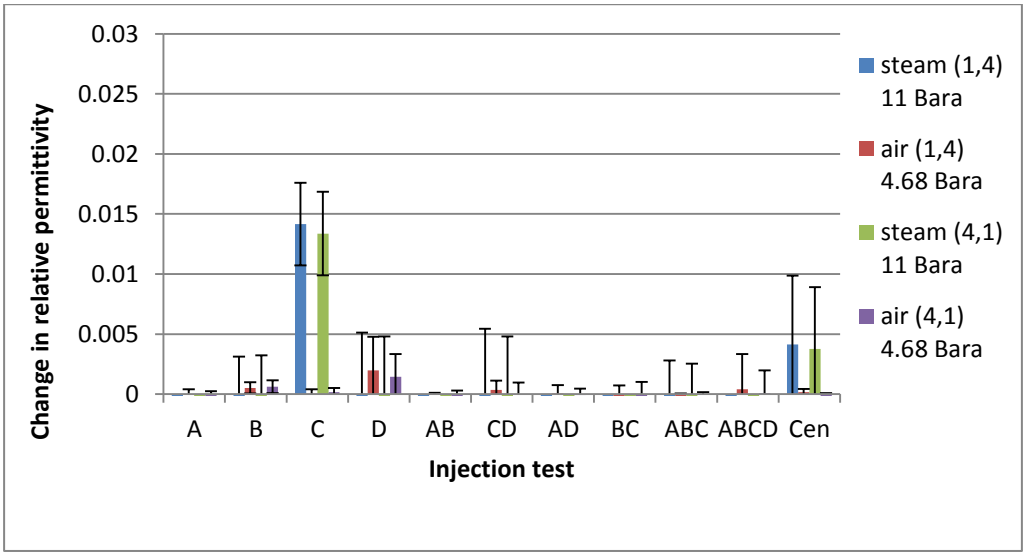

4100
4000
3900
3800
3700
3600
3500
3400
Capacitance fF
1.014
1.016
1.018
1.02
1.022
1.024
1.026
1.028
1.03
Relative Permittivity
Pair (2,1)
Pair (4,1)
Pair (3,2)
Pair (4,3)
Linear (Pair (2,1))
Linear (Pair (4,1))
Linear (Pair (3,2))
Linear (Pair (4,3))

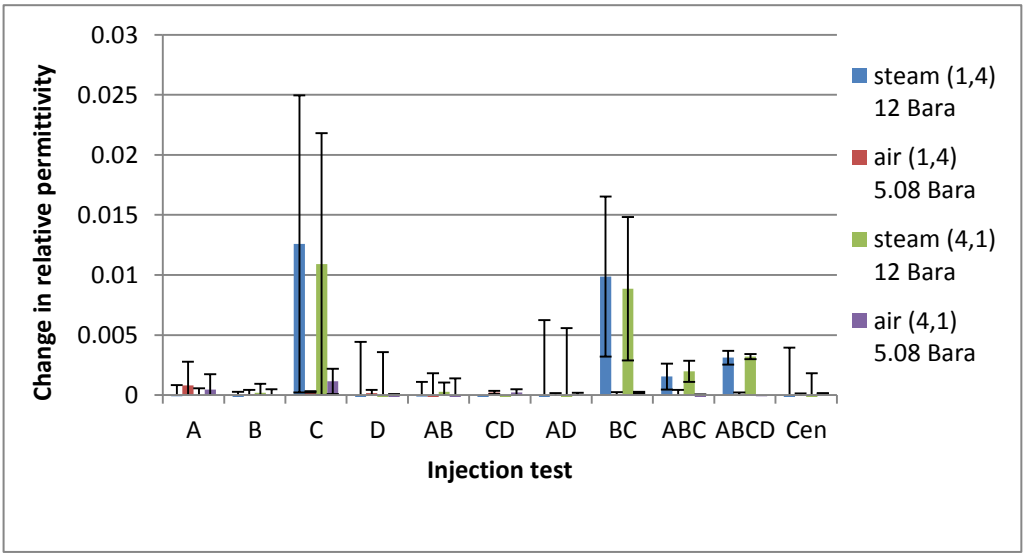

280
275
270
265
260
255
Capacitance fF
1.014
1.016
1.018
1.02
1.022
1.024
1.026
1.028
1.03
Relative Permittivity
Pair (3,1)
Pair (4,2)
Linear (Pair (3,1))
Linear (Pair (4,2))

9.2 Appendix 2:

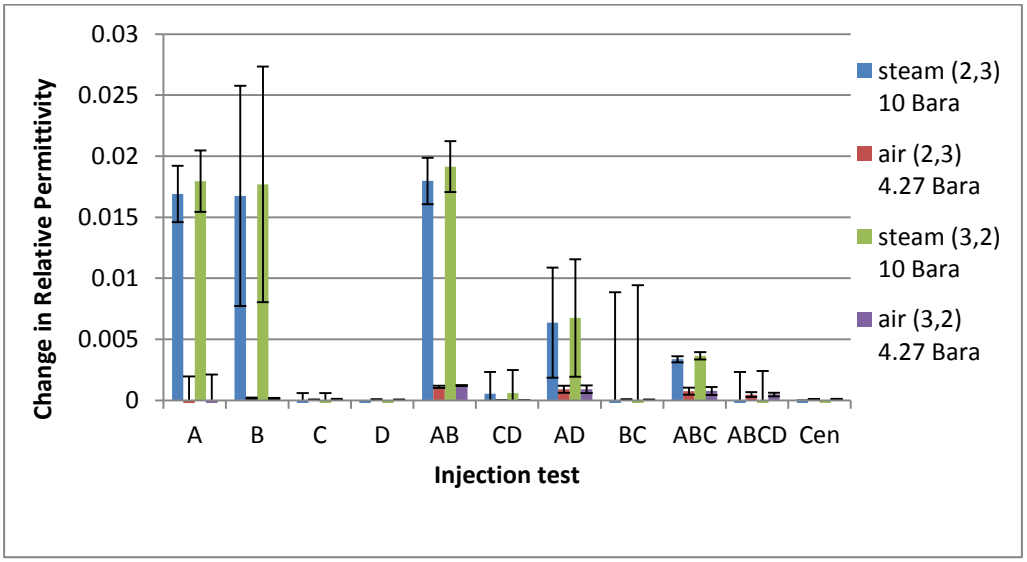
Results for the average change in relative permittivity Results for electrode pairs (1, 4) and (4, 1):

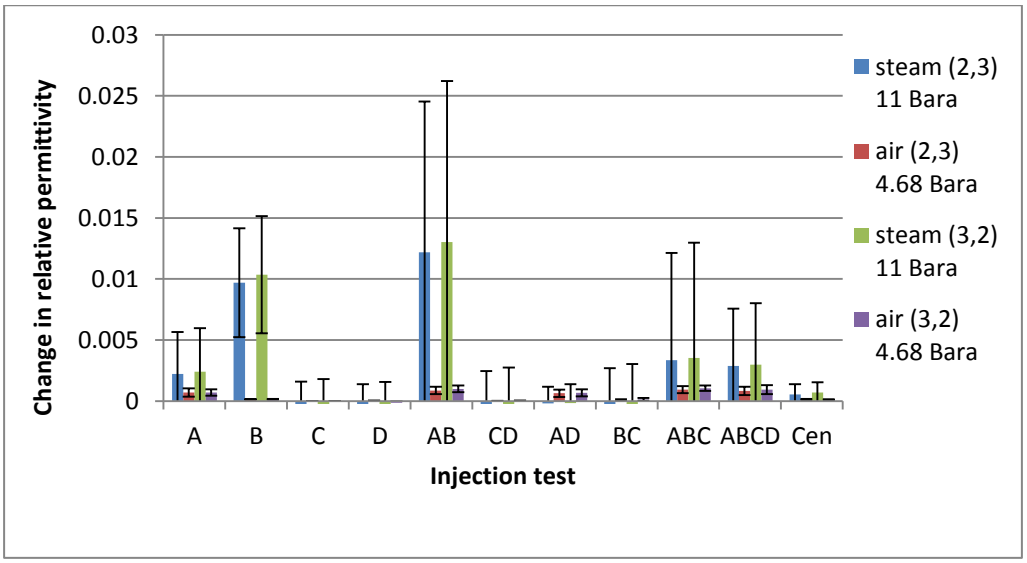


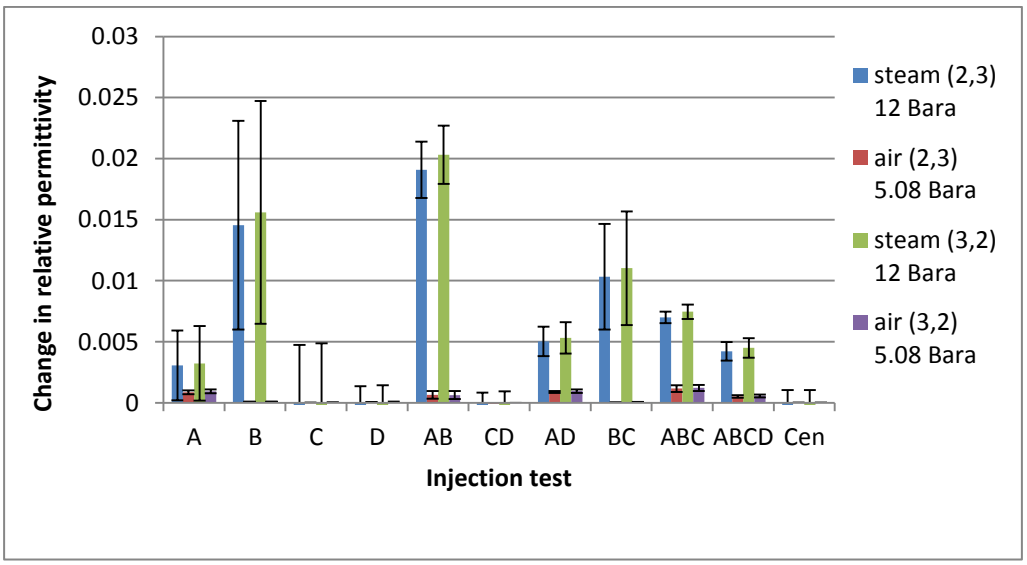




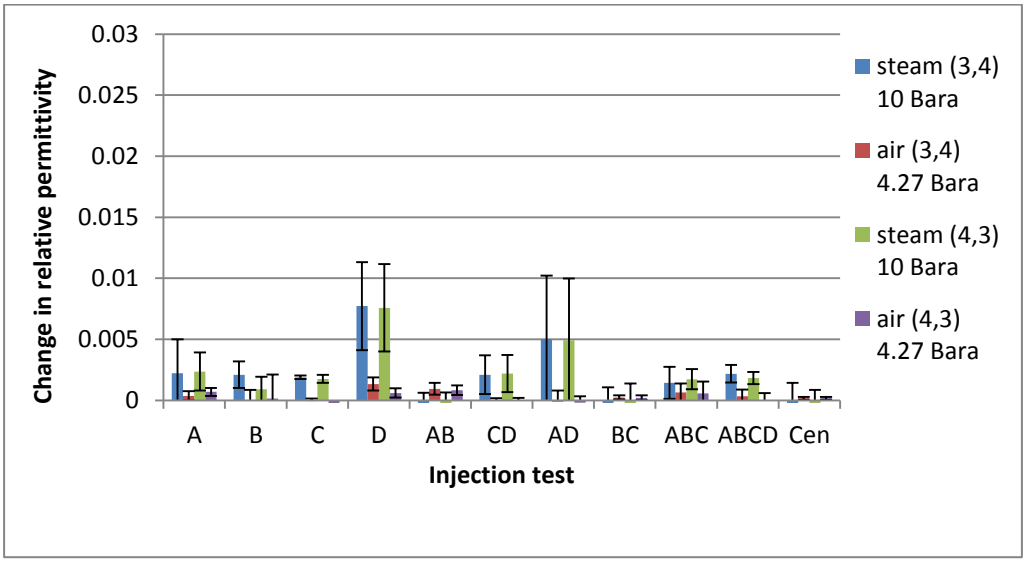
Results for electrode pairs (2, 3) and (3, 2):

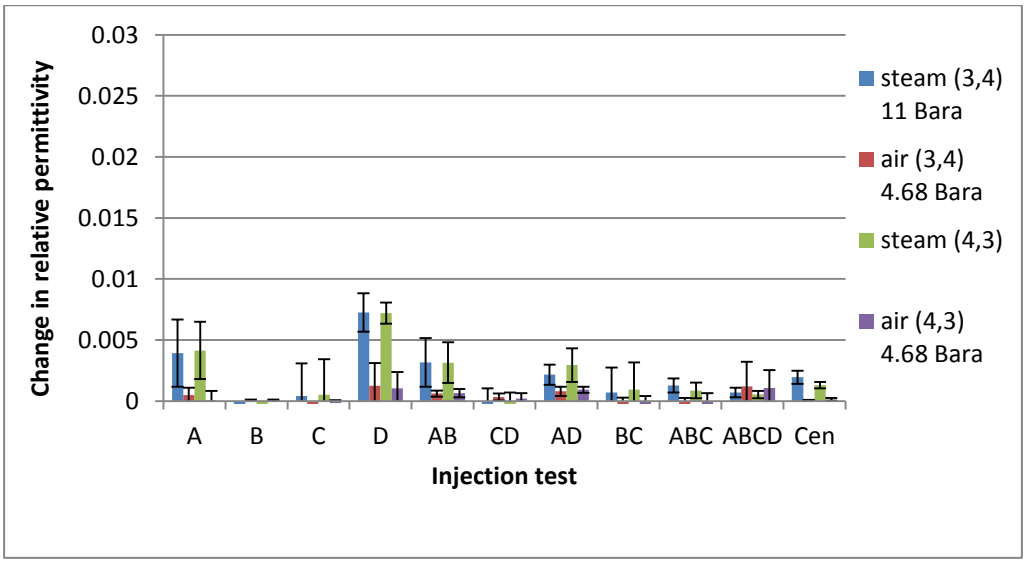


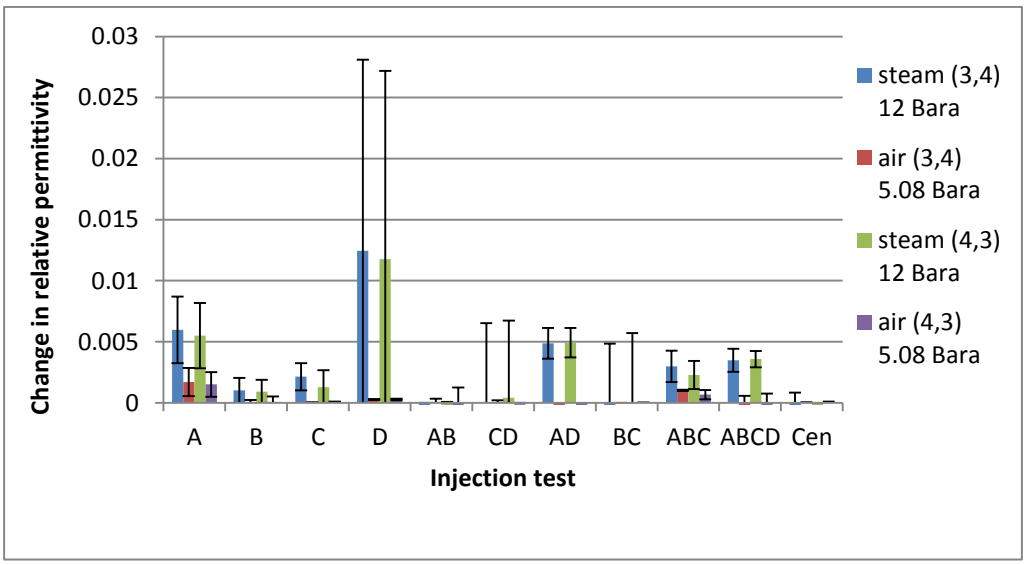




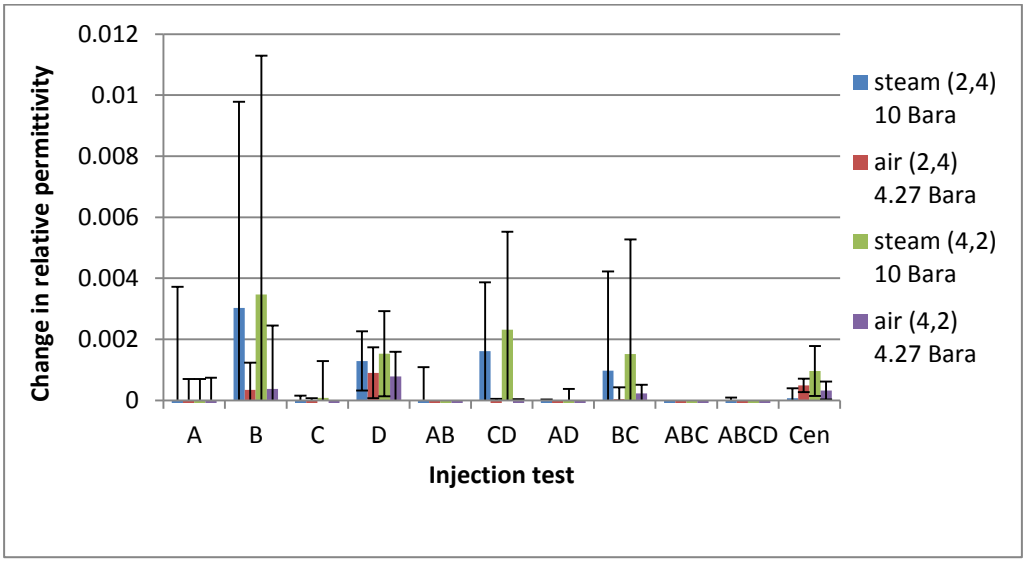
Results for electrode pairs (3, 4) and (4, 3):

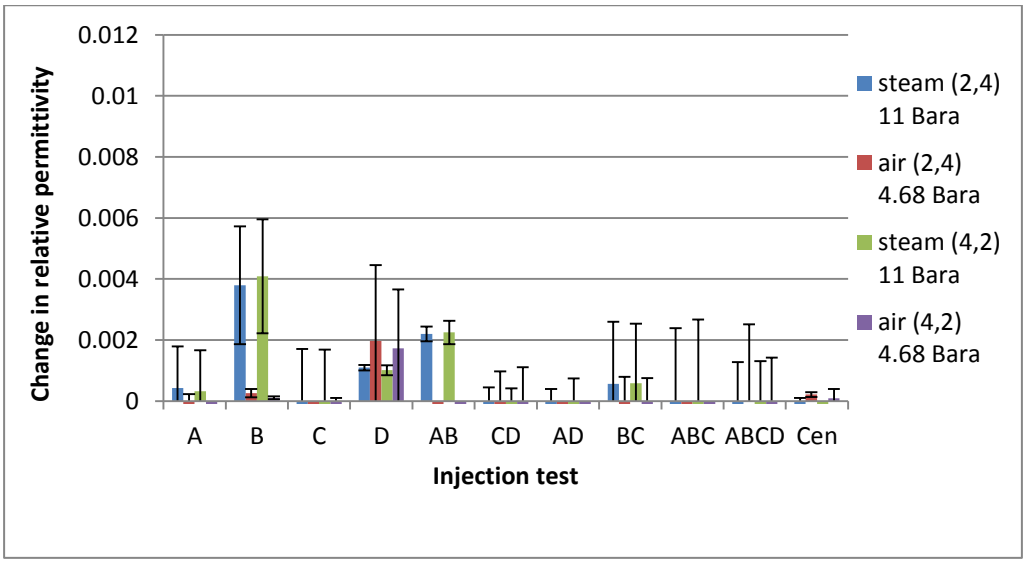


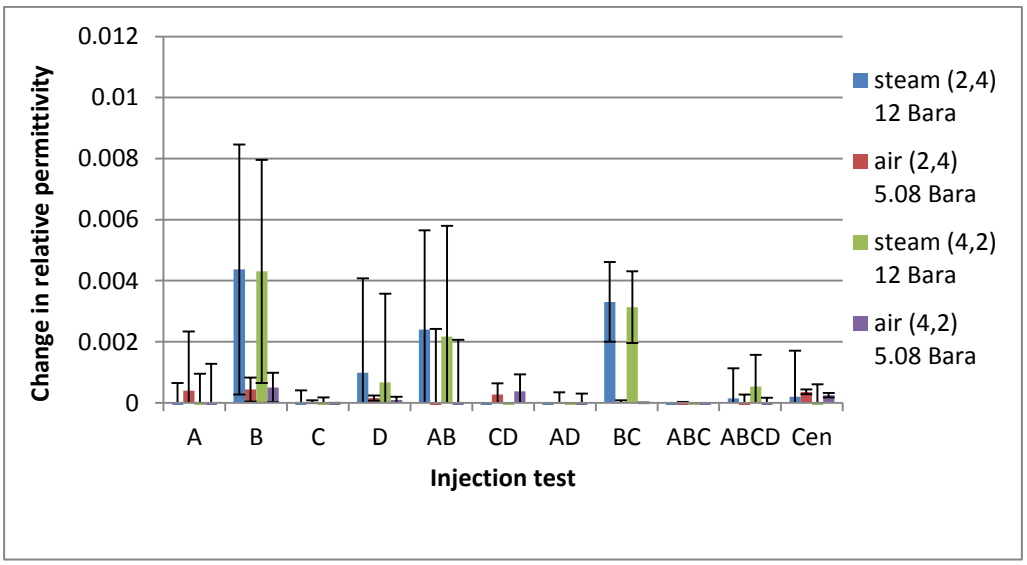




Results for electrode pairs (2, 4) and (4, 2):







9.3 Appendix 3

Maximum permittivity change for 1 droplet against the 3D capacitance program results

